# Nanostructures for surface plasmons

Junxi Zhang* and Lide Zhang

Institute of Solid State Physics, Key Laboratory of Materials Physics, Chinese Academy of Sciences, and Anhui Key Laboratory of Nanomaterials and Nanotechnology, Hefei 230031, China

*Corresponding author: jxzhang@issp.ac.cn

Received March 6, 2012; revised May 30, 2012; accepted May 31, 2012; published July 3, 2012 (Doc. ID 164047)

Surface plasmons (SPs) are electromagnetic excitations existing at the interface between a metal and a dielectric material. Control and manipulation of light based on SPs at the nanometer scale offers significant advantages in nanophotonic devices with very small elements, since the peculiar properties of SPs can be tailored by construction of nanostructures with various interfaces between metals and dielectric materials. Recent progress in nanostructures for SPs is reviewed. Resonance frequencies or wavelengths of SPs can be tuned by design of metal nanostructures, such as nanoparticles, nanorods, nanowires, nanosheets, and nanodisks. Moreover, SP resonance modes can also be tuned by control of the shapes and sizes of nanostructures, where the resonance modes include longitudinal and transversal resonances, dipolar and multipolar resonances, and Fano resonances. Based on SP coupling for metal nanostructures, metal–semiconductor nanostructures, metal–dielectric nanostructures, and metal–polymer nanostructures, propagating and guiding of SP can be achieved through the metal nanostructures and the hybrid structures. Additionally, metal nanostructures exhibit remarkable field enhancement effects (e.g., local near-field enhancement, and optical transmission enhancement) due to SP coupling. Furthermore, SP nanostructures perform unique focusing and imaging characteristics at the nanometer scale beyond the diffraction limit. Tailoring SPs by control of the nanostructures is expected to be used for design and development of high-performance optical components and circuits, which offer both potential and challenges for new generations of nanophotonic devices. 

OCIS codes: 160.4236, 240.6680, 230.3990

# Nanostructures for surface plasmons

Junxi Zhang and Lide Zhang

## 1. Introduction

With the rapid development of information and communication techniques, data transmission rates with ultrahigh speed require greatly increasing integration of photonic devices and circuits; it is estimated that data transmission rates will reach 10 Tbit/s by decreasing the element size of the photonic devices and circuits to the nanometer scale. However, it is very difficult for conventional photonic devices to reduce the element sizes to the nanometer scale because of the diffraction limit of light. Excitation of surface plasmons (SPs) can overcome the diffraction limit and provide a promising approach to control and manipulation of light at the nanometer scale.

A plasmon is a quantum of plasma oscillation of the free electrons, and the free electron gas has a collective oscillation relative to the fixed positive ions in a metal. Plasmons with the collective oscillation of the free electrons exhibit unique optical properties: the dielectric constant of the metal $\varepsilon_m$ has the free electron form

$$\varepsilon_m = 1 - \frac{\omega_p^2}{\omega^2}, \tag{1}$$

where $\omega_p$ is the resonance frequency of bulk plasma. For many metals the frequency is in the UV wavelength region. It is noted that light is reflected when the frequency is below the plasma frequency, because the electrons in the metal screen the electric fields of light. However, light with a frequency above the plasma frequency is transmitted, because the electrons cannot respond fast enough to screen it. Metals are shiny in the visible region because their plasma frequencies are in the UV region.

Surface plasmons (SPs) are those plasmons with collective electron oscillations that are confined to an interface between a metal and a dielectric. Furthermore, the combined excitation is called a surface plasmon polariton (SPP) when a SP is coupled with a photon. The SPPs are surface electromagnetic waves that propagate along the interface between the metal and the dielectric.

To understand how to excite the SPPs, first consider a *p*-polarized wave (TM mode for which the electric field vector is parallel to the incident plane) impinging on a smooth planar interface. When an incident angle is larger than a particular critical angle, total internal reflection occurs at the interface [1]. As a result, some surface charges (free electrons) with a collective oscillation are excited at the interface (Fig. 1(a)) [2], causing

Figure 1

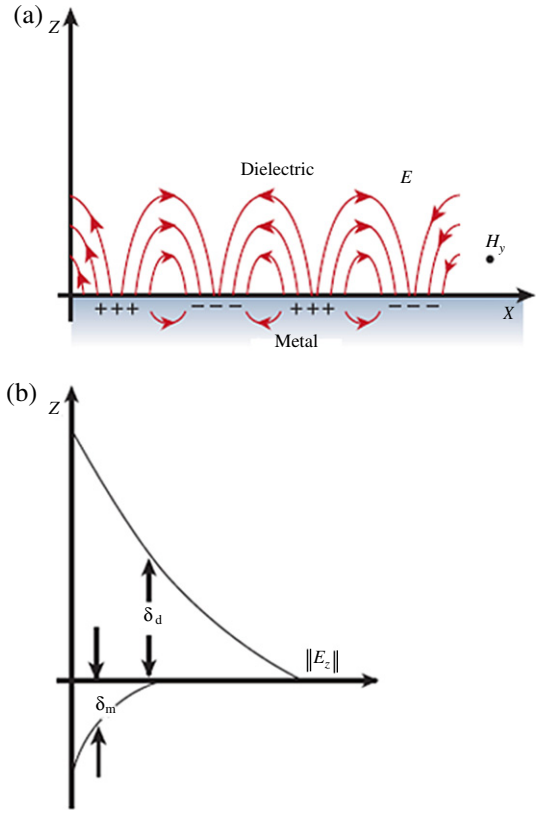


(a) Schematic illustration of electromagnetic wave and surface charges at the interface between the metal and the dielectric material. (b) The locally electric field component is enhanced near the surface and decays exponentially with the distance in a direction normal to the interface. Reproduced with permission from Box 1a and 1b, Ref. [2], © 2003 NPG.

SPP waves to be excited when the oscillating free electrons couple with the photons from the incident wave.

The SPP dispersion relation [2,3]

$$k_{\mathrm{SPP}} = k\sqrt{\frac{\varepsilon_d \varepsilon_m}{\varepsilon_d + \varepsilon_m}} \tag{2}$$

exhibits nonlinear characteristics: the momentum ($\hbar k_{\mathrm{SPP}}$) of the SPP wave is larger than that of the light in free-space photon ($\hbar k$) for the same frequency, which results in a momentum mismatch between the light and the SPP. Such a mismatch must be overcome by coupling light and SPP modes at the interface. Therefore increasing and compensating momentum is indispensable for the excitation of the SPP waves. The momentum of light and the SPP can be matched by using different coupler configurations such as prism couplers [4–7], grating couplers [4–7], fiber and waveguide couplers [8]. Since the SPP momentum is larger than that of the light in free space, the wavelength of the SPPs is shorter than that of the light, and the speed of the SPPs is also slower during wave propagation. As a result, the light can be confined

at the subwavelength or nanometer scale. When

$$\varepsilon_d + \varepsilon_m = 0, \tag{3}$$

the surface charges can generate collective oscillation and SPPs can be excited. In terms of Eq. (1), the SPP frequency is given by

$$\omega_{\mathrm{SPP}} = \frac{\omega_p}{\sqrt{1+\varepsilon_d}}. \tag{4}$$

It can be seen that the SPP frequency is lower than the bulk plasma frequency $\omega_p$.

As mentioned above, the excited SPP waves have associated evanescent fields penetrating into both the dielectric and the metal; they are spatially decaying fields in a direction normal to the interface (e.g., $E_d \propto \exp(-k_{zd}z)$ for $z > 0$, and $E_m \propto \exp(k_{zm}z)$ for $z < 0$) (Fig. 1(b)), where $E_d$ and $E_m$ are the electric fields in the dielectric and the metal, respectively, $K_{zd}$ and $K_{zm}$ correspond to the normal components of the wave vectors in the two media. Furthermore, the penetration depths in the dielectric and the metal, $\delta_d$ and $\delta_m$, are given by [3]

$$\delta_d = \frac{1}{k}\left|\frac{\varepsilon_d + \varepsilon_m}{-\varepsilon_d^2}\right|^{1/2} \tag{5}$$

and

$$\delta_m = \frac{1}{k}\left|\frac{\varepsilon_d + \varepsilon_m}{-\varepsilon_m^2}\right|^{1/2}. \tag{6}$$

Furthermore, the penetration depths can be estimated based on Eqs. (5) and (6). For example, if the metal and the dielectric are silver and silicon oxide, respectively, for a 620 nm wavelength ($\varepsilon_d = 2.127$ and $\varepsilon_m = -15.037 + i1.017$ [9]), $\delta_d = 167.0$ nm and $\delta_m = 23.6$ nm, while for 400 nm wavelength ($\varepsilon_d = 2.160$, $\varepsilon_m = -3.773 + i0.675$ [9]), $\delta_d = 39.0$ nm and $\delta_m = 22.0$ nm. Note that the penetration depth in the dielectric is larger than that in the metal (Fig. 1(b)), and the difference in the penetration depths becomes more distinct for long wavelengths. Based on the short penetration depths of the electric fields of SPPs in the dielectric and the metal, the electric fields of SPPs are concentrated mainly near the interface, and the field concentration is remarkably enhanced at the interface. Nevertheless, the field concentration of SPPs diminishes rapidly away from the interface along the $z$ direction, and the field concentration is larger in the dielectric than in the metal.

SPs in bounded geometries are called localized surface plasmons (LSPs) [10,11]. The LSPs are localized surface electromagnetic excitations existing on those bounded geometry surfaces such as metallic particles and voids of various topologies. The main difference between the SPPs and the LSPs is that the SPPs are propagating surface waves, while the LSPs are nonpropagating excitations of the free electrons of metallic structures coupled to the electromagnetic field. Furthermore, the curved surface of the bounded geometries (e.g., nanoparticles) demonstrates an effective restoring force on the driven electrons, resulting in resonance occurring on the surface, called surface plasmon

resonance (SPR) or localized surface plasmon resonance (LSPR) (e.g., for metallic nanostructures). On the other hand, the excitation conditions are different for the LSPs and the SPPs. The LSPs (LSPR) can be excited by direct light illumination, whereas the SPPs can be excited by matching the frequency and the momentum between the excitation light and the SPPs.

In recent years, fundamental research and development of SP-based nanostructures and devices have received increasing interest because of their unique properties and applications in waveguides, sources (e.g., lasing), near-field optics, nonlinear optics, surface enhanced Raman spectroscopy (SERS), data storage, solar cells (or photovoltaic devices), chemical sensors, biosensors, etc. [2,3].

For instance, integration of multiple silver nanowires with polymer optical waveguides has been used in SPP waveguides for nanoscale confinement and guiding of light on a chip [12]. The waveguide structures can be used to couple light into many nanowires in parallel, which provides a new opportunity in highly integrated photonic circuits. Additionally, nanometer-scale plasmon lasers have been achieved by using a hybrid SPP waveguide consisting of a high-gain CdS nanowire on top of a silver substrate with a separated nanometer-scale insulating layer of $MgF_2$ [13]. The longitudinal cavity mode resonance between the reflective nanowire end facets demonstrates sufficient material gain to achieve full laser oscillation and strong mode confinement with a mode area as small as $\lambda^2/400$. As a result, the deep subwavelength plasmon lasers at visible frequencies suggest new sources that can produce coherent light far below the diffraction limit. Moreover, manipulation of light by means of SPPs propagating along the metal surface can not only allow superlensing, but also provide nanoimaging beyond the diffraction limit based on the LSP mode at the tip of a metal nanoprobe [14]. Recently, a plasmonic Au nanorod metamaterial has offered nonlinear enhancement effects based on the nonlocality of longitudinal SP resonance modes [15]. The nanorod metamaterial can be used for ultrafast low-power all-optical information processing in subwavelength devices owing to the anomalously large changes in optical density.

In addition, a large SERS signal has been detected at silver nanoparticle–nanowire junction located remotely from the laser illumination spot with sensitivities in the few-molecules range [16]; the propagating SPPs as a remote excitation source function as multisite remote-excitation SERS sensing because of the field enhancements. Five-dimensional (integration of wavelength, polarization, and spatial dimensions) optical recording has been performed by exploiting the unique properties of the longitudinal SPR of Au nanorods [17]. Recording using longitudinal SPR-mediated two-photon luminescence can provide an enhanced wavelength and angular selectivity compared with conventional linear detection mechanisms, and a recording disk capacity of 7.2 Tbyte; a recording speed up to 1 Gbit/s can be obtained. Furthermore, plasmonic metal nanostructures offer a considerable reduction in the physical thickness of solar photovoltaic absorber layers (tens to hundreds of nanometers thick) [18], which results in trapping light in thin-film solar cells with increased absorption because of SPs. In this case the extremely thin photovoltaic absorber layers can be expected

to absorb the full solar spectrum with high efficiency. Metamaterials demonstrate a remarkably improved sensitivity for biosensing due to their ability to confine light to the nanoscale regions with field enhancements [19]. Moreover, infrared plasmonic metamaterials based on Fano resonant asymmetry exhibit sharp resonances caused by the interference between subradiant and superradiant modes. As a result, a multipixel array of Fano-resonant asymmetric metamaterials offers a promising platform for multispectral biosensing of nanometer-scale monolayers of recognition proteins and their surface orientation, as well as for detecting chemical binding of target antibodies to recognition proteins [20].

One of the major driving forces in the application of SP fields is manipulation and confinement of light at the subwavlength or the nanometer scale beyond the diffraction limit of light, where the peculiar SP properties are exhibited. Furthermore, the SP properties can be tailored by designing various nanostructures: different interfaces between metal and dielectric nanostructures will exhibit different behaviors involving SP resonances, coupling, propagating, focusing, and imaging. Therefore, construction of novel nanostructures for SPs is indispensable to both the fundamentals of SPs and their potential applications.

Current publications covering a broad area of SPs (or plasmonics), including near-field optics, SERS, waveguides, superresolution, data storage, and sensing, are mostly focused on applications and theory of SPs. However, the survey of SP properties in nanostructures with various configurations is quite limited. This review presents a comprehensive overview of more up-to-date and detailed advances in nanostructures for SPs, and the article is focused mainly on tailoring and modulation of SP properties through the design of different nanostructures. The overview presented is aimed at extending the research area of plasmonics and nanophotonics, as well as proposing new opportunities for significant applications of SPs.

The main contents of this review are presented in seven sections: the next two sections (Sections 2 and 3) present tuning frequencies (or wavelengths) of LSPs by means of metal nanostructures. In Sections 4 and 5, we review coupling, propagating, and guiding of SPPs by use of metal nanostructures and their hybrid structures. We then discuss field enhancement effects of SPs with various nanostructures in Section 6. Sections 7 and 8 address focusing and imaging of SPs performed by use of metal nanostructures. Brief conclusions and remarks on SPs are presented in the final section.

## 2. Tuning Frequencies of Localized Surface Plasmons by Metal Nanostructures

Surface plasmon (SP) modes in bounded geometries are localized surface plasmon (LSPs) [10,11]. The LSPs are surface electromagnetic excitations existing on bounded metal surfaces such as metal particles and voids of various topologies. That is, the bounded surfaces with curved geometries (e.g., nanoparticles) demonstrate an effective restoring force on the

driven electrons, which give rise to a resonance on the surface, the resonance is called surface plasmon resonance (SPR) or localized surface plasmon resonance (LSPR) (e.g., for metal nanostructures). A LSPR originates from absorption and scattering contributions when light reaches the surfaces of the metal nanostructures because of the collective oscillations of free electrons. Moreover, the parameters of the metal nanostructures (e.g., composition, size, and shape) have an influence on the resonance frequencies or wavelengths of the LSPs. For many metals such as Pb, In, Hg, Sn, and Cd, the resonance frequency lies in the UV spectral regions, and small metal structures do not display a strong color effect. Moreover, such small metal structures are also readily oxidized, which strongly prevents LSP excitation. However, the noble metals (e.g., Ag and Au) are exceptional because of their good stability in the air, and their LSPR frequency is pushed into the visible parts of the spectrum owing to their *d*–*d* band transitions. Hence, the excitation of LSPs is most commonly carried out for noble metal nanostructures; thus, the current reports on metal nanostructures for LSPs cover mainly noble metal nanostructures. Within these, the configurations of the metal nanostructures for LSPs involve mainly nanoparticles, nanorods, nanowires, nanosheets, and nanodisks (Fig. 2).

## 2.1. Metal Nanoparticles

The most rapidly growing number of reports on metal nanostructures for LSPs are focused on metal nanoparticles, which include mainly nanospheres, nanoprisms, nanocubes, nanocages, and nanoshells (Figs. 2(a)–2(e)).

### *2.1a. Nanospheres*

El-sayed and co-workers prepared Au spherical nanoparticles by a solution phase method [21]. A chlorauric acid ($HAuCl_4$) solution containing 5 mg of Au was refluxed, and a 1% sodium citrate solution was added to the boiling solution; after the reduction of the Au ions by the citrate ions, the solution was further boiled and then left to cool to room temperature. The prepared Au nanoparticles are nearly spherical, and their average diameter is about 20 nm. Moreover, larger particles can be obtained by the reduction of $HAuCl_4$ with hydroxylamine hydrochloride in the presence of already existing Au nanoparticles. The reducing agent hydroxylamine hydrochloride cannot act as a nucleating but only as a growth agent in slightly acidic conditions. It is demonstrated that the LSP resonance (or LSPR) absorption peaks are clearly visible and undergo redshifts (from 517, 521, 533, to 575 nm) when the nanoparticle size increases (from 9, 22, 48 to 99 nm). For Au nanoparticles that are small compared with the wavelength of light (e.g., with a diameter smaller than 25 nm), the LSPR occurs when $\varepsilon_{mr}(\omega) = -2\varepsilon_d$ based on Mie theory (dipolar modes) [21,22], where $\varepsilon_{mr}$ and $\varepsilon_d$ are the real component of the metal dielectric constant at frequency $\omega$ and the dielectric constant of the dielectric material, respectively. Furthermore, the shifts of the resonance peak result from the change in dielectric constant of the metal nanoparticles due to surface

Figure 2

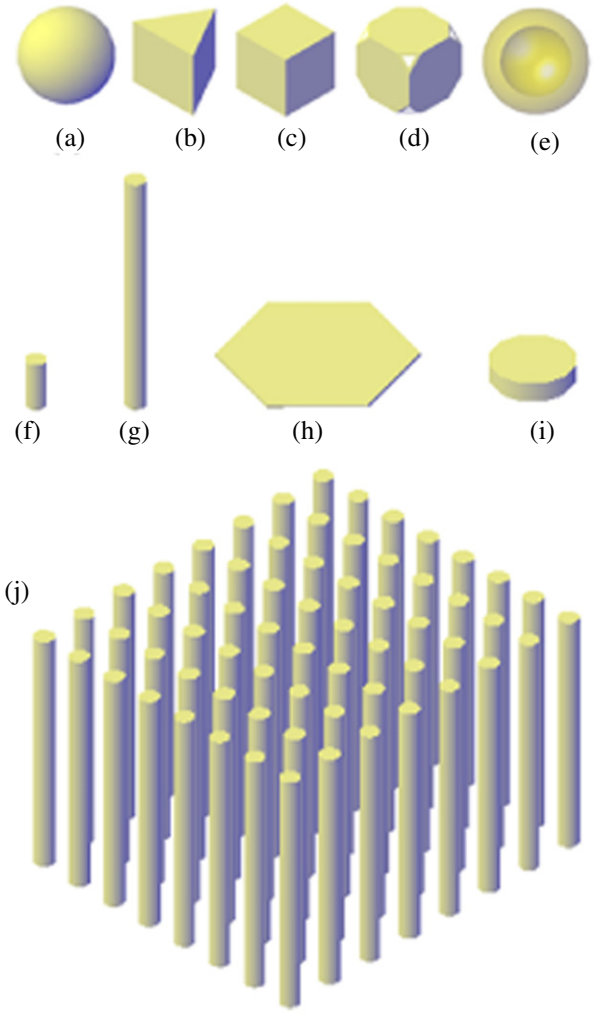


Schematic illustration of configurations of metal nanostructures for LSPs. The sizes are at the nanometer scale (note that nanowire diameter is at the nanometer scale, while nanowire length can be at the micrometer scale): (a) nanosphere, (b) nanoprism, (c) nanocube, (d) nanocage, (e) nanoshell, (f) nanorod, (g) nanowire, (h) nanosheet, (i) nanodisk, and (j) nanowire array.

scattering [22], which is dependent on a particle size smaller than the mean free path of free electrons. For larger nanoparticles (e.g., diameters larger than 25 nm), multipolar (high-order) modes appear; the resonance peak is shifted to longer wavelengths, and its bandwidth increases with increased particle size owing to phase retardation effects. In this case, the absorption band is the superposition of the different multipolar modes.

When nanoparticles are composed of various metals, the composition of the nanoparticles will influence the LSPR properties. For example, bimetallic Au and Ag nanoparticles, usually prepared by simultaneous reduction of the metal salts, have raised particular interest because of both their intense LSPR bands in the visible (around 520 and 400 nm for spherical nanoparticles of Au and Ag, respectively) and their similar fcc crystal lattice constants (4.078 Å for Au, 4.086 Å for Ag).

Figure 3

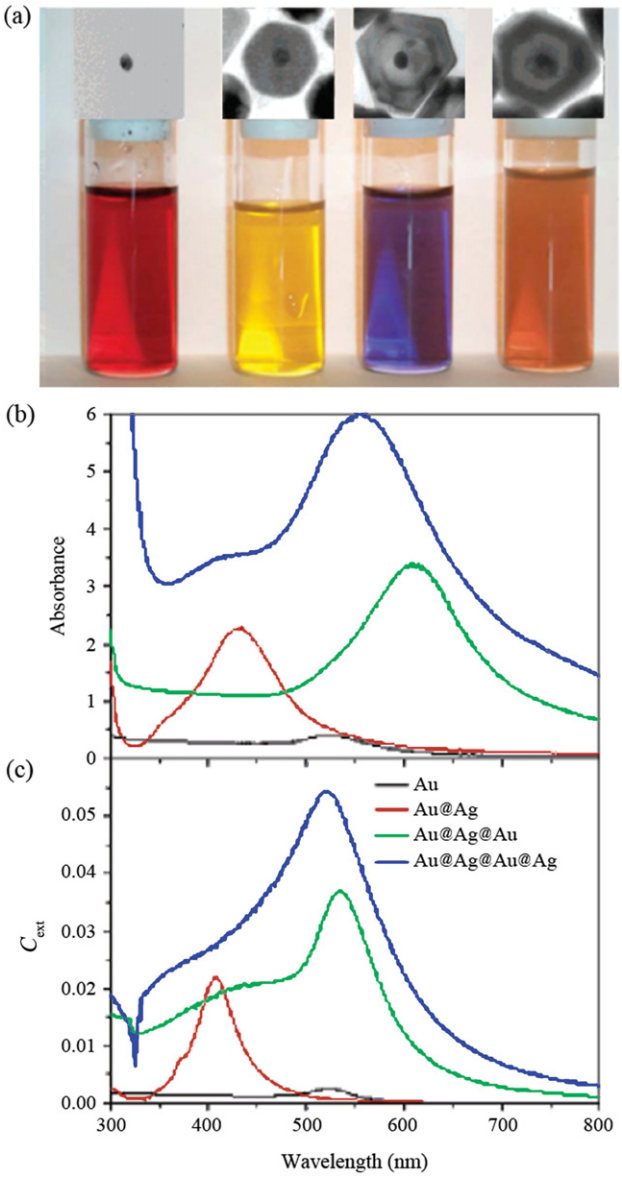


(a) Photographs showing the color change in colloidal dispersions of Au–Ag nanoparticles with an increasing number of layers. (b) UV–visible spectra of colloids containing Au and Au–Ag nanoparticles after the various reduction and deposition steps. (c) Extinction spectra calculated using Mie theory for multilayer concentric spheres: average total particle diameters are 17, 49, 82, and 98 nm for Au, Au/Ag, Au/Ag/Au, and Au/Ag/Au/Ag, respectively. Reproduced with permission from Figs. 4, 5a, and 5b, Ref. [23]. © 2006 ACS.

Moreover, there is a linear relationship between the composition and the resonance band position [23], and the band position lies between those for pure Au and Ag nanoparticles. Furthermore, photographs of various compositions exhibit a continuous color change between yellow and red with increasing Au concentration. On the other hand, core-shell Au and Ag nanoparticles with different layers demonstrate a structure

dependence of LSPR properties [23,24]. Figure 3(a) demonstrates the color change in the Au–Ag nanoparticles with an increasing number of layers. It can be seen that the Au nanoparticles are deep red; upon deposition of an Ag shell, they turn yellow. A second Au shell leads to a blue hue, while deposition of a second Ag shell yields an orange color. This spectacular color change correlates well with large shifts of the corresponding extinction spectra after each deposition step (Figs. 3(b) and 3(c)). The precise position of the resonance bands and the shape of the spectra are found to be very sensitive to the layer thickness. Therefore the LSP resonance frequency can be tuned by the composition of the bimetallic nanoparticles and their layer thickness.

### *2.1b. Nanoprisms*

Many reports have focused on the synthesis and unique optical properties of metal nanoprisms [25–27]. These metal nanoprisms, with large shifts of the LSP resonance wavelengths from visible to infrared regions, will have potential application in biosensors.

Mirkin and co-workers demonstrated conversion of Ag nanospheres into triangular Ag nanoprisms by using a photoinduced method [25,26]. A colloidal suspension of Ag spheres with a diameter smaller than 10 nm was fabricated; then the colloidal Ag nanospheres, passivated with sodium citrate and bis (*p*-sulphonatophenyl) phenylphosphine dihydrate dipotassium, were irradiated with a narrowband xenon lamp light source (center wavelength of 550 nm) for about 50 h. The TEM image shows that the nanoprisms consist of two different sizes (Fig. 4(a) and inset): smaller particles (designated type 1) with an average edge length of 70 nm, and larger particles (designated type 2) with an average edge length of 150 nm. Additionally, the bimodal particle growth process can be monitored by observing the LSP absorption spectra (Fig. 4(b)). It is found that the absorption band at 395 nm disappears for the spherical Ag particles when the irradiation time increases. As a result, two new and strong resonance bands at 680 and 1065 nm appear, which are associated with type 1 and type 2 nanoprisms, respectively. Furthermore, the band for type 1 nanoprisms is initially centered at 680 nm and gradually shifts to 640 nm. This blueshift originates from the tip sharpness of the nanoprisms, while the second strong LSPR band at 1065 nm is assigned with type 2 nanoprisms [25].

In addition, Ag nanoprisms with strong resonance bands in the communication wavelengths have been obtained by a modification of the photoinduced method (e.g., illumination of small Ag nanoparticle seeds), and nanoprisms with high aspect ratios can be synthesized by controlling the illumination conditions. Specifically, the nanoprisms have average lateral dimensions of 110 and 242 nm when LEDs with emission bands centered at 518 nm (green LEDs) and 653 nm (red LEDs), respectively, are used. As a result, the in-plane resonance wavelengths are 621 and 1037 nm with the illumination wavelength of 518 nm. This corresponds to resonance wavelengths of the smaller (side length of 51 nm) and larger nanoprisms (110 nm) formed by using the same illumination wavelength, which are 960 and 1490 nm with the illumination wavelength of 653 nm. Moreover, the nanoprisms formed by illumination of fluorescent tubes with green (546 nm) and

Figure 4

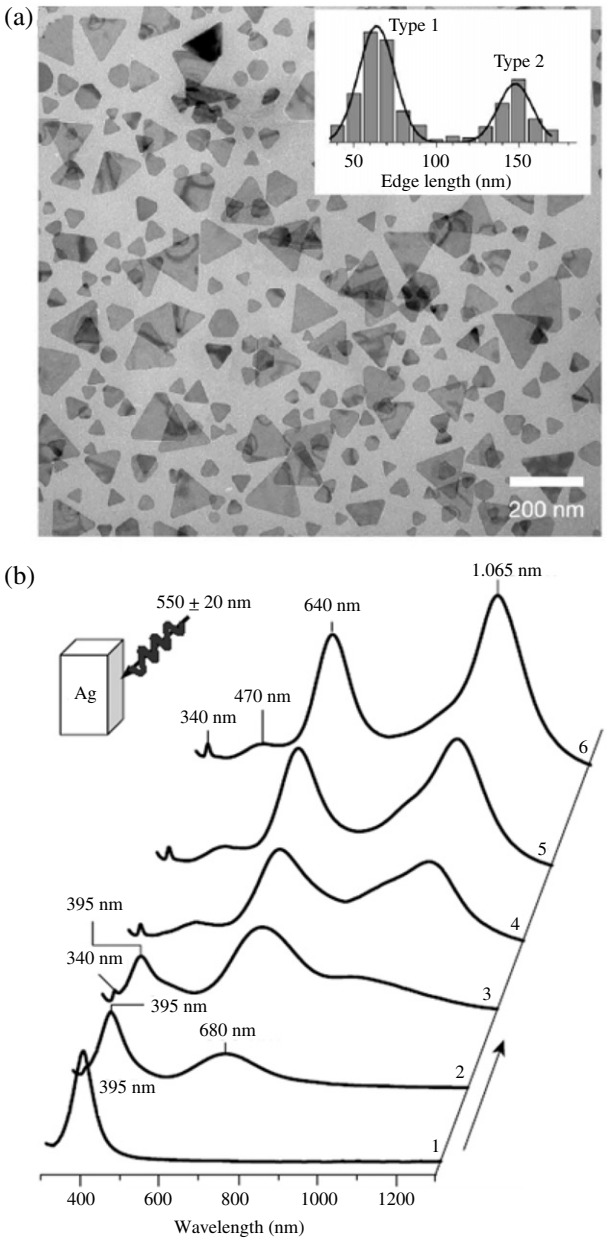


(a) TEM image of Ag nanoprisms formed using single-beam excitation (550 ± 20 nm); inset, histograms used to characterize the size distribution as bimodal. (b) Time evolution of UV–vis–NIR spectra of a silver nanoprism colloid (4.8 ± 1.1 nm spheres). Spectrum 1, initial colloid; 2, after 10 h via the irradiation; 3, after 15 h; 4, after 19 h; 5, after 24 h; and 6, after 55 h. Reproduced with permission from Figs. 1a and 2a, Ref. [25]. © 2003 NPG.

red (610 nm) color filters have side lengths of 123 and 174 nm; the in-plane resonance main wavelengths correspond to 1076 and 1294 nm, respectively.

The reports on LSPR properties of the nanoprisms described above demonstrate an average effect from a large number of nanoprisms.

Recently, Nelayah *et al.* presented a novel method for mapping the spatial variation of LSPs on a single triangular Ag nanoprism by using electron beams instead of photons [28]; this method relies on the detection of LSPR in an electron energy-loss spectroscopy (EELS) of subnanometer electron beams rastered on the nanoprisms. The EELS measurements were carried out in a VG-HB501 scanning transmission electron microscope and fitted with a Gatan 666 spectrometer. Spectra were recorded by using the so-called spectrum-imaging (spim) mode [29], in which the 1 nm diameter focused electron probe was rastered, with a constant spatial displacement of 1–4 nm, over two-dimensional regions of the sample. Figure 5(a) shows deconvoluted electron energy-loss spectra at three distinct positions (A = triangle corner; B = triangle edge; and C = triangle center) on a 10-nm-thick equilateral triangular nanoprism with 78 nm long sides. The spectra vary considerably from one position to the next. Four resonance frequencies are identified at 1.75, 2.70, 3.20, and 3.65 eV, respectively. In comparison, spectra acquired at the corner of a 25 nm long equilateral nanoprism (curve $\alpha$) and at the center of a reference 20 nm quasi-spherical nanoparticle (curve $\beta$) from the same sample are represented by dotted curves. In the latter spectra, the Ag bulk plasmon resonance is at 3.80 eV [30], while the LSPR frequency is found at 3.00 eV. Significant variations in the relative intensities of the different modes are observed as the probe is scanned over the nanoparticle. This effect is quantified by an automatic estimate of the spectrum intensity at the maxima of the different resonances. The amplitude distributions of the first three modes of Ag nanoprisms exhibit a typical threefold behavior characteristic of equilateral triangular prisms: the peaks of the resonance modes at the corners, the edges, and the center of the nanoparticle (Figs. 5(c)–5(e)). The highest energy mode is barely resolved even after deconvolution. The feasibility of mapping the spatial variation of LSPR in the NIR–visible–UV domain shows a spatial accuracy of the order of $\lambda/40$, where $\lambda$ is the wavelength of the related excitation (e.g., 709 nm).

The noble metal nanoparticles described above are not arranged in order, and the spacing of the nanoparticles is variable; in this case the resonance peak is a wide absorption band due to the statistical average effects resulting from the different spacings of the nanoparticles.

Van Duyne and co-workers presented a nanosphere lithography approach to fabricating noble metal nanoparticle arrays [31–38]. Nanosphere lithography is a powerful fabrication technique used to inexpensively produce nanoparticle arrays with controlled spacing and size of nanoparticles. First, a monolayer of hexagonally close-packed nanospheres is self-assembled to form a two-dimensional colloidal crystal deposition mask. The deposition of nanospheres onto the desired substrate can be achieved by spin coating [31], drop coating [32], and thermoelectrically cooled angle coating [39]. These deposition methods require that the nanospheres be able to freely diffuse across the substrate for the requirements of lower-energy configuration. Then the metal is deposited at the threefold interstices on the mask, and the array of triangularly shaped nanoparticles with $P_{6mm}$ symmetry is obtained. The size of the nanoparticles is easily tuned by changing the nanosphere mask diameter and the deposited metal thickness. The resonance wavelength can be systematically tuned from 400 to

Figure 5

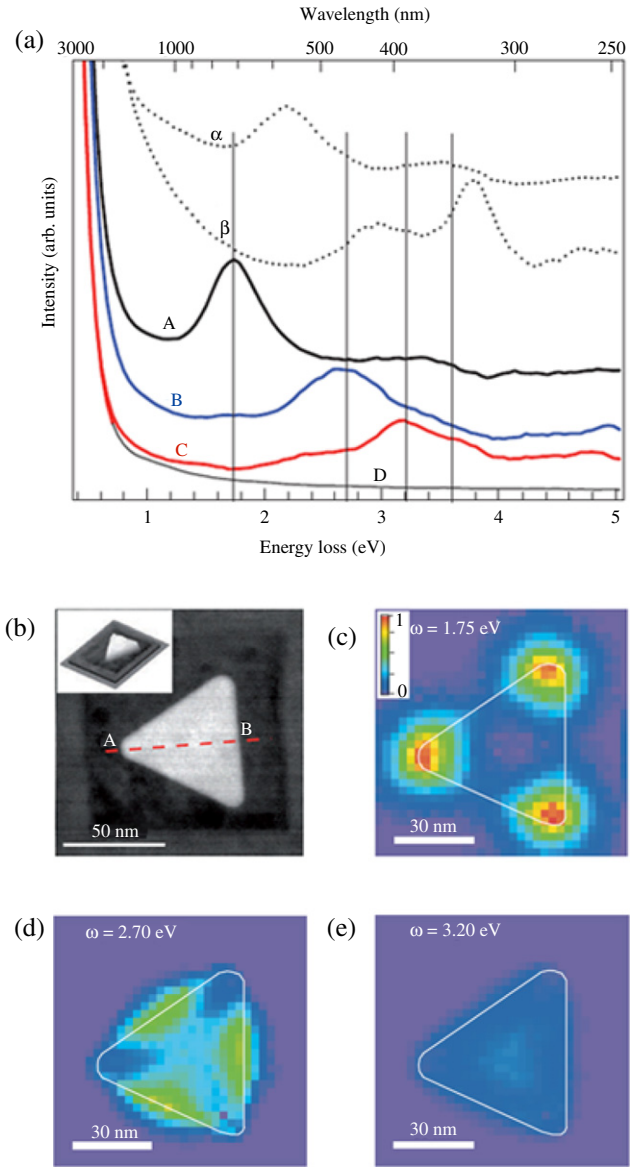


(a) Deconvoluted electron energy-loss spectra (solid curves) measured at, curve A, the corner; B, the edge; and C, the center of the particle; together with D, the spectrum of the mica support. (b) High-angle annular dark-field scanning TEM (STEM) image of the particle. (c)–(e) Distribution of the modes centered at (c) 1.75, (d) 2.70, and (3) 3.20 eV. The outer contour of the particle, deduced from its high-angle annular dark-field image, is shown as a white outline. Reproduced with permission from Figs. 1a, 2a, and 3a, Ref. [28]. © 2007 NPG.

6000 nm by choosing the appropriate nanoparticle width or height [34]. In addition, Van Duyne and co-workers explored the electromagnetic interactions between noble metal nanoparticles by measuring the extinction spectra of two-dimensional arrays of Au and Ag cylinders and trigonal prisms [35]. The extinction spectra typically have a maximum in the 700–800 nm region of the spectrum, and when the lattice spacing decreases, the resonance bands of Au and Ag nanoparticle arrays

demonstrate obvious blueshifts that are due to the radiative dipolar coupling between the nanoparticles and retardation effects.

### 2.1c. Nanocubes

It is noted that two LSPR peaks cannot be obtained for spherical nanoparticles unless the particles are partially embedded in the surface. This indicates that a nanoparticle in contact with a dielectric substrate is shape and size dependent for LSPR behaviors. Cube-shaped nanoparticles are ideal for the production of two resonance peaks, as large polarizations are induced on both top and bottom surfaces of the nanoparticles. For a nonspherical metal nanoparticle, especially a metal nanocube deposited on a dielectric substrate, the plasmon-induced surface charges are located closer to the dielectric screening charges from the surface of the substrate. As a result, the LSPR properties of the metal nanocubes are remarkably altered by the presence of the substrate.

Schatz, Van Duyne, and co-workers observed a new LSPR effect for a single Ag nanocube located on a glass substrate [40]. The Ag nanocube was prepared by a polyol process [41,42]. It was found that there are two resonance peaks when a Ag nanocube interacts with a glass substrate, one of which is redshifted relative to the bulk spectrum (peak 2), and the other blueshifted (peak 1) and considerably narrower (Fig. 6(a)) [40]. Note that the blueshifted peak is quite a bit narrower than the redshifted peak. To understand the physical origin of these peaks, they explored the near-field behaviors for peaks 1 and 2 based on the finite difference time domain (FDTD) calculation, this time for a larger nanocube (90 nm), as well as for a series of scattering spectra that are generated by moving the nanocube toward the surface. Peak 1 is associated with large fields farther from the surface, while peak 2 is associated with large fields closer to the surface (Figs. 6(c) and 6(d)). These spectra show that the dipolar mode associated with the solution spectrum shifts into a broad peak at 550 nm when the nanocube gets within a few nanometers of the surface (Fig. 6(b)). In addition, a peak appears at 430 nm that becomes more distinct as the particle approaches the surface. The single Ag nanocube can offer new opportunities in chemical sensing applications.

Recently, Xia and co-workers reported a simple and robust approach based on seeded growth for producing Ag nanocubes with edge lengths over a broad range of 30–200 nm [43,44]. In a typical synthesis, single-crystal Ag seeds in a spherical or cubic shape were first prepared by means of a polyol process that used $CF_3COOAg$ as a precursor to elemental Ag [45]. The seeds were collected and then mixed with $AgNO_3$ in ethylene glycol at an elevated temperature to form Ag nanocubes. Furthermore, the sizes of Ag nanocubes were varied by adjusting the amounts of Ag seeds and/or $AgNO_3$ added into the reaction system. The edge length of these Ag nanocubes increased from 36 to 58, 99, 144, and 172 nm, respectively, when the amount of $AgNO_3$ added into the reaction solution increased from 10 to 50, 75, 100, and 200 μL. The major LSPR peaks of these Ag nanocubes display a continuous redshift from 430 to 468, 497, 513, and 537 nm, and the Ag nanocubes obtained from the reactions with the addition of 50, 75, 100, and 200 μL of $AgNO_3$ exhibit relatively broad resonance peaks, which can be attributed to their large sizes and thus the involvement of multipole excitations in

Figure 6

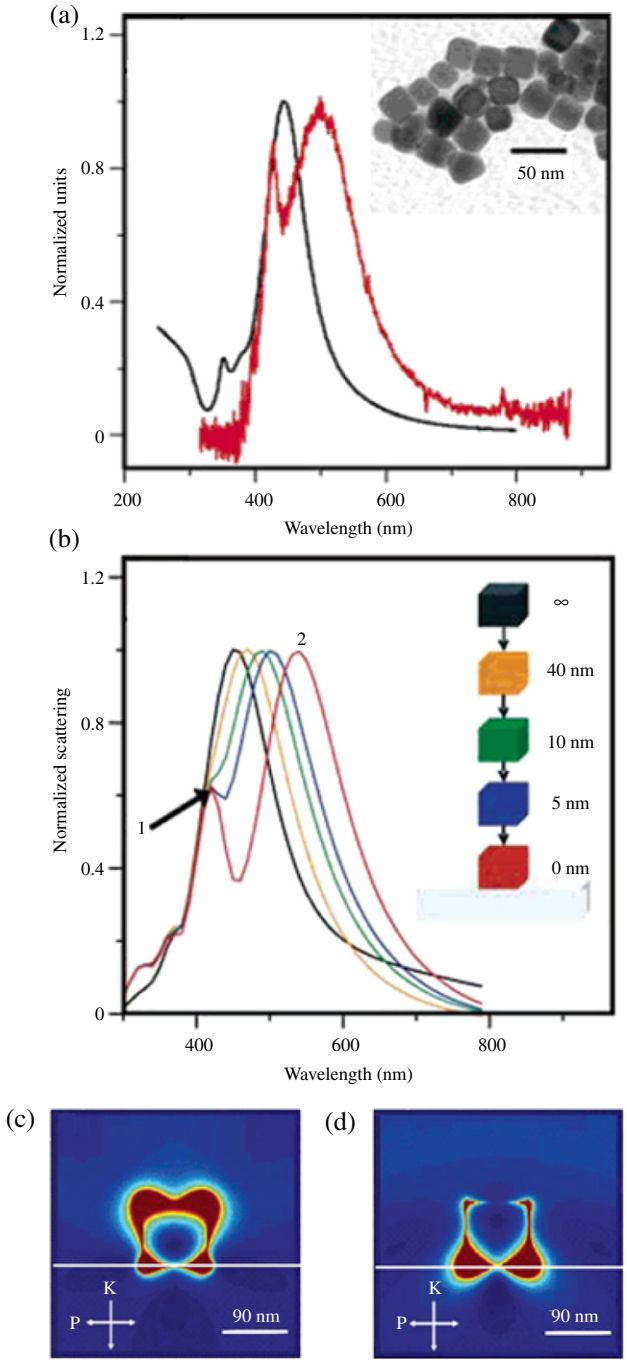


(a) LSPR spectra of nanocube ensemble extinction (black) and single nanocube dark-field scattering (red) in an $H_2O$ environment. (b) FDTD theory showing the emergence of a second peak as a single nanocube (90 nm diameter) approaches a dielectric substrate. (c), (d) the field intensities for peaks 1 and 2 of the nanocube in contact with the substrate (the white line in the field pattern images represent the substrate). Reproduced with permission from Figs. 1A and 2, Ref. [40]. © 2005 ACS.

addition to dipole excitation [46]. Moreover, the edge length of Ag nanocubes increases from 38 to 40, 45, 56, and 76 nm by adding 300, 200, 100, 50, and 20 μL of the single-crystalline Ag seeds to the reaction solutions, followed by the addition of 50 μL of $AgNO_3$. As the number of Ag seeds in the reaction solution decreases, the edge length of the Ag nanocubes increases. The major resonance peaks of these Ag nanocubes also demonstrate a continuous redshift from 400 to 489 nm with increasing edge length. These results suggest that both methods of quenching the reaction at different times and varying the amount of $AgNO_3$ precursor added into the reaction solution provide reliable and precise routes to adjust Ag nanocubes in a broad range of sizes. On the other hand, it is found that the local field enhancement is located around the sharp corners of the nanocubes [46]; the field enhancement factor is very large. The result indicates that the metal nanocubes can be expected to be applied to surface enhanced Raman spectroscopy (SERS) because of to their large field enhancement effects.

If one combines Au and Ag into a core-shell configuration, its resonance frequency can be potentially tailored and finely tuned by varying the size and shape of the core, the thickness of the shell, and the coupling between the core and the shell.

Recently, Xia and co-workers reported an easily managed route to the synthesis of Au/Ag core-shell nanocubes with a relatively high yield in an aqueous solution [47]. The edge lengths of the cubes can be finely controlled from 13.4 to 50 nm by using single-crystal spherical Au nanocrystals as the seeds and cetyltrimethylammonium chloride (CTAC) as a capping agent to direct the growth of Ag shells. The thickness of the Ag shells can be precisely controlled in the range of 1.2 to 20 nm because of the spherical shape and high uniformity of the Au seeds and because of the critical shell thickness at which the SP excitation of the core will be completely screened by the shell. Figure 7 shows UV–vis spectra taken from aqueous suspensions of Au/Ag core-shell nanocubes with different thicknesses for the Ag shells (1.2, 2.1, 3.1, and 4.5 nm) [47], where the edge length of the nanocubes increases from 13.4 to 20 nm. For a small thickness of the shells (e.g., 1.2 nm), the Au/Ag nanocubes show two characteristic peaks located at 510 and 410 nm, corresponding to the Au core and the Ag shell, respectively. Moreover, the peak intensity from the Au nanocrystal seeds decreases as the thickness of the Ag shell increases. When the thickness increases to a critical point of 3.1 nm, the peak from the Au seeds disappears, and the peak from the Ag cubes remains. In addition, when the edge length of the Au/Ag nanocubes further increases beyond 20 nm, the spectra exhibit only the characteristic features from pure Ag nanocubes; the major resonance peaks of the Ag nanocubes display a continuous redshift with increasing size. For instance, when the edge length of the nanocubes increases from 24.4, 30.4, and 42.6 to 50.4 nm, the major peaks are shifted from 421, 432, and 454 to 466 nm, respectively. For the sizes of 42 and 50 nm, a split of the resonance peaks around 390 nm occurs, which indicates that the corners of the Ag nanocubes became sharper than those of the smaller nanocubes [48]. This work demonstrates an easily managed and powerful approach to the fabrication of Au/Ag core-shell nanocubes with high yields.

Figure 7

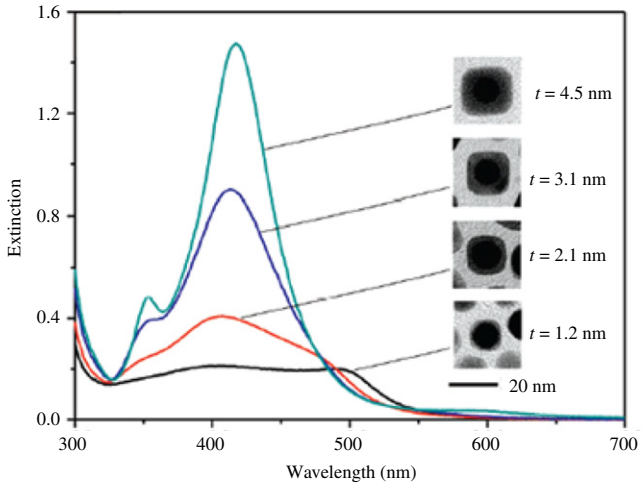


UV–vis extinction spectra of Au/Ag core_shell nanocubes with different thicknesses ($t$) for the Ag shells. Reproduced with permission from Fig. 6A, Ref. [47]. © 2010 ACS.

### 2.1d. Nanocages

Over the past few years, many research efforts have been focused on developing novel Au nanostructures to achieve LSPs in the near-IR (NIR) region. Xia and co-workers found that the galvanic replacement reaction between Ag templates and $HAuCl_4$ in an aqueous medium could lead to the formation of hollow nanostructures with controllable void size, wall porosity, and shell thickness [42,49,50]. This class of nanostructures is denoted nanocages, which consist of hollow interiors and porous walls. Moreover, the LSPR peaks of the resultant nanostructures can be continuously shifted from the blue (400 nm) to the NIR (1200 nm) region by controlling the molar ratio of Ag to $HAuCl_4$ and thus the extent of replacement, alloying, and dealloying.

Furthermore, they demonstrated that corrosive etching of single-crystal Pd nanocubes could be used to transform them into nanocages by controlling the reaction time [51]. The Pd nanostructures display distinctive colors, since the resonance frequency is strongly dependent on the wall thickness: the aqueous suspensions change from yellow to orange to purple as the Pd nanocubes are transformed into hollow boxes and then porous cages. The Pd nanocubes exhibit a resonance peak at 410 nm, which is consistent with the results of discrete dipole approximations calculations [52], and the peak is redshifted to 430 nm as holes appears in their surfaces. The formation of hollow structures with thick walls (and relatively rough inner surfaces) results in the resonance peak at 443 nm. The extinction peak is further shifted to 452 nm when the wall of the nanoboxes is thinned to 8 nm [51]. Once the product is evolved into nanocages with an edge length of 48 nm and a wall thickness of 6 nm, the peak is shifted to 520 nm.

In addition, Xia and co-workers synthesized Au nanocages by using the galvanic replacement reaction between Au precursor salt solutions and Ag nanostructures prepared through polyol reduction [53–56]. First, the Au precursor was selected as $HAuCl_4$, and then Au could be deposited epitaxially on the surface of the Ag nanocubes owing to the electrochemical potential difference between the two species. Concurrent with this deposition, the interior Ag was oxidized and removed, together with alloying and dealloying. Eventually, Au nanocages formed (Fig. 8(e)), and the composition of the nanocages could be altered by the galvanic replacement reaction. Moreover, the resonance frequency of the Au nanocages can be tuned by changing the amount of Au precursor added to the suspension of Ag nanocubes; the resonance band of the nanocages exhibits large redshifts from the visible to the NIR wavelengths (Fig. 8(g)) [56]. Additionally, the relative intensity of the scattering and absorption cross sections of the Au nanocages can be modulated by varying their size. It is predicted that the Au nanocages have a large absorption cross section (about $20 \times 10^{-15}$ $m^2$) based on the discrete dipole approximations calculations. Therefore Au nanocages will be attractive materials for biomedical applications because their resonance frequency can be tuned into the NIR, where the attenuation of light by blood and soft tissue is greatly reduced.

On the other hand, Xia and co-workers presented a class of potential photothermal therapeutic agents based on Au nanocages with a size less than 50 nm and a strong LSPR absorption peak tunable in the NIR region [57]. The Au nanocages with the targeted edge length of 45 nm were synthesized by using the galvanic replacement reaction between Ag nanocubes and chloroauric acid. By simply controlling the molar ratio of the Ag nanocubes to the chloroauric acid, the resonance peak can be tuned over a broad spectral range from the visible to the NIR with a central wavelength of 810 nm. The absorption ($C_{abs}$) and scattering $C_{sca}$ cross sections are designed to be $3.48 \times 10^{-14}$ $m^2$ and $1.41 \times 10^{-14}$ $m^2$, respectively. Thus the large absorption cross section of the Au nanocages might be the key factor contributing to the reduction of the thermal damage threshold; cells without derivatization by immuno Au nanocages exhibit no observable loss of viability under the same experimental conditions. These results suggest that the immuno Au nanocages with a size less than 50 nm might be promising photothermal therapeutic agents for cancer treatments.

Based on the synthesis of the nanocages with individual composition, they presented another easily managed method for synthesis of Au–Ag alloy nanocages with a controlled wall thickness [58]. The key is to use a water-soluble thiol as an etchant to selectively dissolve the Ag remaining inside the Au–Ag nanocages. The overall thickness and the resonance peak position of the nanocages can be precisely tuned by varying the reaction time or the concentration of the thiol. This method is advantageous because it does not require additional metal precursors, and there is no substantial modification to the wall composition and structure of the product as typically seen with other etchants. Additionally, the unique approach to tuning the resonance frequency can be done entirely in an aqueous system.

Figure 8

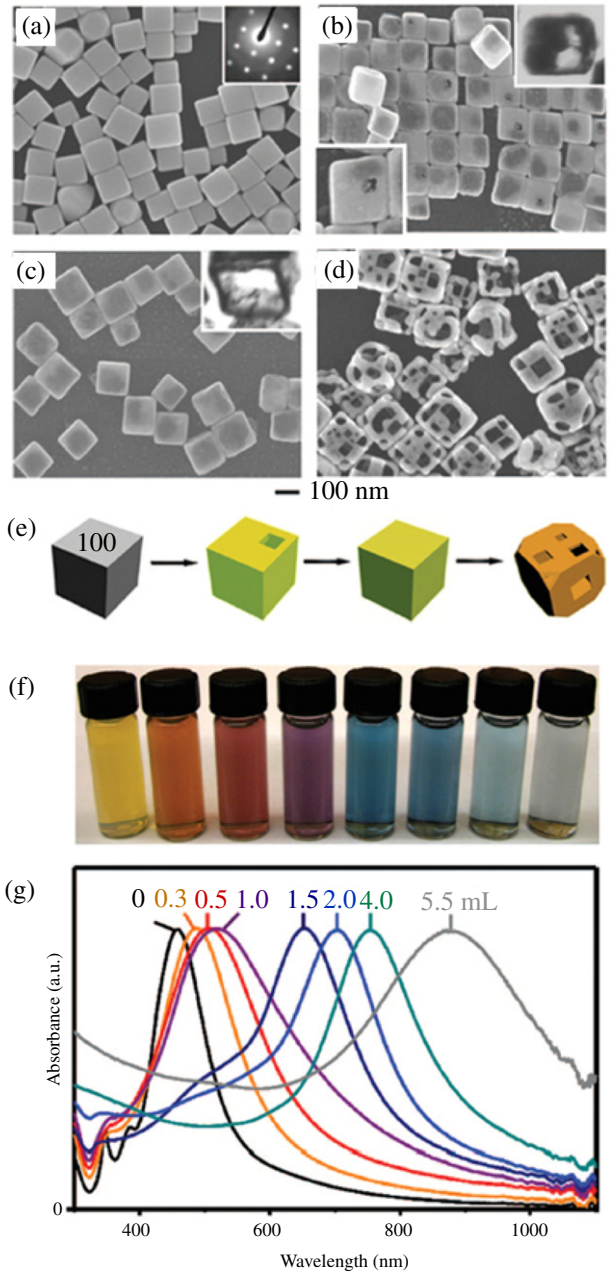


(a) Scanning electron micrograph (SEM) of Ag nanocubes. (b) SEM of product after 0.30 mL of 1 mM $HAuCl_4$ solution was added to a 5 mL 0.8 mM Ag nanocube suspension. (c) SEM of product after 0.50 mL of $HAuCl_4$ solution was added. TEM (inset) of a microtomed sample reveals the hollow interior of the nanobox. (d) SEM of product after 2.25 mL of $HAuCl_4$ solution was added; porous nanocages were produced. (e) Illustration summarizing morphological changes. Coloration indicates the conversion of an Ag nanocube into an Au/Ag nanobox, then a predominately Au nanocage. (f) Vials containing Au nanocages prepared by reacting 5 mL of a ~0.2 nM Ag nanocube suspension with different volumes of a 0.1 mM $HAuCl_4$ solution. (g) the corresponding UV–visible absorbance spectra of Ag nanocubes and Au nanocages. Reproduced with permission from Figs. 1 and 6, Ref. [56]. © 2008 ACS.

### 2.1e. Nanoshells

Nanoshells are metal and dielectric core–shell nanoparticles consisting of a dielectric core and a metal shell [59]. The LSPR behavior of the nanoshells is extraordinarily sensitive to the inner and outer dimensions of the metal shell layer [60]: the shift of the resonance peak results from both the dimensions and the dielectric properties of the dielectric core and the metal shell. Moreover, the hybrid resonance response can be tuned by an interaction between the LSPR supported by the inner and the outer surfaces of the metal shell layer [61].

Halas and co-workers proposed that the LSP resonance frequency of Au-coated $Au_2S$ nanoprticles (Au nanoshells) could be tuned by changing the structure sizes of the nanoparticles [60]. The configuration of the $Au_2S$ core coated with Au shell occurs during the reduction of $Au_2S$ nanoprticles to Au nanoparticles by mixing $Na_2S$ in $HAuCl_4$ solutions with controlled volume ratios. The Au-coated $Au_2S$ nanoparticles have an average diameter of 40 nm at the end of the reaction. The resonance peak exhibits large shifts from 650 to 900 nm during the growth process of the Au-coated $Au_2S$ nanoshells. The large peak shifts in the core–shell nanoparticles are dependent on both the radius of the $Au_2S$ core and the Au nanoshell thickness: the resonance peak width originates from the reduced mean free path of the conduction electrons in the Au nanoshells as well as the size distribution of the nanoparticles.

Furthermore, Halas and co-workers investigated the geometrical parameters that controlled the sensitivity of the resonance wavelength of a $SiO_2$–Au nanoshell to changes in its dielectric environment [62]. For a nanoshell with $SiO_2$ core radius of 60 nm and total particle radius of 68 nm, the dipolar resonance displays a redshift of 28 nm in ethanol by the addition of dodecanethiol. As the refractive index of the dielectric environment increases, the resonance peaks redshift, and the strength of the quadrupolar resonance in comparison with the dipolar resonance becomes more significant. Although the quadrupolar resonance also redshifts, the dipolar resonance is more sensitive to changes in refractive index. It is found that the larger nanoshells (e.g., total particle radius of 81 nm) have a sensitivity of 296.4 nm/RIU compared with 233 nm/RIU for the smaller nanoshells (e.g., the radius of 68 nm) [62]. Therefore, the resonance sensitivity may be further enhanced by fabricating larger nanoshells with thinner Au shells.

Prodan and Nordlander explored the structural tunability of metal nanoshells using time-dependent local density approximation [63]. It is demonstrated that the optical response can be dominated by two collective LSP modes corresponding to the symmetric mode and the antisymmetric mode. For larger nanoshells, the calculation shows only weak size dependence with a slight redshift with increasing the shell size. For the smallest nanoshell, this resonance mode is slightly blueshifted, as the nanoshell size increases, the symmetric mode redshifts continuously. In addition, the LSP excitation in the nanoshell is particularly sensitive to changes in its local dielectric environment.

Recently, Chau *et al.* reported enhanced LSPR in an Ag shell nanocylindrical pair connected by a nanobar, interacting with a TM incident plane wave, studied by use of the finite element method [64], which

Figure 9

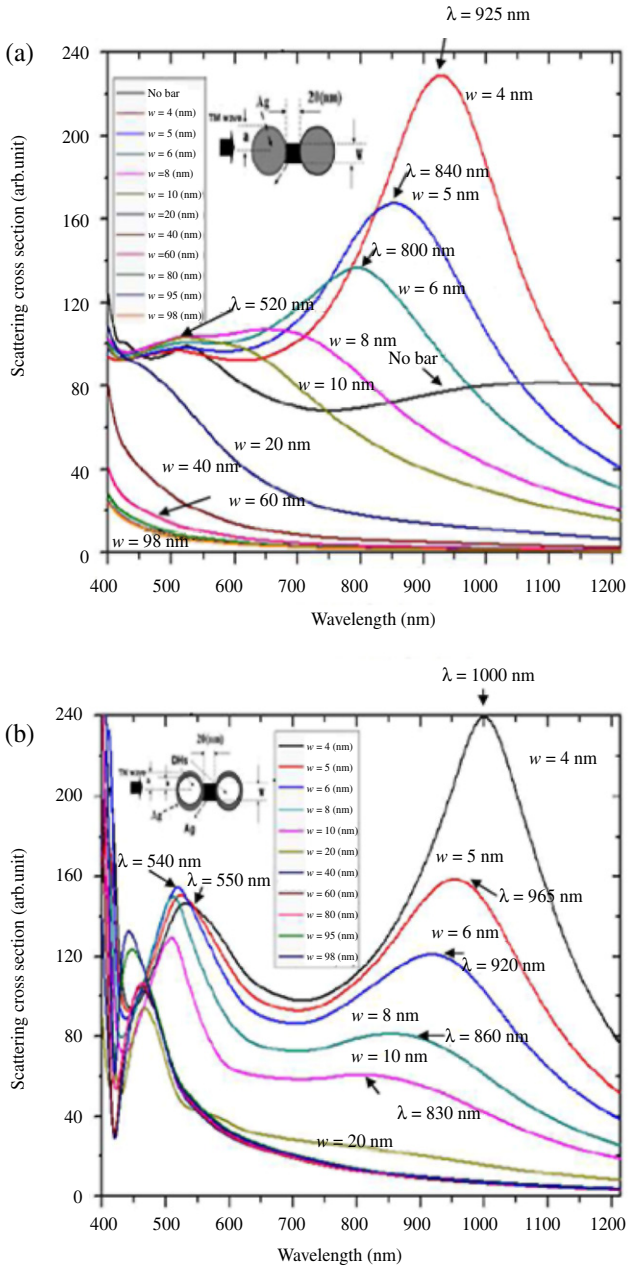


The difference in scattering cross sections on (a) a solid Ag nanocylinder pair connected by a Ag nanobar and (b) Ag shell nanocylinder pairs connected by a Ag nanobar of different widths ($w$), which are illuminated with a TM electromagnetic plane wave propagated in the nanochain direction. Reproduced with permission from Fig. 3, Ref. [64]. © 2010 OSA.

involves the particle–particle interaction. The enclosure of an Ag shell nanocylindrical pair with dielectric hole forms an open-cavity model, and the electromagnetic field is effectively confined in the gap of the pair to generate high local field enhancement. The nanobar, which connects two identical Ag shell nanocylinders, and the dielectric constant in dielectric holes are the key factors that provide additional variables to

explore for the tuning of the near-field optical properties between the nanocylindrical pairs. They investigated the difference in LSPR on a solid Ag nanocylinder pair connected by a Ag nanobar (Fig. 9(a)) and a Ag shell nanocylinder pair connected by a Ag nanobar (Fig. 9(b)) with different widths of Ag nanobar, which were all illuminated with a TM wave propagating in the nanochain direction. The widths of the Ag nanobar were varied from 4 to 98 nm, the gap was set to $g = 20$ nm, and the shell thickness was $d = 0$ nm. It can be seen that the performance of the shell nanocylinder pair is quite different from that of the solid nanocylinder pair (Fig. 9): an obvious redshift and the scattering cross section enhancement can be found when the nanobar width is smaller than 8 nm, which results from the combination of LSPs and a narrow Ag nanobar whose width is smaller than its skin depth (near 10 nm). Because the light is absorbed by a greater volume of metal in the gap, the intensity of the scattering cross section of the solid Ag nanocylinder pair decreases as the nanobar width becomes larger than 10 nm (Fig. 9(a)). In contrast, dipolar or quadrupolar resonances can be induced in the shell nanocylinder pair owing to the symmetries of the charge distributions in the Ag shell nanocylinder pair: there is strong electromagnetic coupling between the inner and outer shell surfaces when the thickness is small compared with the nanocylinder radius. This results in LSP mode splitting similar to that in the case of a thin metal slab, which is characterized by symmetric and asymmetric mode branches. As a result, two clear resonance peaks can be found when the nanobar width is less than 10 nm. Therefore the LSPR effects obtained from the shell nanocylinder pair is superior to that of the solid nanocylinder pair.

## 2.2. Metal Nanorods

Theoretical calculations and experimental measurements indicate that the LSP resonance wavelength exhibits a redshift of 47 nm as the diameter increases from 10 to 100 nm for spherical Au nanoparticles [23], whereas for prolate ellipsoids the longitudinal resonance wavelength promotes a large redshift of 92 nm as the aspect ratio of the ellipsoids increases from 2.5 to 3.5. The theoretical calculation indicates that the transverse resonance of Au nanorods 15 nm in diameter occurs at 520 nm. In contrast, the longitudinal resonance wavelength depends on the aspect ratio: for an aspect ratio of 2.6, the longitudinal resonance peak appears at 720 nm; when the aspect ratio increases to 12, the resonance band is shifted to 1700 nm [65]. This is because the free electrons in the metal move along the long axis of the nanorods with weaker restoring forces (corresponding to large resonance frequencies), where the lengths of the nanorods are larger than the mean free paths of the electrons in the metal.

Many groups have explored the LSP resonance frequency of noble metal nanorods fabricated by the electrochemical deposition approach [66–72], solution phase route [42,73–75], and electron beam lithograph technique [76]. Liu and co-workers presented a new approach to fabricate Au nanorods by controlling the volume of the growth solution [73,75]. In a typical synthesis, 0.08 M cetyltrimethylammonium bromide (CTAB) and 250 μM $HAuCl_4$ aqueous solution were prepared as the growth

Figure 10

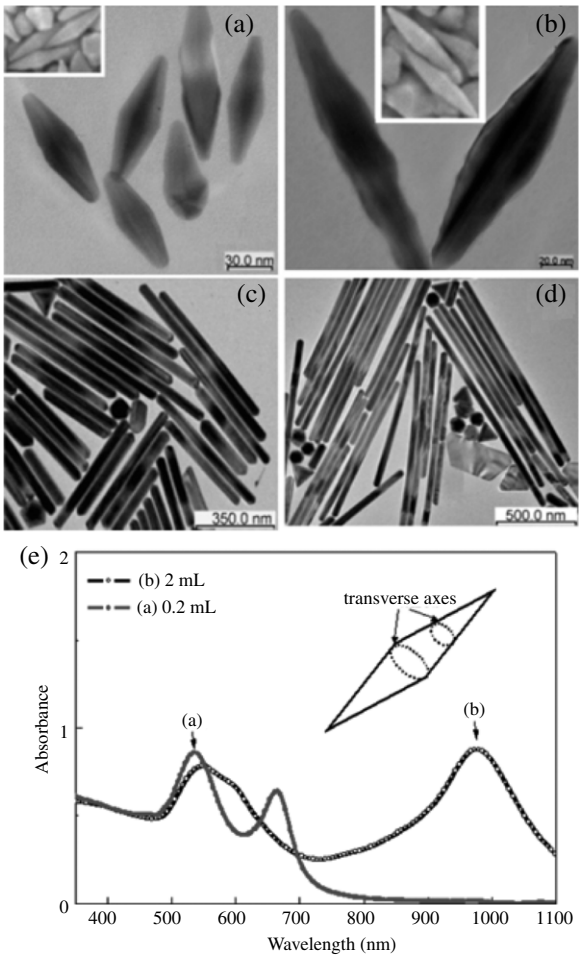


TEM images of the Au nanorods. Seed solutions after (a) first (0.2 mL), (b) second (2 mL), (c) third (20 mL), and (d) fourth (200 mL) additions of growth solution. The inset shows the NIR image of the corresponding samples. (e) Extinction spectra of Au fusiform nanorods: curve (a), after the first (0.2 mL) growth solution was added and, curve (b), after the second (2 mL) growth solution was added. Reproduced with permission from Figs. 1 and 4, Ref. [73]. © 2005 ACS.

solution. Then, 3–4 nm Au seeds (0.02 mL) were placed in a beaker. Subsequently, four quantities (0.01, 0.1, 1, and 10 mL) of freshly prepared ascorbic acid (10 mM) solutions were mixed with 0.2, 2, 20, and 200 mL growth solutions, respectively. After ascorbic acid was added, the growth solution became colorless as Au ions were reduced to Au atoms. After that, 0.03 and 0.3 mL $AgNO_3$ (0.025 mM) solution were added to 0.2 and 2 mL growth solution, respectively. Finally, these four colorless solutions were added to the Au seed solution one by one at 45 s intervals, and the Au nanorods were obtained.

Furthermore, the Au nanorod length can be extended to 2 μm, and the aspect ratio can become as high as 70 by increasing the addition of the growth solution (Figs. 10(a)–10(d)). The resonance absorption spectra of the Au nanorods exhibit two bands (Fig. 10(e)) [73]: the

shorter-wavelength band is attributed to the transverse resonance mode, and another absorption band at a longer wavelength corresponds to the longitudinal resonance mode. Moreover, the longitudinal resonance band exhibits an obvious redshift and wider full width at half-maximum (FWHM) with increasing aspect ratio. The Au nanorods that are 60 nm in diameter and 6 μm in length exhibit a longitudinal resonance band in the mid-IR [77], as well as a transverse resonance band at the visible wavelengths. Detailed tuning of the resonance frequency of longitudinal and transverse modes as well as dipolar and multipolar modes of noble metal nanorods will be presented in Section 3.

## 2.3. Metal Nanowires

The pioneering work on noble nanowire arrays embedded in porous anodic aluminium oxide (AAO) templates was presented by Martin and co-workers [67,68,78]. At that time, the size of the nanowires could not be controlled easily because of the out-of-order nanopores of the AAO templates. After Masuda reported a highly ordered porous AAO membrane in 1995 [79], fabrication of ordered noble nanowire arrays within the AAO membranes has become a promising approach through a template-based synthesis route [78,80].

Recently, we prepared noble metal nanowire arrays embedded in AAO membranes by an electrochemical deposition method [81]. As a special example, because of the longer resonance wavelength for Cu than those for Ag and Au, the performance of Cu nanowire arrays are discussed here (Fig. 11(b)). Note that it is difficult for Cu to give rise to LSP excitation because of its instability in air compared with Ag and Au. Therefore controlled preparation of Cu nanowire arrays is of importance for LSP excitation. Figure 11(c) shows the LSPR spectra of Cu nanowire arrays with the current density of the electrochemical deposition. It is seen that the resonance peak exhibits distinct redshifts from 575 to 690 nm when the absolute value of the current density increases from −2.09, −2.18, −2.30, −2.52, to −2.84 mA/cm$^2$. This is because the aspect ratio of the Cu nanowires increases owing to the increase of the growth rate with increasing current density. Moreover, the resonance band becomes wider with increasing current density value. The noble metal nanowire arrays may exhibit opportunities in nanophotonic devices, SERS substrates, and biosensors.

In addition, we fabricated Ag–Cu alloy nanowire arrays embedded in AAO membranes by an electrochemical deposition approach from a mixing electrolyte solution containing $Ag^+$ and $Cu^{2+}$ ions [82]. The LSPR wavelengths of the Ag–Cu alloy nanowire arrays can be modulated by tuning the molar ratio of $Ag^+$ and $Cu^{2+}$ ions in the precursor salt solutions. When the ratio is less than 2:20, two resonance peaks appear (Fig. 12), corresponding to the resonances of Ag and Cu, respectively. After an annealing treatment, the resonance peak corresponding to Cu disappears, and that of Ag presents a redshift. Moreover, this redshift can be up to 85 nm when the molar ratio of $Ag^+$ to $Cu^{2+}$ is reduced to 1:20, which is attributed to the transferable electrons from Cu atoms.

Figure 11

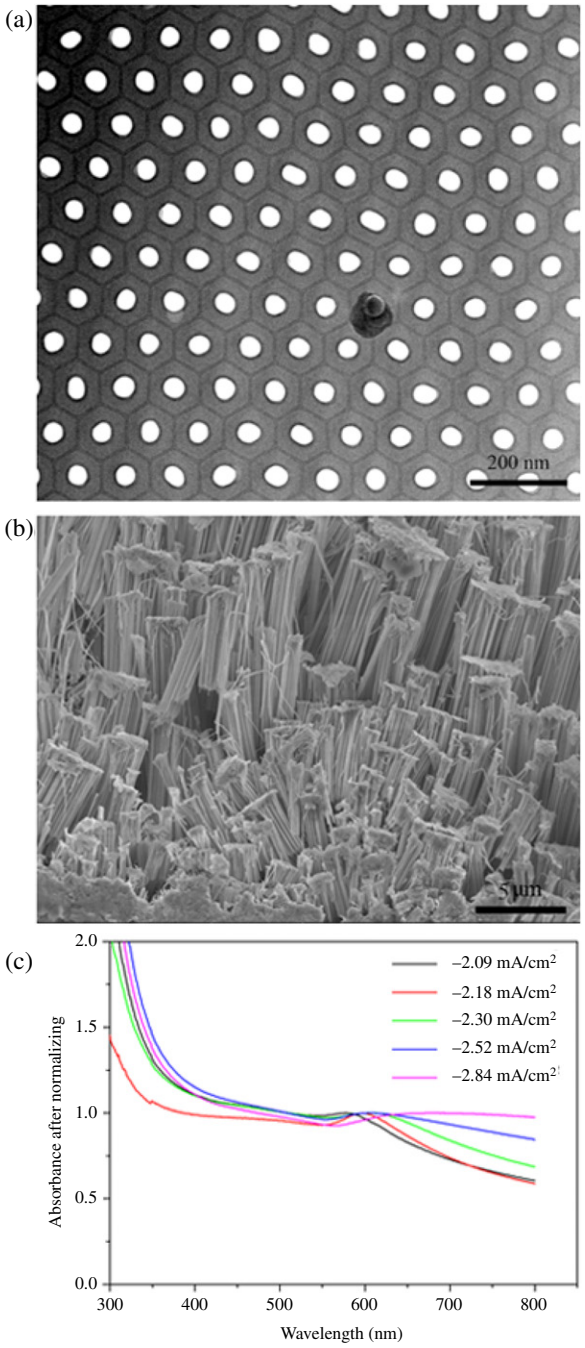


(a) TEM image of porous AAO membrane obtained after a second anodization for 640 min. The pore diameter and spacing are 50 and 105 nm, respectively. The TEM sample was prepared by an ion milling technique (Gatan Precision Ion polishing system with two penning ion guns, Model 691) at 5 keV with milling angles of 7° for 8 h, sequential angles of 4° for 30 min, and final angles of 3° for 25 min. (b) SEM image of Cu nanowire arrays fabricated by a electrochemical deposition process at −150 mV (versus SCE) for 330 s after a partial removal of alumina. (c) UV-via-NIR absorption spectra of Cu nanowire arrays embedded in anodic alumina membranes with the various current densities.

Figure 12

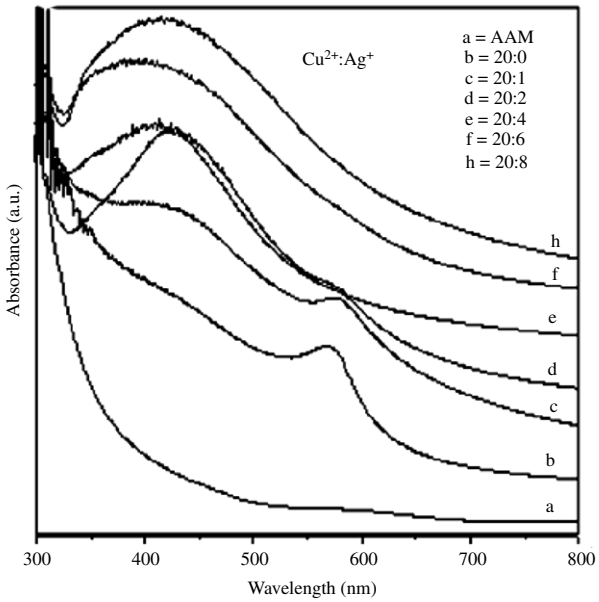


UV-via absorption spectra for as-deposited Ag–Cu nanowire arrays embedded in AAO membranes from the precursor salt solutions with different molar ratios of $Ag^{+}$ and $Cu^{2+}$ ions. Reproduced with permission from Fig. 4, Ref. [82]. © 2008 Elsevier.

## 2.4. Metal Nanosheets

Ultrathin nanosheets exhibit a well-tunable LSP resonance frequency (or wavelength) in the NIR wavelengths over a broad spectral range owing to their large aspect ratios. Pd nanosheets demonstrate enhanced photothermal stability compared with Au and Ag nanostructures because of their significantly higher bulk melting point. Recently, Zheng and co-workers reported an easily managed synthesis of free standing hexagonal Pd ultrathin nanosheets using carbon monoxide as a surface confining agent [83]. In a typical synthesis of Pd nanosheets, palladium (II) acetylacetonate, poly(vinylpyrrolidone) (PVP), and a halide salt were dissolved in a solvent (such as dimethylformamide (DMF)). The resulting homogeneous solution was transferred to a glass pressure vessel; after being charged with CO to 1 bar, the vessel was heated from room temperature to 100°C and kept at this temperature for 3 h with stirring. The color of the reaction mixture changes from yellow to light blue and finally to dark blue with the reaction. When DMF is used as the solvent, reaction in the presence of both PVP and CTAB produces colloidal Pd blue, composed of uniform hexagonal nanosheets with an edge length of 60 nm; the thickness of the nanosheets is less than 10 atomic layers. The use of CO is critical for growing the ultrathin Pd nanosheets. Without CO, the products contain only twinned nanoparticles, since the strong adsorption of CO molecules on the basal (111) planes of Pd nanosheets prevents growth along the [111] direction and is responsible for directing the formation of the sheetlike structure. In addition, PVP serves as an effective coating to stabilize the nanosheets

Figure 13

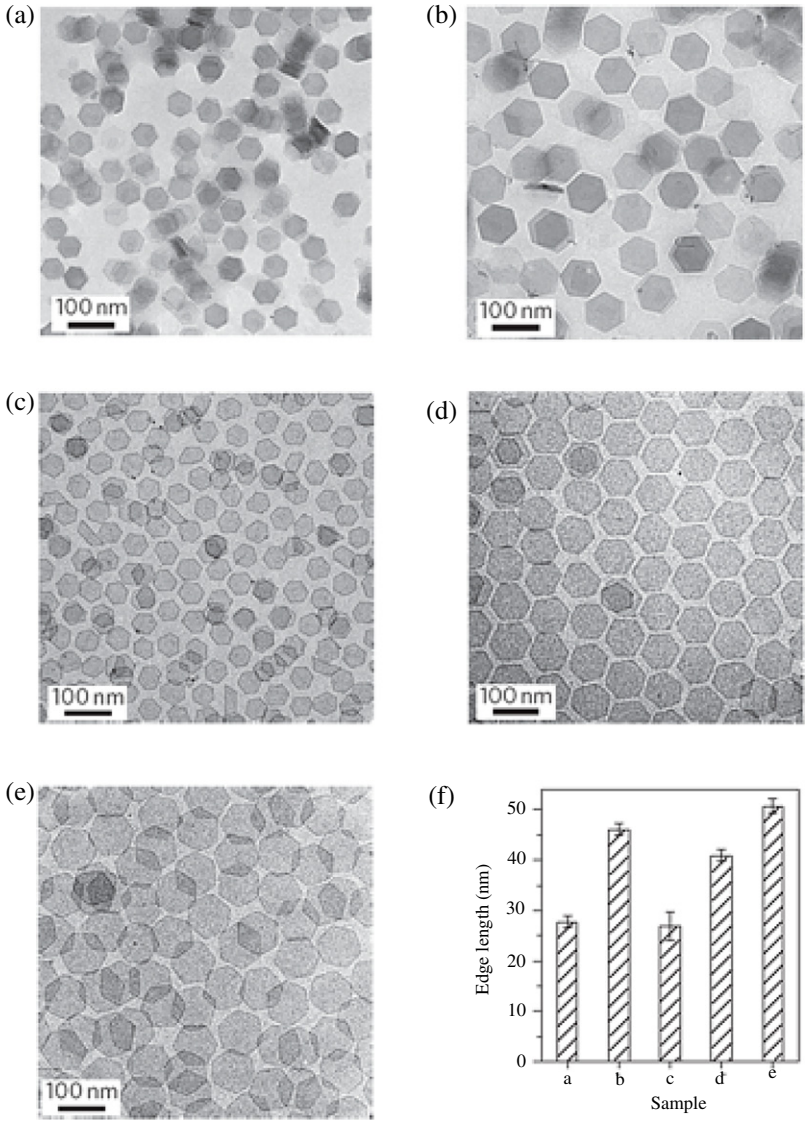


TEM images of the Pd nanosheets produced under different reaction conditions. (a), (b) Pd nanosheets collected following (a) 0.5 h and (b) 1.5 h reactions, using CTAB as the $Br^-$ source. (c), (d) Nanosheets collected following 3 h reactions using (c) NaBr and (d) TBAB as the $Br^-$ source. (e) Larger nanosheets grown by using the Pd nanosheets in (d) as seed particles. (f), Edge lengths of samples (a)–(e). Error bars in (f) are the standard deviations of the edge length distributions. Reproduced with permission from Fig. 2, Ref. [83]. © 2011 NPG.

from agglomeration, and the CTAB plays an important role in the preferential growth of uniform hexagonal sheets.

By varying the reaction solvent and time, the edge length of the uniform nanosheets is tunable between tens and hundreds of nanometers. First, formation kinetics studies show that the nanosheet size increases with reaction time: the Pd nanosheets grown in DMF for 0.5, 1.5, and 3 h had edge lengths of 28, 46, and 60 nm, respectively (Figs. 13(a) and 13(b)) [83].

Figure 14

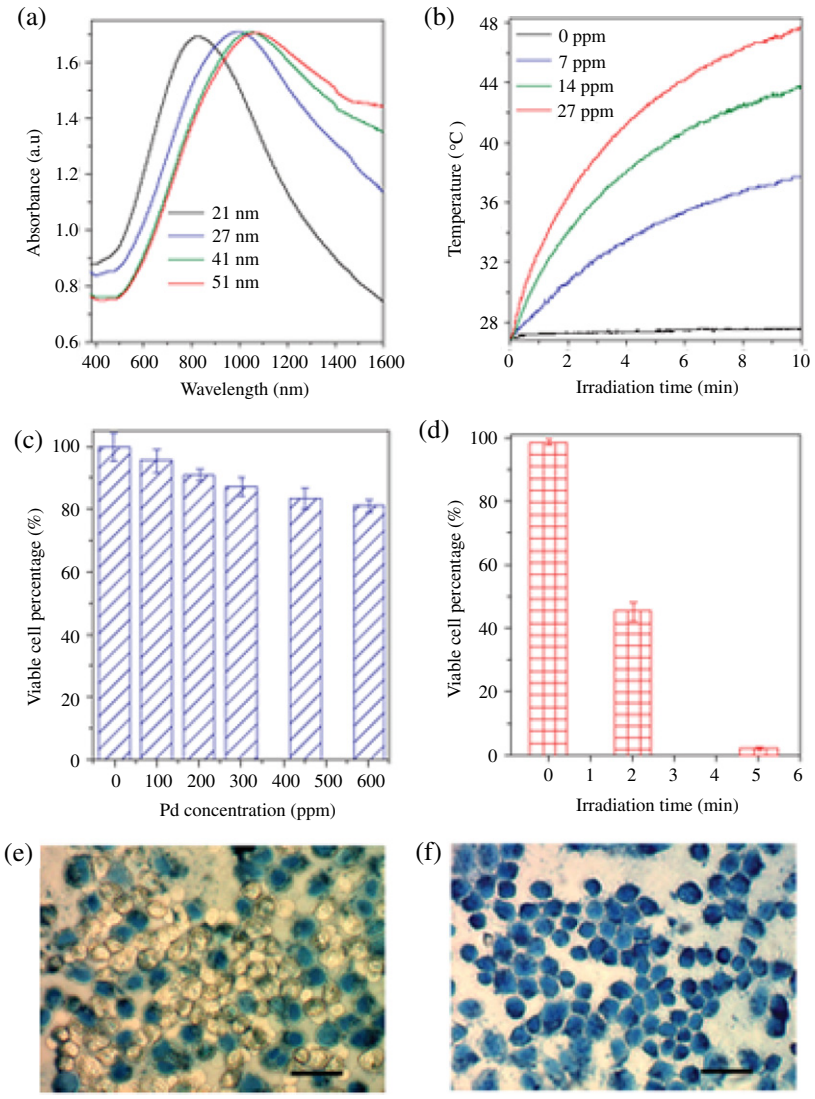


Optical absorption and photothermal properties of Pd nanosheets. (a) Absorption spectra of hexagonal Pd nanosheets with average edge lengths of 21, 27, 41, and 51 nm. (b) Photothermal effect of Pd nanosheets. The temperature versus time plots were recorded for various concentrations of Pd nanosheets (edge length, 41 nm) on irradiation by a 1 W laser. (c) Viability of healthy liver cells incubated for 48 h with different concentrations of Pd nanosheets. (d) Viability of human hepatoma cells upon irradiation by an 808 nm laser with a power density of 1.4 W $cm^{-2}$ for various periods. Before irradiation, the cells were incubated with Pd nanosheets (20 μg $ml^{-1}$) for 12 h. Cell viabilities were measured by standard MTT assay. (e), (f), Micrographs corresponding to (e) 2 min and (f) 5 min irradiation. Dead cells are stained with trypan blue. Error bars in (c) and (d) are the standard deviations of the means of five independent determinations. Scale bars, 50 μm. Reproduced with permission from Fig. 3, Ref. [83]. © 2011 NPG.

Larger Pd nanosheets can also be readily synthesized by using smaller nanosheets as the growth seed (Figs. 13(d) and 13(e)). Furthermore, the

edge length of the Pd nanosheets can be controlled by varying the reaction solvent, and the average edge lengths for nanosheets produced in the reactions for 3 h using dimethylpropionamide, 2-phenylethanol and benzyl alcohol as the solvent are 35, 125, and 160 nm, respectively.

Furthermore, the utrathin hexagonal Pd nanosheets exhibit well-defined and tunable LSPR peaks in the NIR region (Fig. 14(a)). The resonance peak shows redshifts from 826 992, 1045, to 1068 nm when the edge length increases from 21, 27, 41, to 51 nm, respectively (Fig. 14(a)). The ultrathin feature of the Pd nanosheets is key to their unique LSPR properties in the NIR region. Moreover, the aspect ratio $R$, where $R$ is the edge length divided by the thickness of the hexagonal nanosheets, plays an essential role in tailoring the LSPR properties of the nanosheets. When the edge length is fixed at 21 nm, the LSP resonance peaks are calculated at 467, 578, 684, and 860 nm for thicknesses of 6, 4, 3, and 2 nm, respectively. The prepared ultrathin Pd nanosheets yield significant photothermal effects and high electrocatalytic activity for the oxidation of formic acid.

## 2.5. Metal Nanodisks

Similar to metal ultrathin nanosheets, metal nanodisks with a relatively thick size also offer tunable LSPR properties. Chen *et al.* reported synthesis of Ag nanodisks by a solution phase method [84]. The synthetic procedure includes two main steps. First, the truncated triangular Ag nanoplates are obtained by a seed-mediated growth process of Ag particles in the presence of concentrated CTAB. Second, the triangular Ag nanoplate solution is treated by a mild aging process; the shape of the Ag nanodisks is strongly dependent on the aging process. It was found that the nanodisks display a strong LSPR band at around 475 nm. Furthermore, this band can be tuned within 420–560 nm through a mild aging process. Before aging, the spectrum of truncated triangular particles exhibits three main absorption peaks at 584, 444, and 351 nm, which represent in-plane dipolar, out-of-plane dipolar, and quadrupolar resonance modes, respectively. When the aging time changes from 5 min to 4 h, the 584 nm peak quickly exhibits a blueshift, corresponding to the in-plane shape transformation from triangle to circle nanodisks. At the same time, the peak positions of the two out-of plane resonances remain almost unchanged because of the constant thickness of the nanodisks. Continuous aging to 57 h finally gives a single absorption band at 420 nm, which belongs to the spherical nanodisks.

Maillard *et al.* presented synthesis of Ag nanodisks using photoreduction of $Ag^+$ by citration [85]. An aqueous Ag seed colloid was first synthesized by adding sodium borohydrate into a stirring solution of citrate and $AgNO_3$, and this solution was aged for 24 h. Then the growth solution was made by mixing seed colloid, citrate, Ag nitrate, and ultrapure water. Finally, this solution was uniformly irradiated at 457 nm with a linearly polarized Ar laser beam. During the growth process, the particles present a shape evolution, starting with a spherical shape, then more well-defined, triangular, disklike shapes. After a 5 min irradiation, the average particle size quickly increases from 8 to 14 nm as the particle shape remains roughly spherical. The absorption spectrum of

these particles corresponds to the growth. The resonance band at 400 nm increases in intensity from 0.006 to 0.04, while only a weak band at 530 is observed. From 10 to 20 min irradiation, the particle shapes become more and more well defined; on the appearance of a few triangular particles, their average diameter is 38 nm, and their average height is 10.7 nm, corresponding to an aspect ratio of 3.57. At the same time, the absorption band at 400 nm is still increasing. However, two resonance bands appear due to the shape transformation, at 338 and 540 nm. Finally, after 50 and 90 min irradiation, the particles are very similar in shape, most of them being flat particles. The number of small spheres significantly decreases, as observed by spectroscopy in the increase of the disk-related band and the decrease of the peak at 400 nm. This last peak does not completely disappear, even with a low percentage of spheres, since it is also related to a weak quadrupolar resonance mode from the flat particles [26].

Single-crystal Ag nanodisks in equilibrium with spheres could be produced by using colloidal solutions [86]. The nanodisk size can be tuned by adjusting the relative amount of reducing agent. The absorption spectra of Ag nanodisks offer several resonance peaks resulted from the different resonance modes related to the nanocrystal shape and size. The resonance peaks at high and low frequencies are attributed to the transverse and longitudinal resonance modes, which correspond to the polarization along the short and the long axes of the ellipsoid-shaped nanodisks. The energy splitting between the two resonance modes is directly related to the aspect ratio of the nanodisks. Furthermore, the resonance peaks have a redshift with increasing nanodisk size from 30 to 100 nm. The high-frequency peak does not drastically change with the nanodisk size, and the low-frequency peak shifts from 2.57 to 1.73 eV. The redshift of the low-frequency peak is related only to the increase in the disk size because of retardation effects. As a result, the color of the nanodisk solution displays a continuous change from red to green and then to gray when the size is increased. The narrower shape and size distributions for the nanodisks are indispensable to tuning their resonance frequency.

Recently, Huang and co-workers reported LSPR properties of long-range ordered Au nanodisk arrays fabricated on glass substrates by using nanosphere lithography combined with a two-step reactive ion etching technique [87]. The extinction spectra for the nanodisk arrays with different diameters exhibit broad LSPR bands, which can be identified as the in-plane dipolar resonance [88]. They found a redshift of the resonance peak with increasing nanodisk diameter, and reducing the thickness of the Au nanodisks redshifts the resonance peak with narrower FWHM and higher peak intensity. On the other hand, the glass substrate causes a redshift of the LSPR peak and lowers the peak intensity; the redshift arises from the increased refractive index of the nanodisks' surroundings. The existence of a Cr interfacial layer significantly weakens resonance and broadens FWHM. The peak blueshifts with decreasing peak intensity and broadening FWHM when the thickness of the Cr layer increases. These results indicate that the LSPR properties of Au nanodisks are compromised by the existence of a Cr interfacial layer, a component essential for the disks' structural stability on glass substrates.

Compared with single-layered nanodisks, multilayered nanodisks consisting of alternatively stacked metal/dielectric nanodisks exhibit a strong LSPR with enhanced local fields. Zhang and co-workers explored the LSPR of $Au/SiO_2$ multilayered nanodisks prepared on quartz substrates by an electron beam lithography technique [89]. They fabricated singlets and doublets of three-layered $Au/SiO_2/Au$ nanodisks with three different $SiO_2$ thicknesses (e.g., 5, 15, and 25 nm). With the Au layer thickness fixed at 15 nm, the nanodisks are elongated with a 101 nm diameter long axis and a 75 nm diameter short axis. The light scattering spectra demonstrate that the resonance peak of individual nanodisks is significantly redshifted from 675 to 725 nm when $SiO_2$ layer thickness is increased from 5 to 25 nm; this peak shift can be attributed to the variation of the near-field LSP coupling between individual Au layers with the change of the dielectric layer thickness. For longitudinal LSPR where the electrical field is parallel to the disk center–center axis, the resonance wavelength of doublets shifts to red compared with that of singlets, and the shift decays approximately exponentially with the gap between two disks and becomes minor when the gap is larger than 2.5 times that of the relevant disk diameter [90]. In contrast, for transverse LSPR where the electrical field is perpendicular to the disk center–center axis, the resonance wavelength of two coupled disks is always blueshifted [91]. The layered $Au/SiO_2/Au$ nanodisks can be considered two Au nanodisks coupled vertically; the LSP coupling is in transverse mode, since the excitation electrical field is horizontal. It can be expected that the LSP coupling strength would increase with a decrease of the $SiO_2$ layer thickness, and the peak resonance wavelength would blueshift. Therefore, these redshifts result from the longitudinal LSP coupling between two-layered nanodisks, in contrast to the blueshift in single-layered nanodisks. The LSPR behavior can be precisely tuned based on the LSP coupling between each metal layer by changing the dielectric layer thickness between two metal nanodisks.

In addition, Zhang and co-workers compared the scattering spectra and local field distribution for the Au nanodisks of single and multiple layers with the same diameter and the same total volume of metal and dielectric materials [89]. It was found that the scattering intensity is increased by twofold when a 30 nm Au layer is "sliced" evenly into 10 layers; also, the local electrical fields are enhanced for the layered nanodisks because of increased sharp corners (or singularities). Furthermore, the electrical fields inside the Au layers for layered nanodisks are intensified; as a result, the electrical fields within the $SiO_2$ disks are also enhanced in comparison with the single-metal-layer disk. The location of the enhanced fields varies from layer to layer. In this case, the unique electrical field distribution of the layered nanodisks may be employed for nonlinear optical applications because of the enhanced nonlinear effects.

Besides noble metals such as Ag and Au for LSPs, Al represents an interesting system from both fundamental and application points of view because it is an abundant and cheap material compared with the noble metals. A strong interband transition in Al is localized in a narrow energy range around 1.5 eV and is attributed to transitions between a pair of parallel bands [92], where stronger damping with decreased LSPR dephasing time can be expected through interband transitions to

Figure 15

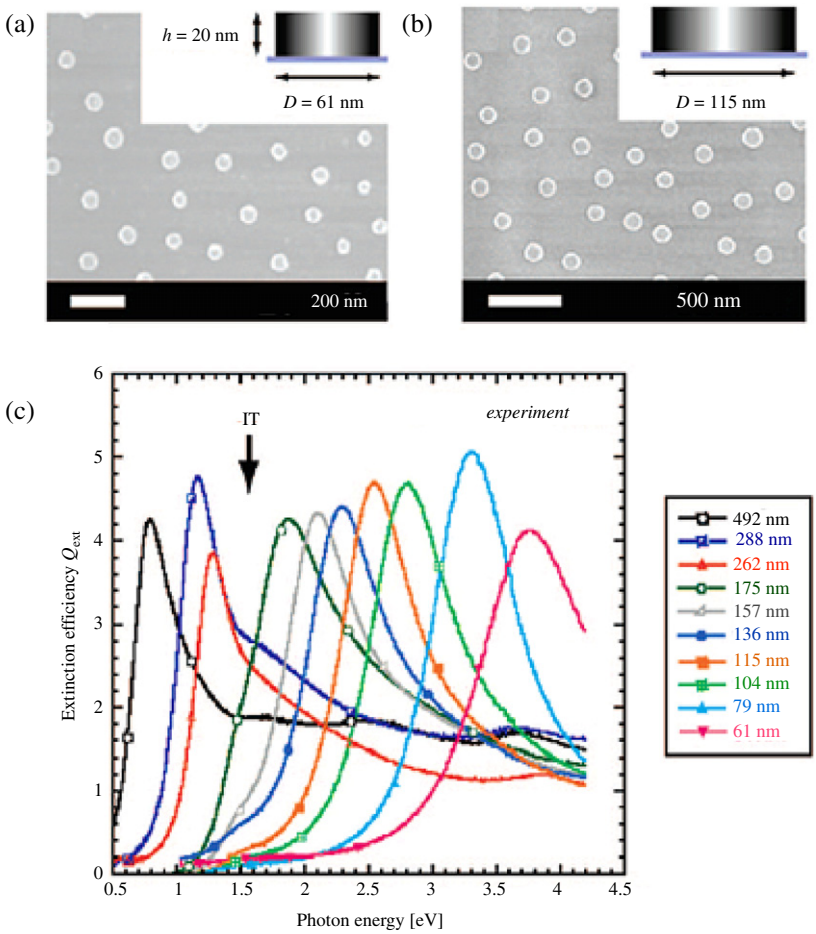


SEM micrographs of Al nanodisks with mean diameter (a) $D = 61$ nm and $h = 20$ nm and (b) for $D = 115$ nm and $h = 20$ nm. (c) Measured extinction efficiencies for Al nanodisks for a range of disk diameters 61 nm $< D <$ 492 nm at constant height $h = 20$ nm. A pronounced peak in extinction efficiency, associated with excitation of the dipolar LSPR, is spectrally redshifted with increasing $D$. An additional feature, always located at 1.5 eV (marked with "IT" and black arrow in the figure) is observed in the spectra and can be associated with the interband transition in Al metal. For $D = 262$, 288, and 492 nm, respectively, one, two, and three additional peaks can be seen on the high-energy side of the dipolar resonance. Reproduced with permission from Figs. 1a, b, and d, Ref. [94]. © 2008 ACS.

electron–hole pairs. Below and above this energy, the interband activity is weak, and Al is very much Drude-like [93].

Langhammer *et al.* presented fabrication of Al nanodisks by a hole-mask colloidal lithography method [94]. Figure 15(c) shows measured extinction efficiencies (extinction cross section in units of nanodisk geometric area) for Al nanodisks with diameters varying from 61 to 492 nm and height of 20 nm as a function of photon energy. The dipolar resonance is redshifted with increasing disk diameter owing to the dependence of the resonance frequency on aspect ratio (Fig. 15(c)). An additional feature,

always located at 1.5 eV, is clearly observed for 157, 136, 115, and 104 nm Al nanodisks to the lower frequency side of the dipolar resonance peak; the resonances result mainly from the absorption contribution to the total extinction cross section. For 79 and 61 nm disks, the former feature is also present but is much weaker and not clearly visible because of the extinction efficiency scale used. This feature can be associated with the mentioned interband transition in Al metal [92]. For larger Al nanodisks, the interband transition peak appears as a shoulder centered at 1.5 eV to the higher frequency of the dipolar resonance peak. Furthermore, for diameters of 262, 288, and 492 nm, respectively, one, two, and three additional peaks can be seen on the high-frequency side of the dipolar resonance peak. These peaks are attributed to the higher-order resonance modes (e.g., quadrupolar, octapolar, and hexadecapolar); in this case, the scattering contribution to the total extinction cross section becomes significant. The absolute extinction efficiency values are found to be comparable with those of Ag and Au nanodisks [95]. The Al nanodisks support long-lived LSPR excitation with large optical cross sections, and these excitations are tunable over a wide frequency range, deep into the UV.

## 3. Tuning Resonance Modes of Localized Surface Plasmons by Metal Nanostructures

Localized surface plasmons (LSPs) are nonpropagating electromagnetic excitations existing on bounded metal surfaces. LSPs exhibit some resonance modes. For one-dimensional metal nanostructures such as nanorods and nanowires we shall explore transversal and longitudinal resonance modes due to their optical anisotropy [23]: while the incident electric field is perpendicular to the axis, the transversal resonance mode can be excited (Fig. 16(b)), and when the incident electric field is parallel

Figure 16

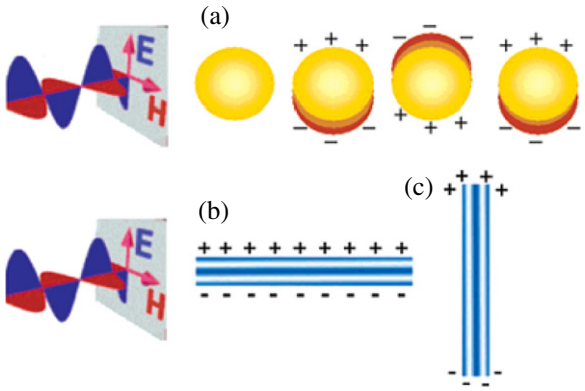


(a) Schematic drawing of the interaction of electromagnetic radiation with a metal nanosphere. (b) Transversal and (c) longitudinal resonance modes of LSPs in a metal nanorod. Reproduced with permission from Fig. 1, Ref. [23]. © 2006 ACS.

to the axis of the nanorods or nanowires, the longitudinal resonance mode can be excited (Fig. 16(c)); in general, the resonance frequency of the longitudinal mode is lower than that of the transversal mode.

On the other hand, for both one- and zero-dimensional metal nanostructures, the dipolar or the multipolar resonance modes can also be excited and tuned by changing the size of the nanostructures. Usually the nanostructures with small sizes offer dipolar resonance modes, while those with large sizes exhibit multipolar resonance modes. Moreover, the frequency of the dipolar resonance mode is lower than that of the multipolar resonance mode. In addition, a unique phenomenon, Fano resonance, appears with an asymmetric line shape owing to the interactions between a superradiant "bright" mode and a subradiant "dark" mode. For example, the interaction between the dipolar and quadrupolar resonances gives rise to the Fano resonance based on a radiative coupling.

## 3.1. Longitudinal and Transversal Resonance Modes in One-Dimensional Metal Nanostructures

### *3.1a. Nanorods and Nanorod Arrays*

Based on LSP excitation by light with different electric field directions, metal nanorods offer different resonance modes. Imura *et al.* investigated the resonance modes of single Au nanorods by using an apertured-type scanning near-field optical microscope (SNOM) [96], where Au nanorods with varied diameters of 15–40 nm and aspect ratios of 2–50 were prepared in micelles using a seed-mediated growth method. The near-field transmission spectra indicate that a broad localized surface plasmon resonance (LSPR) absorption band centered at 520 nm originates from the transverse resonance mode, while other resonance peaks at longer wavelengths are assigned to longitudinal resonance modes. The polarization-dependent transmission spectra of a single Au nanorod shows that the absorption band near 520 nm is effectively excited by light polarized perpendicular to the longer axis of the nanorod, which corresponds to a transverse resonance mode. In contrast, absorption bands around 620 and 740 nm can be assigned to longitudinal multipolar resonance modes when light is polarized along the long axis of the nanorod. Although SNOM can be used to measure the absorption or scattering spectrum of a single nanoparticle [97], SNOM is limited in its ability to spatially resolve the mode structure owing to some technical challenges involved in these experiments.

In order to overcome the inhomogeneous broadening band of the resonance modes of the metal nanorods, recently, N'Gom explored the resonance modes of individual Au nanorods using high-resolution electron energy-loss spectroscopy (EELS) in transmission electron microscopy (TEM) [98]. EELS provides a highly localized spectrum of the excitations of the system within a few atomic layers. The electrons are then collected through a spectrometer to show their energy distribution following their interaction with the sample, thus providing information on the energy exchange with surface modes of the specimen. By means of the EELS method, the transverse and longitudinal resonance modes of

Figure 17

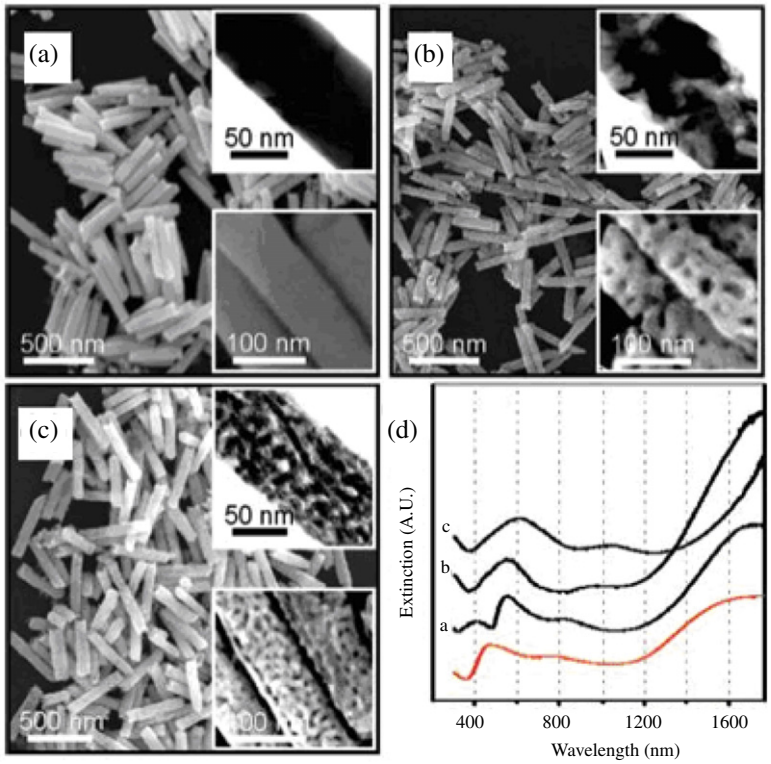


SEM images of (a) smooth Au nanorods ($L = 404$ nm and $d = 85$ nm), (b) nanoporous Au nanorods ($L = 398$ nm and $d = 83$ nm) prepared from the dissolution of Ag from $Au_x/Ag_{1-x}$ alloy nanorods ($x \sim 0.50$), and (c) nanoporous Au nanorods ($L = 420$ nm and $d = 82$ nm) prepared from the dissolution of Ag from $Au_x/Ag_{1-x}$ alloy NRs ($x \sim 0.36$). (d) Visible–near-IR (NIR) extinction spectra for samples a, b, and c corresponding to spectra a, b, and c, respectively. The red solid curve is the spectrum for $Au_x/Ag_{1-x}$ alloy NRs ($x \sim 0.50$, without Ag etching, $L = 400$ nm, and $d = 85$ nm). All the spectra are measured in $D_2O$. Insets are the corresponding enlarged TEM (upper) and scanning electron micrograph (SEM, lower) images. Reproduced with permission from Fig. 2, Ref. [100]. © 2008 ACS.

the Au nanorods were observed; the longitudinal resonance maximum is located at 1.74 eV, corresponding to the theoretical value of an aspect ratio equal to 4 [99], and the transverse plasmon mode is located at 2.47 eV.

Park and co-workers investigated the resonance modes of Au nanorods with different surface morphologies [100]. The Au nanorods were fabricated by an electrochemical codeposition of Au/Ag alloy into the pores of AAO templates and the subsequent etching of Ag from the alloy structure. The surface morphology can be controlled by tailoring the ratio of the $Au_x/Ag_{1-x}$ alloy composition. When the molar ratio of Au is 1, the length and diameter of the Au nanorods are about 404 nm and 85 nm, respectively (Fig. 17(a)). The extinction spectrum shows that a transverse mode appears at 552 nm, and the longitudinal dipolar mode and a higher order mode appear at 1754 and 810 nm, respectively (Fig. 17(d)).

When the molar ratio of Au in the $Au_x/Ag_{1-x}$ alloy composition is 0.50, selective etching of Ag results in porous Au nanorods (Fig. 17(b)). The distinct features are the redshifts of both transverse and longitudinal modes compared with those for the smooth nanorods. The magnitude of the redshifts becomes large as the surface roughness increases; all of the resonance peaks are significantly redshifted (Fig. 17(d)). Moreover, the nanoporous structure induces much larger redshifts in longitudinal modes than in transverse modes. For example, when the nanorod length is 250 nm, the transverse mode at 542 nm is slightly shifted to 598 nm, while the longitudinal mode at 1180 nm moves out to 1480 nm. It can be seen that the chemical environmental change has a greater affect on the LSPR of the porous nanorods compared with that for smooth nanorods; thus, the porous Au nanorods with high surface-to-total volume ratios are expected to develop highly sensitive sensors.

Furthermore, Park and co-workers explored the variation of the resonance modes of the $Au_x/Ag_{1-x}$ alloy nanorods as a function of relative compositions of Au and Ag [101]. The composition of $Au_x/Ag_{1-x}$ alloy nanorods can be controlled by varying the relative concentration of Au and Ag ions in a plating solution. When $x$ is 1, the nanorods are pure Au nanorods without any Ag component. The pure Au nanorods have three distinct peaks at 528, 748, and 1470 nm, corresponding to the transverse dipolar, longitudinal quadrupolar, and longitudinal dipolar modes, respectively. When the molar ratio of Au in the alloy nanorods is 0.75, the nanorods exhibit a transverse mode at 492 nm, while the longitudinal dipolar mode and a quadrupolar mode appear at 1482 and 736 nm, respectively. When the molar ratio of Au is reduced to 0.65 and 0.4, the transverse mode shows a considerable blueshift, while the longitudinal modes demonstrate very slight blueshifts. Compared with pure Au nanorods, the $Au_x/Ag_{1-x}$ alloy nanorods generate LSP excitations over a slightly broader distribution of oscillator frequencies that may lead to a faster decay of LSPs. Moreover, Park and co-workers investigated the resonance modes of multiblock Au/Ag nanorods composed of multisegments [102]. The multiblock nanorods with a block length of about 100 nm show two transverse resonance modes at 410 nm and 555 nm, which originate from the independent charge oscillation of Ag and Au blocks along the short axis due to the lack of coupling at shorter wavelengths, respectively. Additionally, the resonance peaks at 740 and 1090 nm indicate longitudinal higher-order modes, in addition to the tail of a dipolar mode around 1600 nm; the longitudinal higher-order modes result from the cooperative coupling of LSP modes along the long axis of the multiblock nanorods.

The metal nanorods for LSP resonance modes described above are arranged out of order, and the spacing of the nanorods is variable; in this case those LSPR simultaneously cover transverse and longitudinal resonance modes.

Liz-Marzán and co-workers fabricated Au nanorods incorporated within poly(vinyl alcohol) (PVA) thin films with well-defined aspect ratios [72]; the nanorods were subsequently aligned by heating and stretching the PVA films. The LSPR of the Au nanorods before stretching displays two resonance peaks. The same result is observed in the case of a stretched film under nonpolarized light. Although the nanorods are preferentially oriented in one direction, the incident light contains all orientations of

the oscillating electric field, so that both longitudinal and transversal resonance modes are excited simultaneously. However, under light polarized parallel to the stretching direction of the film, the longitudinal resonance mode is selectively excited, whereas under light polarized perpendicular to the stretching direction, only the transversal resonance mode is excited. In addition, the longitudinal resonance demonstrates a redshift for the larger aspect ratios, whereas the transversal resonance is invariable because the nanorod diameter is the same.

A significant characteristic of noble metal nanorod arrays is that the resonance modes can be tuned in a wide range through the structure parameters of the nanorods (e.g., spacing, aspect ratio, and length). Wurtz *et al.* explored transversal and longitudinal LSPR behaviors of Au nanorod arrays fabricated by electrodeposition into thin anodic aluminium oxide (AAO) templates [103]. The spacing of the nanorods can be controlled from 100 to 170 nm, the length of the nanorods is in the range of 50–400 nm, and their diameter is in the range of 10–40 nm. Figure 18(b) shows the experimental extinction spectra of the Au nanorod arrays embedded in the templates for different angles of incidence. At normal incidence, the extinction spectra reveal one single peak at around 520 nm from the transverse LSP excitation. At oblique incidence, the incident electric field includes both *s*-polarized and *p*-polarized components, which correspond the incident electric field perpendicular and parallel to the nanorod axis; in this case the extinction spectra demonstrate two resonance peaks centered around 520 and 650 nm, corresponding to the transverse and the longitudinal resonance modes, respectively. The long-wavelength peak becomes more pronounced at larger angles of incidence, for which this longitudinal resonance is excited more effectively. The angular sensitivity of the spectra reflects the strong anisotropy of the nanorods in the assembly (Fig. 18(b)). Furthermore, the longitudinal resonance mode depends on the incidence angle: the resonance peak shifts towards shorter wavelengths with increasing incidence angle. The angular dispersion of the longitudinal mode depends on the coupling strength from the adjacent nanorods for a decreasing effective interrod distance.

In addition, the longitudinal resonance mode is strongly dependent on both the rod aspect ratio and the distance between the nanorods in the array. An increase in the nanorod aspect ratio leads two splitting resonances, with the transverse mode undergoing a blueshift and the longitudinal mode undergoing a redshift. The influence of the interrod coupling strength can be investigated by changing the spacing of the nanorods from 500 to 100 nm (Fig. 19). For the larger interrod spacing of 500 nm, the field distribution around the nanorods is dominated by the dipolar mode of the longitudinal resonance at 1948 nm. In this case, the field is localized at the nanorod extremities, with a small break in symmetry that due to the presence of the substrate and illumination conditions. The reduction in the interrod distance leads to a blueshift of the longitudinal resonance peak. The most surprising result comes from a dramatic change in both the spatial distribution of the electric field and the power flow in the array. In fact, the electric field is concentrated within the assembly, in the middle part of the rods, as the interrod separation decreases. This evolution corresponds to a simultaneous decrease of the field amplitude at the nanorod extremities.

Figure 18

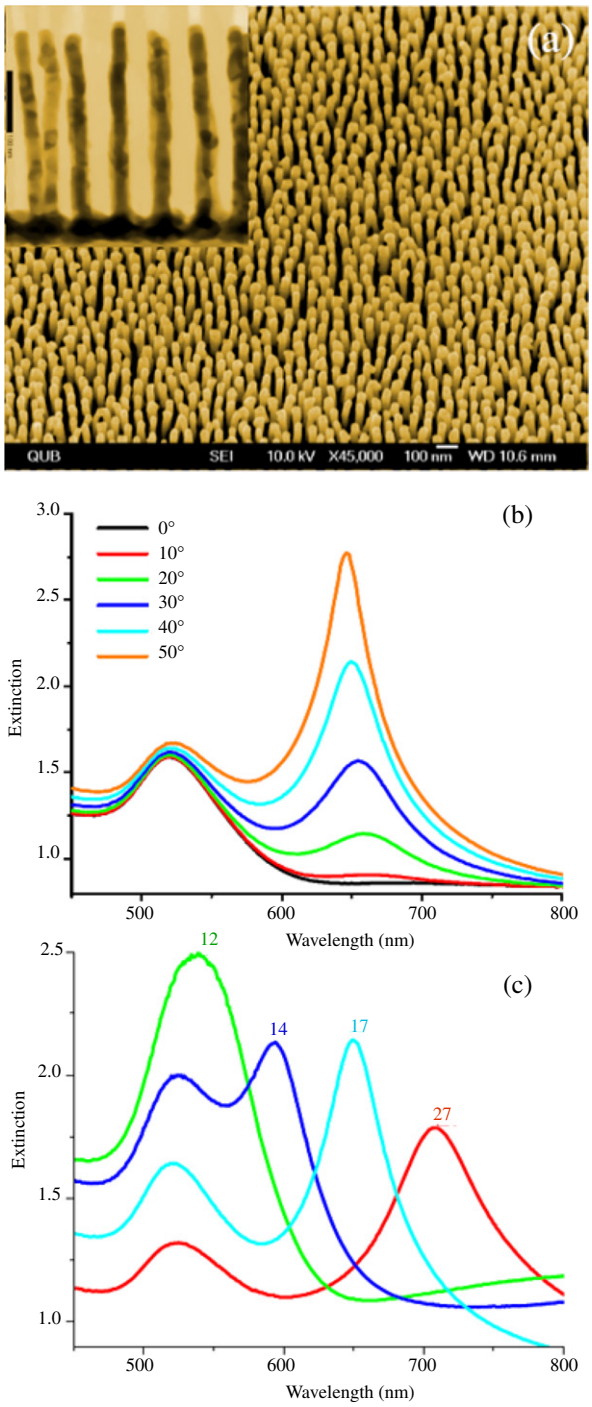


(a) SEM image of an array of Au nanorods in air. Inset, TEM cross section of Au nanorods embedded in AAO (scale bars 100 nm). (b) Zero-order optical extinction spectra for different of angles of incidence. The nanorod length is 300 nm, diameter is 30 nm, and the interrod distance is about 100 nm. (c) Zero-order optical extinction spectra of arrays of Au nanorods in AAO as a function of rod aspect ratio. The nanorod length is 400 nm and the interrod distance is about 100 nm. The curves are labeled according to the rod's aspect ratio, corresponding to rods with diameters ranging from about 15 to 30 nm. Reproduced with permission from Fig. 1, Ref. [103]. © 2008 OSA.

Figure 19

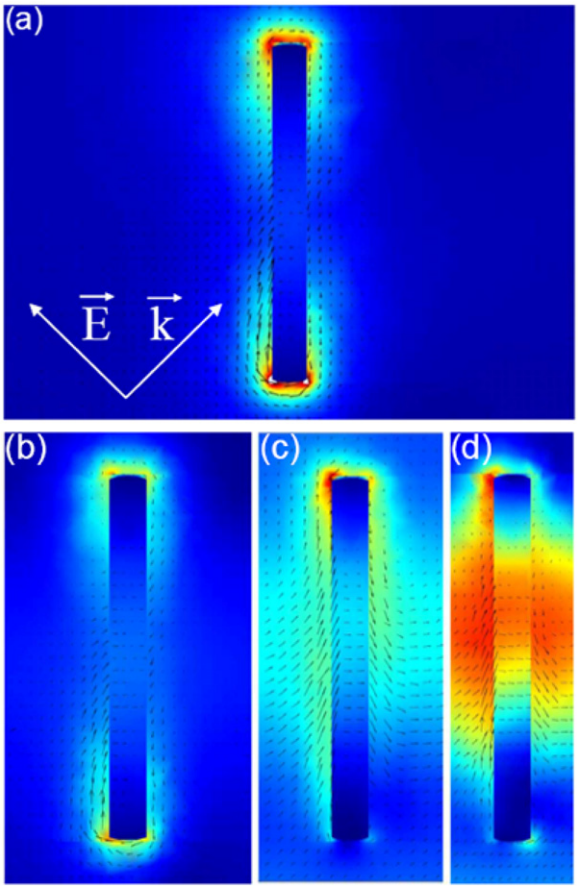


Longitudinal mode's electric field distribution in the primitive cell of the nanorod array for different interrod distances: (a) 500 nm, (b) 200 nm, (c) 150 nm, and (d) 100 nm, calculated by the finite element method. The nanorod length and diameter are 300 and 30 nm, respectively. The nanorods are embedded in an AAO matrix ($n = 6$) and supported by a glass substrate ($n = 1.5$). The superstrate is air ($n = 1$). The angle of incidence of TM-polarized probe light is 45°. The arrows in (a)–(d) show the direction of the Poynting vector. Reproduced with permission from Fig. 4, Ref. [103]. © 2008 OSA.

These properties can also be demonstrated experimentally by gradually tuning the interrod coupling strength, varying the interrod distance from about 170 nm to about 100 nm; this results in a blueshift of the resonance from 1.74 to 2.25 eV [104]. The LSP coupling with different resonance modes between the nanorods will be demonstrated in Section 4 in detail. Based on the strong electromagnetic coupling, the metal nanorod arrays have potential for nanoscale waveguides and nonlinear enhancement applications.

### *3.1b. Nanowires and Nanowire Arrays*

As in metal nanorods, transverse and longitudinal resonance modes can also be excited in metal nanowires and their arrays by light with polarization directions (e.g., an electric field component) perpendicular

and parallel to the nanowire axis, respectively. Schider *et al.* investigated LSPR properties of Au and Ag nanowires deposited on indium tin oxide (ITO) substrates arranged as one-dimensional gratings by electron beam lithography [105]. The extinction spectra of the nanowire gratings display transverse and longitudinal resonance modes, which are excited by the TM (electric field of incident light perpendicular to the nanowire axis) and TE (electric field of incident light parallel to the nanowire axis) waves. It is found that the resonance peak shifts to larger wavelengths with increasing aspect ratios for the TM wave, and the dipolar mode dominates the extinction spectra. In addition, the resonance peaks for Au nanowires are at larger wavelengths than those for Ag nanowires. On the other hand, for the TE wave, a spectrally broad resonance peak for both Ag and Au nanowires is observed; the extinction spectra change mainly as a function of the grating constant, and the profiles of these extinction peaks are only weakly influenced by the material and the cross section geometry of the nanowires. Based on the LSP extinction maximum for the TM wave and the transmission maximum for the TE wave, a maximum extinction ratio of about 26 is achieved at 598 nm. Therefore the metal nanowire gratings can be exploited for a spectral selective nanowire grid polarizer.

N'Gom *et al.* reported LSPR of individual Ag nanowires obtained by an EELS method [98]; the EELS measurements taken at the corner of an Ag nanowire 706 nm long and 50 nm wide indicate two resonance peaks at 1.8 and 3.54 eV, which correspond to the longitudinal and the transverse modes, respectively. Furthermore, it is found that there is a significant shift to lower frequency for the longitudinal mode when the nanowire length increases, while the transverse peak is nearly constant.

Zhou and co-workers presented LSPR behaviors of Ag nanowire arrays embedded in AAO templates prepared by an ac electrodeposition method [106]. The transverse resonance mode appears at about 400 nm for the incident light perpendicular to the surface of the composite film, while the longitudinal resonance mode appears at a longer wavelength when polarized light illuminates the film with an angle of incidence of about 70°. The resonance positions and relative intensities are affected by the diameter and the aspect ratio of the nanowires as well as the polarization direction of the incident light. Because of the anisotropy, the absorption spectra of Ag nanowire arrays show an intensive longitudinal resonance at a longer wavelength when illuminated with polarized light. When the polarization direction changes, every 90° the longitudinal resonance peak changes from the maximum to the minimum and the transverse resonance peak displays a reverse change in intensity. With the increase of the aspect ratios, the screening parameter of the longitudinal resonance approaches infinity; thus, the longitudinal resonance peak shifts toward a longer wavelength continually.

## 3.2. Dipolar and Multipolar Resonance Modes in Metal Nanostructures

Dipolar and multipolar LSP resonance modes exhibit obvious size dependence; for example, when a spherical nanoparticle's diameter is approximately 5–50 nm, the resonance mode is mainly dipolar, because

the conduction electrons in the metal are excited in phase with the incident electromagnetic field. However, when the dimensions become larger, the excitation of higher-order harmonic or multipolar modes can be excited as a result of phase retardation of the applied field inside the material [10]. Because metal nanorods have an anisotropic shape, they support more complicated resonance modes than spherical nanoparticles. For example, small nanorods display dipolar resonances that oscillate along both the short and long axes, which are known as transverse and longitudinal modes, respectively. However, when the length becomes significantly larger than the diameter, longitudinal higher-order modes appear as a result of the retardation (or dephasing) of the field within the nanorods [76,107,108]. The identification of higher-order resonance modes is important, because it provides not only greater understanding of their physical properties, but also a spectroscopic fingerprint that can be used to characterize and assess the quality of such structures, and the multipolar resonance modes are of fundamental interest and are important for applications related to near-field or far-field imaging and sensing.

### 3.2a. Nanoparticles

Mirkin and co-workers presented a synthetic approach and separation procedure for synthesizing and isolating large quantities of Au nanoprisms with uniform edge lengths and thicknesses [109]. The synthetic procedure involves the preparation of small Au seed nanoparticles ($d = 5.2 \pm 0.6$ nm), and the subsequent three-step growth of seeds in an aqueous solution containing the capping agent cetyltrimethylammonium bromide (CTAB), $Au^{+}$ ($HAuCl_4 \cdot 3H_2O$), a reducing agent (ascorbic acid), and NaOH. In these cases, a mixture of spherical and triangular Au nanoparticles (nanoprisms) was produced. Moreover, the nanoprism growth process can be monitored in real time by UV–vis–NIR spectra. The spectra clearly reveal two distinct resonance bands: the first band appears at 532 nm, assigned to the dipolar resonance associated with the spherical Au nanoparticles, and its intensity correlates with the concentration of Au nanoparticles in solution. The second band is observed initially at 750 nm, assigned to the dipolar resonance of the Au nanoprisms, and this band redshifts as the growth process continues; at the end of the growth process it appears at 1296 nm in conjunction with another band that appears at 814 nm. After 30 min the reaction stops, as indicated by fixed dipolar resonances at 532 nm for the spherical particle products and at 1300 nm for the nanoprisms. When the nanoprisms are predominantly separated from the spherical particles, a broad band at 800 nm appears, which originates from the in-plane quadrupolar mode of the nanoprisms. This assignment is based on the characterization of these prisms in discrete dipole approximation calculations [110]. In the assignment of the quadrupolar resonance, the possible contributions from nanoprisms of smaller edge lengths have been considered; the intensity of the quadrupolar resonance from large prisms is much greater than the intensity of the dipolar resonance of any remaining small-edge-length prisms in solution.

Halas and co-workers explored the LSP resonance modes of a concentric nanoshell [111]. The concentric nanoshell, consisting of alternating layers

Figure 20

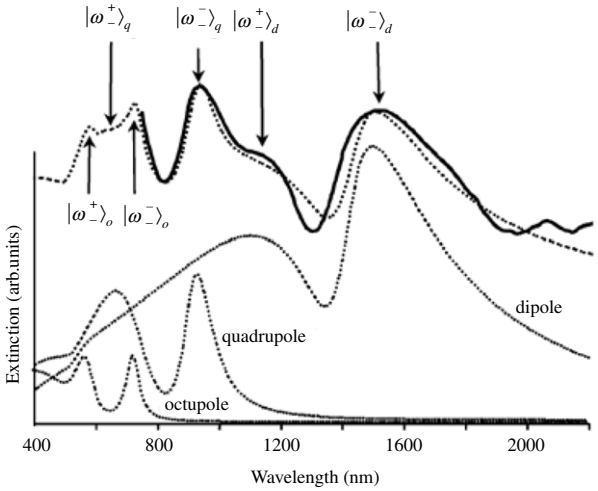


Experimentally measured extinction spectrum of a concentric nanoshell particle (solid curve) and the theoretical extinction spectrum (dashed curve) calculated by using an experimentally obtained dielectric function for gold. The various order multipoles of the plasmon are plotted individually (dotted curves) to show the multimodal structure of the overall concentric nanoshell plasmon response. The modes are labeled on the total extinction spectrum. Reproduced with permission from Fig. 4, Ref. [111]. © 2004 ACS.

of dielectric and metal, was fabricated by first growing a uniform nanoscale layer of Au around a $SiO_2$ nanoparticle core [59], then coating this nanoparticle with a $SiO_2$ layer of controlled thickness [112], followed by a second thin Au layer. The tunable resonance modes arise from the interaction and mixing of two fixed-frequency LSPs, that of a sphere (the outer surface of the metal shell layer) and a cavity (the inner surface of the shell layer). The hybridization of the sphere and cavity LSPs gives rise to two new resonance modes, referred to as "bonding" and "antibonding" plasmons by analogy with molecular orbital theory [63]. The energies of these two eigenmodes are determined by the strength of the interaction between sphere and cavity LSPs, which is controlled by the thickness of the shell layer. A thin shell results in strong LSP mixing, while a thick shell effectively isolates the LSPs of the two surfaces. The symmetric mode $|\omega_-\rangle$ is assigned when the inner and outer surfaces of the nanoshell are similarly polarized (large net dipole moment), while the antisymmetric mode $|\omega_+\rangle$ is assigned when the inner and outer surfaces are oppositely polarized. The antisymmetric antibonding plasmon mode is at higher frequencies than the symmetric bonding plasmon mode. Figure 20 shows the experimental extinction spectrum of concentric $SiO_2/Au/SiO_2/Au$ nanoshells with the dimensions $R_1/R_2/R_3/R_4 = 80/107/135/157$ nm, respectively. In this spectrum the observed resonances are due to the strong mixing of the $|\omega_-\rangle$ modes of the inner shell and of the outer shell. In addition, higher-order multipolar modes are excited in the shell layers and participate in the LSP hybridization owing to the size of the composite nanoparticle. In this case the quadrupolar and octupolar hybrid modes are responsible for the higher-frequency resonant response measured in this structure;

these multipole contributions from each shell layer mix with one another and contribute to the overall LSP response. The complex structure of the concentric nanoshell LSPs indicates a sum of the contributions of the dipolar and higher-order hybrid multipolar modes.

Recently, Burrows and Barnes theoretically investigated the LSP resonance modes of the individual Ag nanoparticles and two-dimensional nanoparticle arrays [113]. The dipolar (at 548 nm) and quadrupolar (at 427 nm) modes are excited simultaneously for individual sphere-shaped nanoparticles, and the dipolar and quadrupolar modes both contribute to the far-field angular scattering profile; the resulting preferential forward scattering occurs as a result of constructive interference of the radiation of the two modes in the forward direction and destructive interference in the backward direction. Finite-element modeling shows that the collective behavior of a square array of 100 nm diameter Ag nanospheres can differ strongly from the behavior of individual nanospheres. Rather than the two distinct modes corresponding to the dipolar and quadrupolar modes in the single-particle case, there is just one peak in the optical density of a 185 nm period array with the two modes occurring at very similar frequencies from the combination of the dipolar and quadrupolar modes. Moreover, the dipolar mode leads to strong scattering in directions that are perpendicular to the polarization direction of the incident light. The quadrupolar mode scatters strongly into four lobes, two along the axis of the incident wave vector, and the other two along the axis of the incident electric field. The mechanism that gives rise to this effect is that the presence of neighboring particles radiatively perturbs the collective dipolar mode of the array, and upon reducing the period of the array, this collective dipolar mode shifts to the blue until it overlaps with the quadrupolar mode.

### 3.2b. Nanorods

Aussenegg and co-workers performed the excitation of multipolar resonance modes in Ag rod-shaped nanoparticles (nanorods) fabricated by the electron beam lithograph technique [76]. The length of the three Ag nanorods are 790, 940, and 1090 nm; the short axes and the height of these Ag nanorods are fixed at 85 and 25 nm, respectively. Multiple well-separated resonance peaks are found at particular spectral positions that depend on the length (Fig. 21). For each resonance peak the multipolar order $n$ is indicated, which starts with $n = 1$ for the dipolar peak, while multipolar orders up to $n = 6$ appear. It is found that the resonance peaks assigned to each multipolar order exhibit a specific redshift with increasing length. The amount of redshift for a given length increment is smaller for higher values of $n$. It is noted that the almost linear dependence of the resonance wavelength on the length value is a specific feature of the chosen geometry and not a general property. The multipolar resonance modes with the LSP-induced field enhancement have possibilities for applications in the multistep enhancement of processes as second-harmonic generation.

Schatz, Mirkin and co-workers presented synthesis of Au nanorods embedded into the AAO template by an electrodeposition method [108]. The average diameter of the nanorods is 85 nm, and the average lengths can be tuned from 96, 186, 321, 465, 495, 578, 641, 735, and 1175 nm by

Figure 21

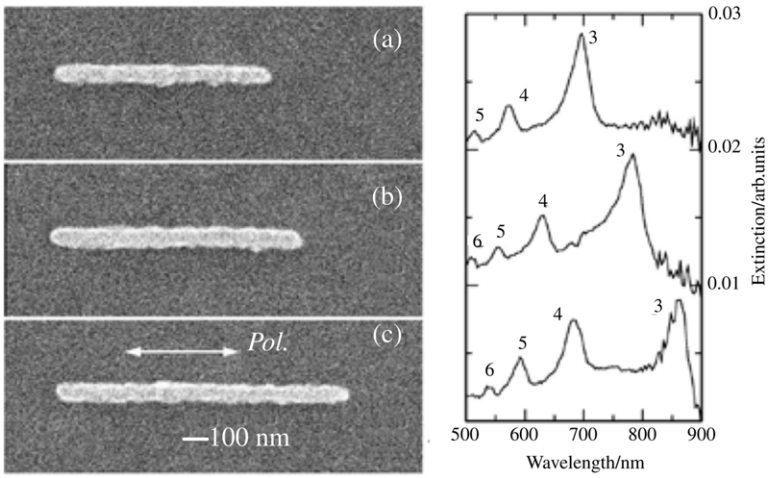


SEM images of three exemplary gold nanorods with a long-axis length of (a) 790 nm, (b) 940 nm, and (c) 1090 nm; the length of the short axis and the height are kept constant at 85 and 25 nm, respectively. The right-hand images are the corresponding extinction spectra, and the numbers indicate the multipolar order $n$ of the respective extinction peak. Reproduced with permission from Fig. 1, Ref. [76]. © 2000 AIP.

control of the number of coulombs passed during the electrodeposition process. When the length is 96 nm, one prominent broad peak around 600 nm is observed (Fig. 22, curve A), which results from both the transverse and longitudinal dipolar modes. The longitudinal mode (labeled I) overlaps the transverse dipolar mode because the aspect ratio (length over diameter) is close to 1; this case is similar to that of a nearly isotropic sphere. One particularly interesting feature is the appearance of both even (labeled II, IV, and VI) and odd (labeled I, III, V, and VII) multipolar resonance modes when the aspect ratio is greater than 4. In addition, both the even and the odd higher-order longitudinal modes (II–VII) are redshifted to longer wavelengths when the aspect ratio increases (Fig. 22, curves B–D). Furthermore, the number of multipolar resonance modes increases with increasing aspect ratio. When the length of the rod reaches 641 nm, the transverse dipolar mode appears at 530 nm, while two other higher-order modes (II and III) appear at 846 and 1197 nm, respectively. In this size regime the longitudinal dipolar mode (I) is redshifted to longer wavelengths and is not detectable in the spectral range. Also, a small shoulder is visible around 660 nm, which corresponds to the onset of multipolar mode IV. As the aspect ratio increases, the transverse mode remains around 530 nm, while the higher-order modes redshift and increase in intensity and number. When the length is 735 nm, the multipolar modes II, III, and IV are at 1397, 966, and 775 nm, respectively, and the multipolar mode V appears at around 660 nm. This same trend is followed in the spectrum for the nanorods that are 1175 nm long, and up to seven multipolar modes appear (Fig. 22D). In the spectra each higher-order mode is resolved from the transverse mode at around 650–700 nm.

Figure 22

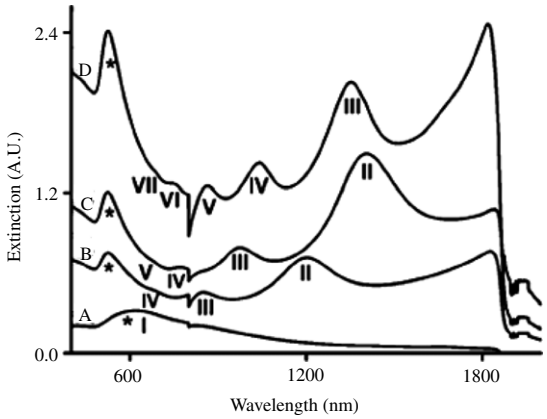


UV–vis–NIR spectra of the (curve A) 96, (curve B) 641, (curve C) 735, and (curve D) 1175 nm long gold rods in $D_2O$. The Roman numerals label the multipole order associated with each plasmon resonance. Orders were assigned on the basis of theoretical calculations. Reproduced with permission from Fig. 2, Ref. [108]. © 2006 ACS.

For the $Au_x/Ag_{1-x}$ (e.g., $x = 0.65$) alloy nanorods described in Subsection 3.1a, when the nanorod length is 328 nm, a longitudinal quadrupolar mode at 737 nm appears [101], and the peak systematically redshifts as the aspect ratio increases. Furthermore, when the observed quadrupolar peak positions are plotted as a function of the nanorod lengths, they have a slope of 1.7. For the length greater than 740 nm, a higher-order longitudinal band appears as a distinctive feature at 890 nm.

Khlebtsov explored the multipolar resonances of Au and Ag nanorods by a T-matrix approach; the particle diameters and aspect ratio were varied from 20 to 80 nm and from 2 to 20, respectively [114]. The scattering, absorption, and extinction spectra are dependent on the nanorod size, aspect ratio, shape morphology, orientation with respect to polarized light, and dielectric environment. The theoretical calculation indicates that the parity of a nanorod multipolar resonance coincides with the parity of its multipolar mode contributions, whose numbers are equal to or greater than the resonance number. The random-orientation resonances are excited most effectively by the TM scattering configurations, except for the short-wavelength resonance, which equals the sum of the dominant dipole TE resonance and the other multipolar mode contributions. Moreover, the even multipolar resonances are maximal at intermediate orientations, whereas the odd multipolar mode can effectively be excited at both perpendicular and intermediate orientations of the nanorod axis with respect to the TM incident wave. In particular, the quadrupolar resonance can be excited only by the TM incident wave, and the resonance magnitude is maximal for orientation of the particle symmetry axis near 54° with respect to the incident light. On the other hand, it is found that the multipolar resonance wavelengths obey a universal linear scaling when plotted versus the particle aspect ratio divided by the resonance number. The refractive index dependence of the multipolar resonance wavelength

also offers some interesting linear scaling properties, and the relative shift of the resonance wavelength is proportional to the relative refractive index increment.

### 3.2c. Nanowires

Similar to the metal nanorods, metal nanowires can also yield dipolar and multipolar resonance modes. In order to obtain a reasonable far-field optical signal, Schider *et al.* prepared Au nanowire arrays on a glass substrate doped with ITO by an electron-beam lithography method [115]. The extinction spectra of the nanowire arrays can be measured over a wide spectral range from 500 to 1050 nm for both normal and oblique angles of incidence by a Carl Zeiss MMS1 microspectrometer coupled to an optical microscope [116]. For oblique incidence the sample is tilted to various angles $\alpha$ between the long axis and the polarization of the incident wave. New extinction bands are observed, which are assigned to even-$j$ modes ($j = 2, 4$), while for perpendicular incidence only modes with odd ($j = 3, 5$) index are excited; additional extinction bands appear for oblique incidence ($\alpha = 20°$). These bands are attributed to LSP modes with an even ($j = 2, 4$) index, together with the modes of odd $j$ from a single dispersion curve. If the sample is further inclined to 45°, only the even modes are significantly excited; the $j = 3$ mode disappears in this case, since it is not excited favorably at this angle of light incidence [115]. The angle of light incidence allows or forbids LSP modes of distinct $j$ values owing to retardation along the long axis of the nanowires.

Vesseur *et al.* reported investigation on LSP eigenmodes of Au nanowires by cathodoluminescence imaging spectroscopy [117]. It is found that emission patterns along the Au nanowire axis are symmetric and strongly wavelength dependent, and different patterns correspond to different resonance modes of the nanowire. Figure 23 illustrates the cathodoluminescence spectra at two different positions indicated by X and Y along a 725 nm long Au nanowire. Gaussian fits on the data show that the resonances peaks of spectrum X are at 540 and 592 nm, while spectrum Y is made up mostly by the 540 and 640 nm resonance (Fig. 23(a)). Furthermore, three clear maxima are observed along the nanowire for the 640 and 690 nm resonances, four maxima are observed for the 592 nm resonance, and five resonances are observed for the shortest-wavelength resonance at 540 nm (Fig. 23(b)) [117]. Based on the observed patterns, the spatial and spectral properties of the wire eigenmodes can determine the LSP dispersion relation on Au nanowire.

## 3.3. Fano Resonances in Metal Nanostructures

Resonance is thought to be an enhancement of the response of a system to an external excitation at a particular frequency. The resonance is usually introduced by means of a harmonic oscillator with periodic forcing. When the frequency of the driving force is close to the eigenfrequency of the oscillator, the amplitude is growing toward its maximal value. However, some systems may exhibit the opposite phenomenon, in which their response is suppressed if some resonance condition is met. For instance, consider two weakly coupled harmonic oscillators in a system

Figure 23

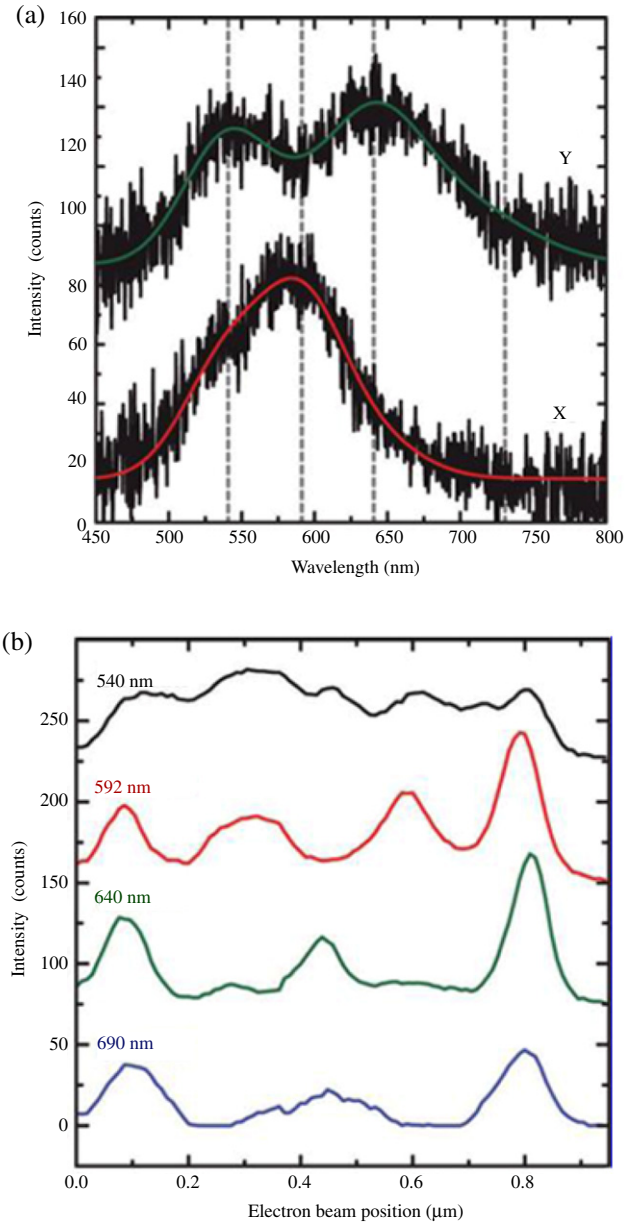


(a) Cathodoluminescence spectra taken at two different positions along a 725 nm long Au nanowire (black curves); green and red curves are fits to these data by a set of four Gaussian resonances at center wavelengths of 540, 592, 640, and 690 nm, respectively, indicated in the figure by vertical dotted lines. (b) Fitted intensity of each resonance plotted as a function of electron beam position. The 640 and 690 nm modes show three maxima, the 592 nm mode shows four maxima, and five maxima are vaguely observed for the 540 nm mode. Reproduced with permission from Fig. 3, Ref. [117]. © 2007 ACS.

where one of them is driven by a periodic force; there are two resonances located close to the eigenfrequencies $\omega_1$ and $\omega_2$ of the oscillators [118]. One of the resonances of the forced oscillator demonstrates the standard enhancement of the amplitude near its eigenfrequency $\omega_-$; the other is

the resonance $\omega_+$ with an unusual sharp peak in the amplitude. The first resonance is characterized by a symmetric profile, described by a Lorentzian function and known as a Breit–Wigner resonance, while the second resonance is characterized by an asymmetric profile, which results in total suppression of the amplitude of the forced oscillator at the eigenfrequency of the second oscillator $\omega_2$. The amplitude of the first oscillator becomes zero as a result of destructive interference of oscillations from the external force and the second oscillator. The phase of the single forced oscillator exhibits a $\pi$ jump at the resonance, meaning that below the resonance the oscillator is in phase with the driving force, and it becomes out of phase above the resonance. In the case of two coupled oscillators at the resonance of the second oscillator there are effectively two driving forces acting on the first oscillator, which are out of phase and cancel each other. This example demonstrates one of the basic properties of Fano resonance [118], namely, resonant destructive interference, which makes it unique among other resonances.

In 1961, in a quantum mechanical study of the autoionizing states of atoms, Ugo Fano discovered a new type of resonance that now bears his name [119]. In contrast to a Lorentzian resonance, the Fano resonance exhibits a distinctly asymmetric shape resulting from the constructive and destructive interference between a narrow discrete resonance with a broad spectral line or continuum [120]. Moreover, in nanostructures, Fano resonance originates from interactions between a superradiant "bright" mode and a subradiant "dark" mode, and it is are characterized by a pronounced minimum in the scattering spectra. For example, the interaction between the dipolar and quadrupolar resonances will give rise to Fano resonance based on radiative coupling. Multipolar modes can also interfere with the broad dipolar mode and result in higher-order Fano resonances when the size is increased. Because of the sharpness of the asymmetric peaks, Fano resonances show enhanced sensitivity to the local dielectric environment. These conditions can be satisfied by using tunable coupled LSP structures made of conventional LSP materials (Ag or Au nanostructures), such as nanoparticles, nanocavities, nanorods, and nanowires.

### *3.3a. Nanoparticles*

Fano resonance involves a continuum of incident photons (I), a superradiant bright mode (B) that couples to (I), and a subradiant dark mode (D) that does not couple to (I) but instead couples to the bright mode via a near-field interaction. At frequencies resonant with both the bright and the dark modes, the former will be excited via two pathways: $|I\rangle \rightarrow |B\rangle$ and $|I\rangle \rightarrow |B\rangle \rightarrow |D\rangle \rightarrow |B\rangle$. At the Fano minimum, these two pathways destructively interfere and cancel the polarization of the bright mode. The result is a narrow minimum in the scattering and extinction spectra. These mode interactions are absent in the simpler clusters such as dimer and trimer with a superradiant brightmode and without a subradiant dark mode in their scattering spectra. In this case structural complexity is required for the clusters to support interacting bright and dark modes; breaking the symmetry of the dimer or the trimer will give rise to the formation of new dark modes.

Recently, Capasso and co-workers reported self-assembled nanoparticle clusters for Fano resonance [121]. The nanoparticle clusters, composed of seven equivalent elements (so-called heptamers), support complex LSP mode interactions that lead to Fano interference; that is, the strong electromagnetic coupling between seven particles creates new LSP modes that support Fano resonances. Coupling between the bright and dark modes can be explained by group theory, as both modes share symmetries from the same irreducible representation [122]. Fano resonance is exhibited in the calculated extinction spectrum of a heptamer (Fig. 24(a)). The interfering bright and dark modes of the cluster can be characterized by surface charge density plots at their resonances. The charge density plot of the bright mode at its peak at 1160 nm shows the charge oscillations in each nanoshell oriented in the same direction, resulting in strong scattering due to the constructive interference of their radiated fields. The charge density plot at the dark-mode peak at 1490 nm shows only the dark mode, indicating that the bright mode is suppressed and that energy is stored in the dark mode [121]. Here, the charge oscillations in the individual nanoshells are oriented in different directions, resulting in the destructive interference of their radiated fields. The dipole moment of the outer hexagon is similar in magnitude but opposite in sign to the dipole moment of the central particle, which leads to strong destructive interference of their radiating fields [122]. Moreover, the scattering spectrum at each orientation demonstrates a strong Fano minimum at 1450 nm (Fig. 24(b)) [121]. This isotropy is consistent with the symmetry of the heptamer ($D_{6\,h}$ point group), which supports isotropic, in-plane resonances [122]. The peaks between 800 and 1300 nm are higher-order modes that arise from retardation effects created by the large incidence angle (Fig. 24(b)). Figure 24(c) shows the calculated scattering spectra of a heptamer for different polarization angles, where the cluster geometry is identical to that used in Fig. 24(a), and these spectra display Fano minima at 1450 nm, with asymmetric line shapes that match the experimental spectra. The nanoshell separation modeled here is smaller than that used for the trimer calculations to account for the strongly redshifted Fano minimum. This redshift is probably due to a combination of at least three factors: (i) smaller nanoshell separation due to inhomogeneous self-assembled monolayer coverage, (ii) a higher-refractive-index environment near the cluster due to excess polymer deposition, and (iii) increased capacitive coupling between the nanoparticles due to nanoshell faceting.

In addition, Capasso and co-workers measured the scattering spectra of the quadrumer for different orientations of the incident electric field [123]. At 0°, the spectrum shows a smooth broad electric dipolar peak. At 45°, a narrow Fano minimum emerges at 1080 nm, which increases in magnitude for larger orientation angles. The Fano resonance strength strongly depends on the polarization of the incident electric field and originates from the orientation-dependent capacitive coupling within the cluster. The differences in the quadrumer geometry along its two symmetry axes result in the pronounced anisotropy of the Fano resonance. In particular, the interaction between the two central nanoshells of the cluster qualitatively changes as the polarization of the dark mode shifts from one axis to the other.

Figure 24

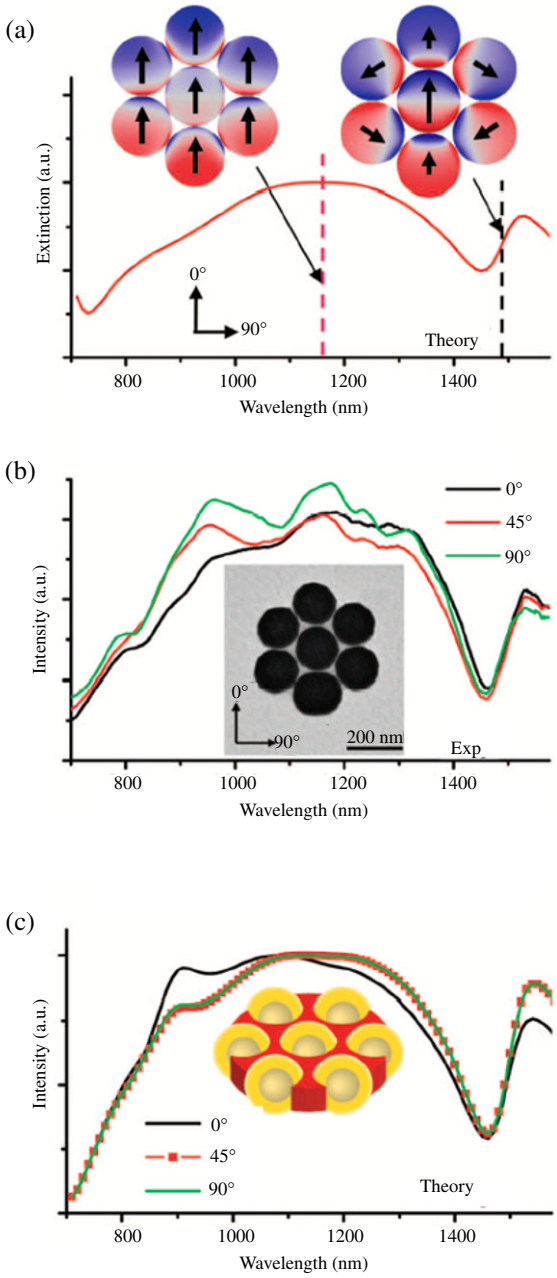


Fano-resonant behavior of a plasmonic heptamer. (a) Calculated extinction spectrum and charge density plots for a heptamer excited at normal incidence. The nanoshells have dimensions $[r_1, r_2] = [62.5, 85]$ nm, and the cluster has 1.6 nm gap separations and is embedded in a cylinder with a dielectric constant $e = 2.5$. The Fano minimum is at 1450 nm. The charge density plot of the heptamer is at 1490 nm. (b) TEM image and spectra of a heptamer at three different incident electric-field orientation angles. The nanoshells are measured to have average dimensions $[r_1, r_2] = [62.5, 85]$ nm. The Fano minimum at 1450 nm is isotropic for these orientation angles. (c) Calculated scattering spectra for a heptamer with a geometry matching that in (a), for the three orientation angles in (b). Reproduced with permission from Fig. 3, Ref. [121]. © 2010 AAAS.

Figure 25

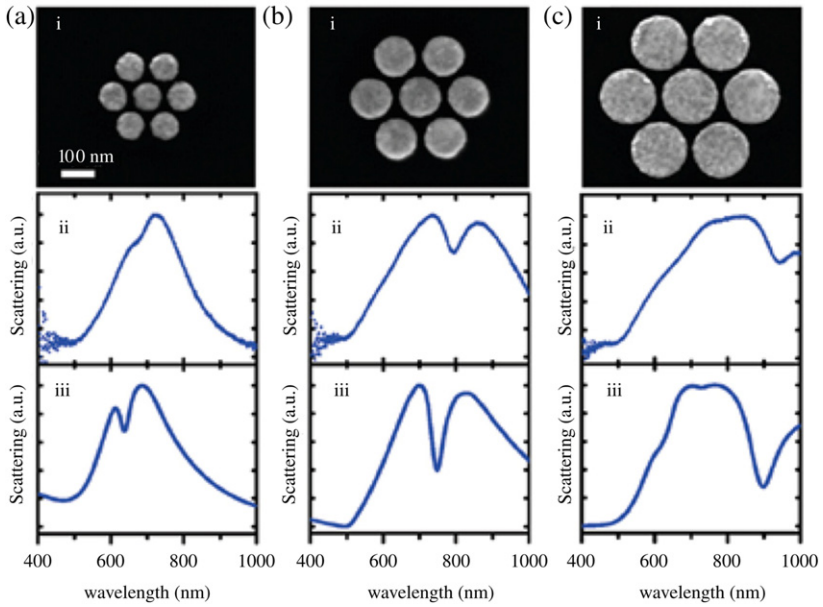


Size dependence of the scattering spectrum of a heptamer: (a) 85 nm diameter constituent particles, (b) 128 nm diameter particles, (c) 170 nm diameter particles. In all cases, the gap sizes between the particles in the heptamers were nominally ∼15 nm. (i) SEM images. (ii) Experimentally obtained dark-field scattering spectra, obtained with unpolarized light, of each individual cluster shown in (i). (iii) Finite difference time domain (FDTD) calculations of the dark-field spectral response of the same structure. Reproduced with permission from Fig. 1, Ref. [124]. © 2010 ACS.

Furthermore, Nordlander, Halas, and co-workers explored Fano resonance of heptamer nanoparticle clusters dependent on the size and local dielectric environment [124]. The Fano minimum is strongly dispersive toward lower energies with increasing cluster size, and the Fano line shape becomes broad. The smallest heptamer, with the diameter of 85 nm, offers a relatively narrow resonance near 700 nm (Fig. 25(a)), which is the bright superradiant bonding mode. Since the overall structure size is small, this mode does not radiate strongly and is quite narrow. For the intermediate size heptamer, with the diameter of 128 nm, the bright mode is redshifted to approximately 750 nm and significantly broadened owing to the increased radiation damping (Fig. 25(b)): the Fano resonance at 750 nm is now very obvious. For the largest heptamer, with the diameter of 170 nm, the superradiant mode shifts to nominally 900 nm and is remarkably broad (Fig. 25(c)); a strong Fano resonance is induced at 900 nm. For a heptamer this large, the subradiant mode radiates slightly, resulting in a slight broadening of the line width of Fano resonance. Moreover, the subradiant mode appears to redshift more strongly than the superradiant mode with increasing heptamer size because of the stronger hybridization of the higher-order modes. On the other hand, the complex interference phenomena underlying the formation of Fano resonances in coupled LSP systems are highly sensitive to the dielectric environment in the junctions of the overall

structure. In ambient air, the Fano resonance appears at 750 nm, while in immersion oil with a refractive index of 1.5, the Fano resonance is shifted to 900 nm, which indicates a very obvious redshift of Fano resonances with the increasing refractive index of the surrounding medium. The nanoparticle clusters for Fano resonance, with a higher-sensitivity optical response than the uncoupled plasmonic systems, can be expected to be applied to sensing and detection based on the coherent plasmonic phenomena.

Very recently, Zhou and Odom demonstrated that two-dimensional Au nanoparticle arrays can support Fano resonance [125]. The nanoparticle arrays (diameter of 160 nm and period of 400 nm) fabricated by using soft interference lithography offer a new type of subradiant mode (out-of plane lattice resonance) with an extremely narrow linewidth (FWHM of 5 nm). The subradiant mode originates from the out-of-plane dipolar coupling between large nanoparticles in the two-dimensional nanoparticle array. Compared with the in-plane modes, the out-of-plane dark subradiant modes can be statically tuned by changing the nanoparticle height or continuously tuned by changing the incident excitation angle. Because of interference between the narrow (subradiant) out-of-plane resonance and broad (superradiant) in-plane resonance, strongly coupled nanoparticle arrays show a Fano-type asymmetric profile. Furthermore, the coupled nanoparticle arrays can effectively trap the incident light and induce a large field enhancement both in the plane of the array as well as the surrounding volume. The field enhancement is dominated by the strong out-of-plane dipole interactions between the large nanoparticles. Therefore, the subradiant out-of-plane modes in the large nanoparticles offer an attractive way to achieve nanometer localized optical field enhancements with continuous spectral tenability and well-defined optical hot spots over large areas on different substrates. In this case, the enhanced local fields and extremely narrow linewidths based on the out-of-plane modes have promising applications in sensors, surface enhanced Raman spectroscopy (SERS), and nonlinear optics.

Recently, Spinelli *et al.*, by means of FDTD calculations, systematically studied the effect of Ag nanoparticle shape and substrate on LSP-mediated light coupling to a high-index substrate [126]. The dipolar resonance is strongly redshifted when the shape is changed from a sphere to a cylinder because of the increased near-field coupling of the dipolar field with the substrate. Furthermore, strong Fano-type line shapes appear in the transmission spectra owing to the interference of the direct and scattered light fields, and destructive interference leads to reduced transmission below resonance and is thus very sensitive to particle shape. The light coupling spectra are dominated by Fano resonances for the corresponding dipolar and quadrupolar scattering modes; varying the particle shape from spherical to cylindrical leads to large shifts in Fano resonance for the dipolar mode. Fano resonances based on the interference between the scattering and the transmission of light offers opportunities for light trapping in thin-film solar cells.

Fano resonances can also observed in a nanoparticle trimer due to the interference and interaction of electric and magnetic modes. Fano resonance between the fields radiated by electric and magnetic modes breaking the symmetry of the trimer system leads to a strong interaction

between the modes. Assemblies of strongly coupled plasmonic nanoparticles can support highly tunable electric and magnetic resonances in the visible spectrum [127]. The Fano resonance associated with the interactions between electric and magnetic modes can be applied to controlled nanoscale optical emission, SERS, and sensors.

Pakizeh and co-workers presented an intrinsic Fano resonance from Pd nanoparticles; the intrinsic Fano resonance originate from the coupling between the free and bound electron response of the metal Pd, and the degree of the Fano asymmetry is simply linearly proportional to the imaginary part of the interband contribution to the dielectric function Pd nanoparticles [128].

### *3.3b. Nanocavities*

For broken symmetric structures, Fano resonances originate from the interaction between the superradiant bright mode and the subradiant dark mode. Nordlander and co-workers explored Fano resonance in a concentric ring/disk cavity consisting of a disk inside a thin ring [129,130]. The interaction between the dipolar disk and ring LSPs results in a hybridized low energy bonding resonance and a higher-energy antibonding resonance. The higher-energy antibonding dipolar mode is superradiant, while the lower-energy bonding resonance is subradiant, because the individual dipole moments of the disk and ring are aligned oppositely. The increased interactions between the resonances of the ring and the disk also result in larger field enhancements. For the concentric structure, the field enhancement for the dipolar bonding resonance is 140, and for the broad dipolar antibonding resonance it is 10. In contrast, for the nonconcentric structure, the corresponding values are 250 and 50, respectively. It can be seen that the nonconcentric ring/disk cavity gives rise to much larger electromagnetic field enhancements than the symmetric system and that the multipolar modes can become dipolar active through hybridization. In symmetry broken structures, the dark quadrupolar ring LSP couples to the superradiant antibonding dipolar disk-ring mode; this coupling induces an asymmetric Fano resonance in the extinction spectrum similar to the electromagnetically induced transparency phenomenon. Additionally, the incident light can couple directly to the quadrupolar ring mode through simply changing the incident angle, and this direct coupling interferes between the quadrupolar ring mode and the superradiant mode to alter the line shape of the Fano resonance. As the angle of incidence is changed from perpendicular to grazing, the shape of the Fano resonance is continuously modified from a characteristic asymmetric resonance to a symmetric feature. The broken symmetric cavities based on the Fano resonance exhibit a high LSPR sensitivity and have potential applications in sensing.

Furthermore, Nordlander and co-workers presented an experimental investigation of the higher-order Fano resonances of LSP nanocavities that are due to the coherent coupling between the superradiant and subradiant LSP modes [120,131]. The higher-order Fano resonances can arise in larger dolmen-type nanocavities with broken synmmetry if the dipolar, continuum-like spectrum of the nanoscale resonator is broad enough to overlap with the narrow octupolar resonances. The Fano

Figure 26

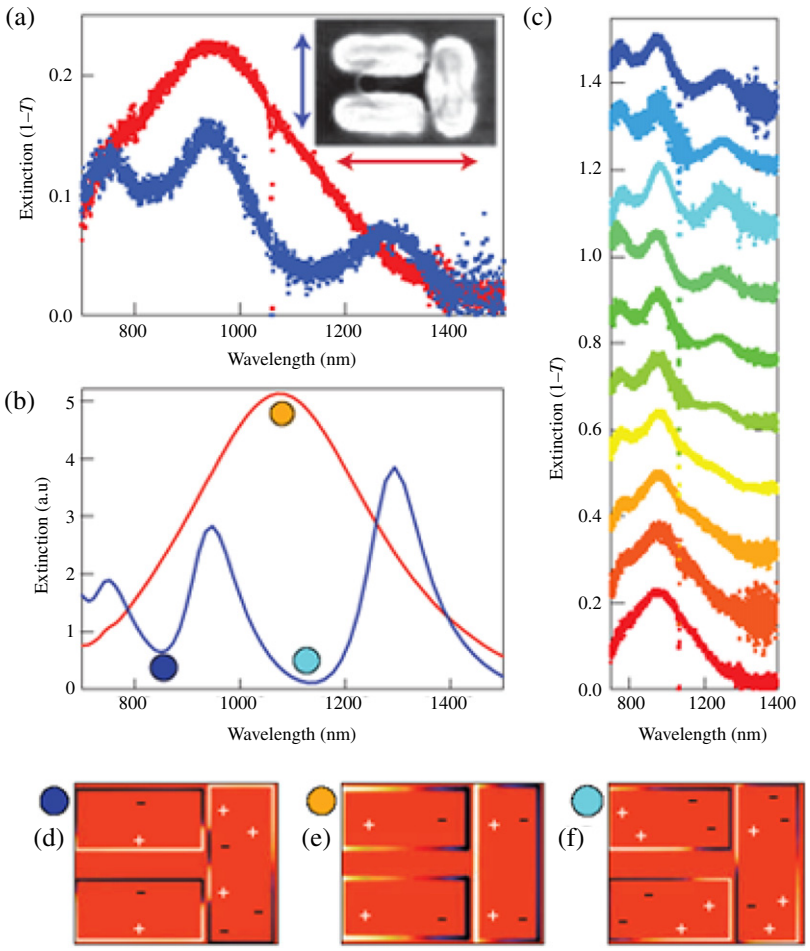


Larger dolmen cavity, exhibiting multiple Fano resonances. (a) Experimentally observed single-dolmen structure extinction spectra for the two polarizations indicated in the inset. (b) Numerically calculated extinction spectra. (c) Measured extinction spectra as the polarization of the incoming light beam is continuously rotated between the two principal directions. (d), (f) Surface charge distribution for the mode corresponding to the high-energy and low-energy dip in the extinction spectrum for perpendicular polarization, and (e) for the mode at the extinction peak for parallel polarization. Reproduced with permission from Figs. 4c–4e, Ref. [120]. © 2010 NPG.

interferences are clearly visible at wavelengths of 850 and 1100 nm for polarization perpendicular to the pair axis (Fig. 26(a), blue curve). On the other hand, the surface charge distributions (Figs. 26(d)–26(f)) indicate that the monomer dipolar and quadrupolar modes are mixed with each other. The extinction dip of this bigger dolmen at 850 nm results from the dispersive coupling of the dimer dipolar mode with a quadrupolar in the monomer slab, while that at 1100 nm results mainly from a coupling between the monomer dipolar mode and dimer bonding mode; because of the strong near-field coupling, the latter can couple back to higher-order modes in the monomer, hence resulting in the observed mode mixing. For an incident polarization along the pair axis

the extinction spectrum is the sum of the individual dimer and monomer spectra (Fig. 26(a), red curve). In addition, both the spectral position and the width of these Fano line shapes depend very sensitively on the dielectric gap between the individual resonators sustaining the dark and bright modes, respectively. For both geometries, the depths of the Fano dip increases with decreasing gap size owing to increasing coupling between dipolar and quadrupolar modes.

Very recently, Zhu and co-workers reported a remarkably simple planar nanostructure consisting of a single metal nanodisk with a missing wedge-shaped slice; the planar nanostructure supports Fano resonance [132]. For a symmetric nanodisk (slice angle $\theta = 0°$), the extinction spectrum only exhibits a dipolar disk resonance centered at 600 nm. When a wedge is sliced from the nanodisk, this resonance blueshifts and an additional shorter wavelength resonance appears near 450 nm with increasing the slice angle. Moreover, the bonding and antibonding hybridized resonance modes are found due to the interaction of the disk LSPs with the slice LSPs. For a slice angle $\theta = 45°$, the antibonding resonance begin to appear on the short wavelength around 400 nm, and the intensity of the resonance enhances with increasing slice angle. For a slice angle of 90°, a prominent asymmetric Fano resonance appears. In this broken geometry, the Fano line shapes result from the coupling between the dipolar mode supported by the disk and the quadrupolar mode supported by the edge of the missing wedge slice. As a result, both disk size and wedge angle influence the properties of the resonance. The broken symmetric disks provide an important substrate for high-sensitivity LSPR sensing applications.

### 3.3c. Nanorods

Recently, Altug and co-workers reported an asymmetric hetero-oligomer nanostructure for directional double Fano resonances. The hetero-oligomer nanostructure was designed by combining two dimer structures such that their resonance modes with opposite decay characteristics (i.e., short-lived and long-lived modes) were in simultaneous spectral overlap [133]. The dimer structures are named side-to-side and collinear dimmers. Figures 27(c)–27(e) present SEM images of the fabricated symmetrically coupled, asymmetrically coupled, and uncoupled structures. Note that the dimers are closely placed to permit near-field coupling between them (Figs. 27(c) and 27(d)); this coupling yields excitation of double Fano resonances in the final structure. For the uncoupled case (blue curve), dark modes are not excited because of the negligible near-field interaction between the dimers, and the spectrum traces a sum of their individual bright resonances. The asymmetrically coupled structure shows a clear excitation of the dark modes (black curve), which appear as narrow peaks inside the extinction dips of the bright resonances (labeled I and II in Fig. 27(b)), and double Fano resonances appear in the asymmetrically coupled hetero-oligomer. Furthermore, Fan *et al.* analyzed the double Fano resonances in the hetero-oligomer nanostructures by using a temporal coupled mode theory [134]. Based on the asymmetric hetero-oligomer structure consisting of side-to-side and collinear configurations, one can simultaneously acquire hybrid modes of different radiative decay characters (dark–bright) overlapping

Figure 27

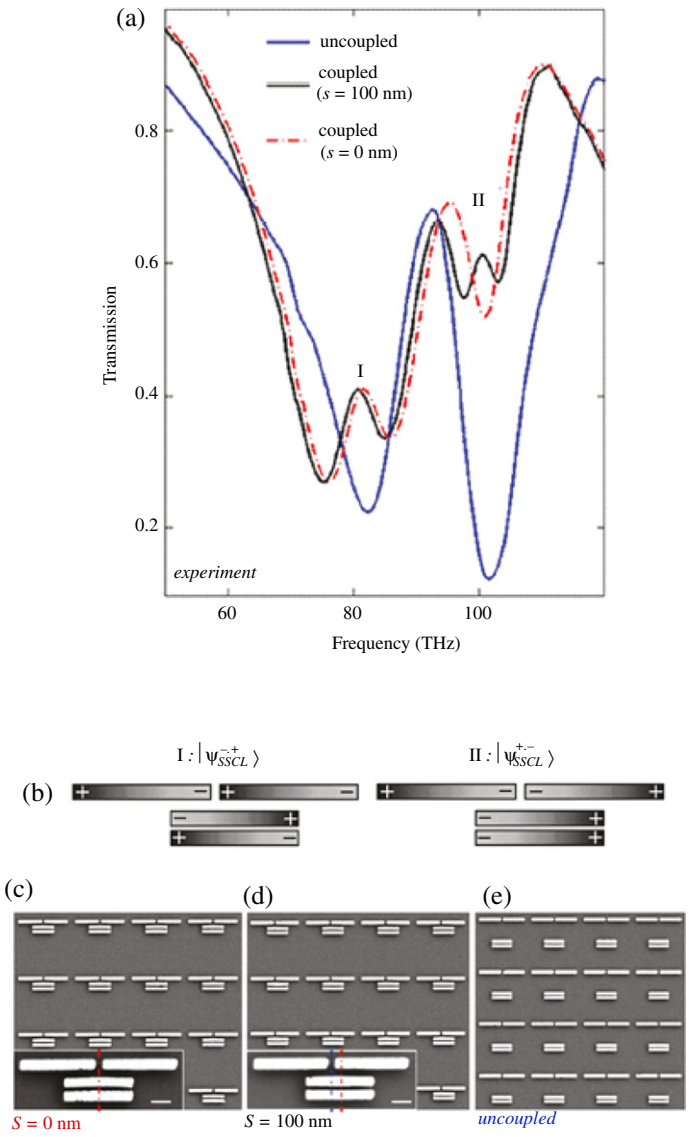


(a) Experimental transmission spectra of uncoupled (blue curve), asymmetrically coupled (black curve), and symmetrically coupled (red dashed curve) hetero-oligomer structures. Excitation of only the bright modes ($|\psi^{+}_{SS}\rangle$ and $|\psi^{+}_{CL}\rangle$) is observed in the uncoupled configuration, while double Fano resonances are clearly visible in the asymmetrically coupled configuration ($|\psi^{\pm,\mp}_{SSCL}\rangle$). Only a single Fano resonance is seen in the symmetrically coupled structure ($|\psi^{-,+}_{SSCL}\rangle$). (b) Top-view charge distributions representing the excitation of dark modes at respective Fano resonance in asymmetrically coupled configurations. (c)–(e) SEM images of (c) symmetrically coupled, (d) asymmetrically coupled ($s = 100$ nm), and (e) uncoupled hetero-oligomer structures. Images with higher magnification are shown in the insets to (c), (d), where the white bar is 200 nm long. Reproduced with permission from Figs. 4b–4f, Ref. [133]. © 2011 ACS.

at different ends of the spectrum with respect to the single dipolar resonance. In this case, if a near-field coupling is established between the side-to-side and the collinear configurations, one can achieve the simultaneous excitation of both hybrid dark modes through the hybrid bright modes. The composite modes of the coupled system result in the double Fano resonances because of the simultaneous overlapping of the multiple radiant and subradiant hybrid modes. Double Fano resonances in the hetero-oligomer structures have potential applications in biosensing and highly directional on-chip antenna.

Wang and co-workers explored Fano resonances of an Au nanorod array coupled with a semicontinuous nanorod film [135]. The nanorod-film hybrids can be tuned into Fano resonance when the film is adjusted to the percolating regime. It is found that the optical transmission of the percolating films is enhanced around the LSPs of the films (ranging from 650 to 920 nm) and decreases around the short-axis LSPs (530 nm) of the nanorod array. The calculated transmission enhancement $\Delta T/T$ at 800 nm reaches the maximum value of 55% and apparently redshifts as the Au nanorod length increases. Random distributions of the nanoparticles broaden the enhanced transmission peak in $\Delta T/T$. The central wavelengths of the nanorod-film hybrids are very close to the long-axis LSPs of the Au nanorod array, which confirms strong plasmonic coupling between the Au nanorod array and semicontinuous film. In addition, they presented a theoretical investigation on Fano resonances in plasmonic nanorod dimmers by the FDTD method [136,137]. A bright mode nanorod (short rod) and a dark mode nanorod (long rod) form a nanorod dimmer, wherein the short and long nanorods in the dimmer support dipolar and quadrupolar modes, respectively. The Fano resonance appears when the nanoemitter is placed at the dimer apex near the short nanorod; however, no Fano resonance is seen with the nanoemitter placed in the gap of the dimer. Fano resonance in the semicontinuous nanorod film offers nonlinear enhancement effects, which have potential application in highly sensitive SERS substrates.

### 3.3d. Nanowires

Nordlander and co-workers presented Fano resonances in a metal photonic crystal consisting of an Au nanowire grating on a single-mode ITO slab waveguide [120]. When the light is incident normal to the structure, Fano resonance appears in a TE polarization due to the coupling between the nanowire array and the slab waveguide, and the narrow waveguide mode interferes with a continuum of vacuum states. In a TM polarization, the incident light can excite a particle LSPs across the nanowires, which can interfere destructively with the narrow waveguide resonance.

Recently, Chen and co-workers theoretically explored the effect of the applied magnetic field on the LSP properties of the nanowire coupled to two quantum dots [138]. When the magnetic field $H_0 < 1.5$ T, there is interference between the localized and delocalized channels of the incident LSPs [139]. It is found that the transmission spectrum presents symmetric double peaks without the applied magnetic field, and the separation between these two peaks is reduced when the magnitude of

the magnetic field is increased. In the presence of the magnetic field, the dispersion relations of LSPs are upwardly displaced. Furthermore, the interference between the localized and delocalized channels of the incident LSPs can also occur when the exciton energies of the two quantum dots are appropriate chosen, which results in the symmetric double peaks and the Fano line shape in the transmission spectrum. The double peaks will gradually combine, and the Fano line shape will be smeared out in the presence of the magnetic field. Therefore, one can control the scattering of the LSPs by varying the magnitude of the applied magnetic field.

# 4. Coupling of Surface Plasmons by Use of Nanostructures

## 4.1. Metal Nanostructures

Both localized surface plasmon (LSP) and surface plasmon polariton (SPP) modes exhibit coupling effects when nanostructures are close together. The coupling of surface plasmons (SPs) between nanostructures offers a unique strategy to tune the spectrum and strength, as well as the spatial distribution and polarization, of local electric fields in and around the nanostructure [140,141]. For example, SP coupling between a pair of metal nanoparticles has been used to generate a strongly confined and enhanced electric field at the junction of the pair, allowing intense surface enhanced Raman spectroscopy (SERS) [142,143] for achieving improved sensitivity of the resonance to the local environment [144,145], and also photonic propagation and wave guiding [146]. Near-field coupling generated by changing the coupling distance has also been used to design plasmon rulers for measuring nanoscale distances [147,148] and metal nanoshells and nanoboxes for visible–near-IR (NIR) tunable absorbers and scatterers [56,149]. With the goal of optimally designing and exploiting near fields, the fundamental study of SP coupling has been the subject of numerous studies and remains a topic of intense current interest [150].

### *4.1a. Metal Nanoparticles*

LSP mode interaction between metal particles that are close together gives rise to coupling; the coupling results in resonances that are different from that of a single particle. The distance between the particles, as well as the strength of their individual interaction with the incident field, determines the nature of these resonances. For a given incident field, the enhanced near field that develops between an isolated pair of coupled metal particles are stronger than those that exist if the pair is part of a large array of coupled particles [151].

When metal nanoparticles are assembled into two-dimensional arrays, the local electric field of each particle will overlap with that of its neighboring particle; as a result, intense resonance modes appear due to the coherent SP coupling between the nanoparticles [152]. The nanoparticle size and interparticle distance exhibit a remarkable influence on the

coherent SP coupling in two-dimensional Ag nanoparticle arrays. The SP coupling peak shows redshifts from 416 to 493 nm with increasing nanoparticle size (e.g., 46, 59, 86, 128, 160, 194, to 287 nm) [153]. For nanoparticles smaller than about 86 nm, the coupling peak is less intense and broader. For larger particles, the coupling peak is fairly strong and broad owing to the phase retardation of the incident light. On the other hand, when the packing density of the nanoparticles is low, the interparticle distance is correspondingly large, and the SP coupling is weak; but when the number of nanoparticles increases, the interparticle distance decreases, and the SP coupling became stronger. Furthermore, it is observed that for small particles the coupling peak exhibits redshifts and becomes broad as more particles are self-assembled. In contrast, for nanoparticles larger than 128 nm, a blueshift and narrowing of the SP mode occur. The nanoparticles with intermediate sizes exhibit mixed behavior characterized by redshifts and blueshifts as well as spectral broadening and narrowing. Therefore, there is an optimal particle size around 86 nm with corresponding optimal interparticle distance of about 107 nm that results in the most intense and the sharpest coherent SP coupling mode.

El-Sayed and co-workers systemically investigated the SP coupling in metal nanoparticle pair arrays [154]. The LSP spectra of the Au nanodisc pair arrays with different internanodisc separation gaps (e.g., 212, 27, 17, 12, 7, and 2 nm) exhibit distinct differences for two different polarization directions of the incident light. The LSP resonance strongly redshifts with a decreasing interparticle gap for the polarization direction parallel to the interparticle axis, while the LSP resonance exhibits a very weak blueshift with a decreasing gap for the polarization direction perpendicular to the interparticle axis [154]. The resonance shifts result from the electromagnetic coupling of the single-particle plasmons. The dipole–dipole interaction is attractive for parallel polarization, which results in the reduction of the SP resonance frequency (redshift of the SP band), while that for the perpendicular polarization is repulsive, resulting in the increase in the resonance frequency (blueshift) [91]. The resonance shift reflects the strength of the interparticle electromagnetic coupling; therefore the interparticle interaction is very strong for parallel polarization because of the larger shift of the resonance peak. Furthermore, for polarization along the interparticle axis the interparticle SP coupling strength decays nearly exponentially with decay length, which is roughly about 0.2 in units of the particle size for different nanoparticle sizes, shapes, metal types, and medium dielectric constants. A dipolar-coupling model based on dipole–dipole interactions qualitatively indicated the decay of the particle SP near-field as the cubic power of the inverse distance.

Recently, a strong SP near-field coupling between neighboring nanoparticles was observed in a self-assembled ring of polystyrene-functionalized 40 nm Au nanoparticles [155]. Single-particle dark-field scattering spectroscopy demonstrates that the geometry of the assembly is very important, as quasi one-dimensional coupling occurred evenly along the ring circumference but independently of the ring curvature. The spatially resolved scattering spectra indicate the presence of two additional SP bands that are redshifted from the single nanoparticle resonance and are polarized parallel to the local ring segment. The

nanoparticle assemblies with small interparticle distances present a promising route for manipulating SP coupling in chemically assembled structures, as well as for realizing functional plasmonic devices such as antennae and waveguides.

Furthermore, the electromagnetic coupling between nanoparticles can be explained by following the principles of molecular hybridization with different LSP modes [156]. The LSP modes of two interacting metal nanoparticles ($\Psi 1$ and $\Psi 2$) hybridize either in-phase ($\Psi 1 + \Psi 2$) or out-of-phase ($\Psi 1 - \Psi 2$). When the incident light field is polarized parallel to the interparticle axis, the in-phase combination is a lower-energy bonding mode ($\sigma$) and the out-of phase mode ($\sigma^*$) is a higher-energy antibonding configuration. However, when the polarization is perpendicular to the interparticle axis, the in-phase combination is an antibonding mode ($\pi^*$) while the out-of phase one is a bonding mode ($\pi$). It is noted that the coupling and the resulting LSP shifts are weaker for the latter transverse polarization.

Alivisatos and co-workers investigated the SP coupling of symmetric and asymmetric nanoparticle dimers [157]. For the symmetric dimer consisting of 40 nm Ag nanoparticles, the scattering spectra show two distinct resonance modes: the lower-energy bonding mode at 517 nm results from the longitudinal coupling of the particle plasmons ($\sigma$), and the higher-energy antibonding mode at 456 nm is due to the transverse coupling of the particle plasmons ($\pi^*$, Fig. 28(b)), as expected from the plasmon hybridization model for a homodimer (Fig. 28(c)). For the size-asymmetric dimer consisting of a 20 nm nanoparticle and a 40 nm Ag nanoparticle, the scattering spectra demonstrate two resonance modes at 422 nm and 481 nm for transverse coupling and at 420 nm and 486 nm for longitudinal coupling, respectively (Fig. 28(f)). Furthermore, the in-phase combinations ($\Psi 1 + \Psi 2$) of the individual particle plasmons display longitudinal coupling at 486 ($\sigma$) and the transverse coupling at 422 nm ($\pi^*$), while the out-of-phase combinations ($\Psi 1 - \Psi 2$) present the longitudinal coupling at 420 nm ($\sigma^*$) and the transverse coupling at 481 nm ($\pi$), and the out-of-phase modes ($\sigma^*$ and $\pi$) are weaker in intensity compared to the in-phase modes ($\sigma$ and $\pi^*$). In addition, exploration of a heterodimer consisting of a 30 nm Ag nanoparticle and a 40 nm Au nanoparticle indicates that the bonding modes are redshifted with respect to the Au nanoparticle LSP resonance; however, the antibonding modes are also redshifted with respect to the Ag nanoparticle LSP resonance owing to the coupling of the Ag particle LSP resonance to the quasi-continuum of interband transitions in Au.

On the other hand, a theory of the coupling of evanescent optical fields between metal nanoparticles has been developed by using an electrostatic approximation. The key result is a description of the coupling coefficients that explicitly contain the effects of the electric field from one particle acting on the surface dipoles of another, and it explains the relationship between the geometry, surface modes, and the LSP resonances of the particles [158]. The theory also explores the key factors that control the SP coupling between nanoparticles, which lead to changes in resonances and two different resonance modes. It is demonstrated that the coupling between a simple pair of nanoparticles leads to resonance frequency splitting and the formation of a asymmetric dark mode; the dark mode is associated with little scattering of light

Figure 28

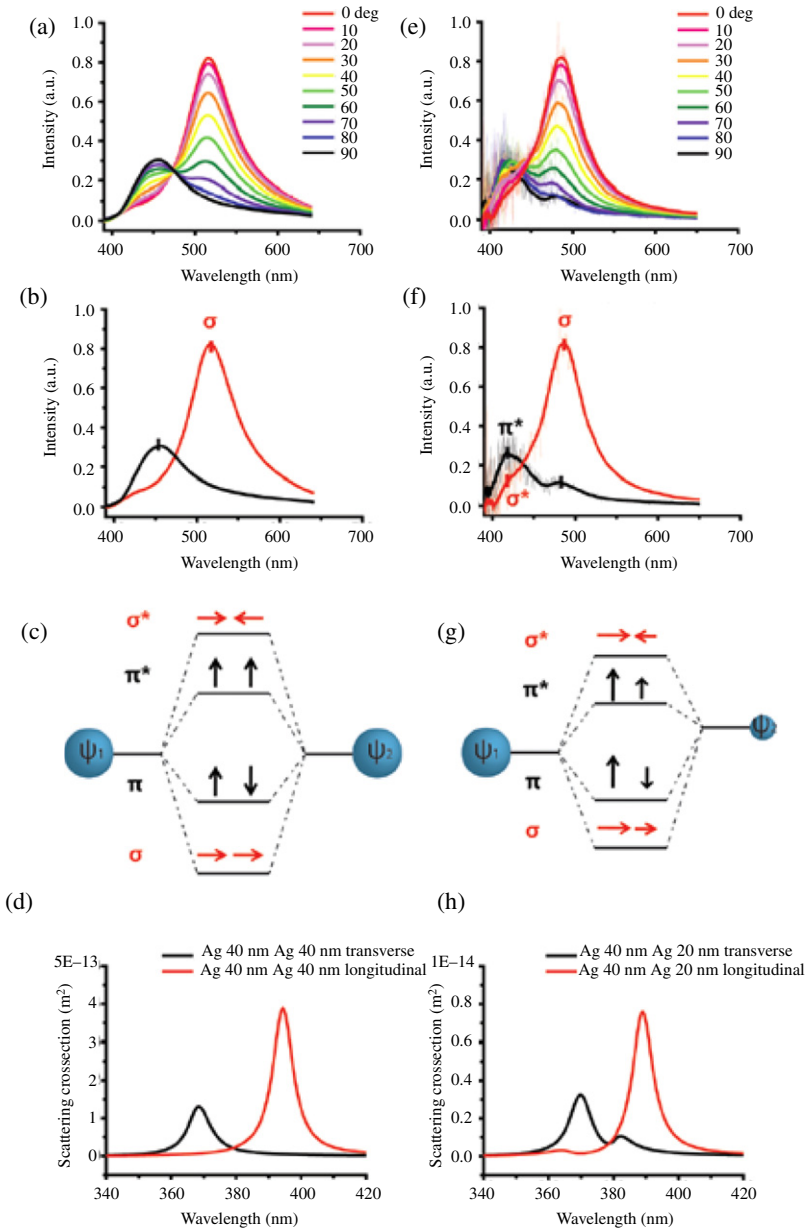


Plasmon coupling of symmetric (a)–(d) and size-asymmetric (e)–(h) silver nanoparticle dimers. Scattering spectra from a symmetric (a) and an asymmetric (e) dimer as a function of the polarizer angle (0°–90°). Two extreme cases from the polarization experiments of the symmetric and the asymmetric dimer are presented in panels (b) and (f), respectively. These match well with the hybridization model (c), (g) and with the scattering spectra predicted using a coupled dipole–dipole model in the quasi-static approximation (d), (h). Reproduced with permission from Fig. 2, Ref. [157]. © 2010 ACS.

but large evanescent electric fields. In this case, the dark mode has low radiation damping compared with an associated bright mode.

### 4.1b. Metal Nanorods

Noble metal nanorods exhibit transverse and longitudinal LSP resonance modes that correspond to the electric field perpendicular and parallel to the length axis, respectively. The resonance excitation and scattering of the longitudinal mode of metal nanorods are inherently polarized along the length axis. SP coupling between metal nanorods occurs when they are close together and their SP modes interact, which results in resonances that are different from that of a single nanorod [159]. The SP coupling between metal nanorods is highly dependent not only on their interrod spacing but also on their relative orientation.

The coupling between Au nanorods at an extremely close approach with interrod distances smaller than 2 nm has been investigated by Funston and co-workers [160]. The shape anisotropy of the nanorods leads to different possible orientations of the nanorods within the dimer, resulting in different orientational modes of coupling. Coupling of the rod longitudinal modes when the dimer is arranged end-to-end or side-to-side leads to bonding and antibonding interactions, which corresponds to coupling with a decrease and an increase of LSP mode energy. Figures 29(a) and 29(b) demonstrate the scattering spectra of the nanorods aligned end to end; the intense longitudinal resonance band is redshifted by more than 135 to 816 nm when compared with that of the individual nanorods in these two dimmers (which range from 648 to 679 nm). The longitudinal mode is excited for incident light polarized parallel to the internanorod axis, and the longitudinal modes of the two nanorods interact via an attractive coupling with the opposite poles of the induced dipoles arranged in an alternating fashion, which results in a lowering of the resonance energy compared with that for the longitudinal mode of the individual nanorods. As a result, a redshift of the resonance occurs. Furthermore, when the light is polarized perpendicular to the internanorod axis, the transverse mode is excited; however, no appreciable shift is observed because of the weak coupling in this case. In contrast to the case for nanorods aligned end to end, the spectra of nanorods aligned in a side-by-side configuration are blueshifted by 21 nm to 48 nm compared with single rods (to $\lambda_{max} = 614$ nm). For polarization parallel to the internanorod axis, the low-intensity transverse resonance modes interact attractively and are redshifted as the nanorods approach one another. However, the longitudinal plasmon mode of the nanorods with a repulsive coupling interaction leads to a slight blueshift.

In addition, for nanorod dimers arranged at right angles, the longitudinal and the transverse modes will cause coupling [160]. The scattering spectra of the nanorod dimers arranged in T- and L-shaped configurations are shown in Figs. 29(e) and 29(f). Two well-separated resonance modes are present in the scattering spectra of the nanorods in the L-shaped configuration. For incident light polarized parallel to the internanorod axis, the longitudinal modes of the nanorod dimers oscillate in phase with one another, and the dipoles interact attractively. For incident light polarized perpendicular to the internanorod axis, the longitudinal modes of the nanorod dimers oscillate symmetrically out of phase, and the dipoles interact repulsively. It is noted that the coupled modes are all due to interactions between the longitudinal modes of

Figure 29

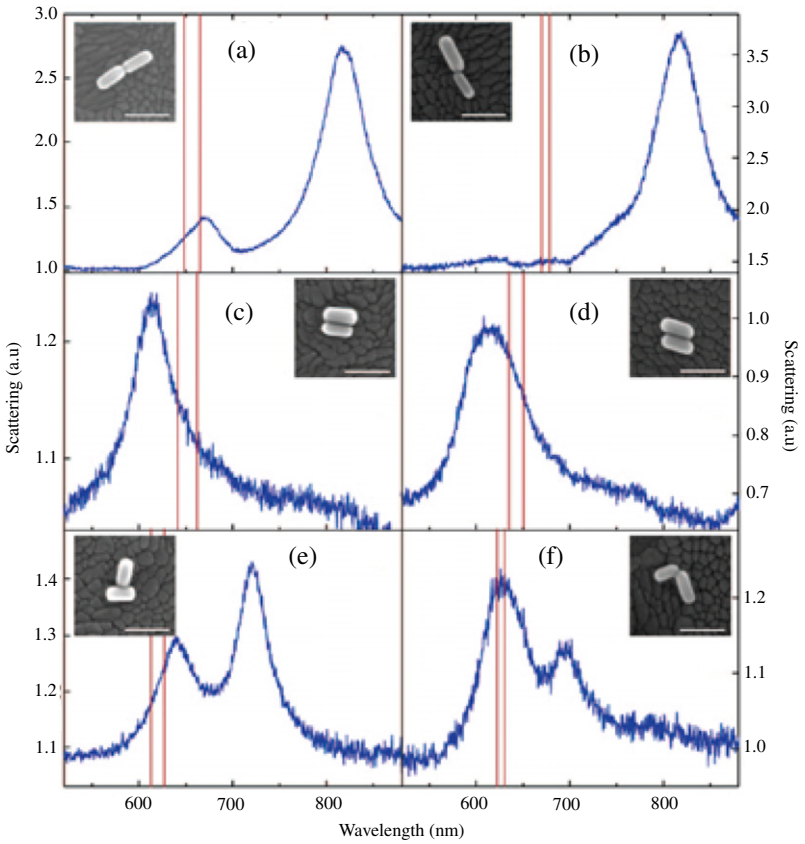


Scattering spectrum for two rods aligned (a) and (b) end to end, (c) and (d) side to side, (e) in a T configuration, and (f) in an L configuration, all on ITO and in air. Insets show the SEM images of the particles giving rise to each scattering spectrum. Scale bar = 100 nm. Reproduced with permission from Fig. 2, Ref. [160]. © 2009 ACS.

the nanorods and not longitudinal-transverse coupling. On the other hand, for the nanorod dimers in a T-shaped configuration, coupling between the longitudinal and transverse modes of the nanorods occurs. Moreover, the light polarized parallel to the internanorod axis results in the excitation of the longitudinal mode of the nanorods; this excitation interacts with a mode of the opposing sign in the center of the other rod, lowering its energy slightly. Conversely, the light polarized perpendicular to the internanorod axis results in the excitation of the rod forming the top rod of the T, which is able to interact to a small degree with a dipolelike mode of the perpendicular nanorod. It is possible that these coupling interactions in the T-shaped dimer are predominantly dipole-induced dipole interactions in character. These results indicate that small changes in nanorod orientation give rise to relative large changes in the SP coupling interaction.

El-Sayed and co-workers explored the orientational dependence of SP coupling in Au nanorods by the discrete dipole approximation method [161]. For end-to-end linkage of nanorods, as the nanorod spacing decreases, the longitudinal resonance band shows redshifts

due to the SP coupling between neighboring nanoparticles, while the transverse resonance band does not show any shift for the end-to-end alignment. On the other hand, for side-by-side linkage of nanorods, the longitudinal resonance band shows blueshifts. In contrast to the longitudinal resonance, the transverse resonance band in side-by-side nanorods displays redshifts. Furthermore, for both end-to-end and side-by-side linkage of nanorods, the coupling strength increases with reduced nanorod spacing or an increased number of nanorods in the assembly. The nanorods with increasing aspect ratios show increasing strength of longitudinal SP coupling for both assembly orientations.

Moreover, the mechanism of the plasmon resonance band shift in the end-to-end and side-by-side configurations can be explained by a dipolar exciton coupling model [161]. Exciton theory predicts that the excited-state levels of the monomer will split into two levels upon dimerization, a lower energy level and a higher energy level relative to the monomer excited state, corresponding to two possible arrangements of the transition dipoles of the chromophores in the dimer (e.g., in phase or symmetric, and out of phase or antisymmetric). For side-by-side or *H*-type dimers (Fig. 30(a)), transition to the lower-energy excited state is forbidden because of the cancellation of the two dipole moments in this configuration, and the spectrum consists of a single band at higher energy with respect to the monomer, for which the interaction between the two transition dipoles of the dimer is repulsive. For end-to-end or *J*-type dimers (Fig. 30(b)), transition to the higher energy state is forbidden because of the cancellation of the two dipole moments in this configuration, and the spectrum shows a single band at lower energy with respect to the monomer, for which the interaction between dipoles is attractive. If the nanorod plasmons are considered to be effectively excitons, the exciton coupling theory can used to explain the optical spectra of the nanorod dimers. For the longitudinal polarization, the side-by-side nanorod dimer represents an *H* aggregate and hence gives rise to the blueshift. Conversely, the end-to-end assembly is a *J* aggregate, resulting in the redshift. For the transverse polarization, the side-by-side configuration is a *J* aggregate (provided that the polarization direction is along the internanorod axis), leading to the redshift, and the end-to-end configuration is an *H* aggregate without any obvious shift of the SP resonance. Capasso and co-workers systematically investigated the coupling effects between metal nanorods with different Au nanorod gaps [162]. The resonance peak shows blueshifts from 740 to 693 nm when the gap along the nanorod long axis increases from 20 to 100 nm. For the interaction between the nanorods along the long axis, the field radiation from nearby nanorods adds destructively to the local dipole field; as a result, the decrease of the force on the electrons in the nanorod lowers their resonance frequency, and thus the resonance yields redshifts. When the spacing between the nanorods along the long axis increases, the radiative fields from neighboring nanorods become weaker; the resonance wavelength displays blueshifts with an increasing Y-gap. On the other hand, the resonance peak shows redshifts from 606 to 653 nm when the gap along the nanorod short axis increases from 20 to 200 nm. For the interaction between the nanorods along the short axis, the field radiation from nearby nanorods adds constructively to the local dipole field. As a result, the enhancement of the force on the electrons in the nanorod increases their resonance frequency. Thus the

Figure 30

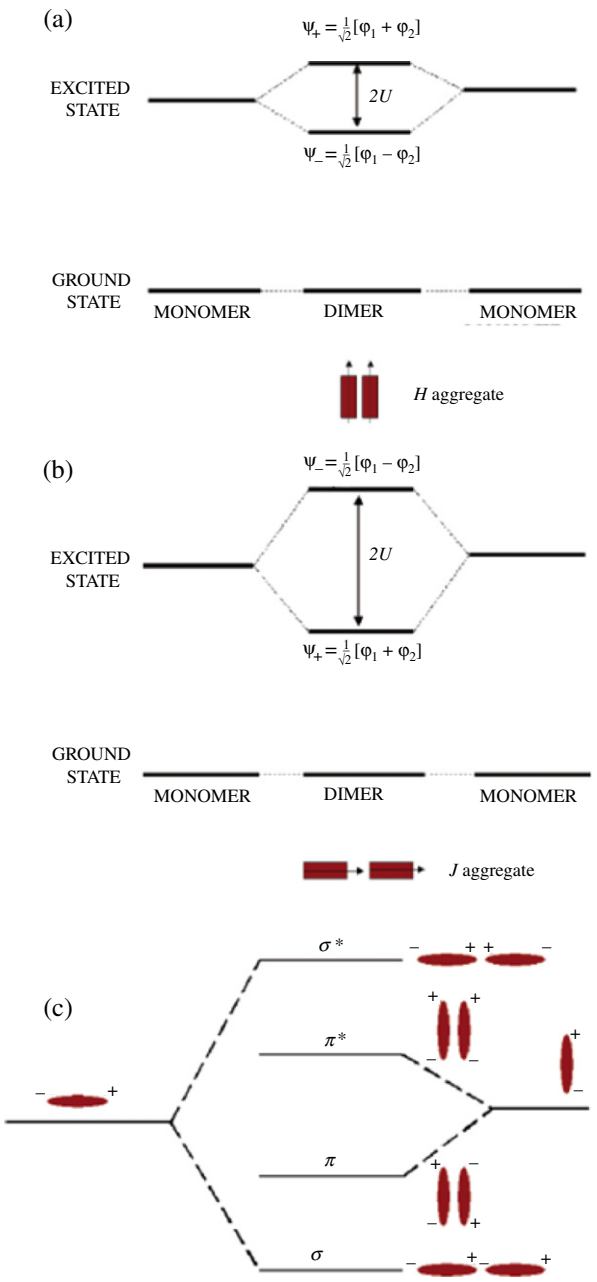


Schematic of the energy level splitting resulting from the dipolar interaction of chromophores in a dimer, showing symmetric ($\Psi_+$) and antisymmetric coupling ($\Psi_-$) of excitons for (a) *H* aggregate geometry and (b) *J* aggregate geometry. (c) Exciton theory picture of the nature of the coupled longitudinal plasmon excitation in nanorod dimers: electromagnetic analogy to molecular orbital theory. Reproduced with permission from Fig. 4, Ref. [161]. © 2006 ACS.

resonance wavelength exhibits blueshifts. When the spacing between the nanorods along the short axis increases, these radiative fields decrease in magnitude, which gives rise to redshifts of the resonance wavelength [163].

In addition, a systematic study of the SP coupling in Au nanorod dimers as a function of the relative orientation between the two nanorods was reported by Wang, Lin and co-workers [164]. The nanorods are linked covalently at their ends through dithiol molecules and form different angles. It is found that the resonance wavelengths of the bonding and antibonding modes remain approximately unchanged. The electric field in the gap region is largely enhanced for the bonding mode, while that for the antibonding mode is even smaller than the far field. Furthermore, as the nanorod angle increases, the higher-energy resonance peak becomes weaker, whereas the lower-energy one becomes stronger. The scattering intensity ratio between the bonding and antibonding modes decays rapidly with an increasing angle between the nanorods. The angle-dependent coupling indicates that large electric field enhancements occur only under excitation of the bonding mode, while the local electric field in the gap region is reduced when metal nanorod dimers are excited at their antibonding mode.

### *4.1c. Metal Nanowires*

When two or more metal nanowires are illuminated at a resonance wavelength, the charge redistribution of the nanowires occurs and results in an electromagnetic coupling between the nanowires. The SP coupling between the nanowires leads to strong localized electric fields at specific wavelengths and a large scattering cross section. Kottmann and Martin explored the SP coupling between two Ag nanowries by a finite elements method [165]. When two Ag cylindrical nanowries with a 50 nm diameter and a separation distance of 5 nm are illuminated with a TE wave, the spectra of the scattering cross section exhibit different resonance peaks. With illumination directions perpendicular and parallel to the major axis between the nanowires, the resonance peak is 340 nm for an individual nanowire, and an additional resonance at 372 nm appears for illumination parallel to the major axis (e.g., the incident electric field perpendicular to the major axis). However, an additional broad resonance peak at 380 nm is observed for illumination perpendicular to the major axis (e.g., the incident electric field along the major axis), and the very strong scattering cross section intensity indicates that the coupling effect is much stronger. Furthermore, for the single nanowire, the field amplitude reaches about 8 (in units of the illumination amplitude) at the resonance and decreases for larger wavelengths (Fig. 31(a)), and the electric field distribution is very homogeneous. The polarization charge distribution in the single nanowire is symmetrical with plus charges on one side of the particle and negative charges on the other side (Fig. 31(d)). For illumination perpendicular to the major axis, the field amplitude in the two interacting nanowires is homogeneous and rather weak (Fig. 31(b)). At the same time, for larger wavelengths the coupling becomes quite strong: the field intensity reaches almost 40 at the resonance ($\lambda = 380$ nm). In this case, polarization charges of opposite signs are confined on the sides of the gap, and the same amount of opposite charges is distributed on the remainder of the particle; when the two nanowires are in phase, the same amount of opposite charges is distributed on the remainder of the nanowire (e.g., the negative charges on the left and positive charges on the right (Fig. 31(e)). For illumination parallel to the major

Figure 31

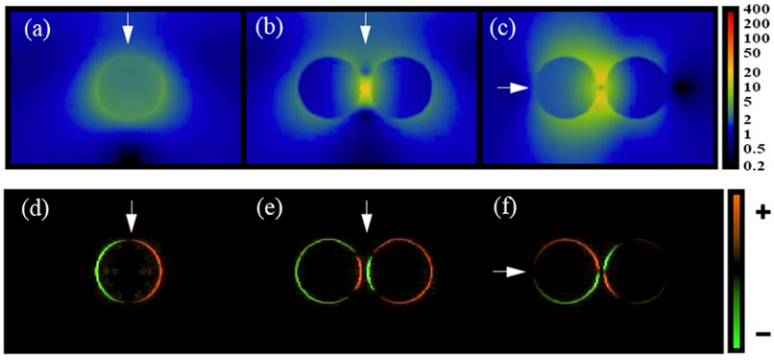


Top, field amplitude distribution as a function of the illumination wavelength (indicated in each frame) for (a) an individual cylinder (277 KB) and (b), (c) two interacting cylinders with a 5 nm separation (321 and 381 KB); the cylinders have a 50 nm diameter. For the interacting cylinders two different illumination directions, indicated by the arrow, are considered. Corresponding main resonances (a) $\lambda = 344$ nm, (b) $\lambda = 380$ nm and (c) $\lambda = 374$ nm. Bottom, polarization charge distribution at the main resonance for (d) a single cylinder and (e), (f) two interacting cylinders with a separation $d = 5$ nm. Illumination direction as indicated. The cylinders have a 50 nm diameter. A different colorscale is used for each part: the charge density is much higher for the coupled cylinders (e) and (f) than for the single cylinder (d). Reproduced with permission from Figs. 2 and 3, Ref. [165]. © 2001 OSA.

axis, a similar enhancement is observed (Fig. 31(c)). In this case, the two nanowires are out of phase, the first (left) nanowire has $\pm$ charges, whereas the second (right) has $\mp$ charges (Fig. 31(f)), which results in a quadrupole charge distribution around the gap between the nanowires. Consequently, the field vanishes in the middle of the gap: this coupling mechanism is governed by retardation. On the other hand, the coupling strength is strongly dependent on the separation distance between the nanowires. For example, considering the illumination direction normal to the major axis, for a separation distance equal to the diameter, there is almost no coupling, but the field enhancement becomes very large for the separation distance (e.g., $\leq$5 nm). When the distance is 2 nm, the field amplitude in the gap exceeds 200 times that of the illumination field [165]. The remarkable near-field enhancement offers an important mechanism for SERS.

In addition, Halterman *et al.* calculated the electromagnetic force between Ag nanowires based on the SP coupling effects, it is found that the electromagnetic force is dependent on the illumination wavelength, separation distance between the nanowires, and angle of incidence of the electric field [166]. Figure 32 shows the near-field electric field patterns for differing incident wave directions and wavelengths when the nanowires are illuminated by a plane wave with a vector direction perpendicular to the major axis of the nanowires (shown in the top panels). For the illumination wavelength of 385 nm, there is a large field enhancement from the corners and within the gap between the nanowires, corresponding to the force that has a maximum at that

Figure 32

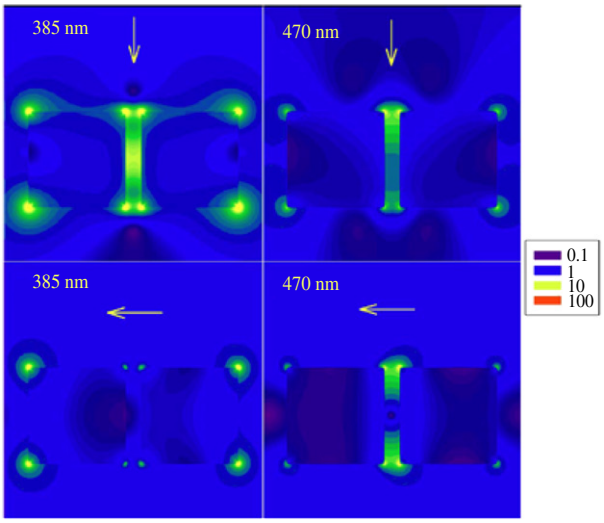


Electric field amplitude contours (normalized by the incident field) for two nanowires illuminated by a plane wave with wave vector direction indicated by the arrows. The separation distance is $d = 5$ nm. The electromagnetic response of the nanowire pair is quite different depending on the angle of incidence and wavelength. In the two upper plots, the electromagnetic response and subsequent attractive force is greatest for the shortest wavelength. Conversely, in the lower plots the response is greatest for the longer wavelength. Reproduced with permission from Fig. 4, Ref. [166]. © 2005 APS.

wavelength. As the illumination wavelength increases to 470 nm, the nanowires are no longer at resonance and the coupling interaction as well as the force between the nanowires decreases. However, when the nanowires are illuminated by a plane wave with a vector direction parallel to the major axis of the nanowires (shown in the bottom panels), different situation are observed. For the illumination wavelength of 385 nm, the electric field is small between the nanowires, although the outer corners are still illuminated; but, as the illumination wavelength increases to 470 nm, the field intensity is enhanced predominantly within the gap as the nanowires are coupled.

Besides the SP coupling between two nanowires, coupling in a linear chain system consisting of large numbers of Ag nanowires has been invesitigated by a scattering matrix method [167]. It was found that the SP coupling is strongly dependent on the nanowire number in the linear chain system. The resonance wavelength monotonically increases with the number of nanowires, and the near-field intensity is strongly dependent on the chain length. For a short chain length (e.g., the number $N = 5$), the SP coupling is strongest in the gap between two adjacent nanowires; only the longitudinal resonance mode exists at its main resonance. However, when the chain length increases to 100, the transverse resonance mode perpendicular to the chain axis becomes dominant, and the coupling field intensity is locally focused at the top and bottom halves of the nanowires perpendicular to the direction of

wave propagation. The coupling differences between the short and the long chain are attributed to the different charge distributions.

In addition, SP coupling in a multilayer structure consisting of a periodic Au nanowires array and a spatially separated thin Ag film with periodic slits has been reported [168]. The SP resonance mode of the multilayer structure depends sensitively on the relative lateral displacement of the Au nanowire array with respect to the textured Ag film, which results from the SP coupling interaction between horizontal SP mode of the nanowire array and the antisymmetric short-range SP mode of the textured Ag film. Moreover, the SP coupling results in a redshifted hybridized SP mode with a significantly narrow linewidth and a large electromagnetic field enhancement. The favorable tunability of this multilayer layer structure makes it a promising substrate both for sensors and SERS.

### *4.1d. Metal Nanoantennas*

Recently, Zhu and co-workers used scanning near-field optical microscopy (SNOM) and finite difference time domain (FDTD) methods to investigate the SP coupling between Ag bow tie nanoantenna pairs and an Ag nanowire [169]. The individual Ag nanowire was transferred to the feed gap of the bow tie antennas by using the poly(methyl methacrylate) (PMMA) nanotransfer method [170], where the lengths of the Ag nanowires with a diameter of 100 nm ranged from 5 to 20 μm, the lengths of the Ag bow tie antennas with a 53° apex angle and 100 nm height varied from 50 to 800 nm, and the distance between the nanowire ends and the tip of the nanoantennas was less than 10 nm. The coupling and emission intensity can be optimized by tuning the nanowire length, the arm length of the bow tie antennas, and the incident angle of the excitation laser. For Ag nanowires with different lengths, it is found that the matching length of the Ag nanowire is around 10 μm for the incident laser wavelength of 672 nm. In addition, based on the emission intensity versus the antenna arm length, increasing the arm length from 50 to 250 nm leads to an increased plasmon emission. However, further increasing the arm length from 250 to 800 nm dramatically decreases the plasmon emission; in this case, the optimized emission intensity can be obtained when the arm lengths are approximately 250 nm. For incident angles of the linearly polarized laser beam from 15° to 60°, the maximum emission intensity is achieved with an incident angle of 28° [169]. As a result, an enhancement factor (e.g., 13.6) of SP coupling between the nanoantenna and the nanowire is achieved. A maximum plasmon emission enhancement factor of 45 can be obtained, corresponding to the 10 μm long Ag nanowire with 250 nm for the arm length of the bow tie antennas and 28° for the incident angle of the excitation laser.

The SP coupling described above is focused on the dipole coupling between the nanostructures. Giannini and co-workers reported the coupling of multipolar SPs with photonic modes in Au nanoantenna arrays (or plasmonic crystals) [171]. This coupling makes possible the efficient excitation of lattice surface modes. The Au nanoantennas have a rectangular shape with a height of 38 nm, a long axis of 450 nm along the $x$ direction, and a short axis of 130 nm along the $y$ direction, while the lattice constants of the plasmonic crystals are

Figure 33

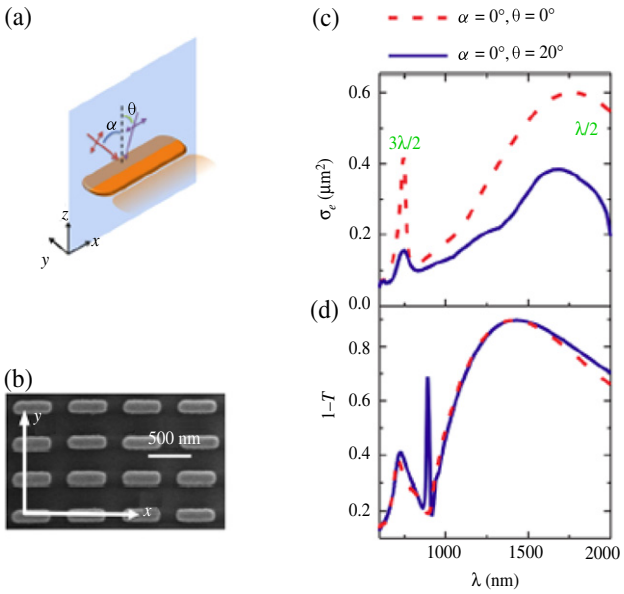


(a) Schematic representation of a single nanoantenna. (b) SEM image of an array of nanoantennas. (c) Extinction cross section of a single gold nanoantenna; and (d) extinction, defined as one minus the transmittance $T$, of an array of antennas. Light is incident at $\alpha = \theta = 0°$ (red dashed curve) and $\alpha = 0°$, $\theta = 20°$ (blue solid curve). Reproduced with permission from Fig. 1, Ref. [171]. © 2010 APS.

600 and 300 nm, corresponding to the $x$ and $y$ axis directions, respectively (Fig. 33(b)). When the incident electric field is polarized parallel to the long nanoantenna axis, the LSP resonances are identified by the maxima in the extinction cross section and are approximated by the relation $L = j\lambda_{\text{eff}}/2$, where $\lambda_{\text{eff}}$ is the effective wavelength in the nanoantenna [172], $j$ is an integer that gives the resonance order, and $L$ is the nanoantenna length along the direction of the polarization vector. Here, $j = 1$ resonance corresponds to the dipolar resonance with a low $Q$ factor (broad resonance) and a large extinction cross section due to the good coupling of the SP to light, and $j > 1$ (e.g., $j = 3/2$) resonance corresponds to multipolar resonances with a lower extinction cross section than the dipolar resonance because of their weaker coupling to light and reduced radiation damping. In contrast to the dipolar resonance, the $3/2\lambda_{\text{eff}}$ resonance does not exhibit substantial shift with respect to the resonance of individual antennas. More interestingly, a sharp resonance appears around 900 nm for an incident angle of $\theta = 20°$ (Fig. 33(d)); the sharp resonance is the lattice surface mode, which is attributed to the coupling of the $3/2\lambda_{\text{eff}}$ resonances of individual nanoantennas with a diffracted propagating wave grazing the surface of the array [171]. Moreover, for the incident angle of $\theta = 20°$, the out-of-normal incidence breaks the symmetry and allows coupling of the incident field to the lattice surface mode. In this case, the $3/2\lambda_{\text{eff}}$ resonance displays a four-lobed (multipolar) field distribution, while the surface lattice resonance mode presents a two-lobed (dipolarlike) distribution. This modification in the field distribution is the result of electrodynamic retardation between the $3/2\lambda_{\text{eff}}$ resonances and the field diffracted in the plane of the array. As

a result of this retardation, the coupling of the multipolar resonances to radiation in certain directions becomes dominant and results in a tenfold enhancement of the emission of dye molecules. The lattice surface modes with multipolar SP coupling will provide new opportunities for fluorescence spectroscopy and fluorescence labeling.

#### 4.1e. Metal Nanoslits

Lee and Park theoretically and experimentally investigated the nature of coupling between SPs and the transmitted light in metal nanoslit arrays [173]. Periodic arrays of nanoslits with a width of 100 nm and a period of 650 nm were fabricated by a dry etching process after electron beam patterning on a 120 nm thick Au film deposited on a flat sapphire substrate. They introduced a notion of "dressed surface plasmon polariton (DSP)" for description of the leaky wave, and the DSP gives rise to an elementary block in the optical transmission problem of the metal slits. For a well-separated SP away from other SPs, it is found that the bare coupling strength is the product of the geometric opening ratio, the aperture momentum, and the Fabry–Perot factor; however, the bare coupling strength exhibits notable changes due to the presence of other SPs. Furthermore, the DSP on the illumination side of the metal film can be described sufficiently with the bare coupling, whereas the DSP on the other side requires the effective coupling obtained by including the effect of SPs on the illumination side. In this case, the real part of the effective coupling strength can be either positive or negative, depending on the film thickness. Therefore, the effective coupling results in enhanced transmission with the redshifted or the blueshifted transmission peaks. Without coupling, the SP is proved to suppress the transmission due to other SPs corresponding to the equipartition diffraction orders. Some of the various features and problems of the optical transmission spectra can be sufficiently explained based on the DSP model.

### 4.2. Metal–Semiconductor Hybrid Structures

Generating strong coupling between individual quantum emitters and photons is indispensable for development of the quantum information science and technology. Metal–semiconductor hybrid nanostructures such as metal nanowires and semiconductor nanostructures [e.g., quantum dots, nanowires, and quantum wells (QWs)] exhibit enhanced optical emission due to the excitation of SPPs with enhanced confinement fields coupled to the semiconductor quantum systems.

#### 4.2a. Metal Nanowires and Semiconductor Quantum Dots

The optical emission of semiconductor nanostructures can be significantly enhanced by the proximity of a metal nanowire supporting SPPs, which is attributed to the effect that the localized fields from SPPs cause the metal nanowire to capture the majority of spontaneous radiation into the guided SP modes [174]. For an optimally placed semiconductor emitter, the spontaneous emission rate $\Gamma_{pl}$ into SPPs can far exceed

the radiative and nonradiative rates ($\Gamma_{rad}$ and $\Gamma_{nrd}$, respectively), which results in highly efficient coupling to SPPs and enhancement of the total decay rate ($\Gamma_{total}$) compared with that of an uncoupled emitter ($\Gamma_0$). The enhancement can be expressed as a Purcell factor, $P = \Gamma_{total}/\Gamma_0$, which for thin nanowires is predicted to be large [174]. The strong coupling is caused by the geometrical effect of tight field confinement of SPPs and occurs far from the SP resonance frequency of the nanowires [175].

Lukin, Park, Akimov and co-workers reported an in-depth investigation on the SPP coupling from a single CdSe quantum dot and an Ag nanowire [176]. The CdSe quantum dots were fabricated onto a glass substrate by a spinning method, then a PMMA layer with a thickness of 30 nm was coated onto the quantum dots. Subsequently, an Ag nanowire of 102 nm in diameter was deposited on top. Finally, the sample was overcoated with a thick layer of PMMA. The closest allowed distance between the quantum dot and the nanowires is determined by the thickness of the PMMA layer and the quantum dot shell radius (5 nm). When the quantum dot is placed proximally to the nanowire end, substantial emission into free space results from SPP scattering at the far end of the nanowire (Fig. 34(c)). The intensity of the scattered radiation from the nanowire end depends on the nanowire diameter (Fig. 34(d)). For a nanowire 25 nm in diameter, hardly any scattering is seen from the end despite the stronger coupling between the emitter and SPPs. However, the scattering is significant for a nanowire 100 nm in diameter. The nanowire of about 100 nm diameter exhibits both reasonable emitter-SPPs couplings and SPPs to far-field scattering; therefore the light emission at the nanowire end (with diameter of 100 nm) originates from the single quantized plasmons scattering off the nanowire end. Moreover, both enhancement and estimated coupling efficiency rapidly decrease as the minimum quantum-dot–nanowire spacing increases, and both become very small for PMMA thicknesses above 100 nm. This establishes direct coupling between individual emitters and individual, quantized plasmons. Moreover, the SPP coupling based on the quantum dot and the Ag nanowire bridges the fields of nanoscale plasmonics and quantum optics and offers a promising opportunity to achieve new levels of control over the interaction of single SPPs and to realize novel quantum plasmonic devices.

On the other hand, they theoretically described a method that enables strong, coherent coupling between individual optical emitters and guided SPP excitations in metal nanostructures at optical frequencies [174]. The individual emitter coupled to a metal nanowire is optically excited and decays with high probability into the SPP modes of the nanowire, and a single-photon source is created by evanescently coupling the nanowire to a nearby dielectric waveguide over a length $L_{ex}$. In order to maximize the transfer efficiency into the waveguide, the longitudinal wave vectors of the SPPs and waveguide should be approximately matched, and $L_{ex}$ should be optimized. Moreover, for a given nanowire radius $R$, the matching condition results in some optimization of parameters such as the waveguide size. It is observed that there is some optimal $R$ where the optimized efficiency $P$ for the single-photon generation is maximized, which corresponds to a balance between achieving large coupling between the emitter and the nanowire and ensuring that the plasmon–guide coupling exceeds the enhanced

Figure 34

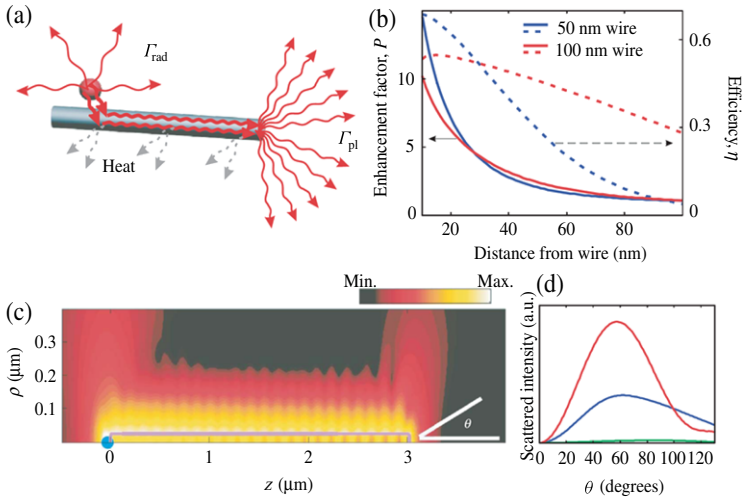


Radiative coupling of quantum dots to conducting nanowires. (a) A coupled quantum dot can either spontaneously emit into free space or into the guided SPs of the nanowire with the respective rates $\Gamma_{rad}$, $\Gamma_{pl}$. (b) Theoretical dependence of the enhancement factor $P$ (solid line) and efficiency of emission into SPs (dashed curve) on distance of the emitter from the nanowire edge. The red (blue) curve corresponds to a wire diameter of 100 nm (50 nm). (c) Simulations of the electric field amplitude (arbitrary units) emitted by a dipole (blue filled circle) positioned 25 nm from one end of a conducting nanowire (whose surface is outlined) 3 μm in length and 50 nm in diameter. The vertical scale ($\rho$) is enlarged compared with the horizontal ($z$) to clearly show the far field of the SPs. Upon hitting the far end of the nanowire, some of the SP energy is clearly scattered into the far field, while the remainder is lost either to dissipation or to backreflection. $\theta$, emission angle. (d), Amplitude of the Poynting vector of the light scattered from the far end of the nanowire, as a function of $\theta$ (see (c)), for wires of diameter 100 nm (red curve), 50 nm (blue) and 25 nm (green). Reproduced with permission from Fig. 1, Ref. [176]. © 2007 NPG.

losses at small $R$. As a result, the optimal single-photon efficiencies exceed 95% in such a system. Such an architecture for quantum communication based on plasmonic devices has several important features. Unlike typical methods of cavity quantum electrodynamics, the SPP excitation covers a broad bandwidth and requires no special tuning to achieve resonance. The operation speeds can also be quite high because of the subwavelength mode volumes associated with the SPPs.

### *4.2b. Metal Nanowires and Semiconductor Nanowires*

SPPs can be concentrated and guided by current-carrying wires, suggesting an integrated approach to optical and electrical signal processing. Lukin, Park, Falk, and co-workers presented a new all-electrical SPP detection technique based on the near-field coupling between guided SPPs and a semiconductor nanowire [177]. The near-field SPP detection scheme consists of an Ag nanowire crossing a Ge nanowire field-effect transistor. The Ag nanowire guides SPPs to the Ag–Ge junction [178],

where they are converted to electron–hole pairs [179] and detected as current through the Ge nanowire, and the Ag nanowire with highly crystalline and defect-free enables SPPs to propagate over distances of several micrometers without scattering into free-space photons. Moreover, their narrow diameter (80–150 nm) supports tightly confined SPP modes, which couple weakly to the far field but strongly to nearby Ge nanowire detectors and optical emitters. In this case, these characteristics demonstrate an efficient and all-electrical detection of quantum-dot emission. The electrical SPP detection is designed by scanning a focused laser beam across an Ag–Ge crossbar device and recording the current ($I_{plas}$) through the Ge nanowire as a function of the diffraction-limited laser spot position (Fig. 35(a)). The current is detected when the laser is focused near the Ag–Ge junction due to the direct photoresponse of the Ge nanowire. Furthermore, the current $I_{plas}$ is largest when the excitation polarization is parallel to the Ag nanowire axis (Fig. 35(c)) and smallest when perpendicular to the axis (Fig. 35(b)).

In addition, the plasmon-to-charge conversion efficiency (typically ranged from 0.01 to 0.1), defined as the ratio of detected charges to the number of SPs reaching the Ag–Ge junction, can be tuned by applying a gate voltage ($V_{gate}$) to an extra electrical contact defined at one end of the Ag nanowire [177]. $I_{plas}$ is enhanced with increased $V_{gate}$ (Fig. 35(e)). These results can be understood by considering electrical plasmon detection as a multistep process. First, the ac electric field of the SPPs generates electron–hole pairs in the Ge nanowire through near-field coupling. Second, the dc electric field within the Ge nanowire separates

Figure 35

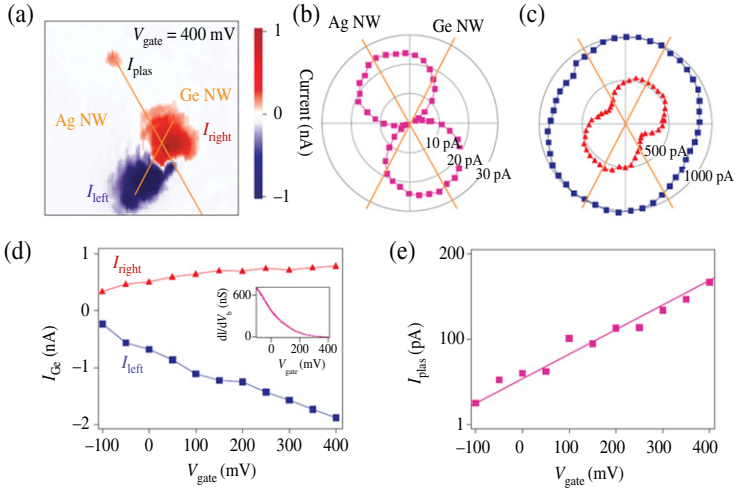


Polarization and gate effects on plasmon detection. (a) $I$ as a function of laser spot position. $V_{gate} = 400$ mV, $V_b = 0$, $P = 3.4$ μW, $\lambda_{ex} = 600$ nm. (b), (c) $I_{plas}$ (b) and $I_{right}$ (red triangles) and $I_{left}$ (blue squares) (c) as a function of excitation light polarization. (d) $I_{right}$ (red triangles) and $I_{left}$ (blue squares) as a function of $V_{gate}$. Inset, gate response of the Ge nanowire conductance in nanosiemens. (e) $I_{plas}$ as a function of $V_{gate}$. Reproduced with permission from Fig. 2, Ref. [177]. © 2009 NPG.

these electron–hole pairs into free charges before recombination takes place; the separated electron–hole pairs are then detected as current. When an SPP pulse is launched in the fundamental mode of the Ag nanowire, as it propagates, the electric field intensity and Poynting vector are monitored as functions of position and time. Once the SPP flux reaches the Ge–Ag junction, it can be reflected, transmitted, absorbed by the Ge nanowire, or scattered to the far field. The simulation results show that a 40 nm diameter Ge nanowire absorbs 20% (50%) of the SPP flux when the Ag nanowire diameter is 100 nm (50 nm) [177]. This large absorption fraction originates from the high absorption constant of Ge and the strong SPP confinement, which increases for smaller Ag nanowire diameters. The strong near-field coupling between single-plasmon emitters and plasmonic nanocircuits can lead to completely new capabilities that are not available with conventional photonics, such as nonlinear switches, single-photon transistors, and quantum nondemolition detectors [180,181]. Considering the inherent metal loss, it is very important to develop nanoscale plasmonic waveguides with both low losses and nanoscale SPP confinement. Ag nanowires are able to support SPP propagation with two-dimensional nanoscale plasmon mode confinement. The major challenge in optically exciting SPPs in Ag nanowires lies in the dispersion relation mismatch for SPs and photons. Although, a quantum emitter in the near field of an Ag nanowire can excite propagating SPPs, as the optical dipolar near field contains large momentum components matching those of SPPs [176,182], the coupling will not lead to easy interconnection with conventional optical components.

Yang and co-workers reported a simple approach to couple SPPs into the Ag nanowires with a $SnO_2$ nanoribbon waveguide [183]. The single-crystalline $SnO_2$ nanoribbon with high aspect ratio, strength, and flexibility can be assembled into optical components, and the $SnO_2$ nanoribbons can also act as a simultaneous nanoscale light source and waveguide. Based on the ingenious design, SPPs can be excited by simply bringing the Ag nanowire into contact with a $SnO_2$ nanoribbon with minimum restriction on the coupling conditions, and SPPs can be launched into the Ag nanowire at arbitrary positions at any orientation. In this case, the assembly of the Ag–$SnO_2$ junction is completely reversible, making it possible to monitor the properties of a single Ag nanowire while varying the interconnection and propagation condition, and the far-field study of the SPP propagation in Ag nanowires is possible. Furthermore, the relative coupling efficiency ($\eta_c$), which is defined as the ratio between the total light input into the Ag nanowire ($I_{in}$, Ag) and the total light output from the $SnO_2$ ($I_{out}$, $SnO_2$) at the Ag–$SnO_2$ junction, can be estimated from the intensity of the Ag nanowire end emission and the radiative coupling loss resulting from the scattering at the wire–ribbon junction. It is found that the coupling efficiency depends strongly on the coupling angle: a smaller coupling angle enhances the coupling of the photons in the dielectric waveguide into SPPs in the Ag nanowire with a smaller scattering loss and results in a higher coupling efficiency. This is because the momentum of photonic modes in the dielectric waveguide along the SPP propagation direction are large and better matched to the plasmonic modes at smaller coupling angles. As a result, higher coupling efficiency can be achieved. In contrast, it will be more difficult for the photons to obtain

Figure 36

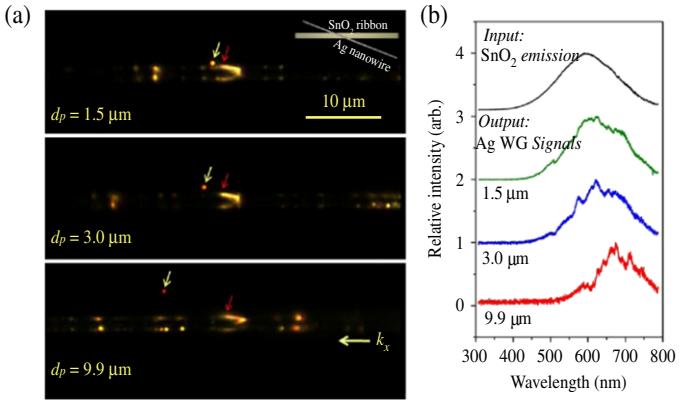


Dependence of Ag nanowire waveguide spectra on the propagation distance ($d_p$). (a) True-color optical microscope images showing Ag nanowire/$SnO_2$ nanoribbon junctions of different propagating distance fabricated by micromanipulation. The coupling angle of the Ag–$SnO_2$ junction was kept constant, so that the coupling efficiency would be the same for all three images. The yellow arrow in each image points to the distal end emission point of the Ag nanowires, whereas the red arrow points to the starting point of SPP propagation. The distance in between the yellow and the red arrows in each image is the actual distance of propagation $d_p$. The color of the end emission from the Ag nanowire contained more red components with increasing $d_p$. The schematic representation of the setup is shown in the inset. (b) Emission spectra of the Ag nanowire corresponding to the images in (a), and the PL spectrum of the $SnO_2$ ribbon (input signal) used in the experiment. Reproduced with permission from Fig. 2, Ref. [183]. © 2009 PNAS.

the large extra $\Delta k_x$ needed to couple into SPPs as the coupling angle increases. Moreover, the SPP propagation loss is clearly dependent on the frequency. As the SPP propagation distance ($d_p$) between the Ag wire tips and the coupling point on the $SnO_2$ ribbon increases, the high-frequency components damp faster than the low-frequency ones, so the frequency distribution of the SPPs is expected to redshift with increasing $d_p$. Moreover, the emission color changes from yellow to orange and then to red at the Ag nanowire tip when the propagation distance $d_p$ increases from 1.5 to 3.0 and to 9.9 μm (Fig. 36), which indicates a much smaller propagation loss with larger $d_p$ as the frequency decreases [183]. Similarly, the propagation length calculated from the slope of the plots shows strong frequency dependence, increasing from 6.2 μm (for 532 nm) to 11.3 μm (for 650 nm) and finally to 20.2 μm (for 980 nm) IR excitation. The direct photonic–plasmonic coupling is essential for incorporating low-loss Ag nanowire waveguides as practical components into high-capacity photonic circuits.

Based on the coupling plasmonic and photonic waveguides, simultaneous realization of subwavelength confinement and low propagation loss is possible. Tong and co-workers reported direct coupling of plasmonic and photonic nanowires using ultracompact near-field interaction [184]. First, light used for excitation is coupled into a standard fiber and then squeezed into the nanofiber through a fiber taper,

Figure 37

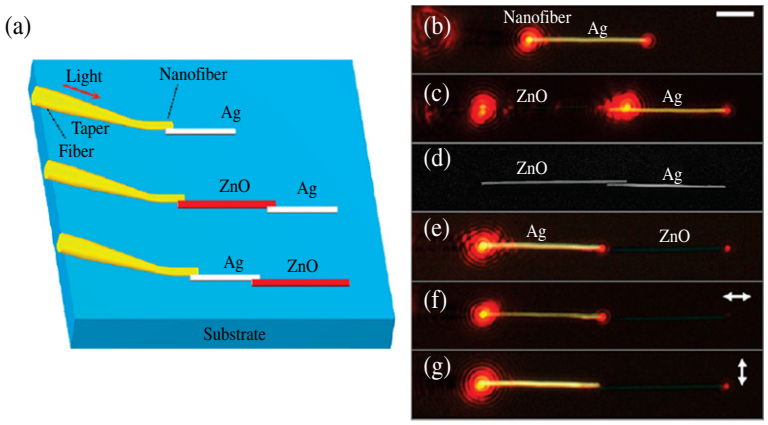


Direct coupling of plasmonic and photonic nanowires. (a) Schematic illustration of light coupling between silica nanofibers (located at distal end of the fiber taper), ZnO nanowires, and Ag nanowires. Light from the nanofiber can excite plasmons in the Ag nanowire directly (top) or via an intervening ZnO nanowire (middle). Plasmons in the Ag nanowire can convert back to light in the ZnO nanowire (bottom). (b), (c), (e) Experimental observations corresponding to the three different coupling schemes illustrated in (a). (d) SEM image of the coupler shown in (c). The diameter of the ZnO nanowire is 340 nm, and the diameter of the Ag nanowire is 320 nm. (f), (g) Microscope images taken with the polarization along and perpendicular to the nanowires shown in (e), respectively. Scale bar in (b) applies to (c)–(g). Reproduced with permission from Fig. 1, Ref. [184]. © 2009 ACS.

yielding quasi-circular-polarization guided modes ($HE_{11}$ modes) with high fractional evanescent fields [185]. Subsequently, the waveguiding nanofiber is brought into contact with ZnO or Ag nanowires by micromanipulation (Fig. 37(a)). All the nanowires are supported on a nondissipative substrate for low-loss operation. The coupling approach is that light from the nanofiber can excite SPs in the Ag nanowire directly (top) or travel through an intervening ZnO nanowire before launching SPs in the Ag nanowire (middle). Conversely, SPs in the Ag nanowire can convert back into light guided by the ZnO nanowire (bottom). Figures 37(b)–37(f) show the observations of the different coupling schemes. When the two types of nanowires are placed close enough (the overlap between the nanowires is about 1–2 μm), the optical near field in a photonic nanowire and the plasmonic near field in a plasmonic nanowire may strongly overlap, which results in highly efficient photon–plasmon conversion in the coupling area. Furthermore, a hybrid coupler with a coupling length as small as 220 nm can be readily assembled by using the ZnO nanowire and the Ag nanowire. The fractional outputs from the Ag nanowire are 4%, 8%, and 64% for 488, 532, and 650 nm light, respectively. It is found that the fractional output of propagating SPPs increases with increased wavelength. As a result, the calibrated coupling efficiency from the ZnO nanowire into the Ag nanowire at 650 nm wavelength is about 82% [184]. Compared with many other coupling schemes for plasmonic nanowire excitation [186], the nanowire-to-nanowire coupling approach offers a much higher

efficiency owing to the tightly confined surface modes (evanescent fields) in the ZnO nanowire as well as light scattering by the Ag nanowire based on the overlap between the incident optical radiation and the propagating SP mode. This work provides promising approaches for the design of nanophotonic and quantum optics devices.

### 4.2c. Metal Grating and Semiconductor Quantum Wells

Another instance of hybrid metal–semiconductor nanostructures is semiconductor QWs placed in the vicinity of a metal nanoslit array. Vasa *et al.* investigated the coherent coupling interaction in the hybrid nanostructure involving a Au nanoslit grating deposited on a GaAs/AlGaAs QW heterostructure [187]. The structure consists of a 10 nm wide GaAs QW layer embedded in an $Al_{0.3}Ga_{0.7}$ barrier grown on a GaAs substrate by molecular beam epitaxy method (Fig. 38(a)). First, on the top side, the barrier with a height of only 20 nm was capped by a 3 nm GaAs buffer to ensure that the QW was close to the surface while maintaining sufficient optical quality. Then an 80 nm thick Au film was deposited on the top surface of the semiconductor buffer.

Figure 38

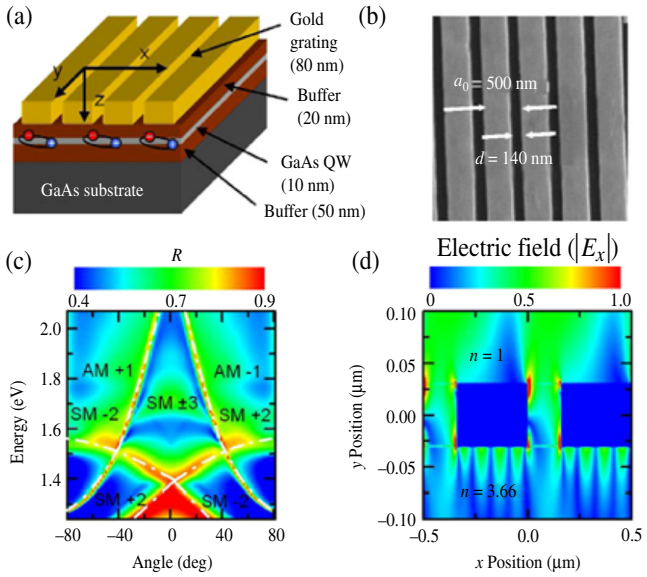


(a) Schematic of the metal–semiconductor hybrid structure consisting of a gold nanoslit grating deposited on a GaAs QW. (b) SEM image of the gold grating with $a_0 = 500$ nm, $d = 140$ nm, and $h = 80$ nm. (c) Calculated angle-resolved far-field reflectivity spectra of this structure. Dispersion relations for different air–metal (AM) and semiconductor–metal (SM) SPP resonances are indicated as dashed-dotted curves. (d) Calculated spatial distribution of the normal electric field $E_x$ for $E_{ex} = 1.517$ eV and $\theta = 38°$, near the crossings of the SM +2, SM −3, and AM −1 SPP resonances, and the PL spectrum of the $SnO_2$ ribbon (input signal) used in the experiment. Reproduced with permission from Fig. 1, Ref. [187]. © 2008 APS.

Finally, an array of 140 nm wide slits with a grating period of 500 nm was created by electron beam lithography. They observed the normal mode splitting between QW excitons and SPPs in the nanoslit array. As a result of the coupling, low-temperature angle-resolved far-field reflectivity spectra reveal a significant shift in the exciton resonance position together with an increase in the radiative exciton damping (Fig. 38(c)). The experiments are corroborated by a phenomenological coupled-oscillator model predicting coupling strengths as large as 50 meV in structures with optimized detunings between the coupled exciton and SPP resonances. The strong coupling can be used to enhance the luminescence yield of semiconductor quantum structures or to amplify SPP waves.

### 4.3. Metal–Dielectric Hybrid Structures

Compared with light propagation in dielectric waveguides, SPP propagation length in metal becomes quite short because of strong absorption by metals at optical frequencies. Therefore a rapid and efficient conversion of SPs into photons is important. Agio and co-workers presented a simple and broadband butt-coupling technique for connecting a metal nanowire and a dielectric nanofiber [188]. The confined SPs of the metal nanowire can be converted into guided photons in the $TM_{01}$ mode of the dielectric nanofiber with a very high efficiency and large bandwidth by use of a simple butt-coupling scheme. As a result, conversion efficiencies above 95% in the visible and close to 100% in the NIR spectral range can be obtained by an appropriate choice of radius and material, such as metal–dielectric hybrid structures consisting of a Ag nanowire 164 nm in radius and a silica nanofiber 342 nm in radius.

The plasmon response of metal–dielectric hybrid nanostructures can be explained by a plasmon hybridization supported by metal nanostructures. Halas and co-workers proposed a hybridization model for the plasmon response of concentric metal–dielectric nanoshells [189]. The hollow metal nanoshell supports plasmon resonances with frequencies that are a sensitive function of the inner and outer radius of the metal shell [190]. For the specific case of nanoshells, the highly geometry-dependent plasmon response can be seen as an interaction between the essentially fixed-frequency plasmon response of a nanosphere and that of a nanocavity (Fig. 39). The sphere and cavity plasmons are electromagnetic excitations that induce surface charges at the inner and outer interfaces of the metal shell, and the strength of the interaction between the sphere and cavity plasmons is controlled by the thickness of the metal shell layer. Moreover, the interaction results in the splitting of the plasmon resonances into two new resonance modes: the lower-energy symmetric or "bonding" plasmon mode $|\omega_-\rangle$ and the higher-energy antisymmetric or "antibonding" plasmon mode $|\omega_+\rangle$ (Fig. 39) [189]. Considering a four-layer nanoparticle consisting of a dielectric core, metal shell, dielectric spacer layer, and a second metal shell, their interaction results in four hybridized plasmon resonances. The thickness of the dielectric spacer layer controls the strength of the coupling between the inner and the outer nanoshell. The resulting plasmon energy shifts depend on the coupling strength and the energy

Figure 39

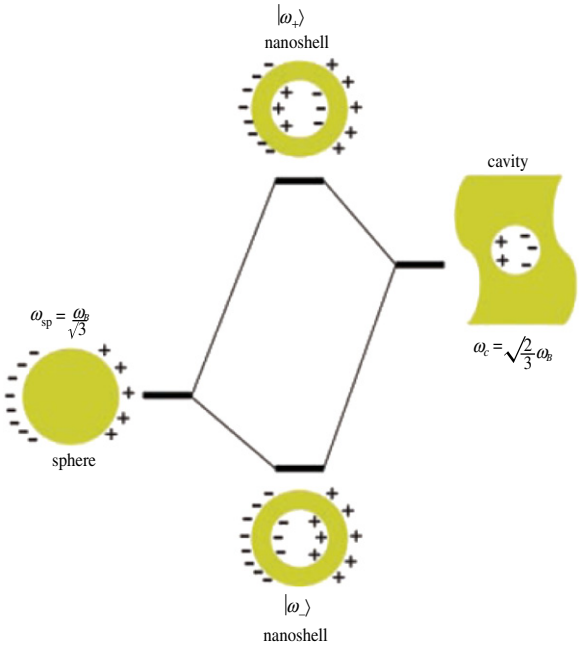


An energy-level diagram describing the plasmon hybridization in metal nanoshells resulting from the interaction between the sphere and cavity plasmons. The two nanoshell plasmons are an antisymmetrically coupled (antibonding) $\omega_+$ plasmon mode and a symmetrically coupled (bonding) $\omega_-$ plasmon mode. Reproduced with permission from Fig. 1, Ref. [189]. © 2003 AAAS.

between the plasmons on the inner and outer shell. In this case, the plasmon energies of the concentric nanoshell structure can be tuned both by changing the dielectric spacer layer and by tuning the plasmon energies of the individual nanoshells. For a small spacing (e.g., 28 nm) of the dielectric layer between inner and outer metal shell layers, the plasmon hybridization coupling is quite strong; when the spacing between inner and outer metal shell layers slightly increases (e.g., 39 nm), the plasmon hybridization coupling is weak. However, the concentric nanoshell shows a fully decoupled plasmon response when the spacing increases to 236 nm.

## 4.4. Metal–Polymer Hybrid Structures

For practical applications of optical data transmission, plasmonic waveguides are expected to be integrated with traditional optical waveguides that connect easily to light sources, guide light for long distances with low loss, and propagate light to many nanowires simultaneously. Although the nanowire plasmonic waveguides described above satisfy the requirements of two-dimensional plasmon mode confinement and low loss, there remains the practical issue of how to couple light into many nanowires. Previous methods for plasmon excitation include prism coupling and focusing of light onto one end of the nanowire with a

microscope objective [178,186]; these methods are not planar and cannot be used on chips.

Pyayt, Xia and co-workers proposed to integrate multiple Ag nanowire plasmonic waveguides with polymer optical waveguides for the nanoscale confinement and guiding of light on a chip [12]. Compared with the traditional method which couples light to a nanowire by focusing a laser beam on the end of a nanowire [186], the light source is rotated by 90° relative to the substrate (from perpendicular to in plane); the light source is still perpendicular to the nanowire and shines onto one of its ends, but instead of focusing a laser beam to a small spot, the confinement of light can be used to guide the light to the end of the nanowire (Fig. 40(a)). When light propagates in the waveguide, it is guided across a narrow area at high intensity over a long distance. Unlike previous methods that allow excitation of only one nanowire at a time, the waveguide makes coupling of light to 20 nanowires along its length

Figure 40

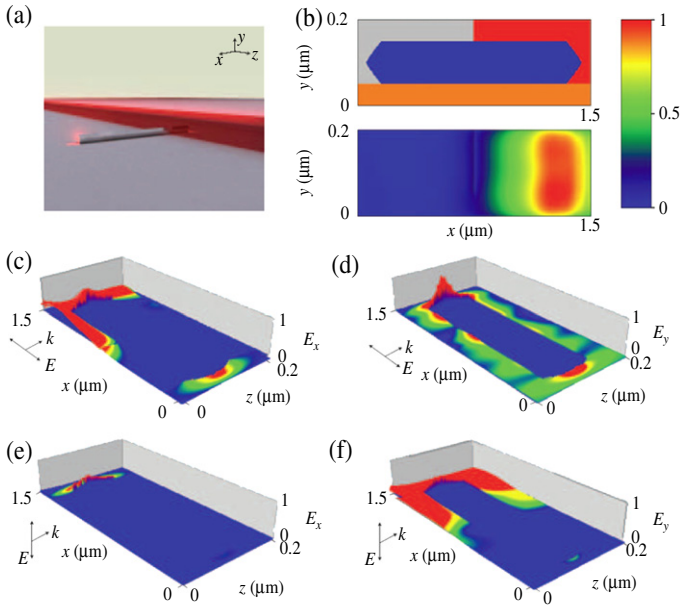


(a) Coupling light to a nanowire by guiding light in the plane of the substrate with a polymer waveguide. (b) Front view of the device (*xy* plane), showing the silver nanowire (blue) with one end in a polymer waveguide (red). The orange and grey regions indicate sol-gel and air, respectively. Below is the corresponding excitation field distribution of light propagating in the waveguide (without nanowire). The color gradient indicates the amplitude of the excitation field. Right, the PL spectrum of the $SnO_2$ ribbon (input signal) used in the experiment. (c) Incident light in the waveguide polarized in the *x* direction excites plasmon propagation along the nanowire (*xz* plane). (d) $E_y$ field component of plasmon propagation along the nanowire. (e) The coupling to the nanowire decreased if the incident light was polarized in the *y* direction. (f) Incident light in the waveguide with $E_y$ polarization excites little plasmon propagation in the nanowire. Reproduced with permission from Figs. 1b and 2, Ref. [12]. © 2008 NPG.

possible before the intensity of the light in the waveguide decreases to half of its initial value. Moreover, the exact number of Ag nanowires in this orientation depends on the concentration of the nanowires in the solution. On the other hand, for incident light polarized perpendicular to the nanowire axis, there is significantly less light propagating along the nanowire; the coupling efficiency is 30 times less for incident light polarized along the nanowire axis (Figs. 40(e) and 40(f)), which indicates that the amount of light coupled into the nanowires is highly dependent on the polarization of the incident light. Therefore one can switch or fine-tune the light emitted from the end of the nanowire simply by adjusting the polarization directions. A major advantage of this design is that the same polymer waveguide can be used to couple light into many nanowires in parallel, simultaneously providing light to a number of nanoscale photonic devices in highly integrated photonic circuits.

## 5. Propagating and Guiding of Surface Plasmon Polaritons through Nanostructures

Surface plasmons (SPs) have two classes of configurations: localized surface plasmon (LSPs) and surface plasmon polariton (SPPs) [11]. LSPs are nonpropagating excitations of the electrons in metal nanostructures that are much smaller than the incident wavelength, which have been described mainly in Sections 2 and 3. The resonance frequency and modes of LSPs are dependent on the shape, size, and dielectric function of metals, as well as the dielectric environment. In contrast, SPPs are electromagnetic waves propagating along the interfaces between metals and dielectric materials. They can be excited on a metal surface by coupling interaction over a large range of frequencies [191].

Once light has been converted into an SPP mode on a metal surface, it will propagate but will gradually attenuate owing to ohmic losses resulted from absorption in the metal and radiative (or scattering) losses. The propagation length of SPPs is thereby limited by the imaginary part of the complex wavenumber $k_{\mathrm{SPP}}$ because of internal damping (ohmic losses), where $k_{\mathrm{SPP}} = k_{\mathrm{SPP}r} + ik_{\mathrm{SPP}i}$, based on the SPP dispersion relation (Eq. (2)). The propagation length of SPPs, $\delta_{\mathrm{SPP}}$, is given by [2,192]

$$\delta_{\mathrm{SPP}} = \frac{1}{2k_{\mathrm{SPP}i}} = \frac{\lambda}{2\pi}\left(\frac{\varepsilon_{mr}+\varepsilon_d}{\varepsilon_{mr}\varepsilon_d}\right)^{3/2}\frac{\varepsilon_{mr}^2}{\varepsilon_{mi}} \tag{7}$$

where $\varepsilon_{mr}$ and $\varepsilon_{mi}$ are the real and the imaginary parts of the dielectric function of the metal, respectively; that is, $\varepsilon_m = \varepsilon_{mr} + i\varepsilon_{mi}$. where $\delta_{\mathrm{SPP}}$ is the distance after which the SPP intensity decreases to $1/e$ of its starting value. The propagation length is usually dependent on the dielectric function of the metal and the incident wavelength based on Eq. (7). For example, for a relatively absorbing metal such as Al the propagation length is 2 μm at a wavelength of 500 nm, while for a low-loss metal Ag, at the same wavelength it is as long as 20 μm. In addition, for a longer incident wavelength, such as the near-IR (NIR) telecommunication wavelength 1.55 μm, the propagation length of Ag increases toward 1 mm [2].

## 5.1. Propagating and Guiding of Surface Plasmon Polaritons through Metal Nanostructures

Various metal nanostructures, such as nanoparticle chains, nanorods, nanowires, nanogaps, gratings, nanoslits, stripes, and thin films, can support propagating and guiding modes of SPPs, which originates from the strong coupling of SPP modes along the surfaces of the nanostructures. Propagating and guiding of SPPs offer new opportunities for developing nanophotonic devices and efficient delivery of light energy at the nanometer scale.

### *5.1a. Metal Nanoparticle Chains*

For an ensemble of nanoparticles, the individual SP properties are additionally influenced by electromagnetic interaction between the nanoparticles. In principle, two types of SPP interaction can be distinguished: far-field interaction and near-field coupling. Far-field interaction is tuned by the scattered light fields of the nanostructures, which are of dipolar character for the nanostructures with sizes much smaller than the light wavelength. Far-field polarization spectroscopy experiments for ordered two-dimensional arrays of Au and Ag nanoparticles with submicrometer interparticle spacing have confirmed that electromagnetic interactions between the nanoparticles are present [193], which demonstrates energy shifts of the SP resonances that are dependent on interparticle distances. On the other hand, near-field coupling is relevant for nearly touching nanoparticles because of the short range of the electromagnetic near fields, of the order of some tens of nanometers [194]. The transport of electromagnetic energy in SPP waveguides consisting of closely spaced metal nanoparticles is dependent on the near-field coupling between the adjacent particles.

Many efforts have been made to construct metal nanoparticle SPP waveguides by a variety of methods such as electron beam lithography [195] and self-assembly [196]. However, all investigations on the optical properties of these waveguides are confined mainly to collective excitations [197,198]. Direct experimental evidence for SPP propagation along metal nanoparticles for SPP waveguides is quite limited. Maier, Atwater and co-workers presented local detection of electromagnetic energy transport below the diffraction limit of light in metal nanoparticle SPP waveguides [199]; the individual nanoparticles with the long axes perpendicular to the waveguide chain axis allow for increased near-field coupling between the particles [200]. For a grid of single Ag nanoparticles with a large interparticle spacing of 1 μm, the interparticle coupling is negligible. The far-field extinction spectrum of the single particles shows a resonance peak at 2.18 eV (corresponding to a resonance wavelength of 570 nm; see Fig. 41), and the exciting light is polarized along the long particle axis, perpendicular to the particle chain axis. Compared with single isolated nanoparticles, the resonance peak of the Ag nanoparticle plasmon waveguides is shifted to higher energies, with a shift of about 100 meV due to near-field coupling between the nanoparticles. Furthermore, energy transport away from the directly excited nanoparticles was probed by the placement of carboxyl-coated polystyrene nanospheres (diameter 110 nm) filled with fluorescent

Figure 41

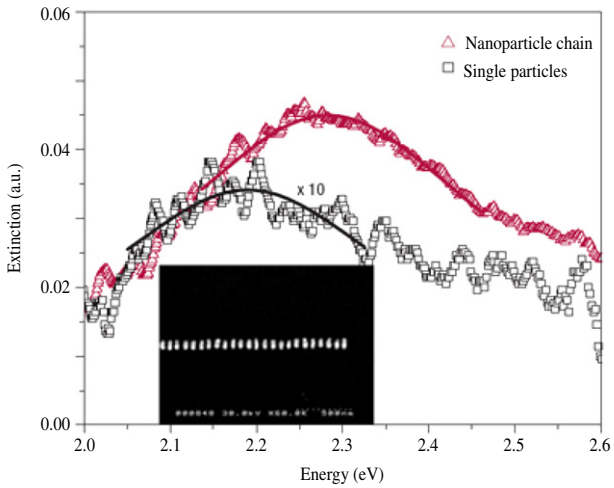


Far-field extinction spectrum of Ag nanoparticle chains and single particles. The far-field extinction spectrum of a plasmon waveguide consisting of Ag nanorods with a 3:1 aspect ratio and a surface-to-surface spacing of 50 nm between adjacent particles shows a plasmon resonance peak shift to higher energies (red triangles and Lorentz fit) compared with the extinction spectrum of isolated, noninteracting particles (black squares and Lorentz fit). The exciting light was polarized along the long axis of the nanorods, perpendicular to the particle chain axis. Inset, scanning electron microscopy (SEM) of the plasmon waveguide layout under study. Reproduced with permission from Fig. 1, Ref. [199]. © 2003 NPG.

molecules in close proximity to the waveguide structure [201]. The fluorescent dyes showed a strong absorption with a peak at 580–590 nm near the resonance wavelength of a single Ag particle, and the 610 nm dye emission is detected in the far field. This scheme permits the observation of energy transport in the following way: first, energy is transferred from the illuminating tip to the SPP waveguide; the excitation subsequently propagates along the nanoparticle structure and excites the fluorescent nanosphere placed on top of the waveguide at a sufficient distance of about 0.5 μm from the excitation source. The SPP energy transport results in the dye emission even when the microscope tip is located away from the dye; consequently, the energy attenuation decay length is about 6 dB per 195 nm [199]. Moreover, larger SPP energy attenuation can be prevented by the interparticle coupling and the use of low-loss substrates, and thus applications for guiding and focusing elements operating below the diffraction limit may be possible.

Besides the few experiment reports on SPP propagation of the nanoparticle chains mentioned above, theoretical investigation of nanoparticle chains for SPP propagation has made remarkable progress by using various calculation methods, such as generalized Mie theory [194], the Green's function [202], closed-form dynamic analysis [203,204], the finite element method [205], the coupled-dipole method [206], and the generalized multipole technique [207].

Quinten *et al.* proposed a subwavelength optical waveguide composed of a linear chain of spherical Ag nanoparticles [194]. Light transport of the long linear chain with constant spacing of spheres was calculated by the generalized Mie theory. When the first particle in the chain is irradiated by light field polarized parallel and perpendicular to the chain axis, efficient guiding light can be observed for the irradiation polarized parallel to the chain axis, and the intensity distribution along the line constantly decreases. Nevertheless, the guiding light is strongly damped for the irradiation perpendicular to the chain axis. This is because other spheres get their SP oscillation energy by coupling for the irradiation at parallel polarization; however, the other spheres cannot guide light without coupling of SPs for the irradiation at perpendicular polarization. Considering Ag nanoparticles of 50 nm diameter, the minimum transmission loss is observed for a center–center distance/radius ratio of approximately 3. In this case a corresponding signal-damping length of 900 nm can be achieved for an interparticle spacing of 25 nm [194]. The obtained attenuation values are promising for the realization of short-distance signal transport by means of the interparticle coupling in the linear nanoparticle chains.

Furthermore, SPP guiding by chains of electromagnetic interacting Au nanoparticles placed near a metal surface are considerably dependent on the scattering cross section of individual particles. It is found that the guiding efficiency increases with decreased interparticle distance in chains owing to enhancement of the coupling interaction [202]. However, propagating SPPs along curved chains is not efficient in the case of chains consisting of relatively small particles because of the weak interaction between the nanoparticles. However, for chains of large particles, the efficiency of SPP bending can be significantly improved. Compared with one linear array, two parallel linear chains of nanoparticle waveguides may achieve relatively long propagation lengths (of several wavelengths) and ultraconfined beam traveling [203].

Although SPPs can propagate without loss of energy under ideal conditions, in fact two physical effects result in the decay of SPP waves as they propagate along the nanoparticle chain: the first effect is ohmic losses due to the finite conductivity of the metal; the second effect is radiative losses due to scattering from the disordered nanoparticle chain.

Markel and Sarychev reported a numerical investigation of SPP propagation in ordered and disordered linear chains of metal nanospheres [208]. Two types of SPP have been found. One is ordinary or quasi-static SPPs, which are mediated by short-range and near-field electromagnetic interaction in the chain; the SPP propagation is strongly affected by ohmic losses in the metal and by disorder in the chain due to absorptive and radiative losses. The other is the extraordinary or non-quasi-static SPPs, which are mediated by longer-range and far-field interaction of the nanospheres. The extraordinary SPPs may experience some ohmic and radiative loss but are much less affected by absorptive dissipation and disorder in the chain than the ordinary one. Therefore the non-quasi-static SPPs become dominant sufficiently far from the exciting tip and can propagate to much larger distances along the chain with little losses of energy. The unique physical properties of the non-quasi-static SPPs can be utilized in all-optical integrated photonic systems. The propagation length in nanoparticle chain waveguides based on the

dipole coupling is usually much shorter because of the large ohmic losses and the radiation damping [194].

Recent research shows that nanoparticles may support higher-order resonance modes. Guided propagation and leaky modes can be obtained in linear chains of nanoparticles with quadrupolar mode coupling [204]. Despite the vanishing bandwidth of the individual quadrupolar resonance in each of the nanoparticles, the overall bandwidth of quadrupolar chain guidance is relatively large owing to the strong coupling between the nanoparticles, even considering realistic losses and frequency dispersion of optical materials. In addition, SPP propagation in a nanoshell particle chain can be enhanced based on low- and high-order mode coupling [205]. The guiding properties of the nanoshell particle chain can be easily tuned for different wavelengths ranging from UV to NIR by the choice of nanoshell particles, and the resonances of the chains are less sensitive to the chain length for operation in the high-order multipolar modes. Moreover, the chain waveguides with multipolar mode coupling provide propagation lengths as great as 1.88 μm, which is beyond what is maximally achieved by conventional solid particle chains. The great SPP propagation length in the chain waveguides is attributed to the large field enhancement between the nanoshells, as well as to far-field effects, which play an important role in low-loss light guiding along nanoshell chains.

Compared with light for SPP excitation, fast electrons possess larger momentum than photons, thus making higher-order SPP excitation possible. For example, quadrupolar plasmons in Ag nanoparticles can be excited by using an electron beam [209]. More important, the excitation of propagating SPPs by electron beams can lower radiation losses because of their light-shielding character. In this case, the nanoparticle chain with the coupled quadrupolar mode excited by an electron beam can achieve greater propagation length along the chain and better spatial confinement. For the multinanowire waveguide, the propagating plasmon mode excited by an electron beam with zero-momentum in the transverse cross section exhibits a greater propagation length because of the inhibition of radiation into the far field [210], and these properties might make fast electrons more useful in communication technology.

### *5.1b. Metal Nanorods*

Metal nanoparticle chains can propagate SPPs along the chain because of the SP coupling between particles. If the nanoparticle chains are extended into nanorod arrays, the local electric field between the nanorods can also be remarkably enhanced because of their strong coupling [211], and in that case metal nanorod arrays also support a guided SPP mode. Recently, Zayats and co-workers proposed that a plasmonic nanorod metamaterial could support the guided mode of SPPs with the field distribution inside the layer determined by plasmon-mediated interaction between the nanorods [19]. The metamaterial consists of a parallel Au nanorod array oriented normally to a glass substrate. This guided SPP mode has resonant excitation conditions similar to the SPP mode of a smooth metal film when the nanorod spacing is smaller than the wavelength. Numerical analysis indicates that the guided SPP mode in the anisotropic planar waveguide

formed by the layer of nanorods is determined by the coupling between the SPP modes of the individual nanorods, and the field of this guided SPP mode is not only largely concentrated within the metamaterial but also substantially extended in the superstrate. The metamaterial can provide high-sensitivity detection in biosensing based on the guided SPP mode in the nanorod arrays. Furthermore, the group velocity in the nanorod array exhibits a nonmonotonic variation as a function of interrod coupling strength. It is suggested that the guiding properties are not obtained for maximum interrod coupling strength but rather for an optimal distribution of the electromagnetic field of the longitudinal mode: in that case, the propagation length of electromagnetic energy in the nanorod array decreases from the value of about 2.7 μm estimated for coupling strengths varying between 1.2 eV and 1.4 eV to a value of 1.66 μm for the maximum coupling strength of 1.7 eV [212]. This increased damping to losses in the longitudinal mode is attributed to an increased overlap between the longitudinal resonance and the interband band edge of Au.

Zhu and co-workers proposed that a type of subwavelength gap waveguide could be used to transport energy in a broad frequency band based on a finite difference time domain (FDTD) calculation [213]. The gap waveguide is composed of two coupled nanorod chains. When the pairs of coupled nanorods are closely arranged in the direction perpendicular to the nanorod axis, the gaps between the nanorods form a linear gap chain (Figs. 42(a)). As a result, the electromagnetic energy can be transported through the gap waveguide along the $x$ direction. Because the cross section of the energy flow confined between nanorod ends of each pair is relatively small, the interval must be sufficiently small that the neighboring nanorod pairs in the $x$ direction can couple to each other and the energy can be transported along the gap. Moreover, the energy flow and the coupling strength decrease with increasing size of the intervals; if the interval is large enough (e.g., 800 nm), little energy can be propagated in the gap because of the weak coupling between adjacent nanorod pairs. To investigate how the energy is transported in this waveguide, Zhu and co-workers utilized two identical dipole sources placed at a distance of 200 nm from the left side of the waveguide to excite the resonance modes. The simulated model structure contains 50 nanorod pairs along the $x$ direction with a 100 nm gap between the two chains. Figure 42(b) shows the intensity distribution of the electric field at the frequency of 130.0 THz, which is lower than the cutoff frequency. It is found that the main part of the input power of the dipole source is coupled into the gap waveguide; only a small part of energy flows along the other ends of the nanorod arrays, and the energy is confined to the gaps in the $z$ direction. In addition, besides the confinement of the energy in the $z$ direction, the energy can also be highly confined in the $y$ direction. In this case the energy is confined in two dimensions of the gap waveguide, and the energy flow cross section of the transverse mode can be restricted to the $y$–$z$ cross section of $70 \times 145$ nm$^2$ ($\lambda/33 \times \lambda/16$) at the frequency of 130.0 THz, the attenuation length of the energy propagation can reach about 16.6 μm ($7.2\lambda$), and the propagating modes can exhibit a broad continuous frequency band from zero up to a cutoff frequency (162.6 THz) by means of tuning the size of the structures [213]. The gap waveguide has potential applications in biosensing and in-plane transmission of electromagnetic energy for subwavelength integrated

Figure 42

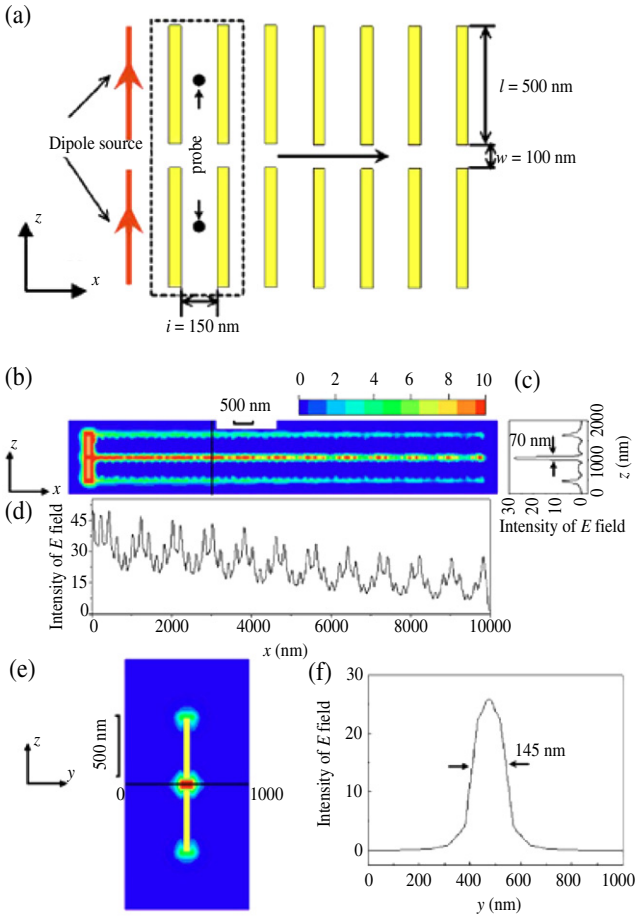


Schematic illustration of the gap waveguide composed of two coupling nanorod chains with the rod length $l = 500$ nm, waveguide width $w = 100$ nm, and interval of two adjacent rods $i = 150$ nm. The dimensions of each rod are 50 nm $\times$50 nm $\times$500 nm. The arrow in the waveguide shows the propagation direction of the energy in the gap waveguide. The red arrows on the left side represent two identical dipole sources, which are employed to excite the resonance in the waveguide. The two black points indicate the probes used to detect the local $H$ field between the first two rod pairs. (b) The intensity of the $E$ field in the waveguide in the $x$–$z$ plane at a frequency of. 130.0 THz. (c) and (d) show the distribution of the $E$ field intensity along lines at $x = 3000$ nm and the waveguide axis, respectively. (e) The intensity of the $E$ field in the cross section of the waveguide in the $y$–$z$ plane at a distance of 3000 nm from the left side of the waveguide. (f) The intensity of the $E$ field along the horizontal black line. Reproduced with permission from Figs. 1 and 3, Ref. [213]. © 2007 AIP.

optical devices owing to the high-intensity electric field in the gap of the nanorods.

### 5.1c. Metal Nanowires

Metal nanowires are promising candidates for SPP waveguides in nanophotonic and nanoelectronic devices because of their strong

confinement and favorable SPP guiding properties along the nanowire axis. Propagating and guiding of SPPs in metal nanowires have been systematically investigated by both far-field [214–220] and near-field [221–223] methods.

For the far-field method, the SPP is first excited by focusing a laser beam coupled into a microscope objective to one end of a nanowire; then the emission from the other end of the nanowire is collected by an objective, and bright- or dark-field optical images are recorded by a CCD detector.

Sanders *et al.* explored the selective emission and propagation of SPPs along Ag nanowires by using a far-field excitation and detection method [214]. SPP can be excited by illuminating an end of a single Ag nanowire with a diffraction-limited laser spot; the emission of SPPs at the other end of the nanowire is observed. Since SPPs can be launched from either end of the nanowire, SPP propagation is reversible in the nanowires (Figs. 43(a)–43(c)). However, SPP modes are not observed to be launched when the laser is focused on the midsection of the nanowire (Fig. 43(d)), because the momentum of the incident photons is not matched to that of the propagating SPPs at the midsection of the nanowire owing to the cylindrical symmetry over the extent of the diffraction-limited spot. Nevertheless, the symmetry is broken at the tapered end of the nanowire where light is scattered into propagating axial SPP modes. Furthermore, SPP propagation modes can couple between overlapping nanowires and fan out from one nanowire into multiple nanowires. When one of these nanowires is excited, the radiation is emitted at the intersection of the overlapping nanowires, which indicates that the intersection scatters propagating SPs into photons. Simultaneously, visible radiation is emitted at the ends of nanowires that cross the illuminated nanowire, which demonstrates the coupling of the SPP propagating modes between adjacent nanowires.

Recently, Xu, Nordlander and co-workers measured the angular distribution of the light emission from propagating SPP modes of an Ag nanowire based on the far-field technique [215]. The light located at the other end of the nanowire is emitted in a cone of angles at nominally 45°–60° with a secondary emission peak at 130°–150° from the nanowire axis when SPPs are excited at one end, and almost no light is emitted along the direction of the nanowire axis (Fig. 44(f)). The angular distribution of the light emission is found to be relatively independent of the shape and length of the nanowire. These characteristics can originate from the Fabry–Perot resonances of the forward- and back-propagating SPPs on the nanowire waveguide. In this case, the emission maximum from the nanowire occurs when standing waves of the SPPs are formed by the internal reflections from the nanowire ends. The strongly angular-dependent emission provides critical evidence for designing coupled nanowire-based photonic devices.

Furthermore, Xu, Nordlander and co-workers investigated of the SPP propagation in Ag nanowires positioned at different distances from dielectric substrates. It was found that the in-coupling efficiency exhibits strong peaks for certain distances between the nanowire and the substrate owing to the coherent interference between incident and reflected light [216]. The coupling between the SPs and the photonic modes of the substrate increases with decreased distance

Figure 43

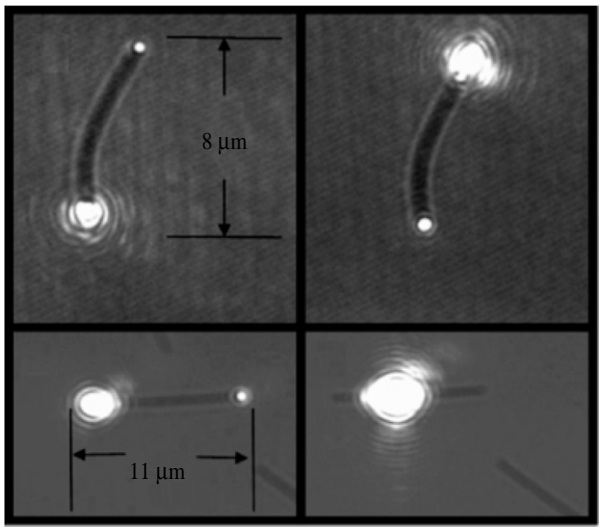


Micrographs showing the spatial sensitivity of launching plasmons. (a) Nanowire with excitation at the bottom end. (b) Same nanowire when excited from the top end. (c) Nanowire excited at left end. (d) Same nanowire with laser positioned at the middle of the nanowire. Notice that the plasmon is not excited in this geometry. Reproduced with permission from Fig 2, Ref. [214]. © 2006 ACS.

between the nanowire and the substrate. As a result, the decay length of SPPs decreases monotonically with decreased distance. Also, the SPP damping becomes very large for a strongly absorbing substrate. Investigation of the effect of the proximal substrate on SPP propagation is an important consideration for designing highly efficient photonic nanowire waveguides.

In addition, they proposed a SPP modulator based on construction of a nanowire branched structure [217]. The nanostructure consists of a short Ag nanowire with one of its ends directly adjacent to a longer trunk nanowire, forming a Y structure, where the two adjacent arms function as input terminals and the remaining end of the longer nanowire as the output terminal. Constructive and destructive interference of SPPs launched onto the trunk nanowire occurs by means of changing the phase or the polarization angle of the incident light at the input terminals. As a result, strongly modulated emission of light at the output terminal is collected. The nanowire-based SPP modulator can be operated as an ultracompact optical component and is also expected to be efficiently coupled to other plasmonic components in future integrated all-optical nanophotonic devices. Besides the roughness degree of the surface on nanowires, the shape of nanowires should be considered to decrease the radiative loss and increase propagation length of SPPs; in particular, bending a nanowire may give rise to additional radiative loss in SPP propagation along the nanowire.

Very recently, Xu, Wang and co-workers experimentally and theoretically investigated the radiative loss of SPP propagation of curved crystalline Ag nanowires with bending radius ranging from 5 to 32 μm [218]. The

Figure 44

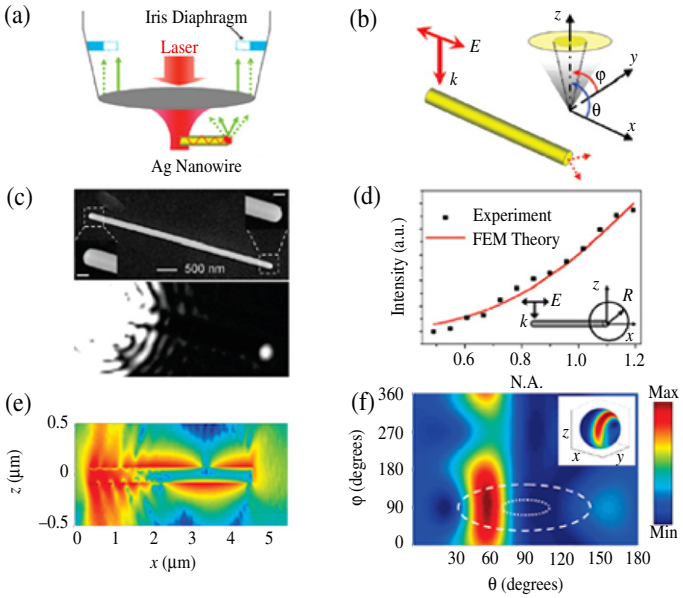


Angular emission measurement. (a) Scheme of the measurement. (b) The coordinates referred to in the experiments. The wave vector and polarization of the incident light are represented by the red arrows. (c) SEM image of a nanowire of length 4.6 μm and diameter 158 nm, and its optical image in a microscope under the excitation of a 633 nm laser spot polarized along the nanowire. The scale bars in enlarged insets showing the wire ends are 100 nm. (d) The measured emission intensity as a function of the N.A. of the objective (black squares). The red curve is the integrated far-field intensity for different N.A. obtained from the simulation. (e) Finite element method calculated distribution of the Poynting intensity around the wire. (f) The calculated emission intensity as a function of angles $\varphi$ and $\theta$ obtained by far-field transformation. The inset shows the corresponding angular distribution on the integration sphere. The white rings of different sizes are the emission angles that can be collected by the objective for N.A. = 1.2 and 0.5, respectively. Reproduced with permission from Fig. 1, Ref. [215]. © 2009 ACS.

radiative loss in the bent nanowire was measured by comparing the light emission intensity at the bent end of the nanowire with different bending radii, where two tapered optical fibers were used, one for directing the SPP excitation of the nanowire and the other for producing a force to bend the nanowire. The results indicate the bending loss increases with decreased bending radius, and the loss reaches 11 dB when the bending radius decreases to 5 μm. Moreover, the energy attenuation coefficient that is due purely to bending demonstrates an exponential relationship with the bending radius, which indicates that the emitted light intensity at the output end of the bent nanowire is very sensitive to the shape deformation of the nanowire. It can be seen that the radiative loss due to the bending nanowire is a critical factor affecting the performance of SPP propagation as signal carriers in nanophotonic integrated devices.

The SPP propagation described above is based on light excitation of SPPs from the end of nanowires. Recently, Novotny and co-workers

reported a direct energy conversion route from electrons to photons accompanying SPP excitation and propagation [219]. LSP gap mode is first excited on one end of an Au nanowire by low-energy electron tunneling; then the gap plasmons couple to the SPP propagation mode at the other end of the nanowire and are converted to propagating photons by edge scattering. The electron tunneling technique provides a nonoptical, voltage-controlled, low-energy route for SPP propagation in SPP waveguides.

On the other hand, near-field investigation of SPP propagation along a metal nanowire can reveal unique and essential characteristics. For instance, Weeber *et al.* showed that SPP propagation conditions along metal nanowires can be determined by calculation of the spatial distribution of the near-field intensity over the nanowire when one end of the nanowire is illuminated by a focused plane wave [221]. Considering an Au nanowire with a length of 1.5 μm, a width of 30 nm, and a height of 15 nm, the electric field distribution in the near-field area is calculated for an observation plane located 10 nm over the top of the nanowire. As a result, for excitation by an incident wavelength of 633 nm, only the area of the nanowire directly illuminated by the incident spot shows in the map. However, when the excitation wavelength is changed to 835 nm, a standing wave pattern over the nanowire can be clearly observed. Furthermore, for the incident wavelength of 633 nm, the electric field intensity along the nanowire axis is strongly damped, and it is found that the detected electric field intensity is reduced to 10% of the normalized intensity for a distance of 250 nm from the entrance of the nanowire. However, for the incident wavelength of 835 nm, the normalized field intensity 1.4 μm away from the entrance end of the nanowire is still 40% and shows a strongly oscillating behavior. The wavelength dependence of SPP propagation behavior can also be confirmed by a similar experiment investigation [178]. These results can be quantitatively explained by Eq. (7) in Section 5. Therefore, the nanowire can be regarded as a promising plasmonic waveguide for excitation with longer wavelengths.

Based on the oscillating behavior seen during the process of SPP propagation along a metal nanowire, Ditlbacher *et al.* presented experimental realization of SPP Fabry–Perot resonators by monocrystalline Ag nanowires with a length of about 18.6 μm and a diameter of about 120 nm [222]. The detailed experimental approach is as follows: a laser beam at normal incidence with respect to the substrate plane is focused onto one end face (input end) of the nanowire by a microscope objective with a laser wavelength of 785 nm (Fig. 45(a)), and the polarization direction of the incident light is along the nanowire axis. In these cases, the incident laser intensity is scattered into a SPP mode; then the SPP propagates toward the distal end of the nanowire. A clear near-field image of the SPP field along the nanowire can be obtained by a scanning near-field optical microscopy (SNOM) (Fig. 45(c)), which indicates the modulation of the near field of the propagating SPP mode along the nanowire due to SPP reflection at the distal nanowire end face. Figures 45(e) and 45(f) show scattered light spectra taken from both the input and the distal ends of the nanowires with lengths of 8.3 μm (diameter 75 nm) and 18.6 μm (diameter 120 nm), respectively. It is found that the linewidth of the SPP resonator mode increases with

Figure 45

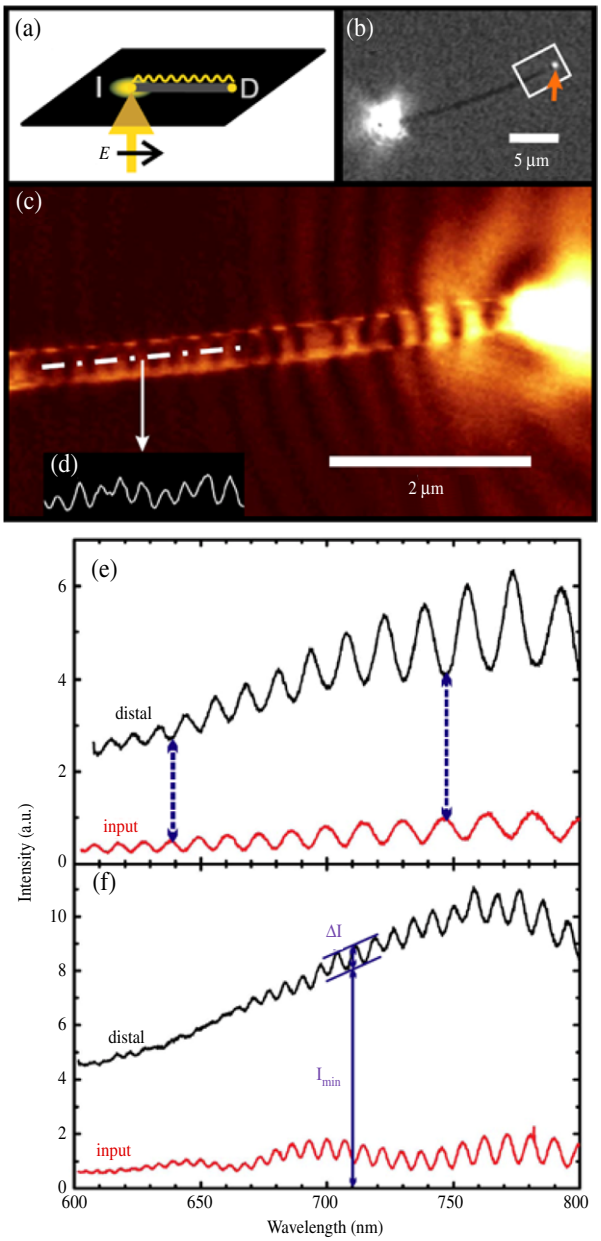


SPP propagation along the 18.6 µm long silver nanowire. (a) Sketch of optical excitation; *I* is the input and *D* the distal end of the wire. (b) Microscopic image. The bright spot to the left is the focused exciting light. The arrow indicates light scattered from the distal wire end. (c) Scanning near-field optical microscope (SNOM) image. The image area corresponds to the white box in (b). (d) 2 µm long cross section along the dashed-dotted line in (c). (e), (f) Scattered light spectra of the nanowire distal and input end faces. (e) spectra for a 8.3 µm long silver nanowire, diameter 75 nm. The vertical arrows highlight the spectral match between signal maxima and minima at the input and the distal end faces, respectively. (f) Spectra for a 18.6 µm long nanowire, diameter 120 nm. The arrows define $\Delta I$ and $I_{\min}$. Reproduced with permission from Figs. 2 and 4, Ref. [222]. © 2005 APS.

increased nanowire length because of the increased losses of the SPP mode. The scattered light intensities from the input and distal ends of the nanowire correspond to the transmission and reflection intensities of a resonator constituted by two mirrors facing each other. Moreover, the relative modulation depth of the spectra ($\Delta I/I_{\min}$) is dependent on the nanowire length for the incident light wavelength of 785 nm, and the modulation depth decreases with increasing nanowire length; in this case, great propagation lengths of about 10 μm and reflectivity of about 25% on the end face can be achieved [222], which indicates that the Ag nanowire can function as a highly efficient SPP Fabry–Perot resonator. This nanowire resonator can be expected to be a basic element for the design of nanophotonic devices.

Recently, Verhagen and co-workers presented a highly confined SPP propagation mode excited on metal nanowires through an adiabatic mode transformation process [223]. The SPP mode was first excited in a metal stripe, and then the stripe was tapered down to the desired nanowire size; the SPP propagation mode was subsequently confined in the nanowire. Phase- and polarization-sensitive near-field microscopy indicates the antisymmetric polarization nature of the excited nanowire mode, which gradually evolves from the fundamental SPP mode propagating at the substrate side of the metal stripe. The SPP mode transformation technique may be applied to nanofocusing elements.

### *5.1d. Metal Nanogap*

SPPs can also propagate in a narrow nanogap formed between two parallel metallic plates. This guiding element is called a SPP gap waveguide (SPGW). Tanaka *et al.* presented an I-shaped SPGW consisting of a narrow gap region located in a wide gap region between two metal plates [224]. The electric fields of SPPs can be confined near the narrow gap region, and SPPs can be guided in the narrow gap region because of the low phase velocity of SPPs in the narrow gap region. In this case one can control the phase velocities of SPPs by altering the gap width on a nanoscale. Moreover, they designed H-plane and E-plane optical circuits consisting of straight and branched bent SPGWs [224]. Exploration of the SPP propagation for different SPGW structures (e.g., slab–slab, slab–plate, and staggered slab–slab) demonstrates that the nanometric field confinement can be controlled by using a SPGW with a staggered slab–slab structure without a large change in the propagation constant [225]. These optical circuits composed of SPGWs can perform efficient functions of guiding, branching, and bending SPP waves.

Wang *et al.* proposed nanoscale Mach–Zehnder interferometers based on coupling SPGW structures composed of splitting and recombining gap waveguides with a gap width of 30 nm [226]. They observed the splitting of the input signals evenly into two interferometric SPGWs and then the recombination of the split signals in the output end (Fig. 46). The SPGW structures can display potential applications in switches, directional couplers, and controlling the flow of SPPs.

In addition, using the FDTD method, Pile *et al.* explored the dispersion and electric field distribution of SPP modes guided by metal nanogaps

Figure 46

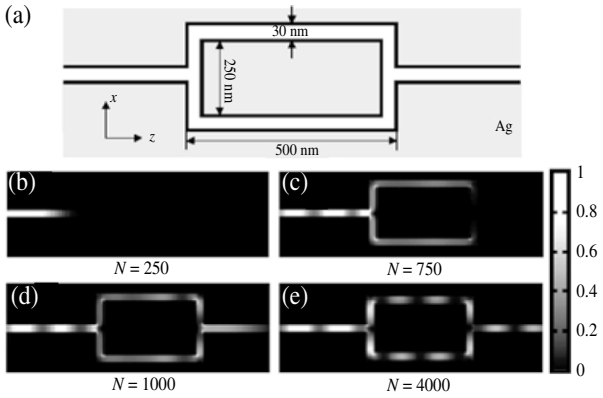


(a) Mach–Zehnder interferometric structure with splitting and recombining MGWs. (b)–(e) $|E|^2$ time evolution of light through the structure, corresponding to $|E|^2$ in the structure at various moments from $t = 250\Delta t$ to $4000\Delta t$, which cover the progression of an electrical field from a transient state to a steady state ($t \geq 4000\Delta t$) as a light wave is coupled into the leading guide. $N$ denotes elapsed time. Reproduced with permission from Fig. 1, Ref. [226]. © 2004 OSA.

[227]. They found a periodically changing and strongly localized electric field along the nanogap, and this field is nondecaying along the nanogap in the absence of dissipation, which indicates a strongly localized SPP eigenmode of the SPGW. For a nanogap with a 100 nm width and a 100 nm height, there is only the fundamental SPGW mode in the Ag–vacuum structure; however, when the height of the nanogap increases (e.g., 1300 nm), the nanogap will support two SPP modes, and the electric field intensity exhibits three distinct maximums that are due to the interference between the fundamental and the second SPGW modes. These SPP modes may be promising options for the design of all-optical nanocircuits and devices because of their long propagation distance, strong localization, and low bend losses.

### 5.1e. Metal Grating

Noble metal periodical gratings can support propagation modes of SPPs. Halas and co-workers experimentally investigated the propagation characteristics of SPPs on Cu and Ag periodical gratings at NIR wavelengths [228]. It was observed that the SPP dispersion behaviors at the Cu–Si interface are similar to those at the Ag–Si interface. For instance, the second-order SPP modes of both Cu and Ag gratings exhibit the same group velocity with a small plasmonic band gap of magnitude 32 meV (Fig. 47(b)), which is most likely due to the similarity of the dielectric properties of Ag and Cu in the wavelength range. Furthermore, the second-order SPP excitation is at higher energy than that of the first-order SPP excitation, and therefore the SPP band gap associated with the dispersion of the second-order SPP excitation (31 meV) is significantly larger than that of the first-order SPP excitation (13 meV) (Fig. 47(c)), which indicates that higher-order SPP excitations have larger plasmonic bandgaps. On the other hand, the plasmonic band

Figure 47

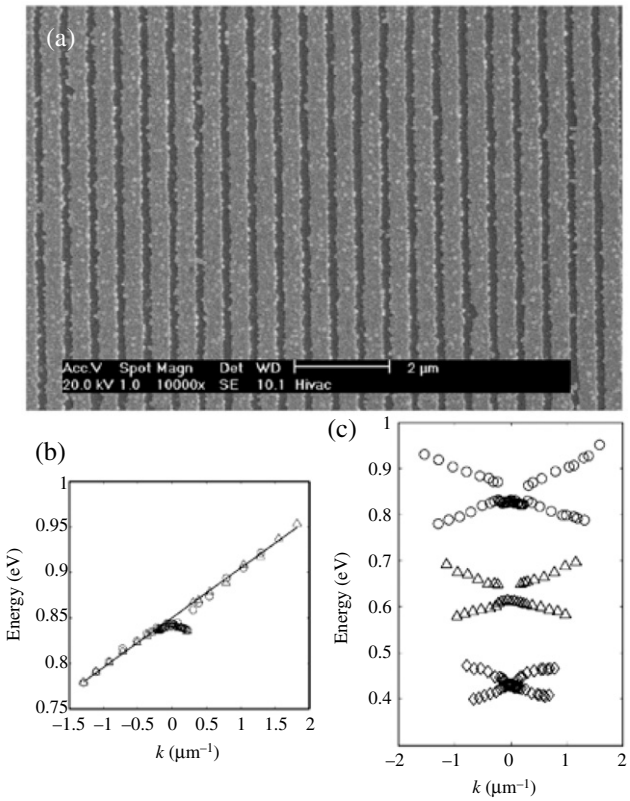


(a) SEM image of copper grating with period 555 nm. (b) Dispersion curve for second-order metal-silicon interface plasmon for an 833 nm period sample composed of copper (◯) and silver (△). The group velocity of the excitation is $8.36\times10^7$ m/s (0.96*c*). (c) Dispersion curve for copper–silicon interface plasmon for first-order 833 nm excitation (◊), for first-order 555 nm excitation (△) and second-order 833 nm excitation (◯). The corresponding band gaps are 13 meV (◊), 35 meV (△), and 31 meV (◯). The error in the band gap measurements is 5 meV. Reproduced with permission from Figs. 1a, 2, and 3, Ref. [228]. © 2006 AIP.

gap increases with decreased grating period. The increase in plasmonic bandgap with order has important implications in device design and in coupling considerations in the development of SPP waveguides.

It is known that the propagation length of SPPs is dependent on the internal damping and radiation damping [229]. The internal damping originates from the omhic losses of metal (described above). Nevertheless, the radiation damping results mainly from scattering losses of the structures. Jose *et al.* reported an enhancement of the propagation length of SPPs on an Au grating buried in a glass substrate. Near-field measurements by heterodyne interferometric photon scanning tunneling microscopy show that the FWHM of the SP resonance on the buried grating is reduced to 57% for the prism-coupled SPPs and 77% for the grating-coupled SPPs [230]. The significant reduction in the FWHM of SP resonance indicates that the buried grating particularly reduces the radiation damping of SPPs. As a result, the propagation length of SPPs

on the buried gratings is close to the calculated propagation length on an ideal Au surface, and the propagation length can be further enhanced by fabricating monocrystalline Au film with much lower scattering losses. Therefore, the buried grating with the reduced FWHM of SP resonance can be expected to improve the figure of merit of a grating-incorporated SP sensor.

### 5.1f. Metal Nanoslits

The general nanostructures for SPP propagation are mainly the confined modes near the SP resonance frequency [224,227]. These confined modes show low group velocity and short propagation lengths of SPPs. Veronis and Fan proposed a bound optical mode of SPPs supported by a nanoslit in a thin Ag film deposited on a substrate, where the slit dimension (e.g., where both the width and the thickness are 50 nm) is much smaller than the wavelength (e.g., 1.55 μm) [231]. It is found that the mode size is dominated mainly by the near field of the nanoslit with wide frequencies, and the mode size is far smaller than the wavelength. Moreover, the group velocity of the SP resonance mode is close to the speed of light on the substrate, and the propagation length of SPPs is tens of micrometers at the optical communication wavelength of 1.55 μm [231].

In addition, Catrysse *et al.* presented guided modes of SPPs supported by one-dimensional periodical arrangement of nanoslits in a metal film [232]. They found that the nanoslits with the periodical arrangement exhibited two distinct types of TM guided modes of SPPs propagating in the direction perpendicular to the nanoslits: two degenerate surface modes and a series of effective dielectric slab modes (Fig. 48). The surface modes are confined to the front and back metal–dielectric interfaces because of periodic scattering, while the effective dielectric slab modes originate from the subwavelength electromagnetic propagating state in the nanoslits, which closely resemble the waveguide mode in a dielectric slab. Furthermore, the presence or absence of those SPP modes can be controlled by proper selection of the geometrical parameters and their surface properties.

### 5.1g. Metal Stripes

A thin metal stripe with a thickness of tens of nanometers and a width of a few micrometers can act as a SPP waveguide [2]. Weeber *et al.* presented a near-field observation of propagation modes of SPPs on thin metal stripes by a photon scanning tunneling microscopy [233], where several Ag thin stripes of different widths (e.g., 1.0, 1.6, and 2.5 μm) are connected to a large homogeneous Ag thin film area of 250 × 250 $\mu m^2$ (Fig. 49(a)). It is demonstrated that a strong coupling between SPPs launched on the homogeneous Ag thin film area and the SPP modes supported by the thin stripes is achieved at visible frequencies for stripe widths as narrow as 2.5 μm. Additionally, SPP modes with a sharp transverse confined field can propagate on the metal stripe (Fig. 49(b)). The backreflection of these modes at the end of the stripe leads to a stationary wave with an interference pattern. Furthermore, the fields of the stripe SPP mode can be focused by use of a triangularly shaped stripe termination with a

Figure 48

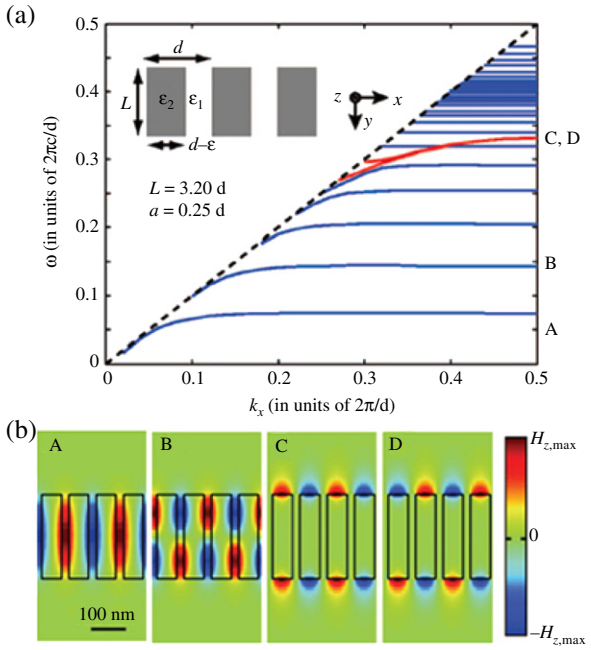


(a) Guided-mode band diagram for TM polarization (first Brillouin zone) when $L = 256$ nm, $d = 80$ nm, and $a = 20$ nm. Shown are two degenerate surface modes (red curves) and a series of effective dielectric slab modes (blue curves); the dashed line is the light line in vacuum. Inset, schematic of a metallic film with periodic slits: $a$ is the slit width, $d$ is the periodicity, and $L$ is the film thickness. The gray regions indicate metal ($\varepsilon_2$), and the white regions represent vacuum ($\varepsilon_1$). (b) $H_z$-field distributions for the two types of guided mode supported by the geometry shown in (a). Distributions are shown for $k_x = 0.50$ in units of $2\pi/d$. Panel A is the fundamental effective dielectric slab mode at $\omega = 0.074$, panel B shows next-higher-order effective dielectric slab mode at $\omega = 0.144$, and panels C and D represent surface modes at $\omega = 0.332$. Red and blue correspond to large positive and negative field values, respectively, and green represents zero field. Reproduced with permission from Figs. 1 and 2, Ref. [232]. © 2006 AIP.

width of 3.5 μm. In this case, the thin metal stripes can be expected to be used for optical addressing purposes.

In general, the metal stripes support confined SPP modes; however, there is a cutoff condition for some metal stripe waveguides [234]. Zia *et al.* performed near-field characterization of propagation and cutoff of SPPs on thin Au stripes with different widths from 500 nm to 6.0 μm. The propagation length of SPPs in the stripes decreases with decreasing stripe width [235]. As a result, the metal stripe supports a finite number of guided SPP modes. Wide stripes may support multiple guided modes; however, narrower stripes may not support guided modes. In particular, the stripe with a width of 2 μm supports only a single quasi-TM leaky SPP mode, and the substantially narrower stripes will exhibit cutoff of guided modes [235]. Furthermore, Zia and Brongersma constructed a general framework to describe the propagation, diffraction, and interference of SPPs. In a double-slit experiment with SPPs, they suggested that

Figure 49

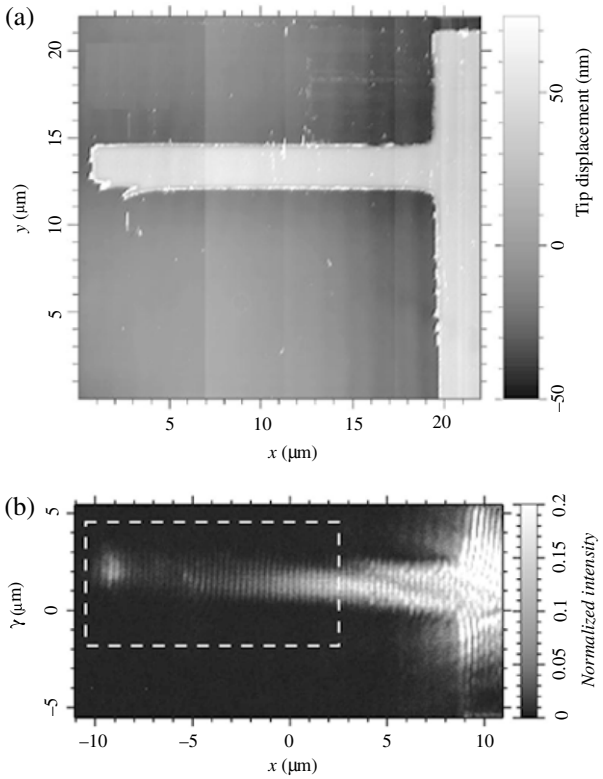


(a) Atomic force microscope images of silver stripe connected to a large homogeneous thin film (60 nm thickness) area of 250 × 250 $\mu m^2$. The width of the stripe is 2.5 μm. (b) Photon scanning tunneling microscope image of the 2.5 μm wide stripe. The tip–sample distance is about 100 nm. Reproduced with permission from Figs. 2b and 6b, Ref. [233]. © 2001 APS.

there was an effective diffraction limit for the lateral confinement of SPP on metal stripe waveguides. These results also provide intuitive evidence to further explore the physics of SPPs and to design new SP nanodevices [236].

In order to reduce the energy loss of SPP propagation on metal stripe waveguides, recently, hybrid SPP waveguides at optical telecommunication wavelengths were proposed based on metal stripes embedded between the dual slab dielectric waveguides with high refractive-index contrast [237]. The symmetric metal stripe waveguides can support long-range SPP (LRSP) modes [238]. In this case, the electric fields of the guided SPP mode are confined mainly in the dielectric core layers, and the propagation loss of SPPs is significantly reduced when the metal stripe width decreases. As a result, the propagation loss of less than 1.0 dB/cm with a stripe width of 1–5 μm can be achieved at a 1.31 μm wavelength [237].

### 5.1h. Metal Thin Films

Thin films with different surface structures support different SPP propagation behaviors. When a SPP propagates on thin metal film with

a periodically textured surface on the scale of the light's wavelength, scattering may lead to the formation of SPP standing waves and the appearance of a SPP stop band [239]. In this case the periodic texturing of the metal surface gives rise to a SPP photonic bandgap when the period is equal to the half-wavelength of SPP modes [2]. Bozhevolnyi *et al.* investigated SPP propagation along line defects in a periodically corrugated metal film surface by SNOM [192,240]. The SPP bandgap effect can be directly observed at the 45 nm thick Au film surfaces with areas of 200 nm wide scatterers arranged in a 400 nm period triangular lattice containing line defects. For the SPP excitation at the 782 nm wavelength, strong reflection of SPPs with an attenuation (below 10% of the average level) and SPP guiding along the line defects in the structure are found [192]. However, strong deterioration of both the SPP reflection and inhibition of SPP propagation appears for a long wavelength of 815 nm. Moreover, SPP bandgap effects can be improved by optimization of the structure parameters.

Recently, Mishchenko *et al.* predicted that graphene p-n junctions can also guide SPP modes [241]. The grapheme is a flat monolayer of carbon atoms tightly packed into a two-dimensional periodical honeycomb lattice [242]. The spatial separation of electrons and holes in graphene gives rise to the existence of a SPP wave confined to the boundary region for wavelengths shorter than the charged domain width. Furthermore, the frequency, velocity, and direction of guiding SPP modes can be easily controlled by the external electric field [241]. This finding indicates that graphene will be a very promising material for nanophotonics.

## 5.2. Propagating and Guiding of Surface Plasmon Polaritons through Hybrid Nanostructures

In addition to the metal nanostructures that can propagate and guide SPP modes as described above, hybrid nanostructures including metal–semiconductor (such as metal nanowires coupled to semiconductor quantum dots, and a metal surface coupled to semiconductor nanowire), metal–dielectric (such as metal–dielectric interfaces, dielectric–metal–dielectric structures, and metal–dielectric–metal structures), and metal–polymer nanostructures that can also support propagating and guiding modes of SPPs.

### *5.2a. Metal–Semiconductor Coupling Structures*

Previous reports indicated that modifying photon fields around quantum dots by using optical cavities can enhance the emission rate of semiconductor quantum dots [243–245]. Chang *et al.* proposed a novel method based on modifying photon fields around quantum dots by a strong coupling between individual quantum dots and guided SPP modes in metal nanowires at optical frequencies. The optical emission of the quantum dots can be almost entirely directed into the SPP modes [174]. In this case, Lukin, Park, Akimov and co-workers experimentally achieved single optical plasmons in Ag nanowires coupled to a CdSe quantum dot [176], wherein the single CdSe quantum dot is optically excited in close proximity to the Ag nanowire. Optical

emission from the quantum dot couples directly to guided SPP modes in the nanowire; as a result, the end of the nanowire lights up (Fig. 34). The efficient coupling is more than 2.5-fold enhancement of the quantum dot spontaneous emission, because the field confinement and reduced group velocity of SPPs can act as a very efficient lens and cause the nanowire to strongly capture the majority of spontaneous radiation into the guided SPP modes. By using the strong coupling between individual optical emitters and propagating SPP modes confined to the metal nanowire, these researchers realized strong nonlinear interactions at the single-photon level. In this case, a single-photon transistor can be constructed because the presence (or absence) of a single incident photon for a small optical gate field is sufficient to allow (or prevent) the propagation of subsequent signal photons along the nanowire [180]. The result opens up new opportunities in quantum information science because of the unprecedented control of the interactions of individual light quanta based on the generation of single quantized plasmons.

Almost simultaneously, Woggon, Fedutik and co-workers presented an exciton–plasmon–photon conversion in a metal–isolator–semiconductor multishell nanostructure [246]. The hybrid nanostructure consists of a single Ag nanowire functionalized by optical emitters (CdSe nanoscrystals) on top of a $SiO_2$-spacer shell. Through this hybrid structure, the exciton–plasmon–photon conversion can be performed based upon the local effect of enhanced spontaneous emission due to a modified density of states near the metal nanowire with the SPP excitation and the propagation in the resonance nanocavity of the nanowire. Furthermore, Wei *et al.* found that the interaction between the excitons in quantum dots and SPP propagation in metal nanowires demonstrated a reverse process [247]; that is, the propagating SPPs in the metal nanowires can excite the quantum dots and result in optical emission, where the energy is directly transferred from the propagating SPPs to the excitons without conversion to photons, and, conversely, the excited quantum dots can also induce propagating SPPs in the nanowire.

In addition, Zhang, Oulton and co-workers demonstrated a nanoscale SPP laser based on a hybrid SPP waveguide consisting of a high-gain CdS nanowire on top of an Ag surface [13], and the Ag surface was separated by a $MgF_2$ insulating layer with a thickness of 5 nm (Fig. 50(a)). When the hybrid structure is optically pumped at a 405 nm wavelength, the emission from the dominant $I_2$ CdS exciton line at 489 nm can be measured (Fig. 50(b)). The emission is the longitudinal cavity modes and allows SPP modes to resonate between the reflective nanowire end facets. In this case, the multiple cavity resonance modes at higher pump powers demonstrate sufficient material gain to achieve full laser oscillation. In addition, this group of researchers found a strong increase of the spontaneous emission rate when the gap size between the nanowire and metal surface decreased (e.g., 5 nm). The emission lifetime measurements revealed a broadband enhancement of the exciton spontaneous emission rate from the nanowire by up to six times owing to the strong mode confinement [13]. This deep subwavelength SPP laser action at visible frequencies demonstrates a new source below the diffraction limit, and the SPP laser may have potential applications in photonic circuits and quantum information technology.

Figure 50

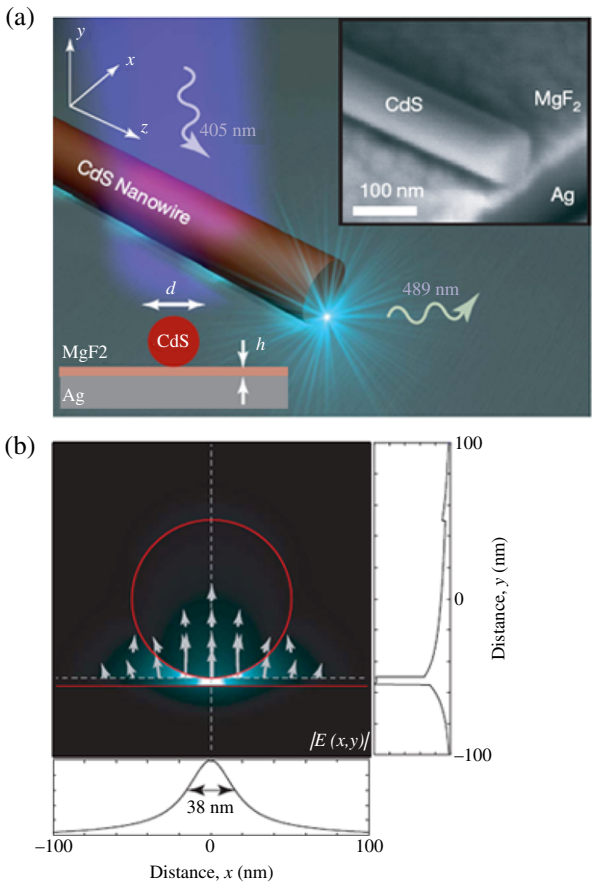


The deep subwavelength plasmonic laser. (a) The plasmonic laser consists of a CdS semiconductor nanowire on top of a silver substrate, separated by a nanometer-scale $MgF_2$ layer. This structure supports a new type of plasmonic mode, and the mode size is a hundred times smaller than a diffraction-limited spot. Inset, SEM image of the plasmonic laser. (b) Stimulated electric field distribution and direction $|E(x, y)|$ of a hybrid plasmonic mode at a wavelength of 489 nm. The cross sectional field plots illustrate the strong overall confinement in the gap region between the nanowire and metal surface with sufficient modal overlap in the semiconductor to facilitate gain. Reproduced with permission from Fig. 1, Ref. [13]. © 2009 NPG.

Zhang and co-workers experimentally demonstrated a nanoscale waveguide with low-loss and broadband features [248]. The waveguide is based on a hybrid SPP strip consisting of a semiconductor strip separated from a metal surface by a nanometer-scale low-dielectric-constant gap (Figs. 51(a) and 51(b)). It is found that the hybrid SPP mode confinement is essentially constant at about 50–60 nm (Fig. 51(d)), and the width of the confined mode is also subwavelength (with $\lambda/12$ and $\lambda/7$ for visible and NIR wavelengths i.e., 633, 808 and 1427 nm, respectively) (Figs. 51(e) and 51(f)). The propagation length of the hybrid SPP mode increases with its operating wavelength and exceeds 20 times its vacuum wavelength (0.3 dB $\mu m^{-1}$) at NIR wavelength ($\lambda = 808$ nm) [248]. Moreover, Fabry–Perot interference spectroscopy confirms that the optical mode

hybridization between a SPP and a dielectric mode concentrates the hybridized mode inside a nanometer thin gap. The nanoscale waveguide will have promising applications in the next generation on-chip optical communication systems, signal modulators, and nanoscale lasers.

### 5.2b. Metal–Dielectric Coupling Structures

Although SPP waveguides consisting of metal–semiconductor hybrid structures provide tight confinement of optical fields, optical losses within the dissipative metal nanostructures are quite large at the visible and telecommunication wavelengths [249]. Zhang, Oulton and co-workers proposed a new hybrid SPP waveguide with low propagation losses at telecommunication wavelengths [250]. The hybrid waveguide is composed of a high-permittivity dielectric nanowire separated from a metal surface by a nanoscale dielectric gap. In this hybrid SPP waveguide, SPPs can propagate over large distances (40–150 μm) with strong confinement of hybrid mode sizes ranging from $\lambda^2/400$ to $\lambda^2/40$ (Fig. 52). The dielectric gap provides the means to store optical energy and results in the SPP propagation mode in the nonmetallic regions with low optical losses. In this case, subwavelength confinement and large propagation length can be obtained simultaneously [250]. Furthermore, the propagation length can be increased to the millimeter range while still maintaining moderate confinement by tuning the geometrical parameters (e.g., the nanowire diameter and the dielectric gap width) of the hybrid structure. The hybrid SPP waveguides extend the capabilities of both plasmonics and semiconductor photonics and offer potential opportunities in nanolasers and optically integrated circuits.

In addition, submicrosecond or nanosecond response times are likely to be too slow for data transport and processing. MacDonald, Sámson and co-workers reported that femtosecond optical frequency pulses could propagate along a metal–dielectric waveguide based on the nonlinear interaction between propagating SPP waves and light in a pump–probe experiment [251–253]. They demonstrated a pulsed plasmonic probe signal generated on an aluminium/silica interface by grating coupling from a pulsed laser beam with a wavelength of 780 nm (Fig. 53(a)). The transient effect of control pulse excitation on the propagating SPP signal could be monitored by varying the time delay between the SPP excitation and optical pump pulses. It was found that the transient response data exhibit two components of the nonlinear response: a fast component with a relaxation time shorter than the 200 fs pulse duration, and a slow component with a relaxation time of about 60 ps (Fig. 53(d)). The fast component is sensitive to the mutual orientation of the pump beam's polarization state and the electron oscillation direction in the signal plasmon wave [251]. These results offer a new principle for a direct terahertz modulation bandwidth with a speed at least five orders of magnitude faster than existing technologies.

On the other hand, Berini proposed that a symmetric thin metal film of finite width embedded in an infinite homogeneous dielectric could support LRSP modes [254,255]. When the metal film becomes thin enough, the coupling of the two SPP waves appears between the two metal–dielectric interfaces; as a result, the SPP waves split into two coupled modes consisting of one symmetric mode and

Figure 51

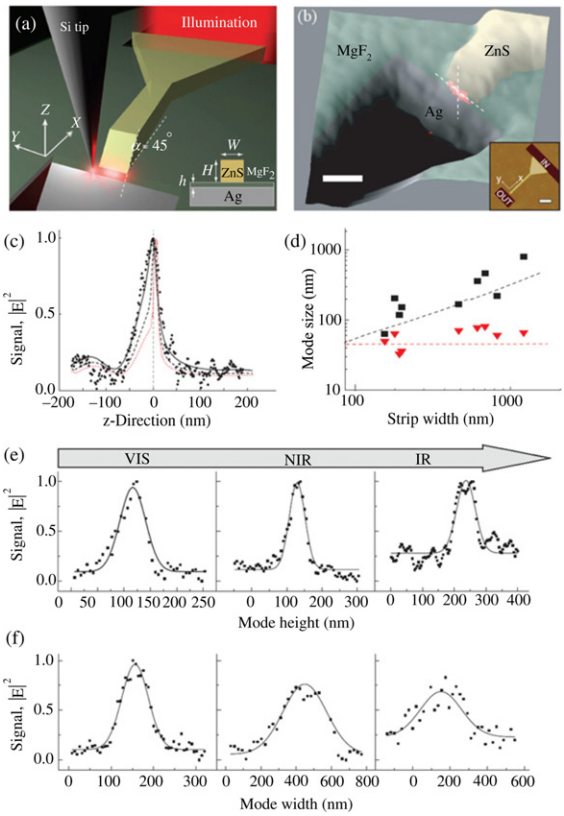


(a) Schematic of hybrid plasmon polariton (HPP) mode size mapping via aperture SNOM. The HPP strips consist of a semiconductor strip separated from a metallic surface by a nanometer-scale low-dielectric-constant gap and are excited by illuminating a metal slit at the input end. (b) Three-dimentional image overlap of the deep subwavelength HPP mode signal (red spot), offering optical confinement significantly below the diffraction limit of light. This degree of optical confinement indicates the devices' potential to create strong light–matter interaction for compact and highly functional photonic components. Scale bar, 125 nm. $MgF_2$ gap $h = 10$ nm, illumination wavelength $\lambda = 633$ nm. Inset, height profile of tapered strip for free space to HPP strip coupling; scale bar, 1 μm. (c) Experimental field intensity (black dots) of the HPP mode compared with different tip–sample separations, $t$, from its exit point. The optical mode height of $\mathrm{FWHM}_z = 53$ nm is deep subwavelength for $\lambda = 633$ nm; HPP strip dimensions $H = 230$ nm, $W = 174$ nm. (d) Summary of experimental HPP mode dimensions yielding the smallest measured mode area of $53 \times 63$ nm$^2$, at $\lambda = 633$ nm. The good agreement between experimental data (mode width, black squares; height, red triangles) and theoretical simulations (dashed curves) confirms that the optical HPP mode is indeed squeezed into the low-dielectric-constant gap: the mode height is independent of the strip width (triangles), whereas the mode width scales with the strip width (squares). (e), (f) Line scans of the mode height and width for wavelengths of the illumination beam of 633, 808, and 1427 nm, featuring broadband, deep subwavelength operation of HPP-based devices. The FWHMs (solid curves) are Gaussian fits to binned data, yielding measured mode areas of $\lambda^2/120$, $\lambda^2/59$, and $\lambda^2/157$, which are deep subwavelength modes for all three wavelengths. Reproduced with permission from Figs. 1a and 2, Ref. [248]. © 2011 NPG.

Figure 52

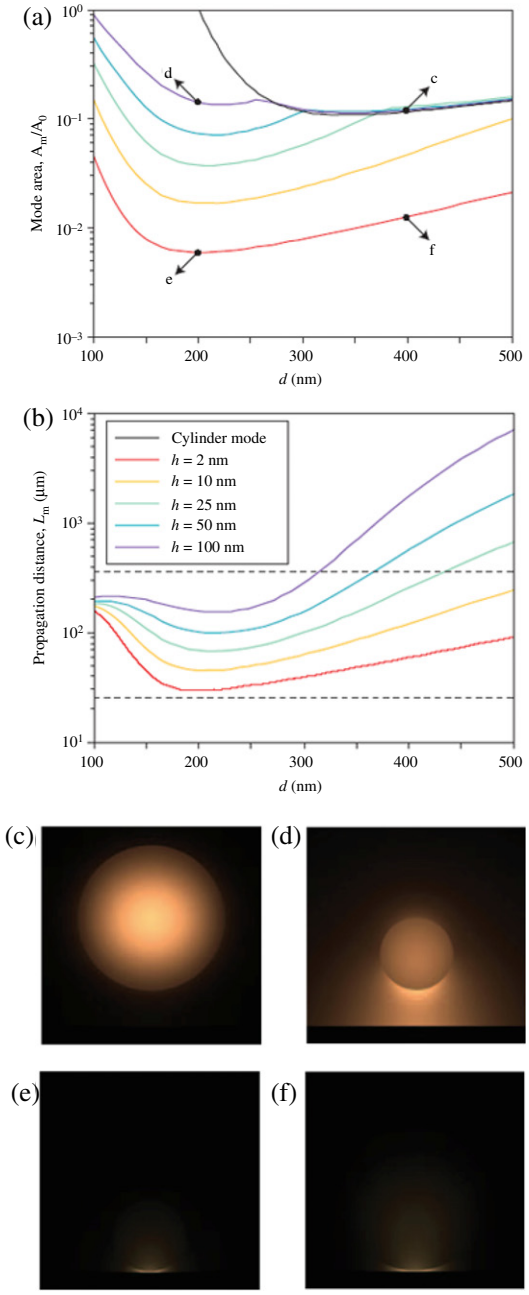


Propagation distance, mode area, and field distributions of the hybrid mode. (a) Mode area, $A_m/A_0$ versus cylinder diameter $d$ for different gap width $h$ (colored curves), compared with the mode area of a pure cylinder mode (black curve). (b) The hybrid mode's propagation distance (colored curves), compared with those of pure SPP modes at metal–oxide (upper dashed black line) and metal–semiconductor (lower dashed black line) interfaces. (c)–(f) Electromagnetic energy density distributions for (c) $[d, h] = [400, 100]$ nm, (d) $[d, h] = [200, 100]$ nm, (e) $[d, h] = [200, 2]$ nm, and (f) $[d, h] = [400, 2]$ nm, corresponding to the points indicated in (a). The legend of (b) applies throughout this figure. Reproduced with permission from Fig. 2, Ref. [250]. © 2008 NPG.

Figure 53

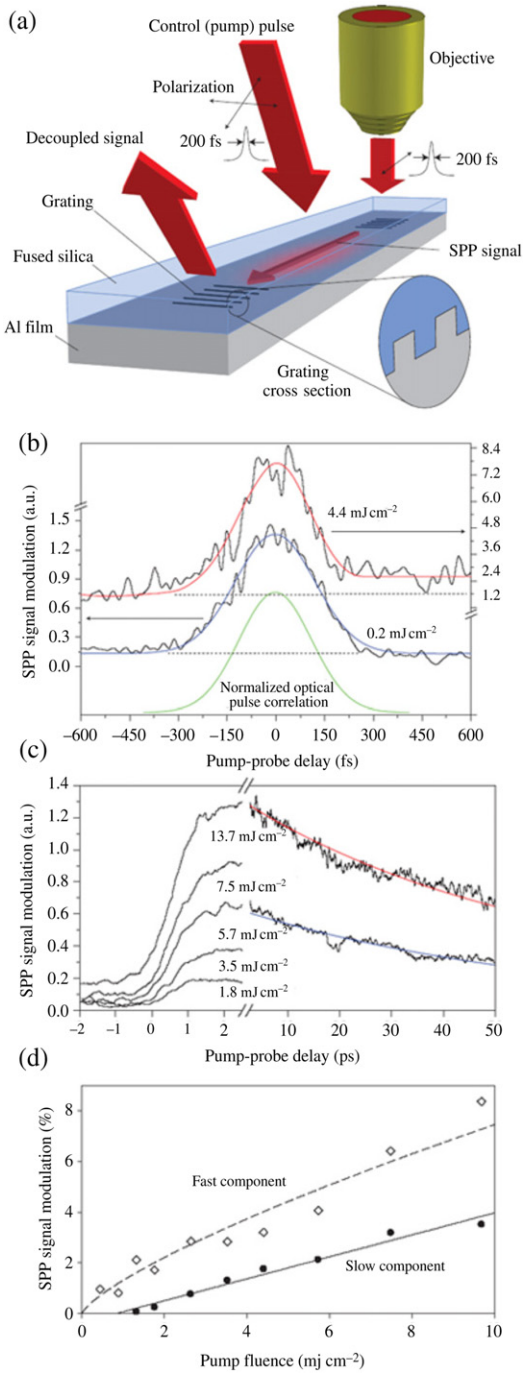


(a) Ultrafast optical modulation of SPP propagation. A plasmonic signal, coupled to and from the waveguide by gratings on an aluminium/silica interface, is modulated by optical pump pulses as it travels between the gratings. (b), (c) Transient pump-induced changes in the decoupled plasmonic signal for pump light polarized (b) parallel (with a normalized trace, in green, of the optical pulse correlation), and (c) perpendicular (for a range of pump fluences as labeled) to the SPP propagation direction. (d) Corresponding peak magnitudes of the fast and slow pump-induced modulation components as a function of pump pulse fluence. Reproduced with permission from Figs. 1 and 3, Ref. [251]. © 2009 NPG.

Figure 54

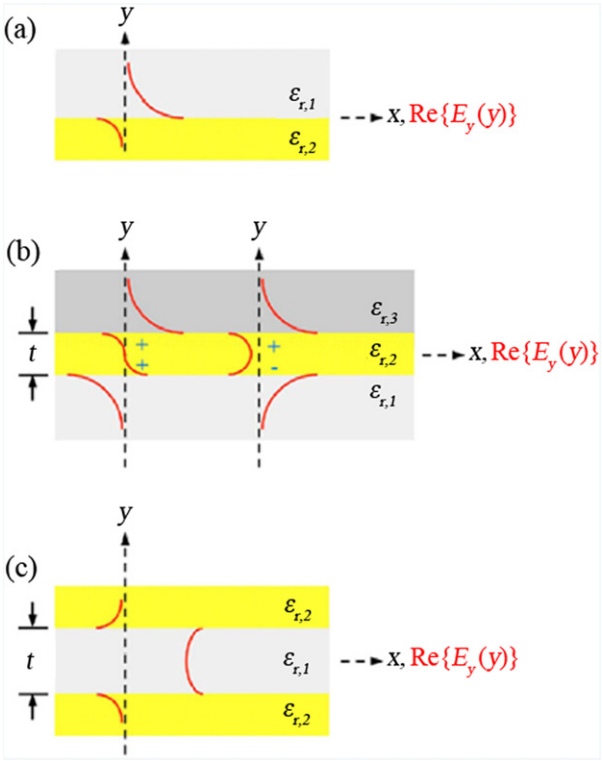


(a) Single interface between a metal ($\varepsilon_{r,2}$) and a dielectric ($\varepsilon_{r,1}$) supporting a bound SPP. (b) Metal slab ($\varepsilon_{r,2}$) of thickness $t$ bounded by semi-infinite dielectrics ($\varepsilon_{r,1}$, $\varepsilon_{r,3}$) supporting two bound SPP modes ($a_b$, $s_b$). (c) Dielectric slab ($\varepsilon_{r,1}$) of thickness $t$ bounded by semi-infinite metals ($\varepsilon_{r,2}$) supporting a symmetric bound mode. The distribution of the main transverse electric field component of the modes is shown as the red curves over the cross section of each structure. Reproduced with permission from Fig. 1, Ref. [6]. © 2009 OSA.

one antisymmetric mode with transverse electric field distributions (Fig. 54) [5,6]. Furthermore, for the symmetric SPP mode, the loss of the electric fields is very low, and the attenuation of the electric fields is much lower than that of SPPs at the single interface. Therefore the symmetric SPP mode is also LRSP [5,6], and the propagation length of the LRSP is very long; the length even reaches the order of centimeters [6,256,257]. However, for the antisymmetric SPP mode, the loss of the electric fields is very large, because the electric fields are concentrated mainly into the metal, and the SPP modes show increasing confinement. Thus the antisymmetric SPP mode is also called short-range SP, and the propagation length of the LRSP is quite short because of the very strong attenuation resulting from the large ohmic losses in the metal [258].

In contrast to dielectric–metal–dielectric structures, metal–dielectric–metal structures can exhibit negative refraction behavior. The negative refraction typically occurs at the interfaces between metal and dielectric, which supports backward waves with a negative displacement [259]. Lezec, Dionne, and Atwater presented an experimental realization of the negative refraction in a visible wavelength region by using a

planar ultrathin $Au/Si_3N_4/Ag$ waveguide [260]. The negative refraction originates from the in-plane isotropic dispersion properties of a TM mode involving coupled SPP modes at the two metal–dielectric interfaces. In this case, the metal–dielectric–metal structures support SPP modes with antiparallel group and phase velocities when the frequency is located between the SPP frequency and the bulk plasmon frequency. As a result, all-angle negative refraction is observed at the interface between this bimetal waveguide and a conventional $Ag/Si_3N_4/Ag$ slot waveguide. This result is expected to be applied in practical negative-index optical designs at visible wavelengths.

In addition, Shin and Fan theoretically proposed that the metal–dielectric–metal structure can served as a negative refraction lens for SPP waves on a metal surface [261] The lens is uniform with respect to a plane of incidence and is capable of focusing propagating SPP waves on the metal surface at all incidence angles. This all-angle negative refraction structure provides a new way of manipulating light at the nanoscale by controlling the propagation of SPPs.

### *5.2c. Metal–Polymer Nanostructures*

Loss compensation and amplification of optical gain play a key role in increasing the SPP propagation length. Loss compensation means that SPP losses are reduced compared with the passive case, while amplification of optical gain means that they are overcompensated. The more confined the SPPs, the greater the attenuation and the greater the required optical gain [258]. SPPs propagating on a metal–dielectric interface exhibit large propagation losses at visible wavelengths. In this case, the propagation losses can be expected to be compensated by gain media.

Gather *et al.* presented direct evidence of SPP propagation with net optical gain over macroscopic distances in LRSP waveguides [262]. The devices consist of a silicon substrate covered with a 20 μm thick transparent polymer layer with a refractive index of $n = 1.55$ and a 4 nm thick Au layer. The net optical gain is provided by an optically pumped layer of fluorescent conjugated polymer adjacent to the metal surface in a dielectric–metal–dielectric SPP waveguide. As a result, a very substantial net gain of 8 $cm^{-1}$ can be obtained at room temperature. The gain can be applied to plasmonic amplifiers and plasmonic waveguide lasers [258]. Grandidier *et al.* also developed a method to partially compensate SPP losses by doping the poly(methyl methacrylate) (PMMA) polymer strip SPP waveguide with PbS quantum dots. The result is a 27% increase of the propagation length at telecommunication wavelengths, corresponding to a 160 $cm^{-1}$ optical gain coefficient [263]. Bolger *et al.* presented amplified spontaneous emission SPs by using a 100-nm-thick Au film coated with 1 μm of PMMA doped with PbS quantum dots. They designed a grating in the metal film and used it to outcouple SPPs at wavelengths near the QD emission. Significant gain reduction may occur because of amplified spontaneous emission SPs, and a 30% increase of SPP propagation length is estimated due to stimulated emission [264].

# 6. Field Enhancement Effects of Surface Plasmons by Use of Nanostructures

## 6.1. Localized Near-field Enhancement Effects in Metal Nanostructures

Near-field intensity near the metal nanostructure is highly enhanced owing to the localized SPP resonance along the interface between metals and dielectric materials, and the enhancement factor strongly depends on the shape and the size of the metal nanostructures. The metal nanostructures such as nanorods, nanotips, and nanogaps exhibit localized near-field enhancement effects. It is noted that the free charge carriers are separated under the influence of the external electric field associated with the propagating light. In this case, the separation of the free charge carriers creates an additional field that oscillates with the same frequency as the external field. As a result, an extremely enhanced light field is achieved close to the metal structure [14]. The near-field enhancement effects of metal nanostructures are of great interest for some applications such as surface enhanced Raman spectroscopy (SERS) [265–267], nonlinear optics [268–271], and nanophotonics [13,176,272].

### *6.1a. Metal Nanorods*

Application of metal nanorods in SERS based on the electric field enhancement requires a weak damping of surface plasmon polaritons (SPPs) (e.g., a slow dephasing of the optical polarization associated with the electron oscillation) [273]. Sönnichsen *et al.* presented plasmon dephasing by use of light-scattering spectroscopy on individual Au nanorods [274]. The Au nanorods exhibit very high quality factors (ratio of resonance energy $E_{\mathrm{res}}$ to linewidth $\Gamma$), while the Au nanospheres have relatively low field enhancement factors. In this case a drastic reduction of the plasmon dephasing rate in nanorods is demonstrated as compared with that for small nanospheres owing to a suppression of interband damping. This result indicates large local field enhancement factors and relatively high light-scattering efficiencies, making metal nanorods extremely interesting for SERS applications.

In addition, Dreaden *et al.* investigated the electric field enhancement of nonradiative exciton relaxation rates in high-aspect-ratio CdTe–Au core–shell nanorod arrays [275]. They calculated the electric field distribution at the wavelength of 770 nm for the CdTe–Au core–shell nanorods of varying aspect ratio, shell thickness, and tilt angle. When the dipolar component of the plasmon field of the Au shell is polarized parallel to the ground-state absorption transition moment of the CdTe core, the enhanced ground-state absorption and exciton–exciton annihilation (Auger recombination) give rise to the second-order nonradiative decay kinetics and the slow nonradiative decay rates. However, when contributions of the plasmon field are nondipolar or perpendicular to the ground-state absorption transition moment of the CdTe core, excited-state absorption processes are believed to dominate, and increasingly rapid first-order decay kinetics are observed. These processes are strongly dependent on the thickness of the Au shell and the

orientation of the nanorod array, but are insensitive to the aspect ratio of the nanorods.

Furthermore, Okamoto and Imura proposed localized electric-field enhancements in metal nanorods by near-field two-photon excitation probability images [276]. A spatially oscillating feature is observed for an excitation wavelength of 780 nm, which is attributed to the longitudinal plasmon mode. A high two-photon excitation probability is found in both ends of the nanorod, which corresponds to the enhanced electric field induced by the "lightning rod effect" at the end edges of the rod. The lightning rod effect may be regarded as an electric-field enhancement arising from polarization due to noneigenmode plasmons. Thus, this methodology provides valuable information for the characteristics of enhanced optical fields and applications in nanophotonics.

### 6.1b. Metal Nanotips

Metal nanotips have enormous near-field enhancement effects due to the strong concentration of free charge carriers at the sharp edges [14]. Many reports have focused on theoretical calculation of the near-field enhancement of the metal nanotips. Bouhelier *et al.* investigated the intensity distribution of the electric fields in an Au coated glass tip; they found that a thin layer of Au film provided stronger field enhancement [277]. However, the penetration through a thin layer is also stronger and leads to a larger far-field background. In contrast, for a thick coating the penetration is much weaker and leads to less far-field background. Moreover, near the cutoff radius, the electric field of the exciting mode couples to SPPs that propagate on the outside surface of the Au layer; the excited SPPs propagate toward the tip end. The symmetry of the radial excitation beam ensures that a strong field enhancement is created at the metal tip. It is shown that radially polarized modes can propagate in optical fibers and that they can be used for subsequent excitation of a tapered near-field geometry.

Behr and Raschke investigated near-field enhancement near the apex of scanning probe tips by a quasi-static approximation [278]. The optical tip–sample coupling sensitively depends on both the tip and the sample material. Of four free-standing tips (e.g., a hyperboloid with apex radius of 10 nm and cone semiangle of 20°, and an incident field with wavelength of 630 nm) of different materials, Au, W, Si, and glass, the Au nanotip has the strongest field enhancement of $E/E_0 = 50$ at the apex as a result of its high conductivity. In contrast, W as a common scanning probe tip material exhibits a comparably moderate field enhancement of 12 because it is a poor conductor in the optical frequency range, and the field enhancement value for W is only slightly above that for Si. This is because both W and Si have strong damping due to absorptive loss. At the same time, a transparent dielectric for glass with a small refraction index has the weakest field enhancement. On the other hand, the tip–sample interaction becomes significant at distances (e.g., 20 nm) below about twice the tip radius; in this case the near-field interaction becomes effective, and the field enhancement then rises superexponentially for distances below the apex radius of 10 nm [278].

Using a full three-dimensional finite difference time domain (FDTD) method, Roth *et al.* also calculated the spatial field distribution of an asymmetrically illuminated nanoscopic Au tip suspended over a planar Au substrate [279]. The tip plasmon response has a significant (up to 70 times) local field enhancement between the tip and substrate, and the enhancement is extremely sensitive to the tip–sample distance. This investigation indicates that the Au nanotip can be applied to tip-enhanced Raman-scattering.

Tanaka *et al.* demonstrated a strongly localized and strongly enhanced optical near field at a metal probe tip with the near-field intensity of $10^3$ times larger than the incident intensity [280]. It is found that the following factors can increase the near-field enhancement on probe tips: using an I-shaped aperture, guidance of SPPs along the gap in a pyramidal structure, adopting a metal with a large value for the real part and a small value for the imaginary part of the absolute value of the relative permittivity, and using a sharp probe tip. Metal probe nanotips have a wide range of applications in near-field optics and nanophotonics.

### 6.1c. Metal Nanogaps

Very strong field enhancement often occurs in nanogaps between plasmonically active nanostructures [281,282]. Ward *et al.* directly measured the field enhancement in subnanometer gaps between Au electrodes based on nonlinear electron tunneling [283]. It is found that the enhancement of the electric field in the tunneling region is dependent on gap size. For gap distances of 1.4, 0.92, and 0.44 Å derived from tunneling measurements, the inferred electromagnetic fields and field enhancement factors are $2.1 \times 10^8$ V m$^{-1}$ and 718, $3.6 \times 10^8$ V m$^{-1}$ and 1230, $5.7 \times 10^8$ V m$^{-1}$ and 1940 (Fig. 55), which indicates that the enhancement factor increases with a reduced gap size of the Au electrodes.

On the other hand, theoretical investigations of the field enhancement effects in metal nanogaps have also been presented. Using a Green's-function surface integral equation method, Jung *et al.* investigated the field enhancement of metal nanostrip gaps [284]. It was shown that the scattering resonance occurs for small nanogaps because of the constructive interference of counterpropagating gap SPPs, and it is found that the resonance wavelength can be tuned over a wide range of 690 to 1110 nm by changing the gap size from 80 to 5 nm. Moreover, the maximum field enhancement with respect to the incident field in the nanogap of 10 nm is close to 40 for an insulator thickness of 10 nm, while for an optimized angle of incidence the enhancement value can be close to 50 along the line passing through the gap center.

Gramotnev *et al.* used the technique of adiabatic and nonadiabatic approximations to investigate the electric field enhancement during nanofocusing of SPPs in tapered metal nanogaps [285]. It is demonstrated that the strong local electric field enhancement depends on the dissipation in the metal and taper angle and that for an optimal taper angle of 14° a maximal field enhancement in the tapered nanogaps between fixed entry and exit widths appears. Furthermore, compared with other structures, such as sharp tapered rods and tapered

Figure 55

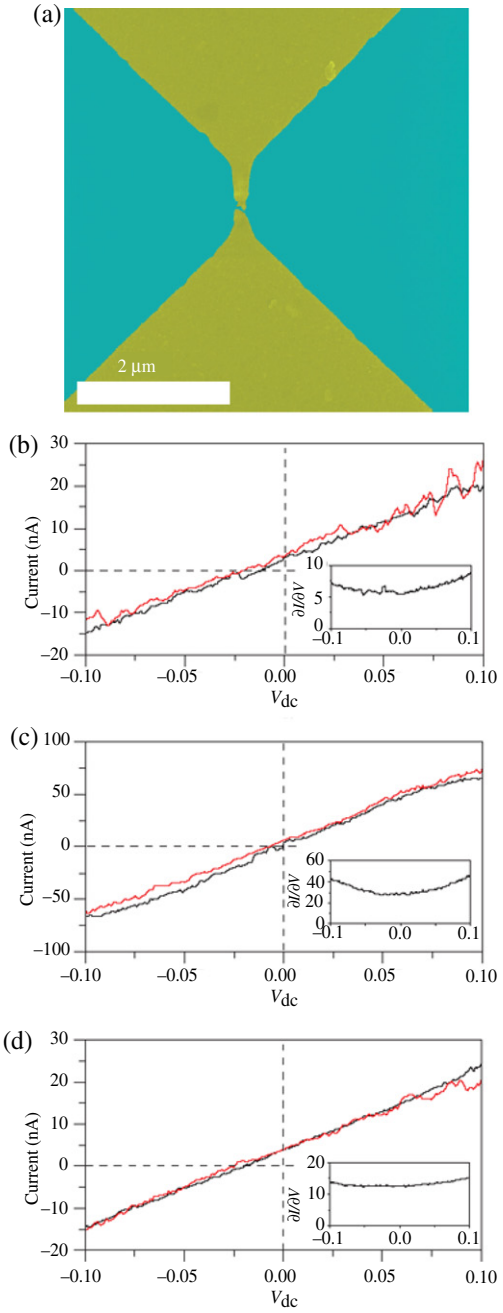


(a) Larger scanning electron microscopy (SEM) view of electrodes and nanogap. (a)–(c) Photocurrent (red, $I_{photo}$) and (1/4) $V_{ac}^2 \partial^2 I/\partial V^2$ (black) as a function of $V_{dc}$ for three different samples. The shared shapes of these curves demonstrate that the photocurrent arises from the rectification process. The different conductances and nonlinearities presumably result from microscopic details of the electrode surfaces and geometry. Insets, conductance in units of μA/V for each device. The gap distances derived from tunneling measurements are 1.4, 0.44, and 0.92 Å. Inferred $V_{opt}$ values are 30, 25, and 33 mV, with uncertainties of 10%. Inferred electromagnetic fields and field enhancements are (a) $2.1 \times 10^8$ V/m and 718, (b) $5.7 \times 10^8$ V/m and 1940, and (c) $3.6 \times 108$ V/m and 1230. Reproduced with permission from Figs. 1c and 2, Ref. [283]. © 2010 NPG.

wedges, tapered gaps are shown to be the best option for achieving maximal field enhancement. This feature of nanofocusing in nanogaps makes it especially promising for the development of applications in near-field microscopy, nonlinear plasmonics, and effective delivery of electromagnetic energy to the nanoscale.

Recently, Kim and Cheng numerically presented the optical field enhancement of gap SPPs based on a circular slit at a metal–dielectric interface [286]. It is found that the combination of the gap SPPs and the propagating SPP launched by the circular plasmonic lens can achieve extremely strong field confinement, and the SERS enhancement factor can be up to $10^{15}$ at the tip of the triangular nanostructures, the nanostructures can be expected to be applied to high sensitive molecule detection by the SERS effect.

## 6.2. Transmission Enhancement Effects by Use of Nanostructures and Nanostructure Arrays

### *6.2a. Nanoholes and Nanohole Arrays*

Tiny holes with sizes smaller than the wavelength of incident light in an opaque metal film exhibit unique optical properties such as strongly enhanced transmission of light through the holes; these intriguing effects are known to be due to the interaction of the light with electronic resonances in metal surfaces [287]. One interesting feature is that metal nanoholes on the output surface can act as a new point source for the light. The enhanced transmission phenomenon presents new opportunities in applications ranging from subwavelength optics, nanophotonics, optoelectronics, and sensing to biophysics.

Considering a single hole milled in a free-standing Ag film. It is assumed that the film is infinitely thin and that the metal is a perfect conductor. The transmission efficiency of light at normal incidence can be approximately given by [288]

$$T = \frac{64}{27\pi^2}(kr)^4, \tag{8}$$

where $k = 2\pi/\lambda$ and $r$ and $\lambda$ are the hole radius and the wavelength of the incident light, respectively. One can see that $T$ scales as $(r/\lambda)^4$, which indicates that the transmission of light is very weak for a very small hole compared with the wavelength of the incident light. The transmission efficiency is attenuated exponentially in terms of the real depth of the hole, and the small hole transmits almost no light [289].

In 1998, Ebbesen and co-workers found that subwavelength hole arrays in a noble metal film with sizes smaller than the wavelength of incident light exhibit extraordinary optical transmission [290,291], and the transmission is much higher than Bethe's prediction from classic diffraction theory. They explored the zero-order transmission spectrum for a Ag hole array fabricated by a focused ion beam with a hole diameter of 150 nm and hole spacing of 900 nm. The absorption peaks become gradually stronger at longer wavelengths, and the maximum transmission intensity occurs at 1370 nm (nearly ten times the hole

diameter). Furthermore, the absolute transmission efficiency is larger than 2 at 1370 nm, calculated by dividing the fraction of light transmitted by the fraction of surface area occupied by the holes; that is, more than twice as much light is transmitted as impinges directly on the holes. However, according to Bethe's classic diffraction theory, the transmission efficiency of a hole of 150 nm diameter is only of the order of $10^{-3}$.

Gordon *et al.* [292] and Elliott *et al.* [293] observed strong polarization dependence in the optical enhanced transmission through elliptical nanohole arrays in metal films, respectively. The polarization characteristics can be controlled by the ellipticity and orientation of the nanoholes. Recently, Melentiev *et al.* demonstrated an approach to control the transmission of light through a single metal nanohole embedded in one-dimensional photonic crystal microcavity. They experimentally achieved 28-fold enhanced transmission of light through a single nanohole in Au film, which indicated that the approach makes it possible to increase the transmission of light through a single nanohole considerably [294]. Yang *et al.* reported enhanced optical transmission in anisotropic three-dimensional nanohole arrays based on SPP excitations. They demonstrated that the SPPs on the hole arrays lead to optical transmission an order of magnitude higher than two-dimensional planar hole arrays, and the optical transmission is at different wavelengths and with different dispersion properties that can be tuned by control of the nanohole shape [295]; therefore the discovery of broadband-tunable localized surface plasmon (LSP) resonance on the same plasmonic substrate provides new opportunities in optoelectronics and optical biosensing.

Investigation of the mechanism and origin of the extraordinary optical transmission has received growing interest [289–291,296–299], and the enhanced transmission of light in optically thick noble metal films occurs both for single holes and hole arrays [2,287,300–305], which originates mainly from the coupling of SPPs to the periodical hole arrays.

Gao, Henzie, and Odom provided direct evidence for the role of SPPs in the enhanced optical transmission of light through metal nanohole arrays [298]. Near-field optical images directly confirm the presence of SPPs on Au nanohole arrays with interhole spacings larger than the SPP wavelength, and far-field spectroscopy reveals a SPP band that contributes a factor $>8$ to the transmission enhancement. Furthermore, the enhancement of transmission is due to tunneling through SPs formed on each metal–dielectric interface [296], and different regimes of tunneling (resonant through a "SP molecule," or sequential through two isolated SPs) are found depending on the geometrical parameters. In addition, the surface modes on the input side couple evanescently to the exit side before being re-emitted into freely propagating light. Moreover, the role of the surface modes is to enhance the field amplitudes above the holes; the enhancement then compensates for the exponential attenuation of the evanescent field in the depth of the nonpropagating hole. As a result, the transmission spectra of such structures are characterized by a set of peaks corresponding to the appearance of modes together with their interference and scattering in and out of the plane [297]. The transmission peak positions $\lambda_{max}$ at normal incidence are given by using the SPP dispersion relation described above due to

the activation of SPPs:

$$\lambda_{\max} = \frac{P}{\sqrt{(i^2 + j^2)}} \sqrt{\frac{\varepsilon_d \varepsilon_m}{\varepsilon_d + \varepsilon_m}}, \tag{9}$$

where $P$ is the hole spacing and $i$ and $j$ are the scattering orders of the hole array. In this case, the SPs generated in the array will propagate along a defined symmetry axis with their own polarization depending on the $(i, j)$ number of the mode. Both surfaces on either side of the holes can sustain SP modes, offset from each other by the difference in $\varepsilon_d$ of the material in immediate contact with the metal surface (typically glass and air), as predicted by Eq. (9).

### 6.2b. Nanoslits

Similar to the metal nanoholes, metal nanoslits can also support enhanced optical transmission. García-Vidal *et al.* theoretically and experimentally explored optical transmission properties of a single nanoslit flanked by a finite array of grooves made on a thick Ag film [306], where a single nanoslit with a width of 40 nm surrounded by ±5 grooves with a length of 10 μm (Figs. 56(a) and 56(b)), was fabricated by a focused-ion-beam technique. A broad maximum transmission around 725 nm is observed (Fig. 56(c)). This maximum, with an enhancement factor of about 6, is due to transmission through the nanoslit waveguide mode. When the nanoslit for different periods from 500 to 800 nm is surrounded by grooves with a nominal depth of 40 nm, the transmission peak shifts to longer wavelengths with increased period; the peak is strongest for the period of 650 nm. As a result, the peak appears at the wavelength coinciding with the nanoslit waveguide mode position. In this case, the optimal groove depth is 40 nm for transmission enhancement. Moreover, García-Vidal *et al.* proposed three main mechanisms that could enhance optical transmission: groove cavity mode excitation (controlled by the depth of the grooves), in-phase groove re-emission (controlled by the period of the groove array), and nanoslit waveguide mode (controlled by the thickness of the metal film). A transmission enhancement of light by up to 2 orders of magnitude can be achieved by tuning these geometrical parameters when all three mechanisms coincide [306].

On the other hand, Lee and Park explored the coupling between SPPs and transmitted light in metal nanoslits, and the coupling strength can be quantitatively determined by introduction of a dressed surface plasmon polariton (DSP) with the simple approximate description of a leaky wave. The coupling constant is found to be the product of the geometric opening ratio, the aperture momentum, and the Fabry–Perot factor [173]. Moreover, they observed that the effective coupling could cause enhanced transmission with redshifted and blueshifted peaks of the DSP resonance wavelength on the air–metal and substrate–metal sides, respectively; this is because the two kinds of film side correspond to the positive (redshift) and the negative (blueshift) real part of the coupling constant. The DSP concept will play an important role as a basic building block for metal nanostructures.

Figure 56

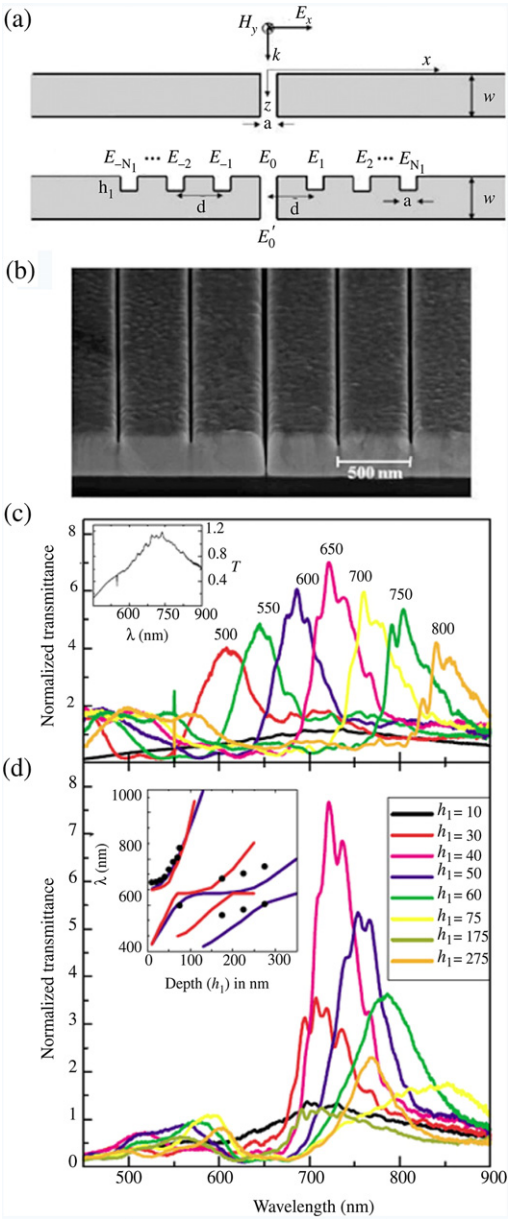


(a) Schematic of a single slit of width $a$ in a metallic film of thickness $w$, and single slit symmetrically surrounded in the input surface by $2N_I$ grooves of depth $h_1$. The separation between adjacent indentations is $d$, and all groove widths are $a$. (b) Electron micrograph image of one of the devices analyzed and then cross sectioned by focused-ion-beam milling. Nominal values are $a = 404$ nm, $w = 350$ nm, $h_1 = 100$ nm, and $d = 500$ nm. Collection of experimental $T(\lambda)$, for different structures formed by a central slit surrounded by $\pm 5$ grooves ($a = 40$ nm) on the input surface of a silver film with $w = 350$ nm. (c) $h_1 = 40$ nm, while the array period ($d$) is varied between 500 and 800 nm. The black curve corresponds to the single-slit case (also reproduced in the inset for clarity). (d) $d = 650$ nm, for different groove depths $h_1$. In the inset, the spectral locations of measured transmission peaks (black dots) are compared with the calculated positions of the surface electromagnetic resonances of silver reflection gratings with square (blue curve) or triangular (red curve) grooves. Reproduced with permission from Figs. 1 and 4, Ref. [306]. © 2003 APS.

Jiao, Wang and co-workers numerically investigated the role of SP in the transmission of the metallic grating with very narrow slits [307]. The Fabry–Perot phenomenon is observed in the SP resonant transmission, and the transmission properties are strongly dependent on the grating depth. In this case the nanoslit arrays can effectively transfer the light, and the transmission peak emerges when the grating depth satisfies the approximate resonant transmission equation.

In addition, Zhang and Wang proposed dual-wavelength transmitted light beaming enhanced by a metal nanoslit based on a guided-mode resonance theory [308]. It is found that the single nanoslit in an optically thick metal film flanked by dielectric gratings on both input and output surfaces can realize enhanced-transmission directional beaming of two wavelengths of light (442 and 633 nm) simultaneously. The proposed nanoslit structures will have potential applications in optical data storage (one beam for writing and the other for reading) [309].

Moreover, sensors for water quality control based on enhanced transmission through periodic metal nanoslits were realized by Karabchevsky *et al.* [310]. Two strong SP resonances were observed in a water environment, and the resonance was found to be highly sensitive to the changes of the analyte's refractive index.

Recently, Gan *et al.* directly observed UV extraordinary optical transmission through Al nanoslits in the far field and in the localized near field [311]. The optical transmission is significantly different between the light-emitting diode (LED) and the detector modes for the same plasmonic structures. The direct observations of the UV extraordinary transmission phenomena will contribute to important applications in the development of novel plasmonic structures for active UV active device, e.g., UV LEDs and UV detectors.

## 7. Focusing of Surface Plasmon Polaritons by Metal Nanostructures

A significant challenge in light manipulation is how to concentrate light from the large scale into the nanoscale. Excitation of surface plasmon polaritons (SPPs) can achieve focusing of light into the nanoscale beyond the diffraction limit, which requires slowing down the optical wave and shrinking the wavelength during the light propagation [312]. In this case, nanofocusing of SPPs can occur when optical energy is compressed and concentrated into the nanoscale. The nanofocusing of SPPs can be achieved by using metal nanostructures with various configurations such as nanoholes, nanoslits, nanorods, nanotips, wedges, grooves, nanoring, nanocorrals, and nanoparticle chains.

### 7.1. Nanoholes

A tiny hole smaller than the incidence wavelength diffracts light in all directions uniformly. The diffraction phenomenon is a fundamental limit for manipulating light at the subwavelength or nanometer scale. Lezec *et al.* overcame this limit with the design of periodical grooves on the

exit side of a cylindrical subwavelength hole in a metal film [313]. The transmitted light emerges from the hole with a small angular divergence, and the periodical grooves can act as an antenna to couple the incident light into SPPs [287]. As a result, the holes surrounded by the grooves give rise to much higher transmission and a more well-focused beam than single holes.

Yin *et al.* proposed constructive interference of SPPs launched by nanoholes arranged on a quarter-circle. The arranged holes can allow SPPs to be focused into an intense spot with a subwavelength width [314]. It is found that focusing of SPPs occurs for an incident polarization parallel to the symmetry axis, and the near-field intensity in the SPP focus spot reaches about 75% of the intensity measured directly above the holes (Fig. 57(c)). However, the focusing can be turned off for transverse polarization owing to the dipolar directionality of the single-hole SPP fields (Fig. 57(e)). Furthermore, it is demonstrated that the high SPP intensity in the focal spot can be launched and propagated on a 250 nm wide metal strip waveguide. Focusing SPPs by the hole arrangement may serve as an initial stage in planar nanophotonic circuits.

Recently, Lin, Roberts, and co-workers experimentally demonstrated two-dimensional focusing with planar plasmonic lenses formed by a cross-shaped nanohole (e.g., width of 40 nm and length of 100 to 300 nm) array in a thin metal film [315]. The cross-shaped nanohole arrays can realize three-dimensional beam manipulation in the optical Fresnel region, and simulations using the finite element method indicate that the amplitude and phase of the transmitted field can be tailored by varying the arm length of the hole near SP resonances at a specific wavelength. Thus the two-dimensional focusing planar structures represent an important step forward in the practical implementation of nanoplasmonic technology.

## 7.2. Nanoslits

Light can be coupled to SPPs on a thin metal film with nanoslits; moreover, the SPPs can be manipulated to generate focal spots by control of the SPP coupling behavior of the nanoslit patterns [316]. Recently, Tanemura *et al.* proposed focusing of multiple-wavelength SPPs into different positions in a two-dimensional plane based on a nonperiodic nanoslit array. The array of the rectangular nanoslits with sizes of 100 and 500 nm in the $x$ and $y$ directions can be designed a triplexer (a three-wavelength multiplexer) that focuses light at the three wavelengths of 820, 850, and 880 nm into different focal positions (e.g., the points $(x, y) = (0, -3\ \mu\text{m})$, (0, 0), and $(0, 3\ \mu\text{m})$, respectively) (Fig. 58) [317]. It is noted that such a nonperiodic nanoslit array is qualitatively different from conventional periodic grating devices, where the output position changes continuously with wavelength. Therefore the proposed structure will provide a simple method of building a multiple-wavelength nanometer-scale photodetector array for optical interconnects, spectral imaging, and sensing applications.

Chen *et al.* presented SPPs focused by a nanoslit-cavity strucuture, where the nanoslit at the bottom of an inverted triangular cavity is

Figure 57

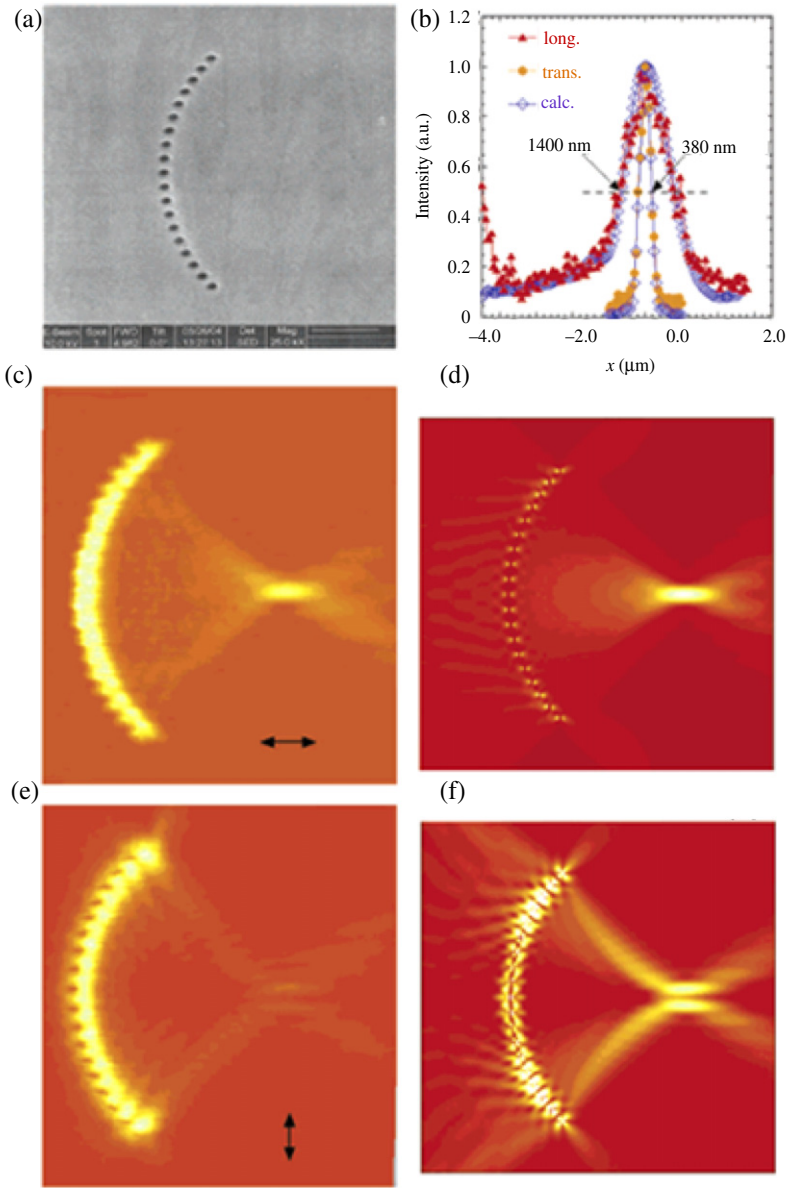


(a) Scanning electron microscopy (SEM) image of 50 nm Ag film containing nineteen 200 nm holes arranged in a quarter-circle with a 5 μm radius; scale bar, 2 μm. (b) Intensity profiles along and transverse to the focal spot together with fits based on the dipolar model. The values of the FWHM for both orientations are indicated. (c) scanning near-field optical microscope (SNOM) image taken at 532 nm incident wavelength and horizontal polarization. The focus of SPP intensity at the center of the circle is clearly seen. (d) Image of the SPP intensity calculated with the dipolar model. (e) SNOM image taken for vertical polarization. The intensity at the focal point is strongly reduced. (f) Calculated image. Note that the contrast is enhanced compared with that in frame (d) to reveal the fine features. Frames (c)–(e) have the same intensity scale. Reproduced with permission from Fig. 3, Ref. [314]. © 2005 ACS.

Figure 58

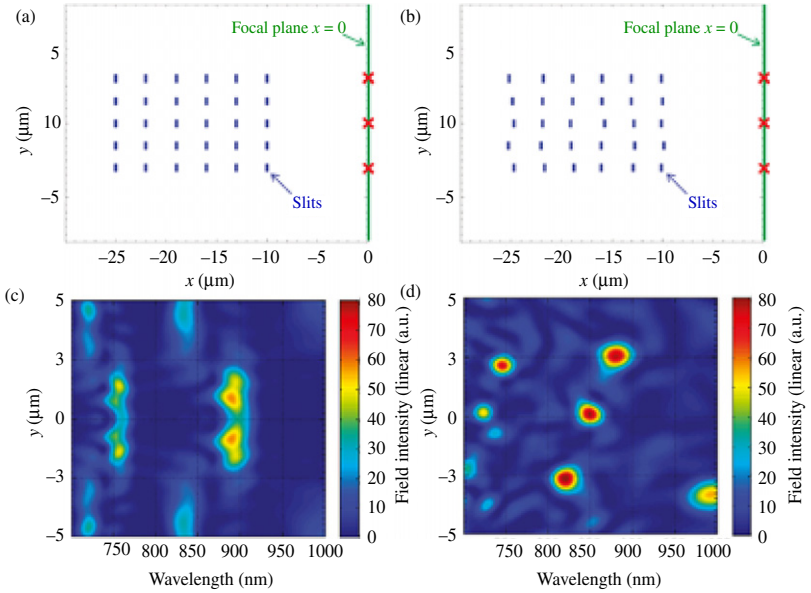


(a) Periodic slit pattern used as the initial guess, and (b) the nonperiodic pattern obtained after 40 iteration steps. The three red crosses represent the locations chosen as the desired focal positions for the wavelengths, 820 (bottom), 850 (middle), and 880 (top) nm. (c) Field intensity at $x = 0$ as a function of position $y$ (vertical axis) and wavelength (horizontal axis) for the periodic pattern shown in (a). (d) Same intensity map for the nonperiodic pattern shown in (b). As a result of the optimization process, three distinct spots emerge in (d), indicating that SPPs at wavelengths of 820, 850, and 880 nm are focused to points $(x, y) = (0, -3\ \mu\text{m})$, $(0, 0)$, and $(0, 3\ \mu\text{m})$, respectively. Reproduced with permission from Fig. 3, Ref. [317]. © 2011 ACS.

surrounded by periodic shallow grooves on both sides of the cavity. It was demonstrated that the shallow grooves can worked as secondary plasmonic nanoantennas to focus SPPs towards the nanoslit during excitation over a wide area [318]. As a result, focusing of SPPs based on the nanoslit-cavity structure can achieve a strong and localized field enhancement for surface enhanced Raman spectroscopy (SERS).

In addition, Chen and Cumming experimentally demonstrated plasmonic lenses based on nanoslits in an Al film made by electron beam lithography and dry etching. They designed two nanoslit lenses at 633 nm with focal lengths of 3 and 6 μm, and the FWHM beam widths (focus widths) at the focal point are 470 and 490 nm, respectively [319]. The nanoslit lenses exhibit potential for light control at the nanometer scale. Lerman *et al.* demonstrated focusing of SPPs by using a plasmonic lens illuminated with radially polarized light. In contrast to linear polarization illumination [320], radial polarization illumination can obtain a sharp focus at the optical axis because of the interference of the out-of-plane field component at the optical axis and the symmetric SPP contribution from all azimuthal angles along the annular slit, which indicates the advantage of radial polarization illumination for nanofocusing applications. Moreover, Yu and Zappe investigated the

influence of the lens size on the focusing performance of plasmonic lenses based on metal nanoslit arrays with variable widths [321]. It was found that the maximum intensity of the focal point becomes greatly enhanced with increasing lens size, while both the FWHM and the focus depth decrease, which indicates that a more concentrated focal point can be achieved for an increased lens size. On the other hand, the total phase difference of the nanoslits should be at least $2\pi$ to yield the a better focusing behavior.

Recently, Davoyan *et al.* proposed nonlinear nanofocusing of SPPs by tapered metal–dielectric–metal slit waveguides [322]. It was shown that the nanofocusing of SPPs can also allow light to be manipulated at the nanoscale. An appropriate choice of the taper angle can achieve an effective compensation of attenuation with the formation of spatial plasmon solitons in order to enhance nonlinear effects.

## 7.3. Nanorods

Metal nanorods can be operated as nanoantennas to confine light into subwavelength or nanometer scales. Becker *et al.* proposed focusing of SPPs by Ag-coated Au nanorods [323], and the focusing can reduce the ensemble SPP linewidth by about 30% through changing the relation between the connecting rod shape and surface plasmon (SP) resonance wavelength. They found that the focusing of SPPs was a new feature of bimetallic core–shell structures. Additionally, the Ag-coated Au nanorods are among the best plasmonic structures known, with up to 50% longer plasmon lifetime than Au nanorods at the same resonance energy, which can make them ideal candidates for nonlinear enhancement, sensing, and light-guiding applications.

On the other hand, Maksymov and Miroshnichenko theoretically investigated active control over nanofocusing of SPPs in a Au nanorod antenna coupled to a photonic crystal nanocavity [324], where the nanocavity is formed by omitting three holes along the Γ–K direction of a triangular lattice (constant of 250 nm and hole radius of 75 nm) of air holes in a 100 nm thick $Si_3N_4$ dielectric membrane; a 900 nm long Au nanorod antenna with a diameter of 135 nm and a 100 nm long oval tip is placed on the backbone of the nanocavity. The full-vectorial three-dimensional simulation demonstrates that light nanofocusing at the tip of the Au nanoantenna can be controlled by altering cavity-mode excitation conditions. In this case the control mechanism for light nanofocusing in a nanorod antenna has a potential application in subwavelength light sources.

Recently, Vogel and Gramotnev theoretically investigated nanofocusing of SPPs in tapered metal nanorods with convex and concave perturbations of the conical shape under the adiabatic approximation conditions [325]. It is demonstrated that the nanorod with a tapered convex shape is more efficient in achieving larger local field enhancements at the tip than a nanorod with a concave shape. Furthermore, the convex tapered nanorod exhibits stronger local field enhancement at the tip of the tapered rod. However, for the concave tapered nanorod, the maximum of the local field enhancement is typically achieved not at the tip but rather at some distance from it on the surface of the rod.

In addition, it is predicted that the strongest local field enhancement is up to about 1600 times for the nanofocusing structure in tapered metal rods [326]. Therefore, these results will be important for optimization and practical fabrication of nanofocusing plasmonic structures and their applications in near-field microscopy and nanophotonic devices.

## 7.4. Nanotips

Tapered plasmonic waveguides demonstrate highly efficient concentration of light energy into nanoscale regions because of the very strong local field enhancement near their tips. In this case, focusing of SPPs by tapered nanotips can be expected to be applied to highly efficient tip-enhanced Raman scattering [327,328]. Stockman theoretically predicted that optical radiation energy could be concentrated in three dimensions at the nanoscale by use of the nanotip of a tapered metal nanowire SPP waveguide, which indicates that the far-field radiation can be efficiently coupled to the near-field zone. As a result, the nanofocusing causes a local field increase by 3 orders of magnitude in intensity and 4 orders in energy density [329].

Furthermore, Verhagen *et al.* experimentally achieved focusing of SPPs by laterally tapered Au waveguides with a tip of 65 nm in diameter [330]. The nanofocusing results from a guided SPP mode with an asymmetric electric field distribution across the tapered waveguide. Field enhancements and focusing efficiency can be optimized by excitation frequency and tip sharpness, which are expected to allow optimization of the possibilities by changing the film thickness, tapering angle, excitation frequency and tip sharpness.

Recently, Lindquist *et al.* achieved three-dimensional nanofocusing of SPPs with patterned Au and Ag pyramids obtained by a template stripping method [331], and the periodic gratings on the four faces of the pyramids convert the linearly polarized light into SPs and subsequently converge to a nanoscale spot at the tip. Three-dimensional finite difference time domain (FDTD) simulations confirm that incident light with a wavelength of 710 nm is focused into a 36 nm $\times$ 36 nm $\times$ 14 nm volume ($5 \times 10^{-5}$ wavelength$^3$) at the 10 nm nanotip.

Besides tapered metal waveguides, hybrid plasmonic waveguides can also focus SPPs at a nanotip. Fang *et al.* proposed that a laterally tapered planar dielectric SPP structure on the top surface of the metal film could achieve nanofocusing of SPPs [332]. Moreover, they experimentally realized nanofocusing by illuminating tapered CdS nanoribbons deposited on a 50 nm thick Ag surface. The near-field optical image indicates that the SPP wave slows down when it propagates toward the tip end and is finally emitted from the taper end, which can be used as a potential light nanosource in future optical circuits.

Recently, Desiatov *et al.* experimentally demonstrated on-chip integration in a silicon platform between a photonic waveguide and a plasmonic nanotip to obtain field enhancement and nanofocusing at the apex of the tip [333]. Both the photonic waveguide and the plasmonic nanofocusing device are made of silicon surrounded by a metallic cladding from both

Figure 59

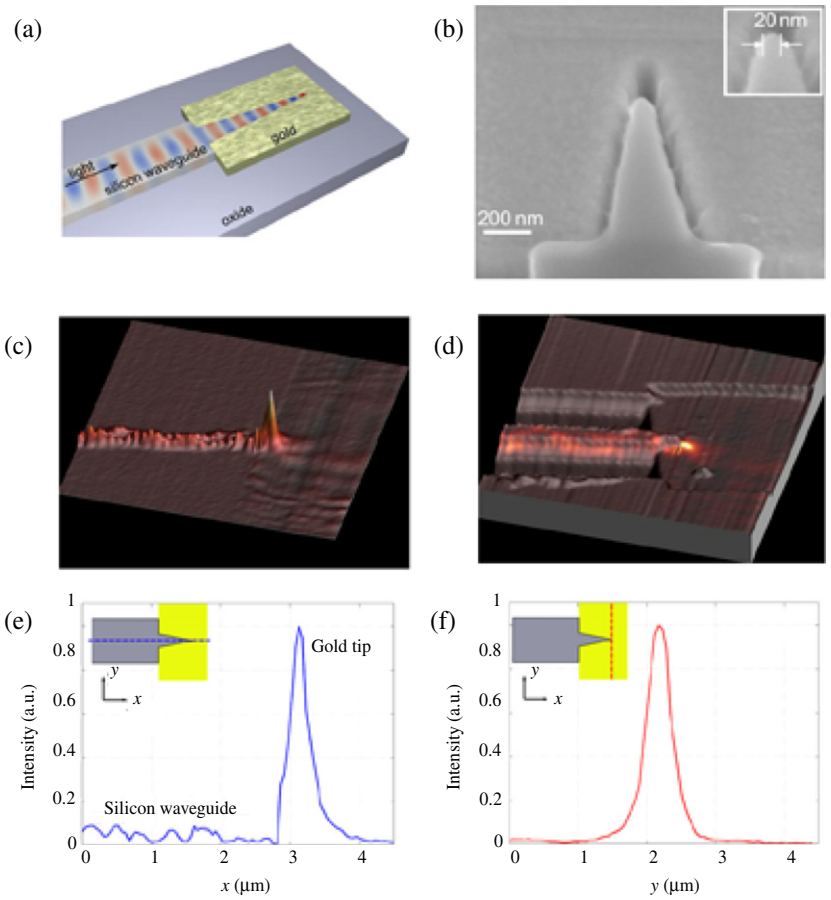


(a) Schematic representation of nanotip focusing device. (b) Magnified SEM image showing the apex of the silicon tip surrounded by metal. Scanning near-field optical microscope (SNOM) measurement results. (c) 3D representation of the near-field signal. (d) 3D collage of the topography and the near-field intensity signal. Profiles of SNOM measurement results. (e) Longitudinal profile showing nanofocusing in the longitudinal direction. The region of low intensity corresponds to the signal in the silicon waveguide, and the peak intensity corresponds to the region near the apex of gold nanotip. (f) Transverse profile showing nanofocusing in the transverse direction. Reproduced with permission from Figs. 1a, 5b, 6 and 7, Ref. [333]. © 2011 OSA.

sides (Figs. 59(a) and 59(b)). The intensity of the electromagnetic field at the apex of the tip was observed to be 10 times larger than the average intensity in the silicon waveguide (Figs. 59(c)–59(f)). They found an order of magnitude enhancement of the intensity at the tip's apex, and the focusing spot size is estimated to be about 50 nm. Therefore the demonstrated device may be used as a building block for "lab on a chip" systems and for enhancing light–matter interactions at the apex of the tip.

On the other hand, He *et al.* numerically presented a compact structure to concentrate light based on the vertical side coupling between a

silicon-on-insulator waveguide and an Au nanostrip [334]. In this study 50% of the optical power launched into the silicon wire can be coupled to SPPs on the Au strip within a coupling distance of 1.2 μm at a 1.55 μm wavelength. As a result, the SPPs are focused to a deep subwavelength focal region with over 50 times enhancement in electric field intensity with a volume of around 20 nm × 20 nm × 7 nm. A much greater enhancement of the focused electric field may be achieved by eliminating reflection off the taper tip.

## 7.5. Wedges

One of the important metal nanostructures supporting SPP nanofocusing is metal wedges because of the concentration of the optical energy into their tip regions on the nanoscale [312]. Gramotnev and co-workers systemically investigated the nanofocusing of SPPs based on sharp metal wedges by using a geometrical optics approach and approximation of continuous electrodynamics [335–337]. It is demonstrated that both a quasi-symmetric (with respect to the charge distribution across the wedge) [335] and an antisymmetric (with respect to the magnetic field) [336] SPP adiabatically slows down and asymptotically stops at the wedge tip with both its phase and group velocities reduced to zero; the adiabatic regime of the nanofocusing of SPPs in the metal wedge may occur if the wedge angle is smaller than the critical angle, which is determined by the dielectric permittivities of the metal wedge and the surrounding dielectric medium. The local field enhancement near the wedge tip is dependent on the structural parameters, dissipation in the metal, and the incidence angle.

Moreover, Moreno *et al.* theoretically explored focusing of electromagnetic modes guided by metal wedges at telecommunication wavelengths (e.g., 1.5 μm) [338]. It was demonstrated that focusing of SPPs can be realized by gradual modification of the wedge geometry along the SPP mode propagation direction, and the SPP propagating mode along a flat surface can be coupled to a tightly confined wedge SP mode by using the gradual deformation of the metal surface.

Yanai and Levy proposed a plasmonic lens with circular wedge configuration for focusing of short-range SPPs and long-range SPPs (LRSPs) [339]. It was found that the long-range and the short-range modes are very different in their focusing properties. The short-range SPP provides a very high-numerical-aperture lens with fast decaying energy and the optical energy is tightly bound to the metal surface with a spot size as small as 125.5 nm for a 600 nm wavelength. In contrast, the LRSP exhibits a slowly decaying field with a larger spot size of 162 nm because of its large depth of focus, which has potential applications in microscopy and sensing.

Recently, Verhagen *et al.* proposed nanofocusing of SPPs in a dielectric wedge on a metal substrate [340]. Full-field simulations indicate that the field enhancement is up to a factor of 180 because of the gradual transformation of the SPP mode propagating on the Ag surface covered with the thin Si film. As a result, the SPPs slow down and become fully confined within the Si film at the critical film thickness of 20 nm. In this case, the nanofocusing is close to the SPP frequency at the Ag/Si

interface. These results demonstrate an alternative route to achieve nanofocusing without the need to fabricate very small metal features.

## 7.6. Grooves

Subwavelength metal grooves as gap SPP waveguides can support channel plasmon polariton (CPP) guiding modes [341]. Bozhevolnyi, Ebbesen and co-workers designed various subwavelength waveguide structures based on metal V grooves [342,343]. These V-groove waveguide structures demonstrate low-loss (propagation length of 100 μm) and well-confined (mode width of 1.1 μm) channel SPP guiding modes, and strong confinement and a sufficiently low propagation loss can be achieved simultaneously. Recently, they proposed radiation nanofocusing with the CPP propagating along subwavelength metal V grooves that were tapered synchronously in depth and in width, and V grooves with a 150 μm length, depths of 1.1–1.3 μm, and angles of 28° were fabricated in a 1.8 μm thick Au layer by the focused ion beam milling method [344,345]. The idea of radiation nanofocusing is based on a gradual decrease of the waveguide cross section and requirements of the mode size along with the waveguide cross section. SNOM measurements demonstrated efficient CPP nanofocusing at telecom wavelengths (e.g., 1480 nm) with an estimated field intensity enhancement of up to 90 [344]. The resonant field enhancement inside the V grooves results from the interference of counterpropagating gap SPP modes between the groove bottom and opening [346]. It is predicted that the intensity of electric field enhancements could exceed 1200 for realistic groove tapers cut into Au at telecom wavelengths [347]. Moreover, a multichannel configuration for delivering nanofocused and enhanced CPP fields to several different spatial locations can be achieved by use of consecutive Y splitters (Fig. 60). Radiation nanofocusing based on the CPP of V grooves is rather versatile and indispensable for future applications in nanophotonic circuits.

Similarly, Choi *et al.* experimentally demonstrated the nanofocusing of SPPs in a tapered Au V groove [348]. The V groove consists of two distinct regions in its cross section: one is a wide upper region 330 μm in depth with groove angle of 70.6°; the other is a narrow lower region 950 nm in depth with groove angle of 17°. It is observed that the enhancement of the square of the electric field amplitude $|E|^2$ is up to 10 with a power efficiency of almost 50% when the gap of the groove decreases from 700 to 45 nm (e.g., $\lambda/40$). Moreover, the field enhancement can be remarkably improved (e.g., the enhancement value of 421) when the output width is decreased (e.g., to 2 nm). The SPP nanofocusing exhibits advantageous tools for nanophotonic circuits and nonlinear optical sensors.

On the other hand, theoretical investigation on nanofocusing of SPPs based on sharp V grooves has been reported widely. Gramotnev demonstrated the efficient adiabatic nanofocusing of SPPs by a sharp metal V groove via a geometrical optics approach [349]. It is found that both the phase and group velocities of an incident symmetric plasmon decreased to zero at the groove tip, and the plasmon adiabatically slows down, eventually dissipating in the metal, and the amplitude of the

Figure 60

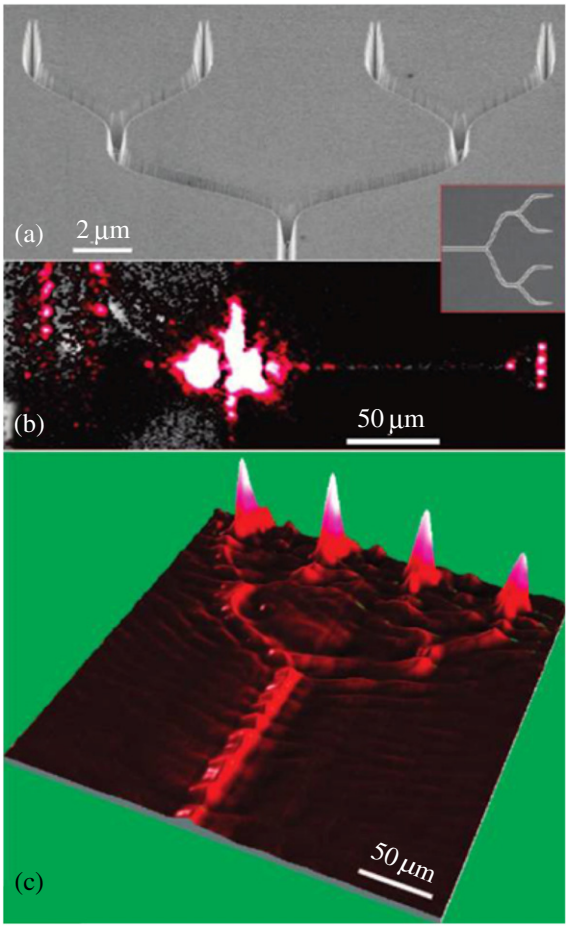


Plasmonic candlestick. (a) SEM image of a multichannel configuration for delivering nanofocused and enhanced radiation to four spatial locations via consecutive 5 μm long Y splitters terminated with 2 μm long tapers (see the inset with an overview SEM image). (b) Microscope image of a coupling arrangement superimposed on the far-field image taken at the excitation wavelength $\lambda = 1500$ nm with an infrared camera, showing the track of CPP propagation and four bright spots at the tapers. (c) Near-field optical SNOM image ($\lambda = 1500$ nm) demonstrating significant signal enhancements realized at the four groove tapers, with signal levels being similar and greatly exceeding even the signal level at the input channel. Reproduced with permission from Fig. 5, Ref. [344]. © 2009 ACS.

plasmon strongly increases near the groove tip. It is also shown that a symmetric gap can effectively support channel plasmon polaritions (CPP) modes along the tip of a metal V-groove.

Moreover, Pile and Gramotnev explored adiabatic and nonadiabatic nanofocusing of SPPs in tapered gap plasmon waveguides using the FDTD simulation [350], they found nanofocusing of SPPs into a gap of 1 nm width with more than 20 times increase in the plasmon energy density in a 1 μm long Ag–vacuum taper. The taper angle increase gives rise to decreasing dissipation and increasing local field enhancement

(efficiency of nanofocusing). However, the SPP reflection losses also increase, which decreases the local field enhancement and efficiency of nanofocusing. The competition of these opposing mechanisms may result in an optimal taper angle. The local electric field exhibits much stronger enhancement than the magnetic field. The maximal electric field enhancement can be achieved with an optimal taper angle of 14° [351]. The nanofocusing in the tapered gaps provides promising applications in near-field microscopy, nonlinear optics, and sensors.

Besides the V grooves for nanofocusing, metal grooves with other configurations can also be used for focusing SPPs [352–355]. Zhao *et al.* presented multiple focal spots of SPPs obtained by a SP-launching diffraction grating consisting of grooves located on concentric arcs. The grating structure can focus SPPs to multiple focal spots [352], and the number of focal spots formed from different diffraction directions is dependent on the ratio of the grating period to the SPP wavelength. The focusing of SPPs with multiple focal spots can accomplish the connection between the far field and multichannel near field for use in nanophotonic circuits.

Recently, Song *et al.* reported near-field nanofocusing through a plasmonic lens containing a Bragg reflector and a converging lens [353]. The lens consists of semitransparent annular grooves milled into a 75 nm thick Au film with different periods along the radial direction. By illuminating the lens with linearly polarized light, they observed two SPP focal spots with a 580 nm separation based on the interference from SPP waves. The two focal spots can be turned into a single spot with a 200 nm FWHM when the radius of every half-groove is increased by 320 nm. The plasmonic lens has potential applications in near-field imaging and sensing.

## 7.7. Rings and Corrals

Interference from excited SPP waves can efficiently achieve focusing of light at the subwavelength or nanometer scale. This case has been confirmed in the arranged nanoholes on a quarter-circle described in Subsection 7.1 [314] and the semitransparent annular grooves mentioned in Subsection 7.6 [353]. The interference intensity is dependent on the SPP reflection from the metal nanostructures, of which circular structures such as rings [314,356–358] and corrals [359,360] can demonstrate stronger reflection of the SPP waves.

Liu *et al.* presented focusing of SPPs by circular plasmonic lens structures milled into optically thick metal films [356]. The circular plasmonic lens consists of Ag slits with the thickness of 27 nm and width of 283 nm, and Ag circular slits with a ring diameter of 14 μm concentrate the SPP waves into the circle center because the waves interfere with one another to create a standing wave. The period (e.g., 245 nm) of the interference fringes is half that of the SPP wavelength (e.g., 490 nm) for 514 nm light excitation. Moreover, it is found that the intensity at the focal spots increases with increased the circle diameter. Plasmonic lenses with circular rings will be expected to be applied to nanophotonic devices and nanosources based on their efficient focusing of SPPs on subwavelength or nanometer scales.

Recently, Zhang *et al.* reported scattering light focusing of SPPs by a single Ag nanoring [358]. Two focal spots with distinct intensities are observed under oblique excitation owing to the interference of the far-field scattering light coupled to SPPs from the nanoring circumference. Moreover, the position of the focal spots can move about 140 nm away from the nanoring center when the incidence wavelength is increased from 476 to 633 nm. Additionally, the focusing intensity can be tuned by changing the polarization directions of the incidence light. It was demonstrated that the intensity is strongest at a polarization angle of 90° and weakest at 0°.

Very recently, Fang, Zhu, and co-workers presented focusing of SPPs by symmetry broken nanocorrals under linearly polarized illumina-

Figure 61

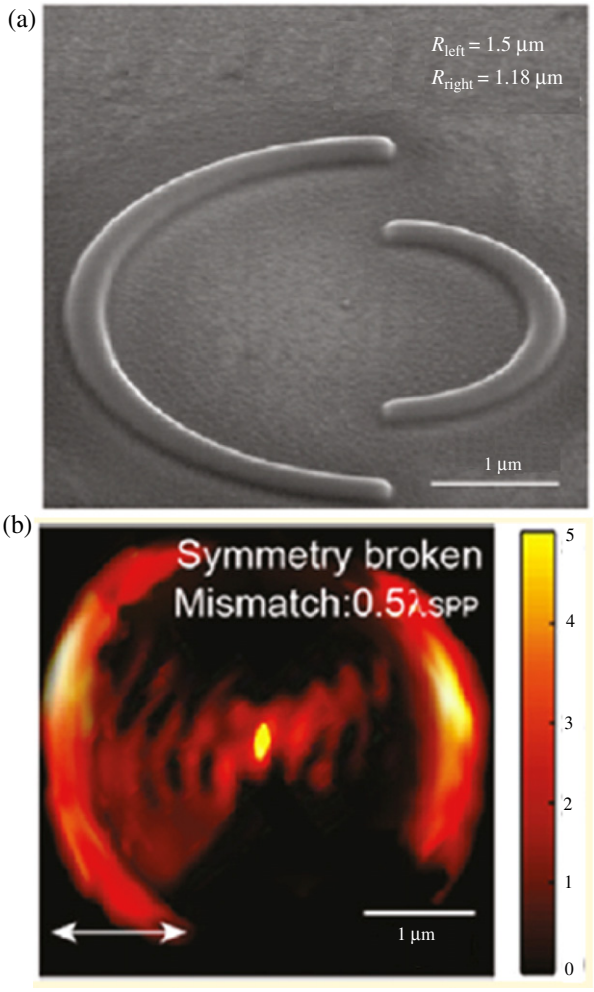


(a) SEM images of symmetry broken plasmonic corral fabricated on Au film. (b) Measured SPP $|E_z|^2$ distribution of the symmetry broken corral with radius mismatch of 0.5λ SPP for linearly polarized illumination taken for the SNOM tip at $h = 50$ nm above the sample surface. Reproduced with permission from Figs. 2d and 4b, Ref. [360]. © 2011 ACS.

tion [360]. The symmetry broken nanocorrals (e.g., 75 nm height and 200 nm width) consist of two Au semicorrals with different radii, $R_{left}$ of 1.5 μm and $R_{right}$ of 1.18 μm, fabricated by using a template stripping method [331,361] (Fig. 61(a)). Near-field optical measurements show that a single subwavelength focal spot with a size of 320 nm can be achieved based on SPP interference in the Au nanocorrals for the SPPs induced by the perpendicular electric field. Furthermore, the SPP interference can be effectively controlled by changing the phase shift of SPPs launched from the right and left semicorrals [360]. The phase shift is dependent on the amount of the symmetry breaking (e.g., radius mismatch). For a radius mismatch of 1.0 $\lambda_{SP}$ corresponding to a phase shift of $2\pi$, the interference pattern results in a dark spot in the center. However, when the mismatch increases to 1.5 $\lambda_{SP}$, the interference results in a stronger focal spot in the center; for a radius mismatch of 0.5 $\lambda_{SP}$, corresponding to the relative phase shift of $\pi$, a sharp focal spot with a field enhancement around 5 is induced by the constructive interference at the center (Fig. 61(b)). Focusing of SPPs by the symmetry broken nanocorrals provides a simple plasmonic lens under linearly polarized light excitation.

## 7.8. Nanoparticle Chains

Based on the focusing regime from metal rings and corrals, curved metal nanopartice chains can also focus SPPs. Radko *et al.* presented focusing of SPPs by parabolic chains of Au nanoparticles fabricated on thin Au films [362]. The parabolic nanoparticle chains consist of 50 nm high Au bumps having lateral cross sections in the form of rounded squares with widths from 160 to 250 nm for different structures. The distance between the bumps in the chains vary (from 250 to 320 nm). The SPP excitation is achieved by direct illumination of a 100 nm wide straight Au ridge with a tuneable (700–860 nm) laser beam polarized perpendicular to the ridge. The robust and efficient SPP focusing into submicrometer spots is attributed to the SPP reflection from the parabolic nanoparticle chains. Moreover, simulations based on the Green's tensor formalism indicate that elliptical corrections for parabolic chains could improve their focusing of slightly divergent SPP beams.

Evlyukhin *et al.* reported focusing of SPPs by curved chains of nanoparticles located on a metal surface [363]. The leakage radiation microscopy indicates that the curved nanoparticle chains with a circle segment can focus SPPs with the focal point located at the chain center, and the focusing efficiency is strongly dependent on the light spot size illuminating the nanoparticle chain. In this case, efficient SPP focusing can be achieved for relatively large spots, while the SPP focusing effect becomes less pronounced owing to the increase in the diffraction divergence of the excited SPP beam. In addition, the focusing regime of SPPs is strongly influenced by the distance between nanoparticles, so that the focusing and directing effects with optimal properties can be obtained when the distance is smaller than the SPP wavelength. Furthermore, they numerically investigated the focusing efficiency of SPPs by using curved chains of metal nanoparticles located on a metal surface based on the Green's function formalisms and the dipole approximation [364]. It is found that the efficiency of the SPP focusing is nonmonotonically dependent on the wavelength of the

external light beam exciting SPPs, and the focusing spot size decreases with decreased light wavelength and is approximately equal to half of the SPP wavelength. On the other hand, the position of the intensity maximum at the focal point on the wavelength scale is determined by the ohmic loss in metal and scattering cross sections of individual particles in the chains. These results will be useful for understanding various SPP scattering phenomena and for development of SPP-based nanophotonic devices.

## 8. Imaging of Surface Plasmon Polaritons through Metal Nanostructures

Although the optical microscope has been widely used for observing small objects, there is still a limitation of its spatial resolution. According to conventional diffraction theory, for a circular aperture illuminated with incoherent light, the minimum distance $\Delta x$ between two object points that a microscope can just resolve can be given by [1]

$$\Delta x = 0.61 \frac{\lambda}{n \sin \theta}, \tag{10}$$

where $\lambda$ is the wavelength of the incident light in vacuum, $n \sin \theta$ is the numerical aperture of the lens, $n$ is refractive index of the medium, and $\theta$ is the angle between the marginal light from the object and the lens axis. In this case, the image resolution can be generally improved by increasing the numerical aperture of the lens. For example, the numerical aperture can increase by filling the space between the lens and the sample surfaces with high-refractive-index materials such as immersion oil or solid materials [365]. However, this method improves the resolution within the limits of available high-refractive-index materials. On the other hand, the SPP dispersion curve exhibits the momentum ($\hbar k_{\mathrm{SPP}}$) if the SPP wave is larger than that of the light in free-space photon ($\hbar k$) for the same frequency [2]. As a result, SPPs as evanescent waves demonstrate the short wavelength and the characteristics of slow light; therefore a high spatial resolution of the object, imaging beyond the diffraction limit of light, can be obtained by excitation of SPPs with short wavelengths or slow light based on diffraction theory [14]. This section presents some metal nanostructures (e.g., superlens or tips, such as films or slab, nanorods and nanowires, gratings) to achieve subwavelength imaging or nanoimaging based on excitation of SPP waves.

### 8.1. Metal Films

Pendry predicated that an Ag slab of negative refractive index material could be used as a superlens to restore not only the phase of propagating waves but also the amplitude of evanescent states [366], which suggested that the superlens could achieve near-field imaging below the diffraction limit. Subsequently, Fang and Zhang numerically investigated the subwavelength imaging of a Ag metamaterial superlens [367]. Figure 62(a) depicts a typical two-dimensional imaging system based

Figure 62

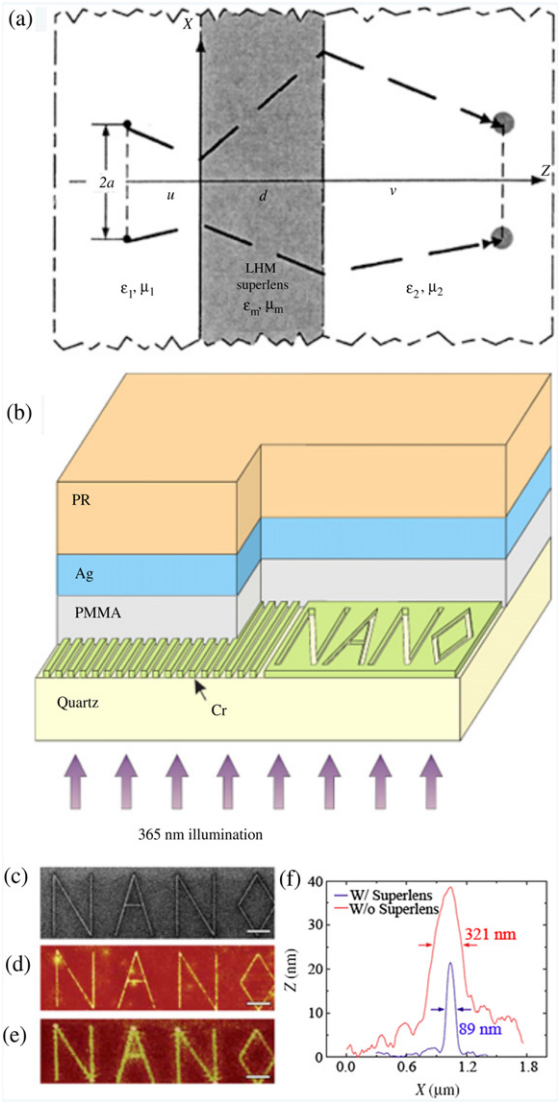


(a) Model of a LHM lens under the radiation of two line current sources. (b) Optical superlensing experiment: the embedded objects are inscribed onto the 50 nm thick Cr. At left is an array of 60 nm wide slots of 120 nm pitch, separated from the 35 nm thick silver film by a 40 nm poly(methyl methacrylate) (PMMA) spacer layer. The image of the object is recorded by the photoresist on the other side of the Ag superlens. (c) Focused ion beam image of an arbitrary object "NANO." The linewidth of the "NANO" object was 40 nm. Scale bar (c)–(e), 2 μm. (d) Aatomic force microscopy (AFM) of the developed image on photoresist with a silver superlens. (e) Atomic force micrograph of the developed image on photoresist when the 35 nm thick layer of Ag was replaced by a PMMA spacer as a control experiment. (f) The averaged cross section of a letter "A" shows an exposed line width of 89 nm (blue curve), whereas in the control experiment, the diffraction-limited FWHM line width is 321 T, 10 nm (red line). Reproduced with permission from Fig. 1, Ref. [367]. © 2003 AIP; Fig. 1 and 4, Ref. [368]. © 2005 AAAS.

on a left-handed metamaterial (LHM). The sources are embedded in medium 1 with uniform and isotropic permittivity $\varepsilon_1$ and permeability $\mu_1$, displaced by width $2a$; the separation from the current sources to the metamaterial slab is defined as the object distance $u$. The electromagnetic field with TM sources travels through the LHM superlens of thickness $d$ with permittivity $\varepsilon_M$ and permeability $\mu_M$ and reaches medium 2, where the images are formed at a distance $v$ to the right-hand side of the superlens. The LHM superlens consists of an Ag slab separated from an object by a spacer layer and coated on the opposite side with an imaging material. In this case, the surface current oscillations (SPPs) can match the evanescent waves from the object through the thin metal slab; thus, the superlens is able to substantially enhance the amplitude of the evanescent field. As a result, a minimal resolution of $\lambda/6$ is obtained by using the 36 nm Ag film as a superlens at a 364 nm wavelength.

Moreover, they experimentally demonstrated sub-diffraction-limited imaging with a 60 nm half-pitch resolution by using a 35 nm thick Ag superlens with illumination wavelength of a 365 nm [368,369]. The Ag superlens can image arbitrary nanostructures with sub-diffraction-limited resolution. The recorded image "NANO" (Fig. 62(d)) shows that the fine features can be reproduced from the mask (Fig. 62(c)) in all directions with good fidelity. It is noted that theTM evanescent waves scattered from the object are coupled into the SPPs of the Ag film, which is a primary component for restoring the sub-diffraction-limited image. For comparison with the Ag film, the control experiment was performed on the same mask with "NANO" embedded in 75 nm planarized PMMA (Fig. 62(e)). Under the same exposure condition, they observed the image of "NANO" with much wider lines, which can be treated as isolated line sources because the lines are a few micrometers apart. Furthermore, the line sources have a broadband Fourier spectrum because the larger Fourier components decay strongly, and only the smaller Fourier components reach the imaging plane. In contrast, for the Ag superlens, an average line width of 89 nm can be resolved (Fig. 62(f)), which is much smaller than that of the diffraction-limited image. In addition, a broad spectrum of subwavelength features can be achieved by proper design of the working wavelength and the thickness of Ag.

The superlens demonstrated above is a metamaterial with an isotropic property. Li *et al.* designed a bilayer metamaterial with an anisotropic property to produce a subwavelength image [370]. The simulation shows that the two complementary anisotropic metamaterials can support the ordinary evanescent modes and focus these modes through negative refraction to form a subwavelength image with a resolution of 30 nm. Recently, Zhao *et al.* also proposed two metamaterial lenses for superresolution imaging based on the effective medium theory [371]. The lenses consist of two different planar dielectric films alternated with thin metal films. The numerical simulation indicates an image with resolution nine times smaller than the light wavelength (365 nm), and the imaging properties can be further optimized by changing the lens thickness. Imaging with high resolution by the two metamaterial lenses can be applied to nanolithography and optical storage. In addition, Kho *et al.* proposed a simpler approach with which sub-100 nm imaging can be achieved over a broad bandwidth lens between 400 and 700 nm [372], where the broadband two-dimensional lens consists of

an oblate spheroidal dielectric cavity embedded beneath a planar metal surface. The bandwidth lens can be used as an indispensable tool for cell–surface interfacial studies that require sub-100 nm hyperspectral imaging analysis.

## 8.2. Metal Nanorod and Nanowire Arrays

Compared with the metal film superlens for imaging, one-dimensional metal nanostrucures (e.g., nanorods and nanowires) can transfer the near-field information of objects from the input side of the structures to the output side owing to the coupling of the SPPs with low loss propagation along the axis of the nanostructures [373]. Kawata and co-workers proposed superresolution near-field imaging by Ag nanorod arrays [374]. Since the longitudinal resonance mode of SPs on the individual nanorod is excited to produce a hot spot in the nanorod end, the enhanced electric fields at the nanorod end provide the intensity of subwavelength imaging. In this case, the near-field components of dipole sources are transferred through the nanorod array to reproduce the source distribution in the other side of the arrays (Fig. 63). As a result, the spatial resolution can be up to 40 nm for the nanorods with 50 nm height and 20 nm diameter based on the calculation by the FDTD method.

Moreover, Zhang and co-workers theoretically investigated subwavelength imaging based on metal–insulator–metal (e.g., Au–$SiO_2$–Au) nanorod arrays [375]. The metal nanorod arrays can transfer the near-field information of the object point by point from one end to the other end of each nanorod because of the transmission of the SPP wave along the nanorods. As a result, the resolution of the nanorod array for coherent light sources is up to 40 nm ($\lambda/20$), several times smaller than that of the Au nanorod array. This result exhibits the great potential of the nanorod array for improving the spatial resolution of subwavelength imaging.

On the other hand, for far-field imaging, the design of nanostructures with long-range propagation of SPP waves is significant. Although the negative refraction metamaterials can be applied to the near-field imaging, reduction of propagation losses in the metamaterials for the far-field imaging is still a challenge, especially at visible wavelengths [376,377]. It is found that metal nanowire arrays as a negative refraction material can propagate SPP waves with low loss [378,379]. Noting that the metal nanowire arrays in a dielectric matrix exhibit strong anisotropic optical properties, when the wavelength is larger than that of the longitudinal SPP mode, the nanowire arrays have the negative permittivity ($\mathrm{Re}\varepsilon_z < 0$) along the nanowire axis and the positive permittivity ($\mathrm{Re}\varepsilon_{x,y} > 0$) in the transverse plane for *p*-polarized waves. In this case, the nanowire arrays are all-angle negative refraction metamaterials with broadband wavelengths from the UV to the near-IR (NIR) region and can be used for superlens imaging [378]. In addition, the metamaterials can operate far from any resonances, which results in a much longer propagation distance because of their low loss at visible frequencies [379]. In this case, the metamaterial can achieve superresolution imaging for a source located 0.5 μm in front of a 2.0 μm thick nanowire array lab at the

Figure 63

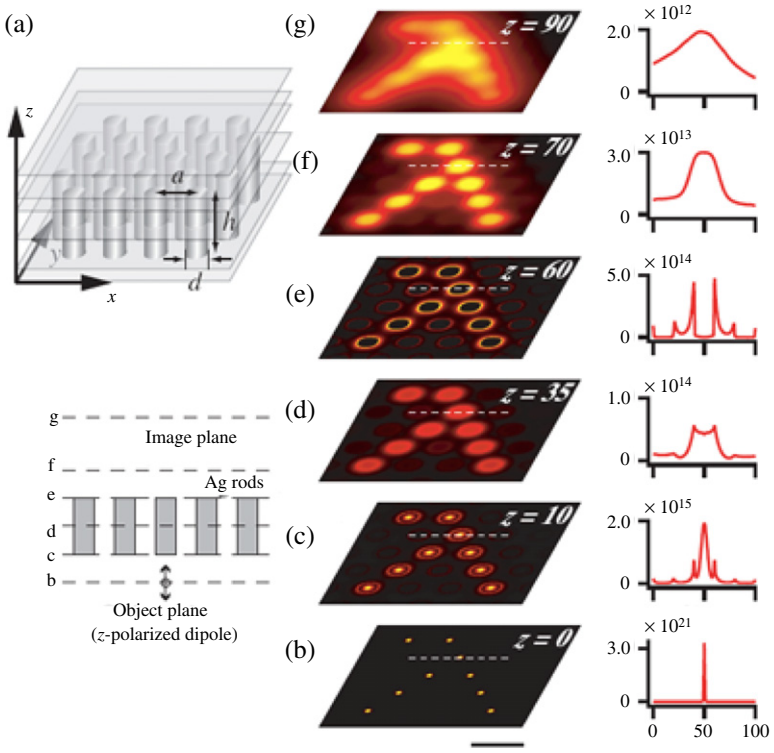


Subwavelength plasmonic image transfer of a character pattern "λ" with a metallic nanorod array device. (a) The structural model of the device, which is constructed of hexagonally arranged silver nanorods of 20 nm diameter, 50 nm height, and with 40 nm pitch, respectively. (b)–(g) Field propagation process in the image transfer obtained at each longitudinal position by the FDTD simulation. The character pattern is composed of an array of $z$-polarized dipoles. Left side images show the cross-sectional intensity distributions in the $x$–$y$ plane. The plots on the right side show the cross-sectional line profiles of dashed lines in the left-hand images. The object plane and imaging plane are defined as $z = 0$ and $z = 70$ nm. The operation wavelength is 488 nm. The scale bar is 50 nm. Reproduced with permission from Fig. 1, Ref. [374]. © 2005 APS.

wavelength of 632.8 nm. An elongated focus point is observed after the nanowire lens [379]. The result shows an effective way to manipulate light propagating in three dimensions over a very broad frequency band.

Furthermore, Casse, Sridhar and co-workers experimentally performed superresolution imaging with low-loss metamaterials consisting of Au nanowire arrays embedded in a porous alumina matrix [380]. The metamaterials have negative permittivity in the nanowire axis direction. When a void pattern object consisting of the letters "NEU" with subwavelength features is illuminated with a laser at 1550 nm, after passing through the metamaterial nanolens, the representative object imaged, consisting of the letters "NEU," 600 nm wide, is clearly observed (Fig. 64). The imaging exhibits a resolution of at least $\lambda/4$ at the NIR wavelengths (e.g., the smallest resolution with edge-to-edge distance of 400 nm), and the metamaterial nanolens can transport

Figure 64

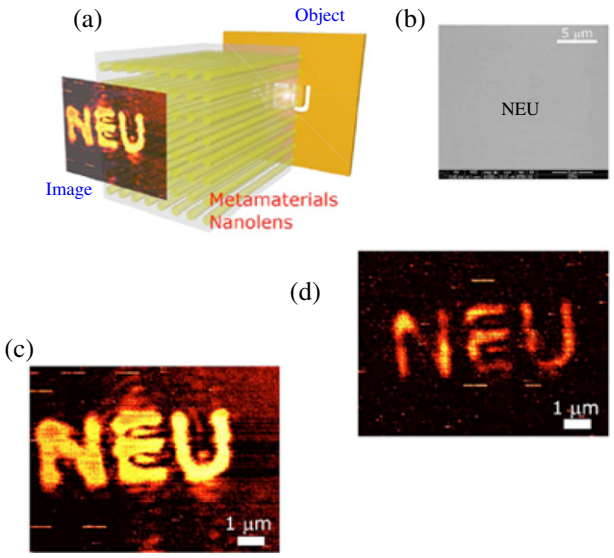


(a) Imaging with subwavelength resolution by the metamaterial nanolens at 1550 nm. The nanolens consists of high-aspect-ratio metal nanowires embedded in a host dielectric medium. This bulk metamaterial transports subwavelength details of an object at a significant distance of more than six times the wavelength (λ). (b) Scanning electron microscopy (SEM) image of the "NEU" letters milled in 100 nm thick gold metallic film. The letters have 600 nm wide arms (0.4λ). (c) Scanning near-field optical microscope (SNOM) scan of the source object in the near-field at 1550 nm wavelength. (d) SNOM scan of the corresponding image by the metamaterial nanolens above the nanolens surface. Reproduced with permission from Fig. 1, Ref. [380]. © 2010 AIP.

both the far-field and near-field components with low-loss over large distances (>6λ). Therefore the nanomaterials have potential applications in transformation optics, nanolithography, and biomedical imaging.

## 8.3. Metal Gratings

The imaging techniques described above are applied to the near-field zone. In contrast, sub-diffraction-limited imaging to the far field is indispensable for many applications in the future. Durant *et al.* proposed an optical far-field superlens (FSL) beyond the diffraction limit with a periodically corrugated metal grating [381]. The FSL exhibits waves scattered in the far field and provides a unique image of the evanescent component of the near field of the object. In this case, a one-to-one relationship between the far-field and the near-field angular spectra can be achieved. Tt is noted that the far-field image is not a direct real-space image of the near field, but an image obtained by Fourier transform.

Furthermore, Liu, Zhang and co-workers experimentally designed a FSL composed of an Ag slab and a one-dimensional subwavelength grating [382,383]. The Ag slab enhances the evanescent waves, and the subwavelength grating converts the enhanced evanescent waves into the

propagating waves. As a result, sub-diffraction-limited imaging can be achieved in the far-field zone. It is demonstrated that the FSL can image a subwavelength object consisting of two 50 nm wide lines separated by 70 nm operating at a 377 nm wavelength. For instance, for a pair of line objects of 50 nm width with a 70 nm gap (Fig. 65(a)), the line pair object has a broad Fourier spectrum within the limit where the Ag FSL operates. It is observed that optical imaging through a conventional optical microscope cannot resolve the line pairs because of the diffraction limit (Fig. 65(b)). Nevertheless, for imaging through the FSL, considering that *s* polarization does not excite SPPs, evanescent waves from the object decay rapidly, leaving only propagation components that result in a diffraction-limited image similar to that from a conventional optical microscope image (Fig. 65(c)). In contrast, for *p* polarization, the evanescent waves from the object gain significant enhancement by the excitation of SPs in the silver superlens and subsequently are converted into measurable propagating waves at the far field. By combination of the evanescent components from the *p* polarization with the propagating components from *s* polarization, the pair of lines of 50 nm width can be clearly imaged (Fig. 65(d)). The strong polarization dependence further confirms that SPP-assisted evanescent wave enhancement plays the key role in imaging through the FSL. Almost simultaneously, Liu, Zhang and co-workers theoretically proposed a two-dimensional sub-diffraction-limited imaging in the far-field zone based on a rotating metamaterial superlens [384], which would consist of a metal–dielectric multilayer and a one-dimensional subwavelength grating. In this case, the proposed metamaterial superlens can operate over a broad range of visible wavelengths intrinsically. The imaging based on those FSLs offer promising applications in nanoimaging and sensing.

In addition, Xu *et al.* theoretically presented a type of planar metal nanoslit lens for subwavelength imaging in the far-field zone [385]. The nanoslits in the Ag slab are designed with variant widths to produce desired optical phase retardations. They demonstrated that the imaging was associated with the manipulation of light retardation by optimum design of the nanoslit waveguides in a metal slab. In contrast to other superlenses, the metal planar lens can realize imaging at any distance from the lens when one selects appropriate geometrical parameters. Wang *et al.* reported subwavelength-resolved bidirectional conjugate imaging between three-dimensional far-field and two-dimensional SPP by using a SPP launching lens [386], which is composed of multiple grooves on a thin Au film according to the Fresnel zone. The SPP launching lens can be used as a microlens to connect multiple channels between far-field and SPP sources.

## 9. Conclusions and Remarks

This review presents a comprehensive overview of up-to-date progress in the field of nanostructures for surface plasmons (SPs). The peculiar properties of the SPs are focused on control and manipulation of light at the subwavlength or nanometer scale beyond the diffraction limit of light; moreover, the properties of the SPs can be tailored by the construction of nanostructures with various interfaces between metals

Figure 65

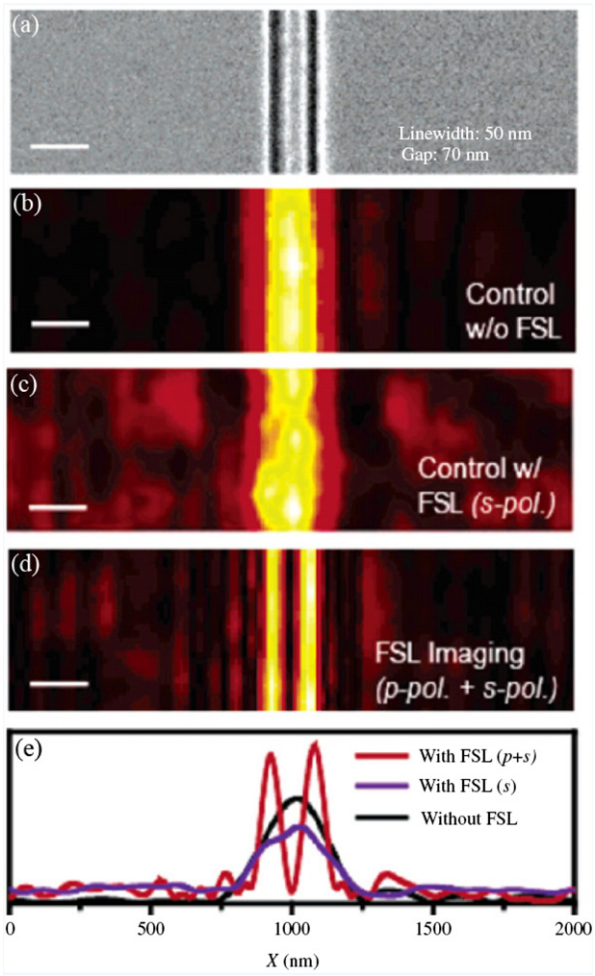


Far-field imaging of a pair of nanowires. (a) SEM image of an object nanowire pair with 50 nm wide slit and 70 nm gap inscribed by focused ion beam on a 40 nm thick Cr film on the quartz substrate. (b) A diffraction-limited image from a conventional optical microscope cannot resolve the two nanowires (N.A. $= 1.4$, $\lambda_0 = 377$ nm). (c) The reconstructed FSL images using *s* polarization is diffraction limited owing to the lack of SP-assisted evanescent enhancement. (d) FSL image combining both *s* and *p* polarizations that resolves the subdiffraction objects due to strong evanescent enhancement via SP excitation at FSL. The scale bars in (a)–(d) are 200 nm. (e) The averaged cross-section image profiles from (b), (c), and (d), respectively. Reproduced with permission from Fig. 4, Ref. [382]. © 2007 ACS.

and dielectric materials. At the various interfaces, SPs exhibit two configurations: one is localized surface plasmons (LSPs), and the other is surface plasmon polaritons (SPPs).

First, LSPs are nonpropagating electromagnetic excitations existing on the bounded metal surfaces, and LSPs give rise to some resonance modes. For zero-dimensional metal nanostructures such as nanoparticles, dipolar or multipolar LSP resonance (LSPR) modes appear, and LSP resonance modes of different orders depend on the size of the

nanoparticles. Furthermore, the resonance frequency or wavelength of LSPs can be tuned by changing the nanoparticle size. In general, the resonance peak exhibits redshifts with increased size. In contrast, one-dimensional metal nanostructures such as nanorods and nanowires give rise to longitudinal and transversal resonance modes due to their optical anisotropy. When the incident electric field is parallel to the axis of the nanorods or nanowires, the longitudinal resonance mode can be excited; while the incident electric field is perpendicular to the axis, the transversal resonance mode can be excited. The resonance frequency or wavelength (especially for the longitudinal resonance mode) is strongly dependent on the aspect ratio of the nanorods or nanowires. In addition, the dipolar or the multipolar LSP modes can also be tuned by changing the size (e.g., aspect ratio, diameter) of nanorods or nanowires. A unique phenomenon, Fano resonance, appears with an asymmetric line-shape due to the interactions between a superradiant "bright" mode and a subradiant "dark" mode. For example, the interaction between the dipolar and quadrupolar resonances will give rise to Fano resonance based on radiative coupling. Fano resonance can be observed in metal nanoparticle clusters, nanocavities with broken symmetry, nanorods, and nanowires. Owing to the sharpness of the resulting asymmetric peaks, systems exhibiting Fano resonances show enhanced sensitivity to the local dielectric environment.

Second, in contrast to LSPs, SPPs are excited electromagnetic waves propagating along the planar and long interfaces between metals and dielectric materials. The SPP waves have associated evanescent fields penetrating into both the dielectric and the metals, which are spatially decaying fields with very small penetrating depths in the direction normal to the interface. Simultaneously, the SPP wave gradually attenuates along the interface because of both ohmic losses arising from the metal and scattering losses resulting from the interface. The propagation length is dependent on the dielectric constants of the metal, incident wavelengths, and surface configurations. Therefore the propagation length can be increased by selecting a low-loss metal (e.g., Ag), by increasing the incident wavelength, and by construction of single-crystalline metal nanostructures or smooth interfaces.

On the other hand, coupling interactions are of importance for both the excitation of SPPs and the propagation of SPPs with low losses. The dispersion curve shows that the momentum of the SPP wave is larger than that of the light in free-space photon for the same frequency. The momentum mismatch must be overcome based on coupling light and SP modes at the interface by different coupler configurations. Strong coupling between light and SPs can result in efficient transportation of optical energy along the interface. For instance, the coupling between light and SPs gives rise to transmission enhancement in metal nanoholes and nanohole arrays. Optical emission of quantum dots can be significantly enhanced and transported by the proximity of a metal nanowire owing to the coupling between the photons from the quantum dots and the SPPs from metal nanowires. LSPR modes appears in two metal–dielectric interfaces because of the coupling of the two SPP waves; the propagation loss is very low (e.g., the propagation length is up to the order of centimeters) and the attenuation of the electric fields is much lower than that of SPPs at a single interface.

Because of the short penetration depths of the electric fields of a SPP wave in the dielectric and the metal, the electric fields of SPPs are concentrated mainly on the interface. Therefore the near-field intensity near the metal nanostructure is highly enhanced, and the enhanced near fields are usually dependent on the shape and the size of the metal nanostructures. Some sharp metal nanoedges, such as nanotips, nanorods, and nanogaps, can result in strong near-field enhancements. Furthermore, sharp metal nanostructures (e.g., rods, tips, wedges, and grooves) can support focusing of light from the large scale into the nanometer scale owing to the enhanced localized near field and slow speed of SPPs with short wavelengths. Besides the nanofocusing by the sharp nanostructure, nanoholes and nanoslits and their arrays with periodical nanostructures can also focus SPPs owing to their strong coupling. In addition, curved metal nanostructures, such as rings, corrals, and curved chains of nanoholes and nanoparticles, can also support nanofocusing of SPPs resulting from the interference or the reflection of the excited SPPs along the curved geometries. Because of the nanofocusing of SPPs, a highly spatial resolution of the object imaging beyond the diffraction limit of light can be obtained by excitation of SPPs with short wavelengths or slow light. In this case, metal nanostructures (e.g., films, nanorod arrays, nanowire arrays, and gratings) can work as a near-field or FSL to achieve subwavelength imaging or nanoimaging.

Finally, as a main part of nanophotonics, SPs have received considerable attention and interests from physicists, chemists, materials scientists, and biologists. A large number of novel and potential applications of SPs, including waveguides, sources (e.g., lasing), near-field optics, nonlinear optics, SERS, data storage, solar cells (or photovoltaic devices), chemical sensors, and biosensors, have been performed because of the unique characteristics of SPs. Control and manipulation of light based on nanostructures for SPs at the subwavength or nanometer scale offers significant advantages and challenges in nanophotonic devices with very small elements, high performance, high efficiency, and high stability. All-optical integration devices based on SPs may be achieved by the optimal design of nanostructures. In particular, SPs open a new and promising opportunity in fields involving the environment, energy, biology, chemistry, medicine, and health.

## Acknowledgments

This work was supported by the National Basic Research Program of China (grant 2012CB932303) and the National Natural Science Foundation of China (grant 10804112). We thank all our colleagues who contributed to this review article.

## References and Notes

1. M. Born and E. Wolf, *Principles of Optics*, 6th ed. (Pergamon, 1980).
2. W. L. Barnes, A. Dereux, and T. W. Ebbesen, "Surface plasmon subwavelength optics," Nature **424**(6950), 824–830 (2003).

3. J. X. Zhang, L. D. Zhang, and W. Xu, "Surface plasmon polaritons: physics and applications," J. Phys. D Appl. Phys. **45**(11), 113001 (2012).
4. A. V. Zayats, I. I. Smolyaninov, and A. A. Maradudin, "Nano-optics of surface plasmon polaritons," Phys. Rep. **408**(3–4), 131–314 (2005).
5. D. Sarid, "Long-range surface-plasma waves on very thin metal-films," Phys. Rev. Lett. **47**(26), 1927–1930 (1981).
6. P. Berini, "Long-range surface plasmon polaritons," Adv. Opt. Photonics **1**(3), 484–588 (2009).
7. A. V. Zayats and I. I. Smolyaninov, "Near-field photonics: surface plasmon polaritons and localized surface plasmons," J. Opt. A, Pure Appl. Opt. **5**(4), S16–S50 (2003).
8. J. Homola, S. S. Yee, and G. Gauglitz, "Surface plasmon resonance sensors: review," Sens. Actuators B Chem. **54**(1–2), 3–15 (1999).
9. E. D. Palik, *Handbook of Optical Constants of Solids* (Academic, 1985).
10. U. Kreibig and M. Vollmer, *Optical Properties of Metal Clusters* (Springer, 1995).
11. S. A. Maier, *Plasmonics: Fundamentals and Applications* (Springer, 2007).
12. A. L. Pyayt, B. Wiley, Y. Xia, A. Chen, and L. Dalton, "Integration of photonic and silver nanowire plasmonic waveguides," Nat. Nanotechnol. **3**(11), 660–665 (2008).
13. R. F. Oulton, V. J. Sorger, T. Zentgraf, R. M. Ma, C. Gladden, L. Dai, G. Bartal, and X. Zhang, "Plasmon lasers at deep subwavelength scale," Nature **461**(7264), 629–632 (2009).
14. S. Kawata, Y. Inouye, and P. Verma, "Plasmonics for near-field nano-imaging and superlensing," Nat. Photonics **3**(7), 388–394 (2009).
15. G. A. Wurtz, R. Pollard, W. Hendren, G. P. Wiederrecht, D. J. Gosztola, V. A. Podolskiy, and A. V. Zayats, "Designed ultrafast optical nonlinearity in a plasmonic nanorod metamaterial enhanced by nonlocality," Nat. Nanotechnol. **6**(2), 107–111 (2011).
16. Y. Fang, H. Wei, F. Hao, P. Nordlander, and H. Xu, "Remote-excitation surface-enhanced Raman scattering using propagating Ag nanowire plasmons," Nano Lett. **9**(5), 2049–2053 (2009).
17. P. Zijlstra, J. W. M. Chon, and M. Gu, "Five-dimensional optical recording mediated by surface plasmons in gold nanorods," Nature **459**(7245), 410–413 (2009).
18. H. A. Atwater and A. Polman, "Plasmonics for improved photovoltaic devices," Nat. Mater. **9**(3), 205–213 (2010).
19. A. V. Kabashin, P. Evans, S. Pastkovsky, W. Hendren, G. A. Wurtz, R. Atkinson, R. Pollard, V. A. Podolskiy, and A. V. Zayats, "Plasmonic nanorod metamaterials for biosensing," Nat. Mater. **8**(11), 867–871 (2009).
20. C. Wu, A. B. Khanikaev, R. Adato, N. Arju, A. A. Yanik, H. Altug, and G. Shvets, "Fano-resonant asymmetric metamaterials for ultrasensitive spectroscopy and identification of molecular monolayers," Nat. Mater. **11**(1), 69–75 (2011).
21. S. Link and M. A. El-Sayed, "Size and temperature dependence of the plasmon absorption of colloidal gold nanoparticles," J. Phys. Chem. B **103**(21), 4212–4217 (1999).
22. P. Mulvaney, "Surface plasmon spectroscopy of nanosized metal particles," Langmuir **12**(3), 788–800 (1996).

23. L. M. Liz-Marzán, "Tailoring surface plasmons through the morphology and assembly of metal nanoparticles," Langmuir **22**(1), 32–41 (2006).
24. B. Rodríguez-González, A. Burrows, M. Watanabe, C. J. Kiely, and L. M. Liz-Marzán, "Multishell bimetallic AuAg nanoparticles: synthesis, structure and optical properties," J. Mater. Chem. **15**(17), 1755–1759 (2005).
25. R. C. Jin, Y. C. Cao, E. C. Hao, G. S. Métraux, G. C. Schatz, and C. A. Mirkin, "Controlling anisotropic nanoparticle growth through plasmon excitation," Nature **425**(6957), 487–490 (2003).
26. R. C. Jin, Y. W. Cao, C. A. Mirkin, K. L. Kelly, G. C. Schatz, and J. G. Zheng, "Photoinduced conversion of silver nanospheres to nanoprisms," Science **294**(5548), 1901–1903 (2001).
27. V. Bastys, I. Pastoriza-Santos, B. Rodriguez-Gonzalez, R. Vaisnoras, and L. M. Liz-Marzan, "Formation of silver nanoprisms with surface plasmons at communication wavelengths," Adv. Funct. Mater. **16**(6), 766–773 (2006).
28. J. Nelayah, M. Kociak, O. Stéphan, F. J. García de Abajo, M. Tencé, L. Henrard, D. Taverna, I. Pastoriza-Santos, L. M. Liz-Marzán, and C. Colliex, "Mapping surface plasmons on a single metallic nanoparticle," Nat. Phys. **3**(5), 348–353 (2007).
29. C. Jeanguillaume and C. Colliex, "Spectrum-image: The next step in EELS digital acquisition and processing," Ultramicroscopy **28**(1–4), 252–257 (1989).
30. F. Ouyang, P. Batson, and M. Isaacson, "Quantum sizes effects in the surface-plasmon excitation of small metallic particles by electron-energy-loss spectroscopy," Phys. Rev. B **46**(23), 15421–15425 (1992).
31. J. C. Hulteen and R. P. Van Duyne, "Nanosphere lithography: A materials general fabrication process for periodic particle array surfaces," J. Vac. Sci. Technol. A **13**(3), 1553–1558 (1995).
32. J. C. Hulteen, D. A. Treichel, M. T. Smith, M. L. Duval, T. R. Jensen, and R. P. Van Duyne, "Nanosphere lithography: size-tunable silver nanoparticle and surface cluster arrays," J. Phys. Chem. B **103**(19), 3854–3863 (1999).
33. T. R. Jensen, G. C. Schatz, and R. P. Van Duyne, "Nanosphere lithography: Surface plasmon resonance spectrum of a periodic array of silver nanoparticles by ultraviolet–visible extinction spectroscopy and electrodynamic modeling," J. Phys. Chem. B **103**(13), 2394–2401 (1999).
34. C. L. Haynes and R. P. Van Duyne, "Nanosphere lithography: A versatile nanofabrication tool for studies of size-dependent nanoparticle optics," J. Phys. Chem. B **105**(24), 5599–5611 (2001).
35. C. L. Haynes, A. D. McFarland, L. L. Zhao, R. P. Van Duyne, G. C. Schatz, L Gunnarsson, J. Prikulis, B. Kasemo, and M. Kall, "Nanoparticle optics: The importance of radiative dipole coupling in two-dimensional nanoparticle arrays," J. Phys. Chem. B **107**(30), 7337–7342 (2003).
36. L. J. Sherry, R. C. Jin, C. A. Mirkin, G. C. Schatz, and R. P. Van Duyne, "Localized surface plasmon resonance spectroscopy of single silver triangular nanoprisms," Nano Lett. **6**(9), 2060–2065 (2006).
37. E. M. Hicks, O. Lyandres, W. P. Hall, S. L. Zou, M. R. Glucksberg, and R. P. Van Duyne, "Plasmonic properties of anchored nanoparticles fabricated by reactive ion etching and nanosphere lithography," J. Phys. Chem. C **111**(11), 4116–4124 (2007).

38. G. H. Chan, J. Zhao, E. M. Hicks, G. C. Schatz, and R. P. Van Duyne, "Plasmonic properties of copper nanoparticles fabricated by nanosphere lithography," Nano Lett. **7**(7), 1947–1952 (2007).
39. R. Micheletto, H. Fukuda, and M. Ohtsu, "A simple method for the production of a 2-dimensional, ordered array of small latex-particles," Langmuir **11**(9), 3333–3336 (1995).
40. L. J. Sherry, S. H. Chang, G. C. Schatz, R. P. Van Duyne, B. J. Wiley, and Y. N. Xia, "Localized surface plasmon resonance spectroscopy of single silver nanocubes," Nano Lett. **5**(10), 2034–2038 (2005).
41. Y. Sun and Y. N. Xia, "Shape-controlled synthesis of gold and silver nanoparticles," Science **298**(5601), 2176–2179 (2002).
42. B. Wiley, Y. G. Sun, B. Mayers, and Y. N. Xia, "Shape-controlled synthesis of metal nanostructures: the case of silver," Chemistry **11**(2), 454–463 (2005).
43. Q. Zhang, W. Li, C. Moran, J. Zeng, J. Chen, L.-P. Wen, and Y. Xia, "Seed-mediated synthesis of Ag nanocubes with controllable edge lengths in the range of 30–200 nm and comparison of their optical properties," J. Am. Chem. Soc. **132**(32), 11372–11378 (2010).
44. E. Ringe, J. M. McMahon, K. Sohn, C. Cobley, Y. N. Xia, J. X. Huang, G. C. Schatz, L. D. Marks, and R. P. Van Duyne, "Unraveling the effects of size, composition, and substrate on the localized surface plasmon resonance frequencies of gold and silver nanocubes: a systematic single-particle approach," J. Phys. Chem. C **114**(29), 12511–12516 (2010).
45. Q. Zhang, W. Li, L.-P. Wen, J. Chen, and Y. Xia, "Facile synthesis of Ag nanocubes of 30 to 70 nm in edge length with CF(3)COOAg as a precursor," Chemistry **16**(33), 10234–10239 (2010).
46. F. Zhou, Z.-Y. Li, Y. Liu, and Y. Xia, "Quantitative analysis of dipole and quadrupole excitation in the surface plasmon resonance of metal nanoparticles," J. Phys. Chem. C **112**(51), 20233–20240 (2008).
47. Y. Y. Ma, W. Y. Li, E. C. Cho, Z. Y. Li, T. K. Yu, J. Zeng, Z. X. Xie, and Y. N. Xia, "Au@Ag core-shell nanocubes with finely tuned and well-controlled sizes, shell thicknesses, and optical properties," ACS Nano **4**(11), 6725–6734 (2010).
48. A. R. Siekkinen, J. M. McLellan, J. Y. Chen, and Y. N. Xia, "Rapid synthesis of small silver nanocubes by mediating polyol reduction with a trace amount of sodium sulfide or sodium hydrosulfide," Chem. Phys. Lett. **432**(4–6), 491–496 (2006).
49. Y. G. Sun and Y. N. Xia, "Mechanistic study on the replacement reaction between silver nanostructures and chloroauric acid in aqueous medium," J. Am. Chem. Soc. **126**(12), 3892–3901 (2004).
50. B. Wiley, Y. G. Sun, J. Y. Chen, H. Cang, Z. Y. Li, X. D. Li, and Y. N. Xia, "Shape-controlled synthesis of silver and gold nanostructures," MRS Bull. **30**(05), 356–361 (2005).
51. Y. J. Xiong, B. Wiley, J. Y. Chen, Z. Y. Li, Y. D. Yin, and Y. N. Xia, "Corrosion-based synthesis of single-crystal Pd nanoboxes and nanocages and their surface plasmon properties," Angew. Chem. Int. Ed. Engl. **44**(48), 7913–7917 (2005).
52. P. Tobiška, O Hugon, A Trouillet, and H. Gagnaire, "An integrated optic hydrogen sensor based on SPR on palladium," Sens. Actuators B Chem. **74**(1–3), 168–172 (2001).

53. J. Chen, F. Saeki, B. J. Wiley, H. Cang, M. J. Cobb, Z. Y. Li, L. Au, H. Zhang, M. B. Kimmey, X. D. Li, and Y. N. Xia, "Gold nanocages: bioconjugation and their potential use as optical imaging contrast agents," Nano Lett. **5**(3), 473–477 (2005).
54. J. Y. Chen, B Wiley, Z. Y. Li, D. Campbell, F. Saeki, H. Cang, L. Au, J. Lee, X. D. Li, and Y. N. Xia, "Gold nanocages: engineering their structure for biomedical applications," Adv. Mater. (Deerfield Beach Fla.) **17**(18), 2255–2261 (2005).
55. S. E. Skrabalak, L. Au, X. D. Li, and Y. N. Xia, "Facile synthesis of Ag nanocubes and Au nanocages," Nat. Protoc. **2**(9), 2182–2190 (2007).
56. S. E. Skrabalak, J. Y. Chen, Y. G. Sun, X. M. Lu, L. Au, C. M. Cobley, and Y. N. Xia, "Gold nanocages: synthesis, properties, and applications," Acc. Chem. Res. **41**(12), 1587–1595 (2008).
57. J. Y. Chen, D. L. Wang, J. F. Xi, L. Au, A. Siekkinen, A. Warsen, Z. Y. Li, H. Zhang, Y. N. Xia, and X. D. Li, "Immuno gold nanocages with tailored optical properties for targeted photothermal destruction of cancer cells," Nano Lett. **7**(5), 1318–1322 (2007).
58. E. C. Cho, C. M. Cobley, M. Rycenga, and Y. N. Xia, "Fine tuning the optical properties of Au–Ag nanocages by selectively etching Ag with oxygen and a water-soluble thiol," J. Mater. Chem. **19**(35), 6317–6320 (2009).
59. S. J. Oldenburg, R. D. Averitt, S. L. Westcott, and N. J. Halas, "Nanoengineering of optical resonances," Chem. Phys. Lett. **288**(2–4), 243–247 (1998).
60. R. D. Averitt, D. Sarkar, and N. J. Halas, "Plasmon resonance shifts of Au-coated Au2S nanoshells: Insight into multicomponent nanoparticle growth," Phys. Rev. Lett. **78**(22), 4217–4220 (1997).
61. E. Prodan, C. Radloff, N. J. Halas, and P. Nordlander, "A hybridization model for the plasmon response of complex nanostructures," Science **302**(5644), 419–422 (2003).
62. F. Tam, C. Moran, and N. J. Halas, "Geometrical parameters controlling sensitivity of nanoshell plasmon resonances to changes in dielectric environment," J. Phys. Chem. B **108**(45), 17290–17294 (2004).
63. E. Prodan and P. Nordlander, "Structural tunability of the plasmon resonances in metallic nanoshells," Nano Lett. **3**(4), 543–547 (2003).
64. Y. F. Chau, Y. J. Lin, and D. P. Tsai, "Enhanced surface plasmon resonance based on the silver nanoshells connected by the nanobars," Opt. Express **18**(4), 3510–3518 (2010).
65. B. M. I. van der Zande, G. J. M. Koper, and H. N. W. Lekkerkerker, "Alignment of rod-shaped gold particles by electric fields," J. Phys. Chem. B **103**(28), 5754–5760 (1999).
66. C. A. Foss, M. J. Tierney, and C. R. Martin, "Template synthesis of infrared-transparent metal microcylinders: comparison of optical properties with the predictions of effective medium theory," J. Phys. Chem. **96**(22), 9001–9007 (1992).
67. C. R. Martin, "Nanomaterials: a membrane-based synthetic approach," Science **266**(5193), 1961–1966 (1994).
68. C. R. Martin, "Membrane-based synthesis of nanomaterials," Chem. Mater. **8**(8), 1739–1746 (1996).
69. J. C. Hulteen and C. R. Martin, "A general template-based method for the preparation of nanomaterials," J. Mater. Chem. **7**(7), 1075–1087 (1997).

70. B. M. I. van der Zande, M. R. Bohmer, L. G. J. Fokkink, and C. Schonenberger, "Aqueous gold sols of rod-shaped particles," J. Phys. Chem. B **101**(6), 852–854 (1997).
71. B. M. I. van der Zande, M. R. Bohmer, L. G. J. Fokkink, and C. Schonenberger, "Colloidal dispersions of gold rods: synthesis and optical properties," Langmuir **16**(2), 451–458 (2000).
72. J. Pérez-Juste, B. Rodríguez-González, P. Mulvaney, and L. M. Liz-Marzán, "Optical control and patterning of gold-nanorod-poly (vinyl alcohol) nanocomposite films," Adv. Funct. Mater. **15**(7), 1065–1071 (2005).
73. H. M. Chen, H. C. Peng, R. S. Liu, K. Asakura, C. L. Lee, J. F. Lee, and S. F. Hu, "Controlling the length and shape of gold nanorods," J. Phys. Chem. B **109**(42), 19553–19555 (2005).
74. H. J. Huang, C. P. Yu, H. C. Chang, K. P. Chiu, H. Ming Chen, R. S. Liu, and D. P. Tsai, "Plasmonic optical properties of a single gold nano-rod," Opt. Express **15**(12), 7132–7139 (2007).
75. H. M. Chen, R. S. Liu, and D. P. Tsai, "A versatile route to the controlled synthesis of gold nanostructures," Cryst. Growth Des. **9**(5), 2079–2087 (2009).
76. J. R. Krenn, G. Schider, W. Rechberger, B. Lamprecht, A. Leitner, F. R. Aussenegg, and J. C. Weeber, "Design of multipolar plasmon excitations in silver nanoparticles," Appl. Phys. Lett. **77**(21), 3379–3381 (2000).
77. G. M. Sando, A. D. Berry, P. M. Campbell, A. P. Baronavski, and J. C. Owrutsky, "Surface plasmon dynamics of high-aspect-ratio gold nanorods," Plasmonics **2**(1), 23–29 (2007).
78. M. Wirtz and C. R. Martin, "Template-fabricated gold nanowires and nanotubes," Adv. Mater. (Deerfield Beach Fla.) **15**(5), 455–458 (2003).
79. H. Masuda and K. Fukuda, "Ordered metal nanohole arrays made by a two-step replication of honeycomb structures of anodic alumina," Science **268**(5216), 1466–1468 (1995).
80. Y. N. Xia, P. D. Yang, Y. G. Sun, Y. Y. Wu, B. Mayers, B. Gates, Y. D. Yin, F. Kim, and Y. Q. Yan, "One-dimensional nanostructures: synthesis, characterization, and applications," Adv. Mater. (Deerfield Beach Fla.) **15**(5), 353–389 (2003).
81. We have not published this study, but present some observations here.
82. X. Y. Hu, Z. Y. Wang, T. C. Zhang, X. Y. Zeng, W. Xu, J. X. Zhang, J. Yan, J. P. Zhang, and L. D. Zhang, "Manipulation of optical properties of Ag/Cu alloy nanowire arrays embedded in anodic alumina membranes," Appl. Surf. Sci. **254**(13), 3845–3848 (2008).
83. X. Q. Huang, S. H. Tang, X. L. Mu, Y. Dai, G. X. Chen, Z. Y. Zhou, F. X. Ruan, Z. L. Yang, and N. F. Zheng, "Freestanding palladium nanosheets with plasmonic and catalytic properties," Nat. Nanotechnol. **6**(1), 28–32 (2011).
84. S. H. Chen, Z. Y. Fan, and D. L. Carroll, "Silver nanodisks: synthesis, characterization, and self-assembly," J. Phys. Chem. B **106**(42), 10777–10781 (2002).
85. M. Maillard, P. R. Huang, and L. Brus, "Silver nanodisk growth by surface plasmon enhanced photoreduction of adsorbed [Ag+]," Nano Lett. **3**(11), 1611–1615 (2003).

86. M. Maillard, S. Giorgio, and M. P. Pileni, "Tuning the size of silver nanodisks with similar aspect ratios: synthesis and optical properties," J. Phys. Chem. B **107**(11), 2466–2470 (2003).
87. Y. B. Zheng, B. K. Juluri, X. L. Mao, T. R. Walker, and T. J. Huang, "Systematic investigation of localized surface plasmon resonance of long-range ordered Au nanodisk arrays," J. Appl. Phys. **103**(1), 014308 (2008).
88. A. Brioude and M. P. Pileni, "Silver nanodisks: optical properties study using the discrete dipole approximation method," J. Phys. Chem. B **109**(49), 23371–23377 (2005).
89. K. H. Su, Q. H. Wei, and X. Zhang, "Tunable and augmented plasmon resonances of Au/SiO2/Au nanodisks," Appl. Phys. Lett. **88**(6), 063118 (2006).
90. K. H. Su, Q. H. Wei, X. Zhang, J. J. Mock, D. R. Smith, and S. Schultz, "Interparticle coupling effects on plasmon resonances of nanogold particles," Nano Lett. **3**(8), 1087–1090 (2003).
91. W. Rechberger, A. Hohenau, A. Leitner, J. R. Krenn, B. Lamprecht, and F. R. Aussenegg, "Optical properties of two interacting gold nanoparticles," Opt. Commun. **220**(1–3), 137–141 (2003).
92. K. H. Lee and K. J. Chang, "First-principles study of the optical properties and the dielectric response of Al," Phys. Rev. B Condens. Matter **49**(4), 2362–2367 (1994).
93. H. Ehrenreich, H. R. Philipp, and B. Segall, "Optical properties of aluminum," Phys. Rev. **132**(5), 1918–1928 (1963).
94. C. Langhammer, M. Schwind, B. Kasemo, and I. Zorić, "Localized surface plasmon resonances in aluminum nanodisks," Nano Lett. **8**(5), 1461–1471 (2008).
95. C. Langhammer, B. Kasemo, and I. Zorić, "Absorption and scattering of light by Pt, Pd, Ag, and Au nanodisks: absolute cross sections and branching ratios," J. Chem. Phys. **126**(19), 194702 (2007).
96. K. Imura, T. Nagahara, and H. Okamoto, "Near-field optical imaging of plasmon modes in gold nanorods," J. Chem. Phys. **122**(15), 154701 (2005).
97. T. Klar, M. Perner, S. Grosse, G. von Plessen, W. Spirkl, and J. Feldmann, "Surface-plasmon resonances in single metallic nanoparticles," Phys. Rev. Lett. **80**(19), 4249–4252 (1998).
98. M. N'Gom, J. Ringnalda, J. F. Mansfield, A. Agarwal, N. Kotov, N. J. Zaluzec, and T. B. Norris, "Single particle plasmon spectroscopy of silver nanowires and gold nanorods," Nano Lett. **8**(10), 3200–3204 (2008).
99. S. Eustis and M. A. El-Sayed, "Determination of the aspect ratio statistical distribution of gold nanorods in solution from a theoretical fit of the observed inhomogeneously broadened longitudinal plasmon resonance absorption spectrum," J. Appl. Phys. **100**(4), 044324 (2006).
100. H. M. Bok, K. L. Shuford, S. Kim, S. K. Kim, and S. Park, "Multiple surface plasmon modes for a colloidal solution of nanoporous gold nanorods and their comparison to smooth gold nanorods," Nano Lett. **8**(8), 2265–2270 (2008).
101. H. M. Bok, K. L. Shuford, S. Kim, S. K. Kim, and S. Park, "Multiple surface plasmon modes for gold/silver alloy nanorods," Langmuir **25**(9), 5266–5270 (2009).

102. S. Kim, S. K. Kim, and S. Park, "Bimetallic gold-silver nanorods produce multiple surface plasmon bands," J. Am. Chem. Soc. **131**(24), 8380–8381 (2009).
103. G. A. Wurtz, W. Dickson, D. O'Connor, R. Atkinson, W. Hendren, P. Evans, R. Pollard, and A. V. Zayats, "Guided plasmonic modes in nanorod assemblies: strong electromagnetic coupling regime," Opt. Express **16**(10), 7460–7470 (2008).
104. P. R. Evans, G. A. Wurtz, R. Atkinson, W. Hendren, D. O'Connor, W. Dickson, R. J. Pollard, and A. V. Zayats, "Plasmonic core/shell nanorod arrays: subattoliter controlled geometry and tunable optical properties," J. Phys. Chem. C **111**(34), 12522–12527 (2007).
105. G. Schider, J. R. Krenn, W Gotschy, B. Lamprecht, H. Ditlbacher, A. Leitner, and F. R. Aussenegg, "Optical properties of Ag and Au nanowire gratings," J. Appl. Phys. **90**(8), 3825–3830 (2001).
106. R. L. Zong, J. Zhou, Q. Li, B. Du, B. Li, M. Fu, X. W. Qi, L. T. Li, and S. Buddhudu, "Synthesis and optical properties of silver nanowire arrays embedded in anodic alumina membrane," J. Phys. Chem. B **108**(43), 16713–16716 (2004).
107. G. Laurent, N. Félidj, J. Aubard, G. Lévi, J. R. Krenn, A. Hohenau, G. Schider, A. Leitner, and F. R. Aussenegg, "Surface enhanced Raman scattering arising from multipolar plasmon excitation," J. Chem. Phys. **122**(1), 011102 (2005).
108. E. K. Payne, K. L. Shuford, S. Park, G. C. Schatz, and C. A. Mirkin, "Multipole plasmon resonances in gold nanorods," J. Phys. Chem. B **110**(5), 2150–2154 (2006).
109. J. E. Millstone, S. Park, K. L. Shuford, L. D. Qin, G. C. Schatz, and C. A. Mirkin, "Observation of a quadrupole plasmon mode for a colloidal solution of gold nanoprisms," J. Am. Chem. Soc. **127**(15), 5312–5313 (2005).
110. B. T. Draine and P. J. Flatau, "Discrete-dipole approximation for scattering calculations," J. Opt. Soc. Am. A **11**(4), 1491–1499 (1994).
111. C. Radloff and N. J. Halas, "Plasmonic properties of concentric nanoshells," Nano Lett. **4**(7), 1323–1327 (2004).
112. L. M. Liz-Marzan, M. Giersig, and P. Mulvaney, "Synthesis of nanosized gold-silica core-shell particles," Langmuir **12**, 4329–4335 (1996).
113. C. P. Burrows and W. L. Barnes, "Large spectral extinction due to overlap of dipolar and quadrupolar plasmonic modes of metallic nanoparticles in arrays," Opt. Express **18**(3), 3187–3198 (2010).
114. B. N. Khlebtsov and N. G. Khlebtsov, "Multipole plasmons in metal nanorods: scaling properties and dependence on particle size, shape, orientation, and dielectric environment," J. Phys. Chem. C **111**(31), 11516–11527 (2007).
115. G. Schider, J. R. Krenn, A. Hohenau, H. Ditlbacher, A. Leitner, F. R. Aussenegg, W. L. Schaich, I. Puscasu, B. Monacelli, and G. Boreman, "Plasmon dispersion relation of Au and Ag nanowires," Phys. Rev. B **68**(15), 155427 (2003).
116. W. Gotschy, K. Vonmetz, A. Leitner, and F. R. Aussenegg, "Thin films by regular patterns of metal nanoparticles: tailoring the optical properties by nanodesign," Appl. Phys. B **63**(4), 381–384 (1996).
117. E. J. R. Vesseur, R. de Waele, M. Kuttge, and A. Polman, "Direct observation of plasmonic modes in au nanowires using high-resolution cathodoluminescence spectroscopy," Nano Lett. **7**(9), 2843–2846 (2007).

118. A. E. Miroshnichenko, S. Flach, and Y. S. Kivshar, "Fano resonances in nanoscale structures," Rev. Mod. Phys. **82**(3), 2257–2298 (2010).
119. U. Fano, "Effects of configuration interaction on intensities and phase shifts," Phys. Rev. **124**(6), 1866–1878 (1961).
120. B. Luk'yanchuk, N. I. Zheludev, S. A. Maier, N. J. Halas, P. Nordlander, H. Giessen, and C. T. Chong, "The Fano resonance in plasmonic nanostructures and metamaterials," Nat. Mater. **9**(9), 707–715 (2010).
121. J. A. Fan, C. Wu, K. Bao, J. Bao, R. Bardhan, N. J. Halas, V. N. Manoharan, P. Nordlander, G. Shvets, and F. Capasso, "Self-assembled plasmonic nanoparticle clusters," Science **328**(5982), 1135–1138 (2010).
122. N. A. Mirin, K. Bao, and P. Nordlander, "Fano resonances in plasmonic nanoparticle aggregates," J. Phys. Chem. A **113**(16), 4028–4034 (2009).
123. J. A. Fan, K. Bao, C. Wu, J. Bao, R. Bardhan, N. J. Halas, V. N. Manoharan, G. Shvets, P. Nordlander, and F. Capasso, "Fano-like interference in self-assembled plasmonic quadrumer clusters," Nano Lett. **10**(11), 4680–4685 (2010).
124. J. B. Lassiter, H. Sobhani, J. A. Fan, J. Kundu, F. Capasso, P. Nordlander, and N. J. Halas, "Fano resonances in plasmonic nanoclusters: geometrical and chemical tunability," Nano Lett. **10**(8), 3184–3189 (2010).
125. W. Zhou and T. W. Odom, "Tunable subradiant lattice plasmons by out-of-plane dipolar interactions," Nat. Nanotechnol. **6**(7), 423–427 (2011).
126. P. Spinelli, C. van Lare, E. Verhagen, and A. Polman, "Controlling Fano lineshapes in plasmon-mediated light coupling into a substrate," Opt. Express **19**(S3 Suppl 3), A303–A311 (2011).
127. S. N. Sheikholeslami, A. García-Etxarri, and J. A. Dionne, "Controlling the interplay of electric and magnetic modes via Fano-like plasmon resonances," Nano Lett. **11**(9), 3927–3934 (2011).
128. T. Pakizeh, C. Langhammer, I. Zorić, P. Apell, and M. Käll, "Intrinsic Fano interference of localized plasmons in Pd nanoparticles," Nano Lett. **9**(2), 882–886 (2009).
129. F. Hao, Y. Sonnefraud, P. Van Dorpe, S. A. Maier, N. J. Halas, and P. Nordlander, "Symmetry breaking in plasmonic nanocavities: subradiant LSPR sensing and a tunable Fano resonance," Nano Lett. **8**(11), 3983–3988 (2008).
130. F. Hao, P. Nordlander, Y. Sonnefraud, P. Van Dorpe, and S. A. Maier, "Tunability of subradiant dipolar and fano-type plasmon resonances in metallic ring/disk cavities: implications for nanoscale optical sensing," ACS Nano **3**(3), 643–652 (2009).
131. N. Verellen, Y. Sonnefraud, H. Sobhani, F. Hao, V. V. Moshchalkov, P. Van Dorpe, P. Nordlander, and S. A. Maier, "Fano resonances in individual coherent plasmonic nanocavities," Nano Lett. **9**(4), 1663–1667 (2009).
132. Z. Fang, J. Cai, Z. Yan, P Nordlander, N. J. Halas, and X. Zhu, "Removing a wedge from a metallic nanodisk reveals a fano resonance," Nano Lett. **11**(10), 4475–4479 (2011).
133. A. Artar, A. A. Yanik, and H. Altug, "Directional double Fano resonances in plasmonic hetero-oligomers," Nano Lett. **11**(9), 3694–3700 (2011).
134. S. H. Fan, W. Suh, and J. D. Joannopoulos, "Temporal coupled-mode theory for the Fano resonance in optical resonators," J. Opt. Soc. Am. A **20**(3), 569–572 (2003).

135. Z. K. Zhou, X. N. Peng, Z. J. Yang, Z. S. Zhang, M. Li, X. R. Su, Q. Zhang, X. Shan, Q. Q. Wang, and Z. Zhang, "Tuning gold nanorod-nanoparticle hybrids into plasmonic Fano resonance for dramatically enhanced light emission and transmission," Nano Lett. **11**(1), 49–55 (2011).
136. Z. J. Yang, Z. S. Zhang, W. Zhang, Z. H. Hao, and Q. Q. Wang, "Twinned Fano interferences induced by hybridized plasmons in Au–Ag nanorod heterodimers," Appl. Phys. Lett. **96**(13), 131113 (2010).
137. Z. J. Yang, Z. S. Zhang, Z. H. Hao, and Q. Q. Wang, "Fano resonances in active plasmonic resonators consisting of a nanorod dimer and a nano-emitter," Appl. Phys. Lett. **99**(8), 081107 (2011).
138. W. Chen, G. Y. Chen, and Y. N. Chen, "Controlling Fano resonance of nanowire surface plasmons," Opt. Lett. **36**(18), 3602–3604 (2011).
139. W. Chen, G. Y. Chen, and Y. N. Chen, "Coherent transport of nanowire surface plasmons coupled to quantum dots," Opt. Express **18**(10), 10360–10368 (2010).
140. Z. Zhang, A. Weber-Bargioni, S. W. Wu, S. Dhuey, S. Cabrini, and P. J. Schuck, "Manipulating nanoscale light fields with the asymmetric bowtie nano-colorsorter," Nano Lett. **9**(12), 4505–4509 (2009).
141. P. K. Jain and M. A. El-Sayed, "Plasmonic coupling in noble metal nanostructures," Chem. Phys. Lett. **487**(4–6), 153–164 (2010).
142. P. L. Stiles, J. A. Dieringer, N. C. Shah, and R. R. Van Duyne, "Surface-enhanced Raman spectroscopy," Annu. Rev. Anal. Chem. **61**(6), 601–626 (2008).
143. S. K. Ghosh and T. Pal, "Interparticle coupling effect on the surface plasmon resonance of gold nanoparticles: from theory to applications," Chem. Rev. **107**(11), 4797–4862 (2007).
144. S. S. Aćimović, M. P. Kreuzer, M. U. González, and R. Quidant, "Plasmon near-field coupling in metal dimers as a step toward single-molecule sensing," ACS Nano **3**(5), 1231–1237 (2009).
145. P. K. Jain and M. A. El-Sayed, "Noble metal nanoparticle pairs: effect of medium for enhanced nanosensing," Nano Lett. **8**(12), 4347–4352 (2008).
146. K. R. Li, M. I. Stockman, and D. J. Bergman, "Self-similar chain of metal nanospheres as an efficient nanolens," Phys. Rev. Lett. **91**(22), 227402 (2003).
147. B. M. Reinhard, S. Sheikholeslami, A. Mastroianni, A. P. Alivisatos, and J. Liphardt, "Use of plasmon coupling to reveal the dynamics of DNA bending and cleavage by single EcoRV restriction enzymes," Proc. Natl. Acad. Sci. U.S.A. **104**(8), 2667–2672 (2007).
148. Y. W. Jun, S. Sheikholeslami, D. R. Hostetter, C. Tajon, C. S. Craik, and A. P. Alivisatos, "Continuous imaging of plasmon rulers in live cells reveals early-stage caspase-3 activation at the single-molecule level," Proc. Natl. Acad. Sci. U.S.A. **106**(42), 17735–17740 (2009).
149. P. K. Jain and M. A. El-Sayed, "Universal scaling of plasmon coupling in metal nanostructures: extension from particle pairs to nanoshells," Nano Lett. **7**(9), 2854–2858 (2007).
150. N. J. Halas, S. Lal, W.-S. Chang, S. Link, and P. Nordlander, "Plasmons in strongly coupled metallic nanostructures," Chem. Rev. **111**(6), 3913–3961 (2011).
151. E. J. Smythe, E. Cubukcu, and F. Capasso, "Optical properties of surface plasmon resonances of coupled metallic nanorods," Opt. Express **15**(12), 7439–7447 (2007).

152. S. Malynych and G. Chumanov, "Light-induced coherent interactions between silver nanoparticles in two-dimensional arrays," J. Am. Chem. Soc. **125**(10), 2896–2898 (2003).
153. M. K. Kinnan and G. Chumanov, "Plasmon coupling in two-dimensional arrays of silver nanoparticles: II. Effect of the particle size and interparticle distance," J. Phys. Chem. C **114**(16), 7496–7501 (2010).
154. P. K. Jain, W. Huang, and M. A. El-Sayed, "On the universal scaling behavior of the distance decay of plasmon coupling in metal nanoparticle pairs: a plasmon ruler equation," Nano Lett. **7**(7), 2080–2088 (2007).
155. W. S. Chang, L. S. Slaughter, B. P. Khanal, P. Manna, E. R. Zubarev, and S. Link, "One-dimensional coupling of gold nanoparticle plasmons in self-assembled ring superstructures," Nano Lett. **9**(3), 1152–1157 (2009).
156. P. Nordlander, C. Oubre, E. Prodan, K. Li, and M. I. Stockman, "Plasmon hybridization in nanoparticle dimers," Nano Lett. **4**(5), 899–903 (2004).
157. S. Sheikholeslami, Y. W. Jun, P. K. Jain, and A. P. Alivisatos, "Coupling of optical resonances in a compositionally asymmetric plasmonic nanoparticle dimer," Nano Lett. **10**(7), 2655–2660 (2010).
158. T. J. Davis, K. C. Vernon, and D. E. Gomez, "Designing plasmonic systems using optical coupling between nanoparticles," Phys. Rev. B **79**(15), 155423 (2009).
159. J. P. Kottmann and O. J. F. Martin, "Retardation-induced plasmon resonances in coupled nanoparticles," Opt. Lett. **26**(14), 1096–1098 (2001).
160. A. M. Funston, C. Novo, T. J. Davis, and P. Mulvaney, "Plasmon coupling of gold nanorods at short distances and in different geometries," Nano Lett. **9**(4), 1651–1658 (2009).
161. P. K. Jain, S. Eustis, and M. A. El-Sayed, "Plasmon coupling in nanorod assemblies: optical absorption, discrete dipole approximation simulation, and exciton-coupling model," J. Phys. Chem. B **110**(37), 18243–18253 (2006).
162. E. J. Smythe, E. Cubukcu, and F. Capasso, "Optical properties of surface plasmon resonances of coupled metallic nanorods," Opt. Express **15**(12), 7439–7447 (2007).
163. C. L. Haynes, A. D. McFarland, L. L. Zhao, R. P. Van Duyne, G. C. Schatz, L. Gunnarsson, J. Prikulis, B. Kasemo, and M. Kall, "Nanoparticle optics: the importance of radiative dipole coupling in two-dimensional nanoparticle arrays," J. Phys. Chem. B **107**(30), 7337–7342 (2003).
164. L. Shao, K. C. Woo, H. Chen, Z. Jin, J. Wang, and H. Q. Lin, "Angle- and energy-resolved plasmon coupling in gold nanorod dimers," ACS Nano **4**(6), 3053–3062 (2010).
165. J. P. Kottmann and O. J. F. Martin, "Plasmon resonant coupling in metallic nanowires," Opt. Express **8**(12), 655–663 (2001).
166. K. Halterman, J. M. Elson, and S. Singh, "Plasmonic resonances and electromagnetic forces between coupled silver nanowires," Phys. Rev. B **72**(7), 075429 (2005).
167. H. S. Chu, W. B. Ewe, W. S. Koh, and E. P. Li, "Remarkable influence of the number of nanowires on plasmonic behaviors of the coupled metallic nanowire chain," Appl. Phys. Lett. **92**(10), 103103 (2008).
168. H. Liu, X. Sun, Y. Pei, F. Yao, and Y. Jiang, "Tunability and linewidth sharpening of plasmon resonances on a periodic gold nanowire array coupled to a thin textured silver film," Appl. Phys. B **104**(3), 665–672 (2011).

169. Z. Fang, L. Fan, C. Lin, D. Zhang, A. J. Meixner, and X. Zhu, "Plasmonic coupling of bow tie antennas with Ag nanowire," Nano Lett. **11**(4), 1676–1680 (2011).
170. L. Jiao, B. Fan, X. Xian, Z. Wu, J. Zhang, and Z. Liu, "Creation of nanostructures with poly(methyl methacrylate)-mediated nanotransfer printing," J. Am. Chem. Soc. **130**(38), 12612–12613 (2008).
171. V. Giannini, G. Vecchi, and J. Gómez Rivas, "Lighting up multipolar surface plasmon polaritons by collective resonances in arrays of nanoantennas," Phys. Rev. Lett. **105**(26), 266801 (2010).
172. L. Novotny, "Effective wavelength scaling for optical antennas," Phys. Rev. Lett. **98**(26), 266802 (2007).
173. K. G. Lee and Q. H. Park, "Coupling of surface plasmon polaritons and light in metallic nanoslits," Phys. Rev. Lett. **95**(10), 103902 (2005).
174. D. E. Chang, A. S. Sørensen, P. R. Hemmer, and M. D. Lukin, "Quantum optics with surface plasmons," Phys. Rev. Lett. **97**(5), 053002 (2006).
175. Y. G. Sun, B. Gates, B. Mayers, and Y. N. Xia, "Crystalline silver nanowires by soft solution processing," Nano Lett. **2**(2), 165–168 (2002).
176. A. V. Akimov, A. Mukherjee, C. L. Yu, D. E. Chang, A. S. Zibrov, P. R. Hemmer, H. Park, and M. D. Lukin, "Generation of single optical plasmons in metallic nanowires coupled to quantum dots," Nature **450**(7168), 402–406 (2007).
177. A. L. Falk, F. H. L. Koppens, C. L. Yu, K. Kang, N. de Leon Snapp, A. V. Akimov, M.-H. Jo, M. D. Lukin, and H. Park, "Near-field electrical detection of optical plasmons and single-plasmon sources," Nat. Phys. **5**(7), 475–479 (2009).
178. R. M. Dickson and L. A. Lyon, "Unidirectional plasmon propagation in metallic nanowires," J. Phys. Chem. B **104**(26), 6095–6098 (2000).
179. I. De Vlaminck, P. Van Dorpe, L. Lagae, and G. Borghs, "Local electrical detection of single nanoparticle plasmon resonance," Nano Lett. **7**(3), 703–706 (2007).
180. D. E. Chang, A. S. Sorensen, E. A. Demler, and M. D. Lukin, "A single-photon transistor using nanoscale surface plasmons," Nat. Phys. **3**(11), 807–812 (2007).
181. D. E. Chang, A. S. Sorensen, P. R. Hemmer, and M. D. Lukin, "Strong coupling of single emitters to surface plasmons," Phys. Rev. B **76**(3), 035420 (2007).
182. Y. Fedutik, V. Temnov, U. Woggon, E. Ustinovich, and M. Artemyev, "Exciton-plasmon interaction in a composite metal–insulator-semiconductor nanowire system," J. Am. Chem. Soc. **129**(48), 14939–14945 (2007).
183. R. Yan, P. Pausauskie, J. Huang, and P. Yang, "Direct photonic-plasmonic coupling and routing in single nanowires," Proc. Natl. Acad. Sci. U.S.A. **106**(50), 21045–21050 (2009).
184. X. Guo, M. Qiu, J. Bao, B. J. Wiley, Q. Yang, X. Zhang, Y. Ma, H. Yu, and L. Tong, "Direct coupling of plasmonic and photonic nanowires for hybrid nanophotonic components and circuits," Nano Lett. **9**(12), 4515–4519 (2009).
185. L. M. Tong, J. Y. Lou, and E. Mazur, "Single-mode guiding properties of subwavelength-diameter silica and silicon wire waveguides," Opt. Express **12**(6), 1025–1035 (2004).

186. A. W. Sanders, D. A. Routenberg, B. J. Wiley, Y. Xia, E. R. Dufresne, and M. A. Reed, "Observation of plasmon propagation, redirection, and fan-out in silver nanowires," Nano Lett. **6**(8), 1822–1826 (2006).
187. P. Vasa, R. Pomraenke, S. Schwieger, Y. I. Mazur, V. Kunets, P. Srinivasan, E. Johnson, J. E. Kihm, D. S. Kim, E. Runge, G. Salamo, and C. Lienau, "Coherent exciton-surface-plasmon-polariton interaction in hybrid metal–semiconductor nanostructures," Phys. Rev. Lett. **101**(11), 116801 (2008).
188. X. W. Chen, V. Sandoghdar, and M. Agio, "Highly efficient interfacing of guided plasmons and photons in nanowires," Nano Lett. **9**(11), 3756–3761 (2009).
189. E. Prodan, C. Radloff, N. J. Halas, and P. Nordlander, "A hybridization model for the plasmon response of complex nanostructures," Science **302**(5644), 419–422 (2003).
190. A. L. Aden and M. Kerker, "Scattering of electromagnetic waves from two concentric spheres," J. Appl. Phys. **22**(10), 1242–1246 (1951).
191. Y. Z. Chu and K. B. Crozier, "Experimental study of the interaction between localized and propagating surface plasmons," Opt. Lett. **34**(3), 244–246 (2009).
192. S. I. Bozhevolnyi, J. Erland, K. Leosson, P. M. W. Skovgaard, and J. M. Hvam, "Waveguiding in surface plasmon polariton band gap structures," Phys. Rev. Lett. **86**(14), 3008–3011 (2001).
193. B. Lamprecht, G. Schider, R. T. Lechner, H. Ditlbacher, J. R. Krenn, A. Leitner, and F. R. Aussenegg, "Metal nanoparticle gratings: influence of dipolar particle interaction on the plasmon resonance," Phys. Rev. Lett. **84**(20), 4721–4724 (2000).
194. M. Quinten, A. Leitner, J. R. Krenn, and F. R. Aussenegg, "Electromagnetic energy transport via linear chains of silver nanoparticles," Opt. Lett. **23**(17), 1331–1333 (1998).
195. S. A. Maier, M. L. Brongersma, P. G. Kik, S. Meltzer, A. A. G. Requicha, and H. A. Atwater, "Plasmonics—a route to nanoscale optical devices," Adv. Mater. (Deerfield Beach Fla.) **13**(19), 1501–1505 (2001).
196. R. A. McMillan, C. D. Paavola, J. Howard, S. L. Chan, N. J. Zaluzec, and J. D. Trent, "Ordered nanoparticle arrays formed on engineered chaperonin protein templates," Nat. Mater. **1**(4), 247–252 (2002).
197. J. R. Krenn, A. Dereux, J. C. Weeber, E. Bourillot, Y. Lacroute, J. P. Goudonnet, G. Schider, W. Gotschy, A. Leitner, F. R. Aussenegg, and C. Girard, "Squeezing the optical near-field zone by plasmon coupling of metallic nanoparticles," Phys. Rev. Lett. **82**(12), 2590–2593 (1999).
198. S. A. Maier, M. L. Brongersma, P. G. Kik, and H. A. Atwater, "Observation of near-field coupling in metal nanoparticle chains using far-field polarization spectroscopy," Phys. Rev. B **65**(19), 193408 (2002).
199. S. A. Maier, P. G. Kik, H. A. Atwater, S. Meltzer, E. Harel, B. E. Koel, and A. A. G. Requicha, "Local detection of electromagnetic energy transport below the diffraction limit in metal nanoparticle plasmon waveguides," Nat. Mater. **2**(4), 229–232 (2003).
200. S. A. Maier, P. G. Kik, and H. A. Atwater, "Observation of coupled plasmon-polariton modes in Au nanoparticle chain waveguides of different lengths: estimation of waveguide loss," Appl. Phys. Lett. **81**(9), 1714–1716 (2002).

201. M. Fujihira, H. Monobe, N. Yamamoto, H. Muramatsu, N. Chiba, K. Nakajima, and T. Ataka, "Scanning near-field optical microscopy of fluorescent polystyrene spheres with a combined SNOM and atomic force microscope," Ultramicroscopy **61**(1–4), 271–277 (1995).
202. A. B. Evlyukhin and S. L. Bozhevolnyi, "Surface plasmon polariton guiding by chains of nanoparticles," Laser Phys. Lett. **3**(8), 396–400 (2006).
203. A. Alù, P. A. Belov, and N. Engheta, "Coupling and guided propagation along parallel chains of plasmonic nanoparticles," New J. Phys. **13**(3), 033026 (2011).
204. A. Alù and N. Engheta, "Guided propagation along quadrupolar chains of plasmonic nanoparticles," Phys. Rev. B **79**(23), 235412 (2009).
205. X. D. Cui and D. Erni, "Enhanced propagation in a plasmonic chain waveguide with nanoshell structures based on low- and high-order mode coupling," J. Opt. Soc. Am. A **25**(7), 1783–1789 (2008).
206. I. B. Udagedara, I. D. Rukhlenko, and M. Premaratne, "Surface plasmon-polariton propagation in piecewise linear chains of composite nanospheres: the role of optical gain and chain layout," Opt. Express **19**(21), 19973–19986 (2011).
207. S. M. Raeis Zadeh Bajestani, M. Shahabadi, and N. Talebi, "Analysis of plasmon propagation along a chain of metal nanospheres using the generalized multipole technique," J. Opt. Soc. Am. B **28**(4), 937–943 (2011).
208. V. A. Markel and A. K. Sarychev, "Propagation of surface plasmons in ordered and disordered chains of metal nanospheres," Phys. Rev. B **75**(8), 085426 (2007).
209. N. Yamamoto, K. Araya, and F. García de Abajo, "Photon emission from silver particles induced by a originates electron beam," Phys. Rev. B **64**(20), 205419 (2001).
210. L. Wang, W. Cai, Y. X. Xiang, X. Z. Zhang, J. J. Xu, and F. J. García de Abajo, "Reduced radiation losses in electron beam excited propagating plasmons," Opt. Express **19**(19), 18713–18720 (2011).
211. J. Aizpurua, G. W. Bryant, L. J. Richter, F. J. García de Abajo, B. K. Kelley, and T. Mallouk, "Optical properties of coupled metallic nanorods for field-enhanced spectroscopy," Phys. Rev. B **71**(23), 235420 (2005).
212. G. A. Wurtz, W. Dickson, D. O'Connor, R. Atkinson, W. Hendren, P. Evans, R. Pollard, and A. V. Zayats, "Guided plasmonic modes in nanorod assemblies: strong electromagnetic coupling regime," Opt. Express **16**(10), 7460–7470 (2008).
213. F. M. Wang, H. Liu, T. Li, S. M. Wang, S. N. Zhu, J. Zhu, and W. Cao, "Highly confined energy propagation in a gap waveguide composed of two coupled nanorod chains," Appl. Phys. Lett. **91**(13), 133107 (2007).
214. A. W. Sanders, D. A. Routenberg, B. J. Wiley, Y. N. Xia, E. R. Dufresne, and M. A. Reed, "Observation of plasmon propagation, redirection, and fan-out in silver nanowires," Nano Lett. **6**(8), 1822–1826 (2006).
215. Z. P. Li, F. Hao, Y. Z. Huang, Y. R. Fang, P. Nordlander, and H. X. Xu, "Directional light emission from propagating surface plasmons of silver nanowires," Nano Lett. **9**(12), 4383–4386 (2009).
216. Z. P. Li, K. Bao, Y. R. Fang, Z. Q. Guan, N. J. Halas, P. Nordlander, and H. X. Xu, "Effect of a proximal substrate on plasmon propagation in silver nanowires," Phys. Rev. B **82**(24), 241402 (2010).

217. Z. P. Li, S. P. Zhang, N. J. Halas, P. Nordlander, and H. X. Xu, "Coherent modulation of propagating plasmons in silver-nanowire-based structures," Small **7**(5), 593–596 (2011).
218. W. H. Wang, Q. Yang, F. R. Fan, H. X. Xu, and Z. L. Wang, "Light propagation in curved silver nanowire plasmonic waveguides," Nano Lett. **11**(4), 1603–1608 (2011).
219. P. Bharadwaj, A. Bouhelier, and L. Novotny, "Electrical excitation of surface plasmons," Phys. Rev. Lett. **106**(22), 226802 (2011).
220. D. Solis Jr., W. S. Chang, B. P. Khanal, K. Bao, P. Nordlander, E.R. Zubarev, and S. Link, "Bleach-imaged plasmon propagation (BlIPP) in single gold nanowires," Nano Lett. **10**(9), 3482–3485 (2010).
221. J. C. Weeber, A. Dereux, C. Girard, J. R. Krenn, and J. P. Goudonnet, "Plasmon polaritons of metallic nanowires for controlling submicron propagation of light," Phys. Rev. B **60**(12), 9061–9068 (1999).
222. H. Ditlbacher, A. Hohenau, D. Wagner, U. Kreibig, M. Rogers, F. Hofer, F. R. Aussenegg, and J. R. Krenn, "Silver nanowires as surface plasmon resonators," Phys. Rev. Lett. **95**(25), 257403 (2005).
223. E. Verhagen, M. Spasenović, A. Polman, and L. K. Kuipers, "Nanowire plasmon excitation by adiabatic mode transformation," Phys. Rev. Lett. **102**(20), 203904 (2009).
224. K. Tanaka and M. Tanaka, "Simulations of nanometric optical circuits based on surface plasmon polariton gap waveguide," Appl. Phys. Lett. **82**(8), 1158–1160 (2003).
225. K. Tanaka, T. T. Minh, and M. Tanaka, "Analysis of propagation characteristics in the surface plasmon polariton gap waveguides by method of lines," Opt. Express **17**(2), 1078–1092 (2009).
226. B. Wang and G. P. Wang, "Surface plasmon polariton propagation in nanoscale metal gap waveguides," Opt. Lett. **29**(17), 1992–1994 (2004).
227. D. F. P. Pile, T. Ogawa, D. K. Gramotnev, Y. Matsuzaki, K. C. Vernon, K. Yamaguchi, T. Okamoto, M. Haraguchi, and M. Fukui, "Two-dimensionally localized modes of a nanoscale gap plasmon waveguide," Appl. Phys. Lett. **87**(26), 261114 (2005).
228. S. P. Sundararajan, J. M. Steele, and N. J. Halas, "Propagation of surface plasmons on Ag and Cu extended one-dimensional arrays on silicon substrates," Appl. Phys. Lett. **88**(6), 063115 (2006).
229. H. Raether, "Surface-plasmons on smooth and rough surfaces and on gratings," Springer Trans. Mod. Phys. **111**, 1–133 (1988).
230. J. Jose, F. B. Segerink, J. P. Korterik, A. Gomez-Casado, J. Huskens, J. L. Herek, and H. L. Offerhaus, "Enhanced surface plasmon polariton propagation length using a buried metal grating," J. Appl. Phys. **109**(6), 064906 (2011).
231. G. Veronis and S. H. Fan, "Guided subwavelength plasmonic mode supported by a slot in a thin metal film," Opt. Lett. **30**(24), 3359–3361 (2005).
232. P. B. Catrysse, G. Veronis, H. Shin, J. T. Shen, and S. Fan, "Guided modes supported by plasmonic films with a periodic arrangement of subwavelength slits," Appl. Phys. Lett. **88**(3), 031101 (2006).
233. J. C. Weeber, J. R. Krenn, A. Dereux, B. Lamprecht, Y. Lacroute, and J. P. Goudonnet, "Near-field observation of surface plasmon polariton propagation on thin metal stripes," Phys. Rev. B **64**(4), 045411 (2001).
234. R. Zia, M. D. Selker, and M. L. Brongersma, "Leaky and bound modes of surface plasmon waveguides," Phys. Rev. B **71**(16), 165431 (2005).

235. R. Zia, J. A. Schuller, and M. L. Brongersma, "Near-field characterization of guided polariton propagation and cutoff in surface plasmon waveguides," Phys. Rev. B **74**(16), 165415 (2006).
236. R. Zia and M. L. Brongersma, "Surface plasmon polariton analogue to Young's double-slit experiment," Nat. Nanotechnol. **2**(7), 426–429 (2007).
237. J. T. Kim, J. J. Ju, S. Park, M. S. Kim, S. K. Park, and S. Y. Shin, "Hybrid plasmonic waveguide for low-loss lightwave guiding," Opt. Express **18**(3), 2808–2813 (2010).
238. I. De Leon and P. Berini, "Amplification of long-range surface plasmons by a dipolar gain medium," Nat. Photonics **4**(6), 382–387 (2010).
239. W. L. Barnes, T. W. Preist, S. C. Kitson, and J. R. Sambles, "Physical origin of photonic energy gaps in the propagation of surface plasmons on gratings," Phys. Rev. B Condens. Matter **54**(9), 6227–6244 (1996).
240. S. I. Bozhevolnyi, V. S. Volkov, K. Leosson, and J. Erland, "Observation of propagation of surface plasmon polaritons along line defects in a periodically corrugated metal surface," Opt. Lett. **26**(10), 734–736 (2001).
241. E. G. Mishchenko, A. V. Shytov, and P. G. Silvestrov, "Guided plasmons in graphene p–n junctions," Phys. Rev. Lett. **104**(15), 156806 (2010).
242. A. K. Geim and K. S. Novoselov, "The rise of graphene," Nat. Mater. **6**(3), 183–191 (2007).
243. D. Englund, D. Fattal, E. Waks, G. Solomon, B. Zhang, T. Nakaoka, Y. Arakawa, Y. Yamamoto, and J. Vucković, "Controlling the spontaneous emission rate of single quantum dots in a two-dimensional photonic crystal," Phys. Rev. Lett. **95**(1), 013904 (2005).
244. K. Hennessy, A. Badolato, M. Winger, D. Gerace, M. Atatüre, S. Gulde, S. Fält, E. L. Hu, and A. Imamoğlu, "Quantum nature of a strongly coupled single quantum dot-cavity system," Nature **445**(7130), 896–899 (2007).
245. T. Wilk, S. C. Webster, A. Kuhn, and G. Rempe, "Single-atom single-photon quantum interface," Science **317**(5837), 488–490 (2007).
246. Y. Fedutik, V. V. Temnov, O. Schöps, U. Woggon, and M. V. Artemyev, "Exciton-plasmon-photon conversion in plasmonic nanostructures," Phys. Rev. Lett. **99**(13), 136802 (2007).
247. H. Wei, D. Ratchford, X. E. Li, H. X. Xu, and C. K. Shih, "Propagating surface plasmon induced photon emission from quantum dots," Nano Lett. **9**(12), 4168–4171 (2009).
248. V. J. Sorger, Z. Ye, R. F. Oulton, Y. Wang, G. Bartal, X. Yin, and X. Zhang, "Experimental demonstration of low-loss optical waveguiding at deep sub-wavelength scales," Nat. Commun. **2**, 331 (2011).
249. D. A. Genov, M. Ambati, and X. Zhang, "Surface plasmon amplification in planar metal films," IEEE J. Quantum Electron. **43**(11), 1104–1108 (2007).
250. R. F. Oulton, V. J. Sorger, D. A. Genov, D. F. P. Pile, and X. Zhang, "A hybrid plasmonic waveguide for subwavelength confinement and long-range propagation," Nat. Photonics **2**(8), 496–500 (2008).
251. K. F. MacDonald, Z. L. Sámson, M. I. Stockman, and N. I. Zheludev, "Ultrafast active plasmonics," Nat. Photonics **3**(1), 55–58 (2009).
252. Z. L. Samson, K. F. MacDonald, and N. I. Zheludev, "Femtosecond active plasmonics: ultrafast control of surface plasmon propagation," J. Opt. A-Pure Appl. Op. **11**, 114031 (2009).

253. Z. L. Sámson, P. Horak, K. F. MacDonald, and N. I. Zheludev, "Femtosecond surface plasmon pulse propagation," Opt. Lett. **36**(2), 250–252 (2011).
254. P. Berini, "Plasmon polariton modes guided by a metal film of finite width," Opt. Lett. **24**(15), 1011–1013 (1999).
255. P. Berini, "Plasmon-polariton waves guided by thin lossy metal films of finite width: bound modes of symmetric structures," Phys. Rev. B **61**(15), 10484–10503 (2000).
256. P. Berini, R. Charbonneau, N. Lahoud, and G. Mattiussi, "Characterization of long-range surface-plasmon-polariton waveguides," J. Appl. Phys. **98**(4), 043109 (2005).
257. W. L. Barnes, "Surface plasmon-polariton length scales: a route to sub-wavelength optics," J. Opt. A-Pure Appl. Op. **8**, S87–S93 (2006).
258. P. Berini and I. De Leon, "Surface plasmon-polariton amplifiers and lasers," Nat. Photonics **6**(1), 16–24 (2011).
259. M. Wegener, G. Dolling, and S. Linden, "Plasmonics: backward waves moving forward," Nat. Mater. **6**(7), 475–476 (2007).
260. H. J. Lezec, J. A. Dionne, and H. A. Atwater, "Negative refraction at visible frequencies," Science **316**(5823), 430–432 (2007).
261. H. Shin and S. H. Fan, "All-angle negative refraction for surface plasmon waves using a metal-dielectric-metal structure," Phys. Rev. Lett. **96**(7), 073907 (2006).
262. M. C. Gather, K. Meerholz, N. Danz, and K. Leosson, "Net optical gain in a plasmonic waveguide embedded in a fluorescent polymer," Nat. Photonics **4**(7), 457–461 (2010).
263. J. Grandidier, G. C. des Francs, S. Massenot, A. Bouhelier, L. Markey, J. C. Weeber, C. Finot, and A. Dereux, "Gain-assisted propagation in a plasmonic waveguide at telecom wavelength," Nano Lett. **9**(8), 2935–2939 (2009).
264. P. M. Bolger, W. Dickson, A. V. Krasavin, L. Liebscher, S. G. Hickey, D. V. Skryabin, and A. V. Zayats, "Amplified spontaneous emission of surface plasmon polaritons and limitations on the increase of their propagation length," Opt. Lett. **35**(8), 1197–1199 (2010).
265. S. M. Nie and S. R. Emory, "Probing single molecules and single nanoparticles by surface-enhanced Raman scattering," Science **275**(5303), 1102–1106 (1997).
266. K. Kneipp, Y. Wang, H. Kneipp, L. T. Perelman, I. Itzkan, R. Dasari, and M. S. Feld, "Single molecule detection using surface-enhanced Raman scattering (SERS)," Phys. Rev. Lett. **78**(9), 1667–1670 (1997).
267. K. Kneipp, M. Moskovits, and H. Kneipp, ed., *Surface-Enhanced Raman Scattering: Physics and Applications*, 2006 (Springer-Verlag).
268. P. Mühlschlegel, H. J. Eisler, O. J. F. Martin, B. Hecht, and D. W. Pohl, "Resonant optical antennas," Science **308**(5728), 1607–1609 (2005).
269. M. Danckwerts and L. Novotny, "Optical frequency mixing at coupled gold nanoparticles," Phys. Rev. Lett. **98**(2), 026104 (2007).
270. A. Bouhelier, M. R. Beversluis, and L. Novotny, "Characterization of nanoplasmonic structures by locally excited photoluminescence," Appl. Phys. Lett. **83**(24), 5041–5043 (2003).
271. P. Ghenuche, S. Cherukulappurath, T. H. Taminiau, N. F. van Hulst, and R. Quidant, "Spectroscopic mode mapping of resonant plasmon nanoantennas," Phys. Rev. Lett. **101**(11), 116805 (2008).

272. M. A. Noginov, G. Zhu, A. M. Belgrave, R. Bakker, V. M. Shalaev, E. E. Narimanov, S. Stout, E. Herz, T. Suteewong, and U. Wiesner, "Demonstration of a spaser-based nanolaser," Nature **460**(7259), 1110–1112 (2009).
273. T. Klar, M. Perner, S. Grosse, G. von Plessen, W. Spirkl, and J. Feldmann, "Surface-plasmon resonances in single metallic nanoparticles," Phys. Rev. Lett. **80**(19), 4249–4252 (1998).
274. C. Sönnichsen, T. Franzl, T. Wilk, G. von Plessen, J. Feldmann, O. Wilson, and P. Mulvaney, "Drastic reduction of plasmon damping in gold nanorods," Phys. Rev. Lett. **88**(7), 077402 (2002).
275. E. C. Dreaden, S. Neretina, W. Qian, M. A. El-Sayed, R. A. Hughes, J. S. Preston, and P. Mascher, "Plasmonic enhancement of nonradiative charge carrier relaxation and proposed effects from enhanced radiative electronic processes in semiconductor-gold core-shell nanorod arrays," J. Phys. Chem. C **115**(13), 5578–5583 (2011).
276. H. Okamoto and K. Imura, "Near-field optical imaging of enhanced electric fields and plasmon waves in metal nanostructures," Prog. Surf. Sci. **84**(7–8), 199–229 (2009).
277. A. Bouhelier, J. Renger, M. R. Beversluis, and L. Novotny, "Plasmon-coupled tip-enhanced near-field optical microscopy," J. Microsc. **210**(3), 220–224 (2003).
278. N. Behr and M. B. Raschke, "Optical antenna properties of scanning probe tips: plasmonic light scattering, tip-sample coupling, and near-field enhancement," J. Phys. Chem. C **112**(10), 3766–3773 (2008).
279. R. M. Roth, N. C. Panoiu, M. M. Adams, R. M. Osgood, C. C. Neacsu, and M. B. Raschke, "Resonant-plasmon field enhancement from asymmetrically illuminated conical metallic-probe tips," Opt. Express **14**(7), 2921–2931 (2006).
280. K. Tanaka, M. Tanaka, and T. Sugiyama, "Creation of strongly localized and strongly enhanced optical near-field on metallic probe-tip with surface plasmon polaritons," Opt. Express **14**(2), 832–846 (2006).
281. J. Jiang, K. Bosnick, M. Maillard, and L. Brus, "Single molecule Raman spectroscopy at the junctions of large Ag nanocrystals," J. Phys. Chem. B **107**(37), 9964–9972 (2003).
282. K. R. Li, M. I. Stockman, and D. J. Bergman, "Self-similar chain of metal nanospheres as an efficient nanolens," Phys. Rev. Lett. **91**(22), 227402 (2003).
283. D. R. Ward, F. Hüser, F. Pauly, J. C. Cuevas, and D. Natelson, "Optical rectification and field enhancement in a plasmonic nanogap," Nat. Nanotechnol. **5**(10), 732–736 (2010).
284. J. Jung, T. Sondergaard, and S. I. Bozhevolnyi, "Gap plasmon-polariton nanoresonators: scattering enhancement and launching of surface plasmon polaritons," Phys. Rev. B **79**(3), 035401 (2009).
285. D. K. Gramotnev, D. F. P. Pile, M. W. Vogel, and X. Zhang, "Local electric field enhancement during nanofocusing of plasmons by a tapered gap," Phys. Rev. B **75**(3), 035431 (2007).
286. H. Chul Kim and X. Cheng, "Gap surface plasmon polaritons enhanced by a plasmonic lens," Opt. Lett. **36**(16), 3082–3084 (2011).
287. C. Genet and T. W. Ebbesen, "Light in tiny holes," Nature **445**(7123), 39–46 (2007).
288. H. A. Bethe, "Theory of diffraction by small holes," Phys. Rev. **66**(7–8), 163–182 (1944).

289. R. Gordon, A. G. Brolo, D. Sinton, and K. L. Kavanagh, "Resonant optical transmission through hole-arrays in metal films: physics and applications," Laser Photonics Rev. **4**(2), 311–335 (2010).
290. T. W. Ebbesen, H. J. Lezec, H. F. Ghaemi, T. Thio, and P. A. Wolff, "Extraordinary optical transmission through sub-wavelength hole arrays," Nature **391**(6668), 667–669 (1998).
291. H. F. Ghaemi, T. Thio, D. E. Grupp, T. W. Ebbesen, and H. J. Lezec, "Surface plasmons enhance optical transmission through subwavelength holes," Phys. Rev. B **58**(11), 6779–6782 (1998).
292. R. Gordon, A. G. Brolo, A. McKinnon, A. Rajora, B. Leathem, and K. L. Kavanagh, "Strong polarization in the optical transmission through elliptical nanohole arrays," Phys. Rev. Lett. **92**(3), 037401 (2004).
293. J. Elliott, I. I. Smolyaninov, N. I. Zheludev, and A. V. Zayats, "Polarization control of optical transmission of a periodic array of elliptical nanoholes in a metal film," Opt. Lett. **29**(12), 1414–1416 (2004).
294. P. N. Melentiev, A. E. Afanasiev, A. A. Kuzin, A. V. Zablotskiy, A. S. Baturin, and V. I. Balykin, "Single nanohole and photonic crystal: wavelength selective enhanced transmission of light," Opt. Express **19**(23), 22743–22754 (2011).
295. J. C. Yang, H. W. Gao, J. Y. Suh, W. Zhou, M. H. Lee, and T. W. Odom, "Enhanced optical transmission mediated by localized plasmons in anisotropic, three-dimensional nanohole arrays," Nano Lett. **10**(8), 3173–3178 (2010).
296. L. Martín-Moreno, F. J. García-Vidal, H. J. Lezec, K. M. Pellerin, T. Thio, J. B. Pendry, and T. W. Ebbesen, "Theory of extraordinary optical transmission through subwavelength hole arrays," Phys. Rev. Lett. **86**(6), 1114–1117 (2001).
297. A. Degiron and T. W. Ebbesen, "The role of localized surface plasmon modes in the enhanced transmission of periodic subwavelength apertures," J. Opt. A-Pure Appl. Op. **7**, S90–S96 (2005).
298. H. W. Gao, J. Henzie, and T. W. Odom, "Direct evidence for surface plasmon-mediated enhanced light transmission through metallic nanohole arrays," Nano Lett. **6**(9), 2104–2108 (2006).
299. G. Ctistis, P. Patoka, X. Wang, K. Kempa, and M. Giersig, "Optical transmission through hexagonal arrays of subwavelength holes in thin metal films," Nano Lett. **7**(9), 2926–2930 (2007).
300. T. Thio, K. M. Pellerin, R. A. Linke, H. J. Lezec, and T. W. Ebbesen, "Enhanced light transmission through a single subwavelength aperture," Opt. Lett. **26**(24), 1972–1974 (2001).
301. A. Krishnan, T. Thio, T. J. Kim, H. J. Lezec, T. W. Ebbesen, P. A. Wolff, J. Pendry, L. Martin-Moreno, and F. J. Garcia-Vidal, "Evanescently coupled resonance in surface plasmon enhanced transmission," Opt. Commun. **200**(1–6), 1–7 (2001).
302. L. Martín-Moreno, F. J. García-Vidal, H. J. Lezec, A. Degiron, and T. W. Ebbesen, "Theory of highly directional emission from a single subwavelength aperture surrounded by surface corrugations," Phys. Rev. Lett. **90**(16), 167401 (2003).
303. E. Popov, M. Neviere, S. Enoch, and R. Reinisch, "Theory of light transmission through subwavelength periodic hole arrays," Phys. Rev. B **62**(23), 16100–16108 (2000).
304. E. Altewischer, M. P. van Exter, and J. P. Woerdman, "Plasmon-assisted transmission of entangled photons," Nature **418**(6895), 304–306 (2002).

305. W. L. Barnes, W. A. Murray, J. Dintinger, E. Devaux, and T. W. Ebbesen, "Surface plasmon polaritons and their role in the enhanced transmission of light through periodic arrays of subwavelength holes in a metal film," Phys. Rev. Lett. **92**(10), 107401 (2004).
306. F. J. García-Vidal, H. J. Lezec, T. W. Ebbesen, and L. Martín-Moreno, "Multiple paths to enhance optical transmission through a single subwavelength slit," Phys. Rev. Lett. **90**(21), 213901 (2003).
307. X. Jiao, P. Wang, L. Tang, Y. Lu, Q. Li, D. Zhang, P. Yao, H. Ming, and J. Xie, "Fabry–Perot-like phenomenon in the surface plasmons resonant transmission of metallic gratings with very narrow slits," Appl. Phys. B **80**(3), 301–305 (2005).
308. J. Zhang and G. P. Wang, "Simultaneous realization of transmission enhancement and directional beaming of dual-wavelength light by a metal nanoslit," Opt. Express **17**(12), 9543–9548 (2009).
309. J. Zhang and G. P. Wang, "Dual-wavelength light beaming from a metal nanoslit flanked by dielectric gratings," J. Opt. Soc. Am. B **25**(8), 1356–1361 (2008).
310. A. Karabchevsky, O. Krasnykov, M. Auslender, B. Hadad, A. Goldner, and I. Abdulhalim, "Theoretical and experimental investigation of enhanced transmission through periodic metal nanoslits for sensing in water environment," Plasmonics **4**(4), 281–292 (2009).
311. Q. Q. Gan, L. C. Zhou, V. Dierolf, and F. J. Bartoli, "UV plasmonic structures: direct observations of uv extraordinary optical transmission and localized field enhancement through nanoslits," IEEE Photonics J. **1**(4), 245–253 (2009).
312. D. K. Gramotnev and S. I. Bozhevolnyi, "Plasmonics beyond the diffraction limit," Nat. Photonics **4**(2), 83–91 (2010).
313. H. J. Lezec, A. Degiron, E. Devaux, R. A. Linke, L. Martin-Moreno, F. J. Garcia-Vidal, and T. W. Ebbesen, "Beaming light from a subwavelength aperture," Science **297**(5582), 820–822 (2002).
314. L. L. Yin, V. K. Vlasko-Vlasov, J. Pearson, J. M. Hiller, J. Hua, U. Welp, D. E. Brown, and C. W. Kimball, "Subwavelength focusing and guiding of surface plasmons," Nano Lett. **5**(7), 1399–1402 (2005).
315. L. Lin, X. M. Goh, L. P. McGuinness, and A. Roberts, "Plasmonic lenses formed by two-dimensional nanometric cross-shaped aperture arrays for Fresnel-region focusing," Nano Lett. **10**(5), 1936–1940 (2010).
316. B. Lee, S. Kim, H. Kim, and Y. Lim, "The use of plasmonics in light beaming and focusing," Prog. Quantum Electron. **34**(2), 47–87 (2010).
317. T. Tanemura, K. C. Balram, D. S. Ly-Gagnon, P. Wahl, J. S. White, M. L. Brongersma, and D. A. B. Miller, "Multiple-wavelength focusing of surface plasmons with a nonperiodic nanoslit coupler," Nano Lett. **11**(7), 2693–2698 (2011).
318. C. Chen, J. A. Hutchison, P. Van Dorpe, R. Kox, I. De Vlaminck, H. Uji-I, J. Hofkens, L. Lagae, G. Maes, and G. Borghs, "Focusing plasmons in nanoslits for surface-enhanced Raman scattering," Small **5**(24), 2876–2882 (2009).
319. Q. Chen and D. R. S. Cumming, "Visible light focusing demonstrated by plasmonic lenses based on nano-slits in an aluminum film," Opt. Express **18**(14), 14788–14793 (2010).
320. G. M. Lerman, A. Yanai, and U. Levy, "Demonstration of nanofocusing by the use of plasmonic lens illuminated with radially polarized light," Nano Lett. **9**(5), 2139–2143 (2009).

321. Y. T. Yu and H. Zappe, "Effect of lens size on the focusing performance of plasmonic lenses and suggestions for the design," Opt. Express **19**(10), 9434–9444 (2011).
322. A. R. Davoyan, I. V. Shadrivov, A. A. Zharov, D. K. Gramotnev, and Y. S. Kivshar, "Nonlinear nanofocusing in tapered plasmonic waveguides," Phys. Rev. Lett. **105**(11), 116804 (2010).
323. J. Becker, I. Zins, A. Jakab, Y. Khalavka, O. Schubert, and C. Sönnichsen, "Plasmonic focusing reduces ensemble linewidth of silver-coated gold nanorods," Nano Lett. **8**(6), 1719–1723 (2008).
324. I. S. Maksymov and A. E. Miroshnichenko, "Active control over nanofocusing with nanorod plasmonic antennas," Opt. Express **19**(7), 5888–5894 (2011).
325. M. W. Vogel and D. K. Gramotnev, "Shape effects in tapered metal rods during adiabatic nanofocusing of plasmons," J. Appl. Phys. **107**(4), 044303 (2010).
326. D. K. Gramotnev, M. W. Vogel, and M. I. Stockman, "Optimized nonadiabatic nanofocusing of plasmons by tapered metal rods," J. Appl. Phys. **104**(3), 034311 (2008).
327. S. Berweger, J. M. Atkin, R. L. Olmon, and M. B. Raschke, "Adiabatic tip-plasmon focusing for nano-Raman spectroscopy," J. Phys. Chem. Lett. **1**(24), 3427–3432 (2010).
328. A. Bek, F. De Angelis, G. Das, E. Di Fabrizio, and M. Lazzarino, "Tip enhanced Raman scattering with adiabatic plasmon focusing tips," Micron **42**(4), 313–317 (2011).
329. M. I. Stockman, "Nanofocusing of optical energy in tapered plasmonic waveguides," Phys. Rev. Lett. **93**(13), 137404 (2004).
330. E. Verhagen, A. Polman, and L. K. Kuipers, "Nanofocusing in laterally tapered plasmonic waveguides," Opt. Express **16**(1), 45–57 (2008).
331. N. C. Lindquist, P. Nagpal, A. Lesuffleur, D. J. Norris, and S. H. Oh, "Three-dimensional plasmonic nanofocusing," Nano Lett. **10**(4), 1369–1373 (2010).
332. Z. Y. Fang, H. Qi, C. Wang, and X. Zhu, "Hybrid plasmonic waveguide based on tapered dielectric nanoribbon: excitation and focusing," Plasmonics **5**(2), 207–212 (2010).
333. B. Desiatov, I. Goykhman, and U. Levy, "Plasmonic nanofocusing of light in an integrated silicon photonics platform," Opt. Express **19**(14), 13150–13157 (2011).
334. X. L. He, L. Yang, and T. Yang, "Optical nanofocusing by tapering coupled photonic-plasmonic waveguides," Opt. Express **19**(14), 12865–12872 (2011).
335. K. C. Vernon, D. K. Gramotnev, and D. F. P. Pile, "Adiabatic nanofocusing of plasmons by a sharp metal wedge on a dielectric substrate," J. Appl. Phys. **101**(10), 104312 (2007).
336. D. K. Gramotnev and K. C. Vernon, "Adiabatic nano-focusing of plasmons by sharp metallic wedges," Appl Phys. B Lasers Opt. **86**, 7–17 (2007).
337. S. J. Tan and D. K. Gramotnev, "Analysis of efficiency and optimization of plasmon energy coupling into nanofocusing metal wedges," J. Appl. Phys. **107**(9), 094301 (2010).
338. E. Moreno, S. G. Rodrigo, S. I. Bozhevolnyi, L. Martín-Moreno, and F. J. García-Vidal, "Guiding and focusing of electromagnetic fields with wedge plasmon polaritons," Phys. Rev. Lett. **100**(2), 023901 (2008).

339. A. Yanai and U. Levy, "The role of short and long range surface plasmons for plasmonic focusing applications," Opt. Express **17**(16), 14270–14280 (2009).
340. E. Verhagen, L. K. Kuipers, and A. Polman, "Plasmonic nanofocusing in a dielectric wedge," Nano Lett. **10**(9), 3665–3669 (2010).
341. S. I. Bozhevolnyi, V. S. Volkov, E. Devaux, and T. W. Ebbesen, "Channel plasmon-polariton guiding by subwavelength metal grooves," Phys. Rev. Lett. **95**(4), 046802 (2005).
342. S. I. Bozhevolnyi, V. S. Volkov, E. Devaux, J. Y. Laluet, and T. W. Ebbesen, "Channel plasmon subwavelength waveguide components including interferometers and ring resonators," Nature **440**(7083), 508–511 (2006).
343. S. I. Bozhevolnyi and K. V. Nerkararyan, "Analytic description of channel plasmon polaritons," Opt. Lett. **34**(13), 2039–2041 (2009).
344. V. S. Volkov, S. I. Bozhevolnyi, S. G. Rodrigo, L. Martín-Moreno, F. J. García-Vidal, E. Devaux, and T. W. Ebbesen, "Nanofocusing with channel plasmon polaritons," Nano Lett. **9**(3), 1278–1282 (2009).
345. V. S. Volkov, J. Gosciniak, S. I. Bozhevolnyi, S. G. Rodrigo, L. Martin-Moreno, F. J. Garcia-Vidal, E. Devaux, and T. W. Ebbesen, "Plasmonic candle: towards efficient nanofocusing with channel plasmon polaritons," New J. Phys. **11**(11), 113043 (2009).
346. T. Søndergaard, S. I. Bozhevolnyi, J. Beermann, S. M. Novikov, E. Devaux, and T. W. Ebbesen, "Resonant plasmon nanofocusing by closed tapered gaps," Nano Lett. **10**(1), 291–295 (2010).
347. S. I. Bozhevolnyi and K. V. Nerkararyan, "Adiabatic nanofocusing of channel plasmon polaritons," Opt. Lett. **35**(4), 541–543 (2010).
348. H. Choi, D. F. P. Pile, S. Nam, G. Bartal, and X. Zhang, "Compressing surface plasmons for nano-scale optical focusing," Opt. Express **17**(9), 7519–7524 (2009).
349. D. K. Gramotnev, "Adiabatic nanofocusing of plasmons by sharp metallic grooves: geometrical optics approach," J. Appl. Phys. **98**(10), 104302 (2005).
350. D. F. P. Pile and D. K. Gramotnev, "Adiabatic and nonadiabatic nanofocusing of plasmons by tapered gap plasmon waveguides," Appl. Phys. Lett. **89**(4), 041111 (2006).
351. D. K. Gramotnev, D. F. P. Pile, M. W. Vogel, and X. Zhang, "Local electric field enhancement during nanofocusing of plasmons by a tapered gap," Phys. Rev. B **75**(3), 035431 (2007).
352. C. L. Zhao, J. Y. Wang, X. F. Wu, and J. S. Zhang, "Focusing surface plasmons to multiple focal spots with a launching diffraction grating," Appl. Phys. Lett. **94**(11), 111105 (2009).
353. W. T. Song, Z. Y. Fang, S. Huang, F. Lin, and X. Zhu, "Near-field nanofocusing through a combination of plasmonic Bragg reflector and converging lens," Opt. Express **18**(14), 14762–14767 (2010).
354. L. Li, T. Li, S. M. Wang, S. N. Zhu, and X. Zhang, "Broad band focusing and demultiplexing of in-plane propagating surface plasmons," Nano Lett. **11**(10), 4357–4361 (2011).
355. J. Wang, W. Zhou, E. P. Li, and D. H. Zhang, "Subwavelength focusing using plasmonic wavelength-launched zone plate lenses," Plasmonics **6**(2), 269–272 (2011).
356. Z. W. Liu, J. M. Steele, W. Srituravanich, Y. Pikus, C. Sun, and X. Zhang, "Focusing surface plasmons with a plasmonic lens," Nano Lett. **5**(9), 1726–1729 (2005).

357. Z. W. Liu, J. M. Steele, H. Lee, and X. Zhang, "Tuning the focus of a plasmonic lens by the incident angle," Appl. Phys. Lett. **88**(17), 171108 (2006).
358. Q. Zhang, X. Y. Shan, L. Zhou, T. R. Zhan, C. X. Wang, M. Li, J. F. Jia, J. Zi, Q. Q. Wang, and Q. K. Xue, "Scattering focusing and localized surface plasmons in a single Ag nanoring," Appl. Phys. Lett. **97**(26), 261107 (2010).
359. A. Drezet, A. L. Stepanov, H. Ditlbacher, A. Hohenau, B. Steinberger, F. R. Aussenegg, A. Leitner, and J. R. Krenn, "Surface plasmon propagation in an elliptical corral," Appl. Phys. Lett. **86**(7), 074104 (2005).
360. Z. Y. Fang, Q. A. Peng, W. T. Song, F. H. Hao, J. Wang, P. Nordlander, and X. Zhu, "Plasmonic focusing in symmetry broken nanocorrals," Nano Lett. **11**(2), 893–897 (2011).
361. X. L. Zhu, Y. Zhang, J. S. Zhang, J. Xu, Y. Ma, Z. Y. Li, and D. P. Yu, "Ultrafine and smooth full metal nanostructures for plasmonics," Adv. Mater. (Deerfield Beach Fla.) **22**(39), 4345–4349 (2010).
362. I. P. Radko, S. I. Bozhevolnyi, A. B. Evlyukhin, and A. Boltasseva, "Surface plasmon polariton beam focusing with parabolic nanoparticle chains," Opt. Express **15**(11), 6576–6582 (2007).
363. A. B. Evlyukhin, S. I. Bozhevolnyi, A. L. Stepanov, R. Kiyan, C. Reinhardt, S. Passinger, and B. N. Chichkov, "Focusing and directing of surface plasmon polaritons by curved chains of nanoparticles," Opt. Express **15**(25), 16667–16680 (2007).
364. A. B. EvIyukhin, A. L. Stepanov, R. Kiyan, and B. N. Chichkov, "Efficiency of surface-plasmon-polariton focusing by curved chains of nanoparticles," J. Opt. Soc. Am. B **25**, 1011–1015 (2008).
365. S. Kawata, ed., "Near-field optics and surface plasmon polaritons," in *Topics in Applied Physics*, 2001 (Springer-Verlag).
366. J. B. Pendry, "Negative refraction makes a perfect lens," Phys. Rev. Lett. **85**(18), 3966–3969 (2000).
367. N. Fang and X. Zhang, "Imaging properties of a metamaterial superlens," Appl. Phys. Lett. **82**(2), 161–163 (2003).
368. N. Fang, H. Lee, C. Sun, and X. Zhang, "Sub-diffraction-limited optical imaging with a silver superlens," Science **308**(5721), 534–537 (2005).
369. H. Lee, Y. Xiong, N. Fang, W. Srituravanich, S. Durant, M. Ambati, C. Sun, and X. Zhang, "Realization of optical superlens imaging below the diffraction limit," New J. Phys. **7**, 255 (2005).
370. G. X. Li, H. L. Tam, F. Y. Wang, and K. W. Cheah, "Superlens from complementary anisotropic metamaterials," J. Appl. Phys. **102**(11), 116101 (2007).
371. Y. H. Zhao, A. A. Nawaz, S. C. S. Lin, Q. Z. Hao, B. Kiraly, and T. J. Huang, "Nanoscale super-resolution imaging via a metal-dielectric metamaterial lens system," J. Phys. D Appl. Phys. **44**(41), 415101 (2011).
372. K. W. Kho, S. Zexiang, and O. Malini, "Hyper-spectral confocal nano-imaging with a 2D super-lens," Opt. Express **19**(3), 2502–2518 (2011).
373. Z. K. Zhou, M. Li, Z. J. Yang, X. N. Peng, X. R. Su, Z. S. Zhang, J. B. Li, N. C. Kim, X. F. Yu, L. Zhou, Z. H. Hao, and Q. Q. Wang, "Plasmon-mediated radiative energy transfer across a silver nanowire array via resonant transmission and subwavelength imaging," ACS Nano **4**(9), 5003–5010 (2010).

374. A. Ono, J. Kato, and S. Kawata, "Subwavelength optical imaging through a metallic nanorod array," Phys. Rev. Lett. **95**(26), 267407 (2005).
375. X. F. Wu, J. S. Zhang, and Q. H. Gong, "Metal–insulator–metal nanorod arrays for subwavelength imaging," Opt. Express **17**(4), 2818–2825 (2009).
376. C. M. Soukoulis, S. Linden, and M. Wegener, "Physics. Negative refractive index at optical wavelengths," Science **315**(5808), 47–49 (2007).
377. M. I. Stockman, "Criterion for negative refraction with low optical losses from a fundamental principle of causality," Phys. Rev. Lett. **98**(17), 177404 (2007).
378. W. T. Lu and S. Sridhar, "Superlens imaging theory for anisotropic nanostructured metamaterials with broadband all-angle negative refraction," Phys. Rev. B **77**(23), 233101 (2008).
379. Y. M. Liu, G. Bartal, and X. Zhang, "All-angle negative refraction and imaging in a bulk medium made of metallic nanowires in the visible region," Opt. Express **16**(20), 15439–15448 (2008).
380. B. D. F. Casse, W. T. Lu, Y. J. Huang, E. Gultepe, L. Menon, and S. Sridhar, "Super-resolution imaging using a three-dimensional metamaterials nanolens," Appl. Phys. Lett. **96**(2), 023114 (2010).
381. S. Durant, Z. W. Liu, J. A. Steele, and X. Zhang, "Theory of the transmission properties of an optical far-field superlens for imaging beyond the diffraction limit," J. Opt. Soc. Am. B **23**(11), 2383–2392 (2006).
382. Z. W. Liu, S. Durant, H. Lee, Y. Pikus, N. Fang, Y. Xiong, C. Sun, and X. Zhang, "Far-field optical superlens," Nano Lett. **7**(2), 403–408 (2007).
383. Z. W. Liu, S. Durant, H. Lee, Y. Pikus, Y. Xiong, C Sun, and X. Zhang, "Experimental studies of far-field superlens for sub-diffractional optical imaging," Opt. Express **15**(11), 6947–6954 (2007).
384. Y. Xiong, Z. Liu, C. Sun, and X. Zhang, "Two-dimensional imaging by far-field superlens at visible wavelengths," Nano Lett. **7**(11), 3360–3365 (2007).
385. T. Xu, C. L. Du, C. T. Wang, and X. G. Luo, "Subwavelength imaging by metallic slab lens with nanoslits," Appl. Phys. Lett. **91**(20), 201501 (2007).
386. J. Y. Wang, J. S. Zhang, X. F. Wu, H. Luo, and Q. H. Gong, "Subwavelength-resolved bidirectional imaging between two and three dimensions using a surface plasmon launching lens," Appl. Phys. Lett. **94**(8), 081116 (2009).

**Junxi Zhang** obtained his B.S. degree in applied physics from Harbin University of Science and Technology, China, in 2001. Then he received his Ph.D degree in condensed matter physics from the Institute of Solid State Physics, Chinese Academy of Sciences, in 2006 under the supervision of Professor Lide Zhang. Currently, he is an Associate Professor in the Institute of Solid State Physics, Chinese Academy of Sciences. He has authored and co-authored over 20 peer-reviewed papers. His current research interests are focused on controlled synthesis of one-dimensional nanostructure arrays, tailoring surface plasmons

(e.g., resonance modes, coupling, propagating, and field enhancements) by metal and metal–dielectric nanostructures, and design of devices for nanophotonics.

**Lide Zhang** graduated from Bejing University in 1964 and completed graduated study at the Institute of Metal Research, Chinese Academy of Sciences, in 1968. From 1979 to 1980 he was a visiting scholar at the Institute of Metal Research, Max-Plank Society, in Germany. From 1987, he began to perform research in nanomaterials and nanostructures and founded a nanomaterial and nanostructure laboratory and an application and development center of nanomaterials at the Institute of Solid State Physics, Chinese Academy of Sciences. Professor Zhang was appointed as the chief scientist of National Major Project of Fundamental Research (973 Project) on Nanomaterials and Nanostructures from 1999 to 2004. In 2006, he was awarded the Second Class of National Natural Science on the preparation study of one-dimensional nanowires and their ordered arrays. He has authored and co-authored more than 370 original papers, and these papers have been cited over 10,000 times. He has also authored and edited 12 scientific references and books.